Modeling the Microstructural and Micromechanical Influence on Effective Properties of Granular Electrode Structures

with regard to Solid Oxide Fuel Cells and Lithium Ion Batteries

Zur Erlangung des akademischen Grades

DOKTOR DER INGENIEURWISSENSCHAFTEN

der Fakultät für Maschinenbau
Karlsruher Institut für Technologie (KIT)

genehmigte

DISSERTATION

von

Dipl.-Ing. Julia Katharina Ott

Tag der mündlichen Prüfung: 25.09.2015
Hauptreferent: Prof. Dr. M. Kamlah
Korreferent: Prof. Dr. H. J. Seifert

Abstract

The objective of this work is to study the microstructure and its influence on parameters relevant for the performance of electrochemical cells—used for energy storage and conversion. For this, the porous electrode microstructure of solid oxide fuel cells (SOFCs) and lithium ion batteries (LIBs) are modeled as a binary mixture of electronic and ionic conducting particles to estimate effective properties.

Reviewing relevant cell losses leads to the conclusion that effective transport properties and the extent of active surface area significantly influence the cell performance. Both parameters are dependent on connectivity of the particles to current collector and electrolyte. To investigate the impact of microstructure on those parameters, particle packings of 10,000 spherical, binary sized and randomly positioned particles are created numerically and densified under consideration of the different manufacturing processes in SOFC and LIB: the sintering of SOFC electrodes is approximated geometrically; and the calendering process and the volume change due to intercalation in LIB are modeled physically by a discrete element approach. A combination of a tracking algorithm and a resistor network approach is developed to predict the connectivity, effective conductivity and active surface area for the various densified structures.

For SOFC, a systematic study of the effect of morphology on the relevant properties is performed for a large number of assemblies with different compositions and particle size ratios between 1 and 10. In comparison to percolation theory, an enlarged percolation area is found, especially for large size ratios. It is shown that in contrast to former studies the percolation threshold correlates to varying coordination numbers. The effective conductivity increases with volume fraction as well as with size ratio. The active surface area—denoted three-phase boundary (TPB) in SOFC—decreases, on the other hand, with size ratio, and best results were achieved for monosized mixtures of 50%:50% volume fraction of electron to ion conducting material. Further, we found significant deviation between the numeric and the analytic results for those calculations: the numerically determined effective conductivities were in general lower than predicted by the analytic approaches. Conversely, the active TPB length found numerically was larger than the one found for the analytic approach. Finally, for both effective parameters—independent of size ratio—increasing densification is beneficial; therein, the densification is a measure for the degree of sintering. In order to assess the impact of the two contrarily improving cell properties, an adapted Tanner-Fung-Virkar (TFV) model was implemented, which allows to estimate the combined effect of those on the effective cell resistance. With this model, the positive influence of densification on the cell efficiency is pointed out as well. It appears that the choice of an appropriate combination of volume fractions and size ratio is much more relevant for cell performance than the choice of one of those factors itself.

Besides the composition, the effect of micromechanics, including contact forces and particle rearrangement, on the electrode microstructure during calendering and intercalation is of relevance in LIB: mechanical particle interactions affect the stress development in the electrode structure, this is associated with mechanical degradation; and it affects the connectivity, which is relevant for the

transport of the reactants. In LIB electrodes, the connectivity of the electron conducting carbon black (CB) is in particular of interest for badly conducting active material, such as $Li_xMn_2O_4$ (LMO) or Li_xFePO_4 (LFP). The importance of the calendering process for the connectivity within the CB network and for the connectivity of AM particle to CB was demonstrated. With a preload correlated to a percolation probability of around 60%, the connectivity is maintained throughout the intercalation process. For the highest studied volume fractions of 15% CB, the best results for connectivity and free surface area were achieved; additionally, this composition is correlated to the lowest intercalation induced stress. Further, the impact of the binder phase on the mechanical behavior was investigated in the framework of dynamic discrete element simulations; therefore, the binder material polyvinylidenefluoride (PVDF) was implemented in form of the Burgers' model. The significant impact of the PVDF distribution within the electrode and of the loading rate on the stress development during loading was demonstrated.

Zusammenfassung

Ziel dieser Arbeit war es, die Mikrostruktur von elektrochemischen Zellen, die zur Energiewandlung und -speicherung eingesetzt werden, zu untersuchen und deren Einfluss auf die Zellleistung zu bestimmen. Zu diesem Zweck wurde die poröse Elektrodenstruktur von Festelektrolyt-Brennstoffzellen (SOFC) und Lithium-Ionen-Batterien (LIB) vereinfacht als Zweikomponenten-Mischung dargestellt, die aus elektronisch und ionisch leitenden Partikeln besteht.

Die Betrachtung der auftretenden Zellverluste in experimentellen Arbeiten legt nahe, dass insbesondere die effektiven Transporteigenschaften und die reaktive Oberfläche der Mikrostruktur von Bedeutung sind. Beide Parameter hängen wiederum von der Anbindung der Partikel zu den Ableitern und der Elektrolytschicht ab. Um den Einfluss der Mikrostruktur auf diese Größen zu untersuchen, wurden Partikelstrukturen generiert, die 10.000 zufällig verteilte Kugeln mit binärer Größenverteilung enthalten. Anschließend wurden diese Kugelpackungen verdichtet, um eine zusammenhängende Struktur zu erzeugen. Der Verdichtungsprozess war dabei an den Fertigungsprozess angelehnt: Das Sintern der SOFC-Elektroden wird rein geometrisch angenähert; Kalandrieren und Interkalation in LIB-Elektroden wird mittels eines Diskreten Elemente Models physikalisch simuliert. Zusätzlich wurde ein Tracking Algorithmus in Kombination mit einem Widerstands-Potential Verfahren implementiert, um die Konnektivität der Partikel, sowie die effektive Leitfähigkeit der verdichteten Strukturen und deren aktive Oberfläche zu bestimmen.

Bei den Brennstoffzellen lag der Fokus dieser Arbeit auf dem Einfluss der Zusammensetzung der Zweikomponenten-Mischung. Zur Untersuchung wurde eine Vielzahl verschiedener Mischungen mit Partikelgrößenverhältnissen von 1 bis 10 erzeugt. Verglichen mit Resultaten der Perkolationstheorie wurde ein vergrößerter Bereich von ausreichend zusammenhängenden Strukturen gefunden. Zudem wurde festgestellt, dass - im Unterschied zu früheren Untersuchungen - kein Zusammenhang zwischen Perkolationsübergang und Koordinationszahl besteht. Die effektive Leitfähigkeit beider Phasen nimmt mit steigendem Volumenanteil der jeweiligen Phase zu, zudem sind grössere Radienverhältnisse günstig. Im Gegensatz dazu wurde die größte aktive Oberfläche, in SOFC als Drei-Phasen Grenze bekannt, für Strukturen ohne Größenverteilung und einem Mischungsverhältnis von 50:50% Volumenanteile gefunden. Die numerischen Ergebnisse weichen stark von den analytisch bestimmten Werten ab: Die effektive Leitfähigkeit ist kleiner und die Drei-Phasen Grenze ist größer als die analytischen Resultate. Neben den vorherigen Betrachtungen ist noch zu festzustellen, dass beide Parameter unabhängig von Mischungs- und Größenverhältnissen durch stärkeres Verdichten positiv beeinflusst werden; die Verdichtung ist dabei ein Maß für den Versinterungsgrad. Um den Einfluss der zwei sich gegensätzlich entwickelnden Parameter zu bestimmen, wurde ein leicht verändertes Tanner-Fung-Virkar (TFV)-Modell eingesetzt, mit dessen Hilfe der kombinierte Einfluss dieser Parameter auf den Zell-Widerstand bestimmt werden kann. Auch bei diesen Untersuchungen wird der positive Effekt der Verdichtung herausgestellt. Darüberhinaus scheint es hauptsächlich wichtig zu sein, dass Volumenanteile dem Größenverhältnis entsprechend gewählt werden - die einzelnen Größen selbst haben weniger Einfluss.

In LIB-Elektroden ist neben der Zusammensetzung auch die Mikromechanik, also Kontaktkräfte und Partikelumordnung, wichtig: Zum einen wird die makroskopische Spannung dadurch beeinflusst, die wiederum mit Zellalterung in Verbindung gebracht wird, zum anderen wirkt sich die Mikromechanik auch auf die Konnektivität der Partikel aus. Konnektivität ist in LIB-Elektroden insbesondere für das Elektronen leitende Leitruß(carbon black (CB)) von Bedeutung, vor allem bei schlecht leitenden Aktivmaterialien, wie z.B. $Li_xMn_2O_4$ (LMO) oder Li_xFePO_4 (LFP). In den durchgeführten Simulationen wurde die Bedeutung des Kalandrierens für das Entstehen von ausreichend Transportpfaden und die Anbindung des Aktivmaterials aufgezeigt. Mit einer Vorspannung, die zu einer Perkolationswahrscheinlichkeit der Struktur von um die 60% führt, kann das leitende Netzwerk während der Interkalation aufrecht erhalten werden. Die besten Resultate für Konnektivität und aktive Oberfläche wurden für die Mischungen mit dem höchsten untersuchten Volumenanteil von CB (15% CB) bestimmt; zusätzlich verursacht diese Mischung auch die geringsten mechanischen Spannungen. Darüber hinaus wurde im Rahmen von dynamischen DEM Simulationen noch der Effekt der Binderphase auf das mechanische Verhalten untersucht; dazu wurde das Bindermaterial polyvinylidenefluoride (PVDF) in Form des Burgers-Modells zur Beschreibung der Kontaktkräfte implementiert. Dabei wurde gezeigt, dass die PVDF- Verteilung in der Elektrodenstuktur sowie die Belastungsrate großen Einfluss auf die Spannungsentwicklung haben.

List of Symbols

Term	Description	Units
$\vec{a}$	acceleration	m/s^2
c_0	initial Li^+ concentration	mol/m^3
c_{max}	maximum Li^+ concentration	mol/m^3
c_x	present Li^+ concentration	mol/m^3
$d^{\iota,\Upsilon}$	distance between centers of particle ι and Υ	m
E	Young's Modulus	GPa
$\vec{f}$	force	N
$\vec{f_N}$	normal force	N
$\vec{f_T}$	tangential force	N
I	current	A
J	moment of inertia	kgm^2
$\vec{j}$	current density	A/m^2
j_0	exchange current density	A/m^2
L	edge length of volume element	m
l	corrugation length in TFV model	m
M	number of solid components in a composite	-
m	mass	kg
$\vec{n}$	contact normal	-
n_i	number of i type particles in a configuration	-
P	percolation probability	-
R	resistance	Ω
r	radius	m
r_c	contact radius	m
R_{ct}	intrinsic charge transfer resistance of TPB	$\Omega\ m^2$
S	specific surface area of porous electrode	m^2/m^3
T	temperature	K
t	time	s
U_s	potential difference across the electrode-electrolyte interface	V
V	volume	m^3
$\vec{x}^{\iota}$	position of particle ι	N
Z_0	overall coordination number	-
Z_c	critical coordination number at which percolation threshold takes place	-
$Z_{k,k}$	number of contacts a particle of species k has to particles of the same species	-

Greek Symbols

Term	Description	Units
$\vec{\Gamma}$	moment	Nm
ϵ	porosity	-
$\dot{\varepsilon}$	strain rate	s^{-1}
ζ	surface area fraction	-
κ	conductivity	S/m
μ	frictional coefficient	-
ν	Poisson's ratio	-
$\overline{\Omega}$	dimensionless partial molar volume	-
ξ	particle number fraction	-
ϕ	solid volume fraction	-
φ	potential	V
σ_{ij}	stress tensor	Pa
σ_h	hydrostatic stress	Pa
τ	tortuosity	-
θ	contact angle	$^\circ$

Subscripts

bulk	bulk properties of material
CB	carbon black phase
eff	effective properties of composite material
i	iteration variable
k	arbitrary phase of composite
l	large particle phase of composite
s	small particle phase of composite

Acronyms

AM	active material
CB	carbon black
DEM	discrete element modeling
EIS	electrochemical impedance spectroscopy
FIB-SEM	focused ion beam scanning electron microscopy
HK	Hoshen-Kopelman algorithm
LCO	$LiCoO_2$

LFP	Li_xFePO_4
LIB	lithium ion battery
LMO	$Li_xMn_2O_4$
LSM	strontium-doped lanthanum manganite
Ni	nickel
NiO	nickel oxide
PBC	periodic boundary condition
PF	packing factor
PVDF	polyvinylidenefluoride
RCP	random close packing
RN	resistor-network approach
SOFC	solid oxide fuel cell
TFV	Tanner-Fung-Virkar
TPB	three-phase boundary
YSZ	yttria-stabilized zirconia

Contents

1. Introduction

Limited availability of today's primary energy resources, along with local and global negative effects of emission of pollutants on the environment, necessitates reconsideration of our energy consumption. Especially, energy conversion processes in gasoline engines and power plants have been questioned: Their upper efficiency limit of heat engines is given by the Carnot cycle, which is a theoretical process assuming an ideally reversible combustion process. In that process, the efficiency is only dependent on the temperature difference between the injection and combustion of the fuel. Due to materials restrictions, the possible temperature difference is limited, and thus, the overall efficiency as well: the electricity production from natural gas varies from 33% for gas turbine units to 55% for combined-cycle power plants [1]. Thus, in the last decade, the search for efficient and clean alternatives for power generation and transportation has been intensified. In that process, electrochemical cells attracted increasing attention in research, e.g. rechargeable batteries for energy storage and transportation and fuel cells for energy conversion. Electrochemical cells convert chemical energy directly in electric energy, without the detour of conversion in thermal energy and mechanical work performed in conventional power plants or combustion engines. Avoiding the Carnot cycle limitations, those cells can potentially convert chemical stored energy in electrical energy in a highly efficient manner. Even nowadays, fuel cells convert fuel in electric energy with an efficiency up to 65%, depending on fuel and conditions. In the future, this may go up to more than 70% [2]. In rechargeable batteries up to 95% of the stored energy can be regained [3]. Clearly, this is not considering the efficiency of the generation of electric energy necessary to charge the cell.

1.1. Electrochemical cells

In general, electrochemical cells are composed of two electrodes connected by an ionically conductive material called electrolyte. The cells use the transfer of electrons in redox reactions to produce an electric current, by physically separating the oxidation (anode) and reduction (cathode) half-reactions in space. When the electrodes are connected, the reaction progresses and the electrons flow from the reductant to the oxidant over the external electrical connection. Ions move through the electrolyte changing between the electrode compartments, thereby, maintaining the system's electrical neutrality. The cell voltage depends on the difference in electric potential of reductant and oxidant materials.

The cells can be classified in two main categories: Open systems, like fuel cells, are supplied with an external masses, whose chemical energy is converted in electrical energy. Closed systems, like batteries, on the other hand, are thermodynamically closed systems, which convert internally stored chemical energy in electric energy. Nevertheless, due to the similarities of the cell structure, working principles, and cell processes, many research methods—experimentally as well as computationally—are similar for the different kinds of electrochemical cells. The preferable system depends on the area of application.

Considering the conversion of fuel, fuel cells offer the cleanest possible process as they produce much less greenhouse emission compared to heat engines. In stationary applications, like small power plants (5 kW – 3 MW), high temperature fuel cells are often favored due to their fuel flexibility. As most of H_2 produced today comes from hydrocarbon resources (typically CH_4), it is energetically advantageous if that can be used directly without further reforming, which, on the other hand, is required in low temperature fuel cells [4]. Additionally, no noble metal catalysts are required at high temperatures, allowing the use of cheaper materials. Besides, the waste heat can be used for heating in residential applications—this increases the efficiency further. A promising representative of high temperature fuel cells is the solid oxide fuel cell (SOFC), which operates at temperatures between 700 and 1000°C. Additionally to highest fuel flexibility, the use of a solid oxide electrolyte reduces corrosion problems, which are occurring in liquid electrolyte systems. The all solid state system has high flexibility in cell design, offering possibilities for further cost reduction and efficiency increase [5]. High temperature fuel cells are best utilized as a steady energy source and not as power source to supply dynamic demands. SOFCs in particular start up slowly, with times ranging from 2 to 6 hours, due to thermal shock problems of the ceramic electrolyte in the composite structure [6].

In the future, the expected shortage of natural oil and gas resources will lead to an increasing usage of alternative energy sources such as solar, wind, and water power. As wind and solar power are not available on demand—they depend on wind intensity and sunshine duration—storage of electric energy with as little as possible losses becomes more and more important. Additionally, for applications requiring varying power demands, such as automotive propulsion, a rechargeable battery is more suitable than a fuel cell, as it can handle regenerative breaking, acceleration and quick initial start-up. For all transported energy supplies—from mobile phones to electric vehicles—lightweight solutions are beneficial. Concededly, in comparison with fuel or gasoline, which stores the energy used in combustion engines and fuel cells, the gravimetric and volumetric energy density (Wh/kg respectively Wh/l) of batteries is still rather low, as illustrated in Fig. 1.1. This leads to large masses (and volumes), which need to be transported, reducing the overall efficiency of e.g. electric vehicles. For those to become comparable in range to today's solutions, the energy density as well as the cell durability needs to be improved. Among battery systems, lithium ion batteries (LIBs) benefit from the properties of the element lithium, which is both the most electropositive and lightest metal. Besides their high electrode potential, the most relevant advantage of LIB cells is the high energy density (Fig. 1.1). This already allows for integrating them into small electronic devices and makes them the system of choice in electric transportation.

Even though the electrochemical cells have large potential, e.g. to reduce greenhouse gas and increase the fuel efficiency, their potential is not yet fully exploited. In order to draw near the theoretical potential and compete with heat engines, efficiency, energy density (especially in LIB), and durability must be improved. Therefore, it is necessary to understand where the deviation from the theoretically excellent performance originates. The power output is limited when the cell supplies current to an external load: the operating voltage drops due to irreversibilites associated with internal charge transfer, conduction and diffusion processes [8]. Additionally, cell degradation during operating life leads to increasing losses. Hence, efficiency decreases further during life-time until cell failure, which in many cases is defined as a certain amount of degradation.

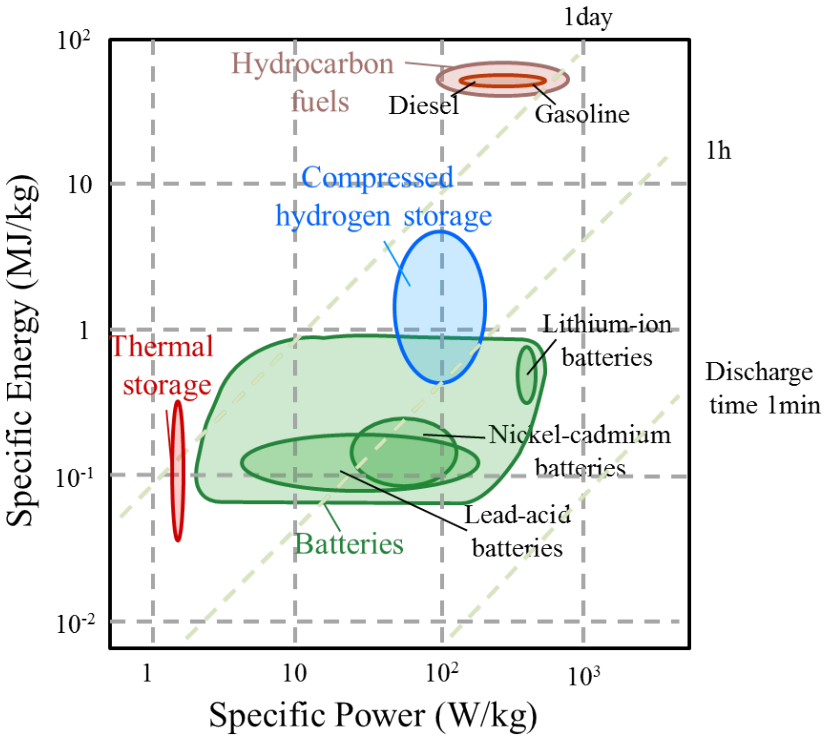

Figure 1.1.: Comparison of power density against energy density of energy storage systems with lines of charge/discharge time [7]

1.2. Cell optimization

To reduce those losses, and thus, improve cell performance, there are basically two different approaches: (i) material selection to optimize the relevant intrinsic material properties and (ii) tuning of the electrode structure. At first, we briefly discuss the selection of materials, which has been intensively investigated. This choice is closely related to the working principles of the cell; therefore, those have to be understood first. Subsequently, the influence of microstructure on electrode performance is briefly introduced.

1.2.1. Material selection

As described previously, fuel cells are open systems, in which the anode and cathode are just charge-transfer media, and the active masses, undergoing the redox reactions, are delivered from the outside of the cell. In SOFC, the reduction and oxidation occur spatially separated by a dense solid electrolyte layer. At the cathode supplied molecular oxygen is reduced

$$\frac{1}{2}O_2 + 2e^- \rightarrow O^{2-}, \tag{1.1}$$

consuming electrons and leading to a positive charging of the cathode. At the anode, the supplied fuel is oxidized by reacting with the ions transported through the electrolyte

$$H_2 + O^{2-} \rightarrow 2e^- + H_2O, \tag{1.2}$$

as shown in Fig. 1.2. During oxidation electrons are set free, and therefore, the anode is charged negatively. Additionally water vapor is formed. The resulting difference in potential leads to a current through an external circuit. The material choice is therefore mainly determined by

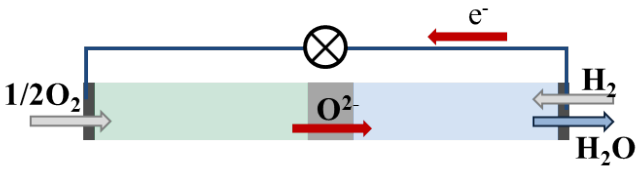

Figure 1.2.: Schematic of solid oxide fuel cell (SOFC)

the dense electrolyte—whose oxygen ion transport properties have the largest impact on the ohmic losses. Although various solid electrolytes with high ionic conductivities at moderate temperatures, such as Scandium-stabilized Zirconia (ScSZ), Cerium oxide (CeO_2), and Lanthanum gallate ($LaGaO_3$), have been explored, yttria-stabilized zirconia (YSZ) is the by far most used solid electrolyte (see [9] for an overview of the different electrolyte materials). Even though its conductivity is lower than in the other materials, its excellent stability in both reducing and oxidizing environments, its processability, and its cost-effectiveness are good reasons for its use. The selection of the electrode material—pure charge-transfer medium—is only limited due to the elevated temperatures and required comparability to the ion-conductor. Besides a thermal expansion coefficient similar to electrolyte, good electronic conductivity and catalytic activity with regards to the proceeding reaction are required. This leads to a nickel (Ni)/YSZ composition for the anode and strontium-doped lanthanum manganite (LSM)/YSZ mixture for cathode in most cells.

Batteries or accumulators, on the other hand, are thermodynamically closed systems, converting internally stored chemical energy in electric energy. In contrast to open systems, the choice of electrode material determines the cell potential and the energy density of closed cells. In LIB, the delivered current is a transport of electrons e^-, from the anode to the cathode, that is correlated with a transport of lithium ions Li^+, also from the anode to the cathode. At the anode, lithium atoms are oxidized

$$Li \rightarrow Li^+ + e^- \tag{1.3}$$

and, at the cathode, the electrons and the lithium ions, which have been transferred from the anode via the external circuit and the electrolyte, respectively, are recombined together by reduction

$$Li^+ + e^- \rightarrow Li. \tag{1.4}$$

The process is schematically depicted in Fig. 1.3. Even though a pure lithium metal anode would

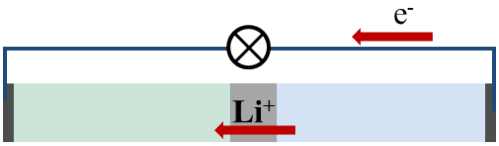

Figure 1.3.: Schematic of lithium ion battery (LIB)

lead for those systems to the highest energy density, its utilization as anodic material is limited

because of safety issues due to the high reactivity. Among the problems, the formation of dendrites at the anode surface is most harmful: those may penetrate the electrolyte and reach the cathode, causing a short circuit in the battery [10]. Such a short circuit in a battery causes overheating and gives rise to thermal runaway.

There exist plenty of other potential candidates, which can be used as anode materials. Carbonaceous materials, like lithium graphite (Li_xC_6), are nowadays widely used as anode material since they provide a high delivered electrode potential. Despite a higher self-discharge rate compared to pure lithium metal, such materials significantly improve the battery reliability in terms of safety. Cathode materials are most commonly insertion compound materials, which allow the reversible insertion of lithium-ions at specific locations of the crystalline host structure. This process is referred to as intercalation. A comprehensive overview of the intercalation process as well as the standard cathode materials can be found in [11] chapter 2 or [12]. Among those materials, LMO and LFP are promising electrode materials for LIBs in terms of cost, high theoretical capacity and stability; however, low electric conductivity limits the field of application. To compensate this, the materials are combined with additives like CB to enhance electric conductivity. The favored material for power batteries used for transportation, where safety issues are crucial, is Li_xFePO_4 at present time: it is the only positive electrode that can pass all safety tests [13].

As the focus of this work is on the microstructure, we used the material properties of the standard materials of both electrochemical cell types.

1.2.2. Microstructure

Besides material selection, tuning morphological parameters is a key to improve cell performance and thus efficiency. Regardless of optimization of bulk properties, the morphology always significantly affects cell performance; therefore, a general understanding of the relation of electrode microstructure and cell performance is essential for tailored cell design. In this context, **effective material properties** are important parameters: they characterize the deviation from the bulk property due to microstructure and composition with a value averaged over the complete electrode structure (or a representative volume element).

The most important step in improvement of cell performance based on morphology was the introduction in form of foam-like, porous electrodes, as illustrated in Fig. 1.4.

In order to increase the reactive area—the energy releasing electrochemical reactions take place when all reactants come in contact—and reduce the diffusion path length, the electrodes are formed of a mixture of small sized particles in the range of a few microns down to several nanometers [14, 12, 15, 16]. In SOFC, that mixture is made of ionic (YSZ) and electric (Ni in the anode, LSM in the cathode) conducting powders [17] in both electrodes. In LIB, the anode is formed of carbonaceous particles; the cathode is made of insertion material and, additionally, CB, which is added to enhance the intrinsically low electrical conductivity of the insertion material [18]. While the porous structure is implemented to increase the reactive area, the reactions can only take place, when all reactants can be transported to the sites. This makes the connectivity within each phase crucial, as the transport of electrons, ions, and further reactants to and from the active sites must be sustained. In summary, the electrode structures of SOFCs and LIBs are very similar: Both form a porous, granular structure, which contains ion conducting particles as well as electron conducting particles. For both, the composite structure leads to the requirement of connectivity within the different conducting phases to achieve sufficient transport of the reactants

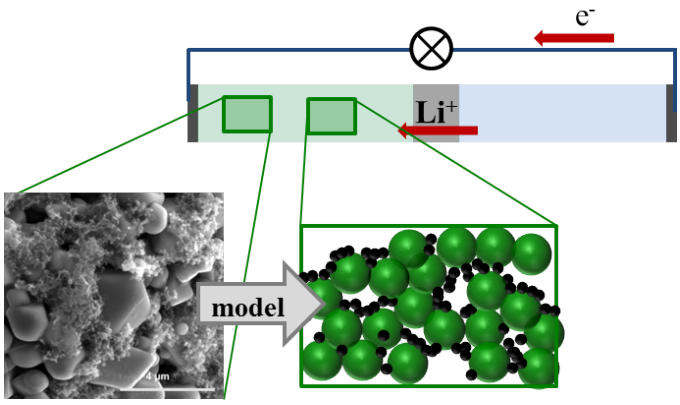

Figure 1.4.: LIB electrodes with section of a real electrode (left) and schematic (right) as usually used to represent the granular microstructure

to the reaction sites. It is most likely that for both the properties relevant for performance are the same as well. This similarities enable us to apply the same methods for the investigations of microstructure, connectivity, and further relevant electrode parameters. It additionally allows us to transfer knowledge from fuel cells—due to their longer history more research has been conducted—to LIB.

Additionally, in both, the particle structure needs to be densified in some way to obtain a connected composite structure. Besides the composition, the fabrication process chosen for densification defines the microstructure to a large extent. Different processes are applied for the two cell types. To take those influences into account, the fabrication processes of the electrodes will be introduced here.

Fabrication process

At first in the design process, composition and particle sizes of the mixtures are specified; subsequently, fabrication processes with variable process parameters enable tailored manufacturing of microstructures.

In SOFC, we will focus on a planar, anode supported design: this means, the anode is thick enough (usually between 0.3 and 1.5mm) to support the cell mechanically during fabrication. In that case, electrolyte and cathode can be very thin ($<20\mu$m), thus the ohmic resistance of the dense electrolyte layer can be reduced significantly [19]. During manufacturing nickel oxide (NiO) and YSZ are mixed according to the desired volume fraction, usually around 55% volume fraction to 45%, respectively. Then, the mixture is die-pressed and sintered. The NiO in the sintered anode structures is reduced to Ni metal on exposure to hydrogen. The LSM–YSZ (weight ratio of 50:50) composite cathode and the pure LSM cathode current collector layer are in turn printed on the surface of dense YSZ film by a brush painting method, followed by a last firing step [17]. Temperature and time of the sintering steps significantly influence the final microstructure of the electrode to a large amount [20].

In LIB, the electrodes are formed from pastes of active material powders, binders, solvents, and additives; the pastes are fed to coating machines to be spread on current collector foils, usually aluminum for the cathode side and copper for the anode side [21]. In a subsequent

calendaring step the electrode material is rolled to obtain homogeneous thickness and improve particle-to-particle contact. The components are then stacked to anode-separator-cathode stacks and filled with the liquid electrolyte. Besides composition, also the calendering step strongly affects the cell characteristics [22, 23]—thus, it should be considered in the investigations of the electrode structure.

In order to tailor an optimized electrode microstructure, we need to inquire how the fabrication processes influence connectivity and active surface area.

Operating life of LIB

Additionally, a cell microstructure defined initially by design and manufacture is expected to evolve during its operating life in both, SOFC and LIB, electrodes [24, 25]. As degradation of LIB, correlated to microstructural evolution among other things, is a serious issue with regard to cell life time, the morphological changes during operating life should be examined. Mechanical interactions, correlated with particle fracture and contact losses, are assumed to irreversibly worsen the cell losses. The mechanical interaction occurs, as the insertion materials of the cathode experience reversible volume changes when the LIB cell is in use: During discharge, the Li^+ ions are intercalated in the host structure, accompanied by a volume expansion of the active material. The volume expansion varies between a few and 300%, depending on the material. This process is reversed during charging of the cell, when the Li^+ ions are deintercalated. Reversible swelling of particles in a limited space obviously leads to mechanical interaction of the particles, which can be accompanied by rearrangement of particles, contact loss and particle failure in the electrode. This, in turn, is correlated with mechanical degradation of the cell [24]. Even though a change in microstructure is assumed to influence the cell performance, the influence of contact forces and particle rearrangement was neglected in the majority of research on mechanical degradation [26] and will therefore be addressed in this work.

1.3. Objectives of this work

The short description of the electrochemical cells, and of the interaction of fabrication, microstructure, and performance given here provides a first impression of the complexity of the systems. An important question for cell optimization is how tuning of the electrode microstructure allows to improve cell performance. Hence, the main objective of the performed investigations in this work was to study the influence of microstructural electrode properties on the cell losses for promising electrochemical cells, namely for SOFC and LIB electrodes. Therefore, the relevant cell losses must be singled out at first; and an adequate investigation method, which enables us to consider the influence of varying electrode composition and different fabrication processes, has to be established subsequently. Based on that, the impact of composition and manufacturing on the relevant electrode properties can then be studied in order to gain general understanding and determine optimization possibilities.

As will be shown in section 2.3, a huge number of experiments has been performed in order to study different compositions and morphologies—and their influence on cell performance. Due to the vast amount of process parameters and environmental factors, it has, however, proven difficult to deconvolute individual parameters experimentally. Nevertheless, a general consensus on the most relevant loss mechanisms was found. To investigate individual properties relevant

for cell performance separately, modeling of the electrode structure is useful to decouple the electrochemical cell processes.

As described previously, the electrode structures of SOFC and LIB are—besides the densification step—very similar; and thus, the same modeling approaches are applicable for their investigation. To find a realistic representation of the experimental findings, different approximation methods were reviewed. There exits a vast number of such methods; they can be roughly divided into averaging methods and approaches based on numerically generated microstructures. 3D microstructures with randomly distributed spherical particles offer the possibility to consider varying compositions as well as the different fabrication processes and evolution of the microstructure. For this, methods to approximate the fabrication step have to be implemented. Additionally, a fast and flexible calculation approach for effective electrode properties, e.g. connectivity and transport properties, has to be established to obtain relevant information on the influence of morphology on electrode losses for varying 3D microstructures.

Regarding SOFC electrodes, the focus is on the impact of composition, morphology, and sintering conditions on the microstructure and transport processes of SOFC electrodes, as previous studies suggested performance improvement with varying size ratio and composition (see section 2.3 and 3.2). Therefore, the adequate range of compositions—sufficient connectivity is required for proper cell functioning—has to be detected; and the impact of varying fabrication conditions on effective transport properties can be studied. Additionally, the combined effect of the most relevant cell parameters should be investigated in order to consider the contradicting influence on cell losses. Based on this, recommendations for electrode optimization can be obtained.

Besides the composition, the effect of micromechanical particle rearrangement on the microstructure of LIB electrodes during calendering and intercalation has to be studied. The influence of mechanical load on connectivity has to be considered to guarantee sufficient transport of the reactants. The amount of calendering, required for reliable cell function, can thus be determined under consideration of the composition. In addition to the effective transport properties, also the mechanical stress, induced by the loading processes, as the stress development is related to mechanical degradation.

In summary, first the relevant cell losses have to be determined, and based on that, an appropriate modeling approach has to be implemented. Comparison of analytically and numerically found results, under consideration of experimental results, allows to assess the accuracy and sources of error due to simplifications. With those methods, the influence of composition and fabrication process on microstructure and on the relevant cell parameter can be studied for SOFC and LIB electrodes in order to obtain recommendations for optimized cell design. Therefore, in chapter 2, the typical loss mechanisms in electrochemical cells are presented. Additionally, experimental findings are reviewed to determine the parameters most relevant for cell efficiency. Further, analytic approximation methods for the relevant cell parameters and the findings based on those are reviewed in chapter 3. subsequently, in chapter 4, the microstructural modeling is presented: At first, the numerical approximation of undensified microstructures is described. The different densification approaches—mimicking the fabrication process—are introduced later in the respective chapters 5.1 and 6.1 separately. The algorithms to determine connectivity and further transport properties are introduced and validated additionally in chapter 4. Subsequently, those approaches are applied for the investigation of SOFC microstructures with focus on varying composition in chapter 5. Then, the LIB electrode structures are studied in chapter 6 under consideration of mechanical loading, modeled with a discrete element method.

2. Efficiency and its link to electrode structure

This theoretical chapter introduces the different loss mechanisms relevant in electrochemical cells; thereby it establishes a first correlation of the losses and the microstructure of the electrodes. Further, experimental studies on the relation of microstructure and efficiency are reviewed, and the properties most relevant for cell performance are determined.

2.1. Basic characteristics of composite materials

As described in section 1.2.2, the electrodes considered here are manufactured from granular powders of both ion and electric conducting particles, resulting in a porous composite structure. In literature, the two types of particles are commonly referred to as ion and electron conducting phases; this denotation was adopted in this work.

To understand the influence of morphology on loss mechanism, the most relevant characteristics of composite materials are introduced first for more clarity. A composite can be described by its porosity ϵ, solid volume fraction of the components ϕ, and particle size ratio or size distribution. In this work, the porosity ϵ is defined as the ratio of pore space V_{por} to total volume

$$\epsilon = \frac{V_{por}}{V_{por} + \sum_i^M V_i} \tag{2.1}$$

and the solid volume fraction ϕ as the ratio of the volume V of one arbitrary phase k to the sum of all solid phases $\sum_i^M$:

$$\phi_k = \frac{V_k}{\sum_i^M V_i} \text{ with } \sum_i^M \phi_i = 1 \tag{2.2}$$

with M as the number of solid components and i as iteration variable.

2.2. Loss mechanisms in electrochemical cells

To get a general understanding of the loss mechanisms[1], we take a look at the processes reducing the power output from the maximum energy possible for a given reaction at equilibrium [27]. As shown in Fig. 2.1, the voltage drops off compared to the open circuit voltage when current is drawn from the electrochemical cell.

[1] It should be noted the term "loss" used here is equivalent to the terms "overpotential" and "polarization" commonly found in electrochemistry literature. In electrochemistry, all three terms refer to the potential difference (voltage) between the thermodynamically determined potential at equilibrium conditions and the potential that is experimentally observed

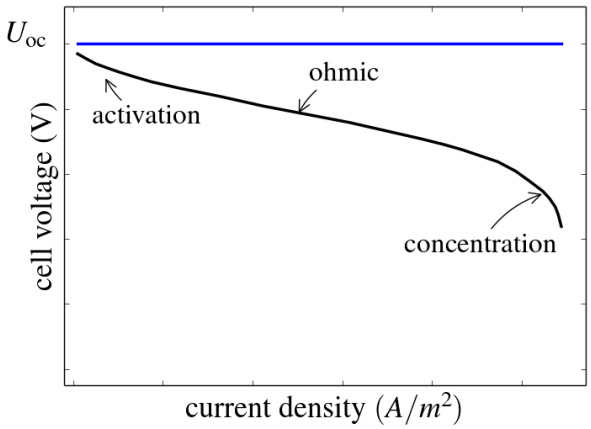

Figure 2.1.: Losses reducing the theoretical cell voltage of electrochemical cells [19, 27]

The losses in electrochemical cells are due to kinetic limitations of reactions and other processes taking place during cell operation and can all be related to transport phenomena [28].

The three main causes for cell losses [19, 27]: (i) ohmic polarization, (ii) activation polarization, and (iii) concentration polarization are briefly described next.

2.2.1. Ohmic losses

The ohmic losses, describing the resistance of flow of ions and electrons, increase constantly with increasing current density $\vec{j}$ over a large range. In general, the transport phenomena within the cells are modeled in each phase separately and linked at the reactive surface. In an arbitrary solid phase k, the charge transport is governed by Ohm's law:

$$\vec{j_k} = -\kappa_k \nabla \varphi_k \tag{2.3}$$

with κ_k the conductivity (in S/m), φ_k the potential (in V) and $\vec{j_k}$ as current density in the solid phase k (A/m^2). Generally, the current density is related to the current I through an area $\vec{a}$ by the surface integral $I = \int_A \vec{j} d\vec{n}$ with $d\vec{n}$ normal to the surface. In a homogeneous field this can be reduced to $I = jA$, assuming the current density is normal to the surface. Under consideration of electrode microstructure and composition, the conductivity is reduced to the effective conductivity, which is the reciprocal of the overall ohmic resistance of the continuous composite material.

Two important characteristics for the evaluation of the conductivity in granular structures are: (i) the percolation probability P_k and (ii) the tortuosity τ_k of the solid phase k. The **Percolation probability** is the likelihood, that particles of the species k—either ionic or electronic conducting—form a connected pathway through the volume element (which in this work is the electrode). This is directly related to the conductivity: Without a percolating path through the structure of one phase, the transport of this charge carrier is impossible and the ohmic resistance of this phase approaches infinity. At a certain—critical—volume fraction of the phase in consideration, a connecting path through the structure is found; at that point, conductivity within this phase is possible. The transition from non-conducting compositions to conducting compositions is referred

to as percolation threshold. Above the critical volume fraction, the effective conductivity of this phase increases steadily as increasing number of connections are formed. This correlation is depicted schematically in Fig 2.2. The analytic determination of the percolation probability P will be explained in detail in section 3.1.2.

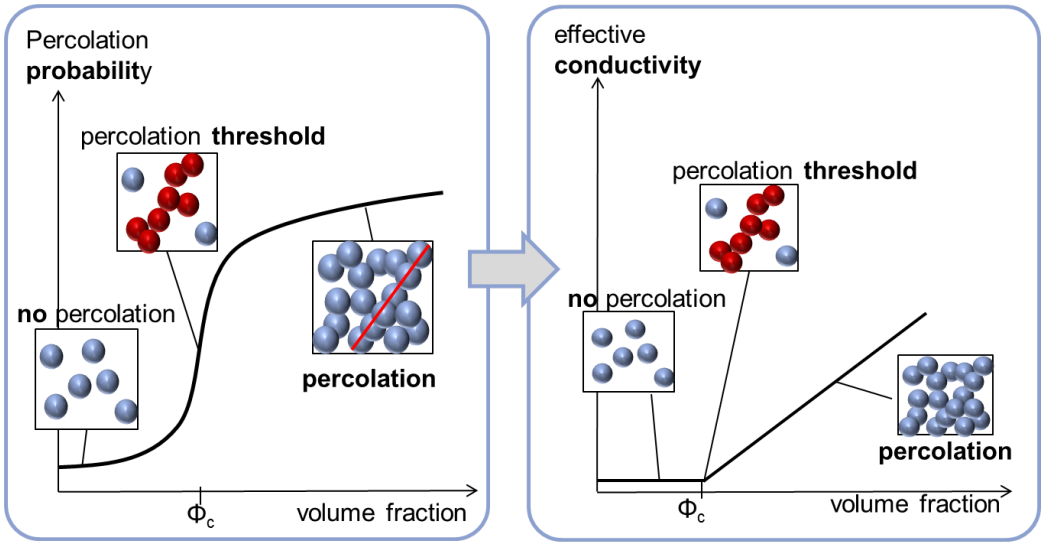

Figure 2.2.: Percolation probability and effective conductivity against volume fraction

The **tortuosity** τ describes the sinousness of the connected pathway through the volume; it was initially defined as the ratio of the real path length l through the composite to the Euclidean distance x [29]

$$\tau = \frac{l}{x}. \tag{2.4}$$

Clearly, the actual length of the transport path influences the effective conductivity of the phase. Owing to the direct relation between tortuosity and transport properties, the tortuosity can also be specified in terms of the experimentally easier accessible transport properties, as discussed for example in [30, 31, 32]. Both, percolation probability and tortuosity, strongly depend on volume fraction, porosity, and particle size ratios of the composition.

In both, solid oxide fuel cell (SOFC) and lithium ion battery (LIB), electrons must be transported from the current collector and ions from the electrolyte layer to the reaction site. Additionally, in SOFC, gaseous fuels need to diffuse through the pore space and reach the active sites. As thus three transport channels have to be in contact for the reactions, these contact zones are called three-phase boundary (TPB) in SOFC. For a TPB to be active, the electronic conducting phase needs to be connected to the current collector, the yttria-stabilized zirconia (YSZ) phase to the solid electrolyte and the pore space to the gas inlet (and outlet). In LIB, the Li^+-ions are transported in the liquid electrolyte, recombine with electrons at the electrolyte-insertion material surface and diffuse inwards due to concentration gradients. For the recombination, electrons need to travel from external circuit to the active material—therefore a connecting path in the electron connecting phase is required. In summary, the energy releasing reactions only take place at zones where all reactants are in contact; thus, connectivity and good transport properties of all phases are essential for cell performance.

2.2.2. Activation polarization

The electrochemical charge-transfer reactions at the electrode/electrolyte interface involve energy barriers, those must be overcome by the reacting species. That energy barrier is called the "activation energy" and results in activation polarization[2], which is due to the transfer of charges between the electronic and the ionic phases. The flux of the reacting species, accompanied by charge transfer, is a function of the potential difference across the local electrode-electrolyte interface U_s and the local concentration of the reacting species across the surface. Many electrode-electrolyte systems show an exponential relation between the flux as well as the current density $\vec{j}$ and the potential drop across the surface; thus, activation losses dominate at low current densities and decrease with increasing current density. The current density $\vec{j}_{\mathrm{BV}}$ at the electrolyte-electrode interface can be given by the Butler-Volmer equation as [8]:

$$j_{\mathrm{BV}} = \vec{j} \cdot \vec{n} = j_0(exp(\frac{F}{2RT}(U_s - U_{oc})) - exp(-\frac{F}{2RT}(U_s - U_{oc})), \tag{2.5}$$

assuming that anodic and cathodic transfer coefficients both equal to 0.5 [33]. In here, $\vec{n}$ is the unit vector normal to the surface, F is the Faraday's constant, R as gas constant and T the temperature. The local overpotential, which is required to overcome the reaction barrier energies at the interface, is defined as $U_s - U_{oc}$ with U_s as the potential difference across the electrode-electrolyte interface and U_{oc} as the voltage of the cell at open circuit (= at equilibrium). Further, the exchange current density j_0 describes the anodic and cathodic current at equilibrium[3] and depends on the local concentration of reactants and products [8]. In SOFC, j_0 can be described as a function of partial pressure in the gas phase [34], and in LIB, it is a function of the local Li-concentration in electrolyte and active material [35].

In electrochemical cells, the current density at an interface is related to the flux of the reactive species through the interface simply by the charge each reactant carries. With charge balance, the local transport of ions and electrons is related by

$$\vec{j}_{io} \cdot \vec{n} = -\vec{j}_{el} \cdot \vec{n} = j_{\mathrm{BV}}, \tag{2.6}$$

with $\vec{n}$ as vector normal to the electrode-electrolyte surface of the particles. To understand the beneficial impact of a porous electrode structure on cell performance, let us take the specific interfacial area per unit of electrode volume S into account (in $\mathrm{m}^2/\mathrm{m}^3$). With this, the overall charge transfer per unit of electrode volume can be calculated as Sj_{BV} by considering the local charge transfer, integrated over all reaction zones. Simplifying the model to a 1D continuous cell level model, the ionic and the electronic conducting phase are no longer resolved separately, but considered as superposed: each point of the electrodes has both properties of the ionic and the electronic phase. Additionally, Sj_{BV} is considered as a source term. Charge conservation for the one-dimensional model leads to

$$\frac{\partial}{\partial x} j_{io} = -\frac{\partial}{\partial x} j_{el} = S j_{\mathrm{BV}}. \tag{2.7}$$

Further, the total current density entering the electron conducting phase is equivalent to the external usable current density of the electrode. Thus, for a constant charge-transfer rate j_{BV},

[2] also denoted as charge-transfer resistance

[3] At equilibrium the overpotential is zero ($U_s - U_{oc} = 0$) and the amounts of the anodic and cathodic current densities (j_a and j_c respectively) are the same and define the exchange current density j_0 ($\mid j_a \mid = \mid j_c \mid = j_0$); thus, the net current density is zero $j(U_s - U_{oc} = 0) = 0$

a larger specific surface area S leads to larger external current densities. As small local current densities can be achieved by a smaller local overpotential. This, in turn, reduces the charge-transfer losses; hence, a large specific interfacial area is beneficial for cell performance.

2.2.3. Concentration losses

Concentration losses are associated with diffusion limitations of the reactants: concentration gradients due to slow mass transport lead to depletion of the species at the interface and thus, a drop in local voltage. This becomes prominent at very high current densities and can be mitigated by providing sufficient pore space [36]. To determine the distributions of reactants, mass and species conservation has to be solved under consideration of the charge-transfer rates. Within the solid phases, the mass diffusion can be estimated with Fick's law, for the gaseous transport several other models exits, e.g. the dusty-gas model [19].

Due to the complexity and the coupled mechanism in the electrode structure, optimizing the microstructure to improve one loss mechanism usually penalizes the other properties. As a result, the question which cell structure leads to best performance is not easily answered and not conclusively solved today. The variety of research on this topic can be divided roughly into three approaches: (i) experimental methods, (ii) analytic description with averaging methods and (iii) so-called Monte-Carlo simulations, which include all approaches that are based on the generation of random numbers. To get an indication of important parameters, experimental findings are shortly reviewed. Subsequently, analytic and numerical methods, which are generally used for estimation of cell properties, are introduced, and their applicability is assessed based on the reviewed experimental studies.

2.3. Experimental research

Huge progress has been made in experimental cell characterization during the last decade. In the early days, SOFC and LIB experiments have been mainly empirical: certain cell design parameters were changed and the cell voltage was monitored. The impact of torosity [37, 38, 39], volume fractions of the solid phases [37, 40, 41, 42], particle size [40, 15, 43] and size distribution [15, 38], electrode thickness [23, 39], and process parameters like temperature and time during sintering in SOFC [44, 45], or pressure during the calendering process in LIB [46, 22] has been studied in that way. Over and above the cited examples, a vast amount of work has been done in this area. The realized studies agree on the fact that the microstructure significantly influences the cell performance. Due to the complex system, there is, however, no consensus on the rate-limiting morphological parameter. Even strongly simplified model experiments have difficulties to decouple kinetic and geometrical effects. Furthermore, as discussed in the reviews by Mogensen and Skaarup [47], Brett et al. [48], or Fergus [49], findings of different studies are difficult to compare due to the various process routes in electrode preparation and, especially in LIB, the manifold material compositions. Slightly more insight can be gained with electrochemical impedance spectroscopy (EIS), which determines dynamic behavior over a large range of frequencies via cyclic loading. Comparing the results for different cell compositions allows to correlate the losses in electrochemical systems to certain processes.

Finally, since Wilson et al. [50] first reported three-dimensional reconstruction of a SOFC electrode in 2006, it is possible to directly obtain information on morphological parameters. In Fig. 2.3, the reconstruction of an entire state-of-the-art SOFC cell is shown exemplarily [17]. Coupling

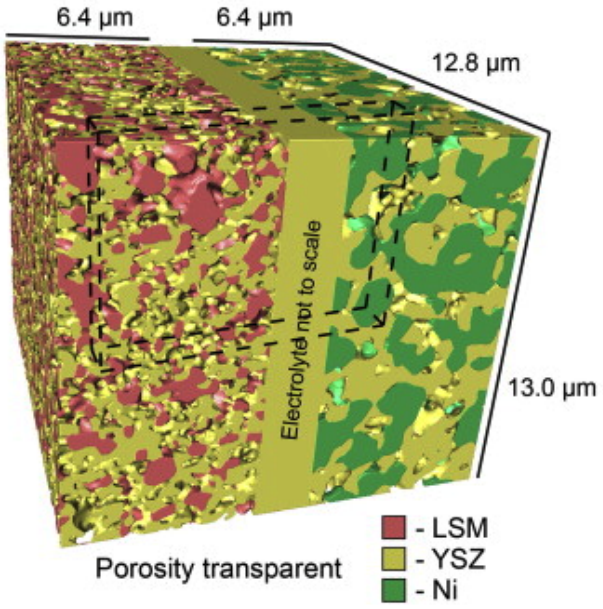

Figure 2.3.: 3D reconstruction image showing the solid phases of a SOFC structure, with cathode on the left and anode on the right side [17]

reconstruction with numerical methods and cell performance measurements permits to correlate certain microstructural aspects to changes in performance. The reconstruction process involves the successive imaging (by SEM) and then milling away (by FIB) of consecutive, closely-spaced slices of material to obtain a series of SEM micrographs, which, when aligned and stacked, form a 3D image of the material's microstructure [51]. A detailed description of this method can be found in [52]. For non-destructive 3D reconstruction of the electrodes, X-ray computed nanotomography (XCT) can be used, as described in detail by Izzo et al. [53]. Further details, including a variety of examples on all kind of energy materials are explained in a review by Cocco et al. [51]. A variety of composite materials has been studied and properties like surface area, connectivity, tortuosity and pore space have been characterized with that approach. Particularly for the determination of connectivity in the phases, three-dimensional information is mandatory.

In the following we will briefly summarize the experimental findings used as a basis for the further modeling work for SOFC and LIB separately.

2.3.1. Findings for solid oxide fuel cells

As discussed in [47], the results from empirical investigations on SOFC electrodes are not conclusive; however, they indicate that the extent of TPB is related to cell performance. Only with 3D reconstructions of the microstructure, the connectivity within the phases can be determined, and thus, the active fraction of TPB—the fraction that actually participates in the energy releasing reaction. Additionally, volume fractions, surface areas, and tortuosity of the phases can be determined. It was demonstrated that good connectivity in combination with a large extent of

active TPB is dominating the cell performance. Furthermore, the effective conductivity of the YSZ phase influences the overall resistivity, whereas the electron conducting phase as well as the gas phase show little influence—when sufficient connectivity is maintained [54, 14]. Presumably, the little influence of the electron conducting phase is due to the fact that the electronic bulk conductivities are orders of magnitudes larger than the ionic bulk conductivity. Further, the influence of the gas phase is negligible as the concentration polarzation is minimal in thin electrodes. The total amount of TPB increases with decreasing particle size; this is significantly influenced by initial particle size and sintering conditions: higher sintering temperatures lead to coarsening of the microstructure. This reduces, on the one hand, the total amount of TPB, but, on the other hand, it improves the connectivity within the phases. The conflicting influence of sintering conditions on cell properties necessitates for a trade-off of connectivity and active TPB. Besides particle size and sintering conditions, the particle size ratio is an important parameter on the extent of TPB and the connectivity as well. So far, it was only investigated for compositions with the same volume fraction for different size ratios of ion conducting to electron conducting particles. That study showed no conclusive trend for size ratios deviating from 1 [14]. Duong and Mumm [14] recommend, however, in their study to consider various volume fractions for the different size ratios in future research as the percolation threshold varies with size ratio.

2.3.2. Findings for Lithium ion batteries

In LIB, the empirical investigations are even more difficult to compare due to the vast variations of cell chemistries used in research [49]. With regard to particle size, one general finding is that small particles are favorable as they provide high surface area and short diffusion distances. When particles become too small (<15nm), processes other than the surface reaction, e.g. diffusion of ions in the electrolyte, become rate limiting and the cell performance is not further improved [43]. In this work, we focus on intermediate particle sizes, assuming that particle size does not play an important role in this range. In Li_xFePO_4 (LFP) electrodes for example, no clear dependence of rate capacity was found for a particle size range of 50–400 nm [16]. In this way, mean particle size effects are excluded; the important design parameters considered here are mechanical compression during calendering and the volume fraction of additives.

In various studies on the impact of calendering via EIS, decreasing contact resistance and increasing charge-transfer resistance (activation polarization) were detected for different cell chemistries [22, 55, 46, 56, 23]. Additionally, calendering increases the contact between particles itself as well as between particles and current collector; it also decreases porosity and free surface area [23], as illustrated in Fig. 2.4. Based on that, the measured decrease in contact resistance is associated

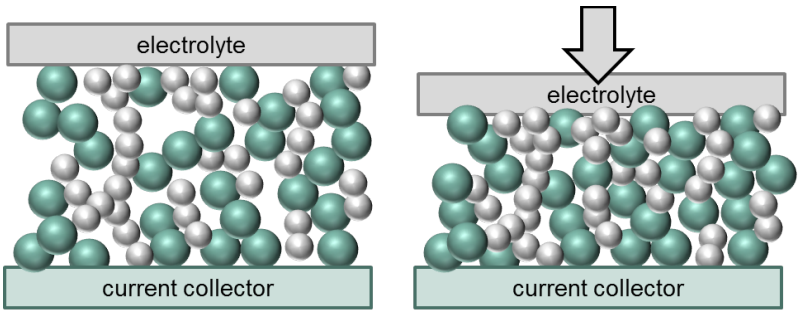

Figure 2.4.: Sketch of the influence of calendering on the electrode microstructure

with increasing contact area, and the detected increase in charge transfer resistance is associated with the decreasing free surface. These conflicting trends in combination led in [22] to a minimum overall resistance of the cell in the range of 30 to 40% porosity. Nevertheless, further investigations are necessary to evaluate the assumptions made about the correlations and subsequently, to find a trade-off for the two opposing effects of increasing charge transfer resistance and decreasing contact resistance. In contrast to those steadily changing cell losses, concentration polarization only becomes relevant for porosities below 10% [22, 55]. Regarding electron conductivity, in [22] a nearly constant value is found for all compression states, in [55], on the other hand, the compression from the uncompressed state to 40% porosity shows large effect on electronic conductivity. Furthermore, Chen et al. [57] reported significant changes of the electron conductivity during calendering the microstructures to porosities between 30 to 50%. Thus, the results here are inconclusive.

With regard to the composition, we focus on standard LIB cells, which are usually composed of the insertion material, conducting powders, such as carbon black (CB)—added to enhance electronic conductivity of the composite electrodes—and a polymeric binder, usually polyvinylidenefluoride (PVDF), which is used for mechanical stability and connectivity. As stated by Qi et al.[58], the cell performance is negatively influenced by poor electronic conductivity. This is in particular relevant for cathode materials with bad intrinsic conductivity, like LFP—its bulk conductivity is below 10^{-7} S/m—or $Li_xMn_2O_4$ (LMO) with conductivities below 10^{-3} S/m. The Li-insertion process is dependent on electron transport, as only active material particles with sufficient electron supply participate in the intercalation process [59]. For the poorly electron conducting materials, the relevance of CB is shown for example in [42, 59, 18]: the specific capacity (gravimetric as well as volumetric) of the tested cells increased with increasing carbon content. Even for better conducting $LiCoO_2$ (LCO) materials, a dependence of cell capacity on CB content was shown in [18]. Besides the dependence on CB content, clear percolation thresholds were shown, demonstrating that a certain amount of additives is required for proper cell performance. The percolation threshold of CB for LMO or LCO materials is usually found between 0 and 15 vol.% of carbon, depending on the active particle size. In [60] for example it was determined at 3 vol. % CB (2 wt. %) in LMO electrodes. For the badly conducting LFP material, the maximum performance is not reached for the maximum tested amount of 15 vol. % CB [42]; the capacity increases rather with increasing CB content. Supposedly, that is due to an increasing number of electron conducting paths; this increases the amount of active material accessible to Li^+/e^- insertion. In summary, a large CB content increases the electrical conductivity and connects the active material particles to the electron conducting network. Nevertheless, it also decreases specific power and energy as the nonactive material occupies volume of the electrode.

The connectivity of the electron conducting network is not only dependent on the composition, it also depends on the calendering. Studying the impact of calendering on electrodes with additives in a weight ratio of CB to binder of 4:5 showed different performance optima for for different amount of additives: For a mixture of 6.4 wt. % CB, the best performance is measured at 40% porosity; for 3.2 wt. % CB it is determined at 20% porosity for 4% binder. Thus, it appears that a lower amount of CB requires a higher amount of densification to reach good performance [61]. Further, comparing different amounts of CB-binder added to the electrode and different compression rates indicates that the composition has more influence on cell capacity than compression [62].

2.3.3. Electrode parameters relevant for performance

Summarizing the experimental findings, in both, SOFC and LIB electrodes, percolation is an issue that has to be addressed: Proper cell performance can only be achieved, when both solid phases in SOFC and the electron conducting phase in LIB is sufficiently connected. Furthermore, in both cell types, inner-phase transport, associated with ohmic losses, as well as the active area, associated with activation losses, are relevant for cell performance. The inner-phase transport, or conductivity is more relevant for the ion conducting phase in SOFC and, in contrast, for the electron conducting phase in LIB. As inner-phase transport properties and active area are assumed to change in conflicting way, a trade-off has to be found. Concentration losses, on the other hand, are negligible when sufficient porosity is maintained ($>$ 10 - 20%). Thus, in the further course of this work, we assume that connected pore-space is granted for porosities higher than 15%.

3. Effective properties of granular media

3D reconstructions provide a great deal of quantitative information about the complexity of electrodes. They offer, however, relatively little predictive capability as they only reflect on few yet existing systems; as they are time-consuming and expensive [63], only few systems have been studied so far. Due to the vast amount of process parameters and environmental influence, there is little consensus as to what constitutes a good microstructure. Deconvoluting the contributions of different variables to microstructural evolution remains challenging [36]. To provide a more complete picture of the connection between microstructure and cell performance, electrochemical cell modeling is an important tool. The modeling is based on charge conservation and mass conservation in combination with the transport and charge transfer equations described in section 2.2. Even though locally resolved, three-dimensional simulations are possible, it is preferable to use a reduced one-dimensional approach without the explicit representation of the microstructure to reduce computational effort. This reduction in computational effort allows to conduct parameter studies with various compositions and electrode morphologies.

In locally resolved 3D-models the material properties are the bulk properties of the different phases; in the reduced one-dimensional models, in contrast, the heterogeneous structure is replaced with a hypothetical material which yields the same response for the same conditions. The equivalent properties of this hypothetical material are referred to as effective properties [64]. Thus, the porous composite electrode material is considered as a homogeneous one-component material with average surface area per unit volume, effective conductivity and diffusivity, effective mechanical properties etc. As the influence of microstructure is condensed to the effective cell properties used as input data, a careful approximation of these parameters is essential. The experimental findings allow to assess the theoretical approximation approaches.

Numerous models have been proposed in the last century for the estimation of effective properties required for simplified electrochemical models of porous composite electrodes. In all kinds of scientific fields, such approximations have been used to assess e.g. elastic properties, thermal properties, electric and fluid transport properties. As this field is too broad to give a complete overview, only the approaches with relevance to the scope of this work will be introduced here. For the interested reader the reviews of Meredith [65], Choy [66] and Torquato[67] provide more detailed information. The equations in the following are given in terms of electric conductivity, even though they are valid for various material properties.

Regarding the approaches, it can be distinguished between averaging methods, derived analytically for simplified microstructures, or Monte-Carlo methods, determined based on numerically generated microstructures. In this chapter, the averaging methods commonly used in research on LIB and SOFC—effective medium theory and percolation theory, respectively—are introduced. Furthermore, the findings based on those methods are summarized; and finally, open questions arising thereby are be addressed.

3.1. Averaging methods

The most basic methods allow to calculate effective properties based on the porosity and the solid volume fractions of the different phases only. As, however, already stated by Hashin and Shtrikman [68], volume fractions and bulk properties of the phases are not sufficient to determine effective properties of random media exactly. Thus, for the derivation of bounds and volume averaging approaches, the microstructure is idealized in some fashion, and exact solutions are found for these idealizations. Calculation of the properties of layered structures in parallel and series connection offer the upper and the lower bounds for the effective properties. Those formulations are known as Wiener bounds or as Voigt and Reuss approximation for elastic modulus [67, 64]. Each value above the upper or below the lower Wiener bounds is physically not sound. The upper bound for M solid phases in parallel is determined as

$$\kappa_{\text{eff}} = \sum_{i}^{M} \kappa_i \phi_i, \tag{3.1}$$

and the lower bound is found assuming the phases in series, i.e.

$$\kappa_{\text{eff}} = \frac{1}{\sum_i^M \frac{\phi_i}{\kappa_i}}. \tag{3.2}$$

Obviously, those bounds allow only for a rough estimate of the effective conductivity due to the large simplification of the microstructure. In the systems representing the electrode structures—one phase is always isolating—the lower bound becomes zero for all cases.

It exists a large number of more rigorous bounds for binary heterogeneous composites, for example the well-known Hashin-Shtrikman (HS) model [68]. In order to obtain more rigorous bounds, the assumptions made about the microstructure, have to be more rigorous as well. Thus, clearly, not all bounds are applicable for all composite materials, as the materials have to match the assumptions made in the derivation of the bounds. Following the argumentation of Carson et al. [69], porous composites can be divided into materials with internal porosity and materials with external porosity. Internal porosity describes materials composed of a continuous matrix structure, which contains enclosed pore space. Materials of external porosity, on the other hand, describe granular materials with a continuous gas phase. The requirements of electrochemical electrodes for sufficient gas transport in SOFC and liquid electrolyte transport in LIB demand materials with external porosity. Carson et al. further proposed that the effective conductivity of materials with external porosity is bounded above by the equation given in effective media theory and below by the lower HS bound. For the derivation of the HS bounds, a two-phase composite material is approximated as a material consisting of spherical particles with cores of one material, surrounded by shells of the second material. The lower HS bound considers the material of higher conductivity as the spherical cores, and the phase with lower conductivity forms the shell. Thus, the less conducting phase is continuous, and additionally, it separates the cores of higher conductivity. As, however, the less conducting phase is isolating in the composites considered in this work, the lower bound is reduced to 0. For the calculation of the upper bound the effective medium theory is introduced next.

3.1.1. Effective medium approximations

Widely used for the estimation of effective transport properties are the effective medium approximations, which were first introduced by Bruggeman in 1935 [70]; they are based on the mathematical solution for the disturbance of a homogeneous field due to a spherical inclusion, as for example derived by Maxwell. To do so, a single sphere of radius r_p and conductivity κ_2 is considered to be in an infinite matrix with conductivity κ_1, as sketched in Fig. 3.1. An unidirectional and constant intensity field $\vec{E}_0$ is applied at great distance of the sphere. The

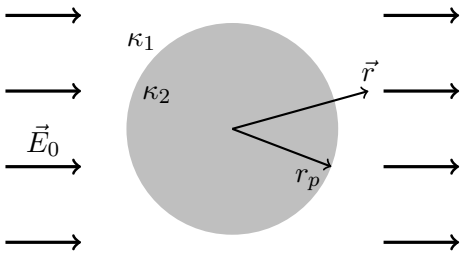

Figure 3.1.: Single spherical inclusion of conductivity κ_2 in an infinite matrix of conductivity κ_1 and an intensity field $\vec{E}_0$ applied at large distance

potential distribution can be determined with Laplace's equation

$$\nabla^2 \varphi = 0, \tag{3.3}$$

as continuity must be satisfied everywhere, including the boundaries of the spherical inclusion. The mathematical solution for the potential distribution inside and around the sphere can be found in e.g. [67], chapter 17. With $\vec{r}$ as the position vector originating in the center of the sphere (see Fig. 3.1), the potential can be given as

$$\varphi = \begin{cases} -\vec{E}_0 \cdot \vec{r} + \beta_{21} \vec{E}_0 \cdot \vec{r} (\frac{r_p}{r})^3, & \text{if } r \geq r_p, \\ -\vec{E}_0 \cdot \vec{r} + \beta_{21} \vec{E}_0 \cdot \vec{r}, & \text{if } r \leq r_p. \end{cases} \tag{3.4}$$

with $r \equiv \mid \vec{r} \mid$ and β_{21}, denoted as the polarizability, defined by

$$\beta_{21} = \frac{\kappa_2 - \kappa_1}{\kappa_2 + 2\kappa_1}. \tag{3.5}$$

The intensity field $\vec{E} = -\nabla\varphi$ can be given as

$$\vec{E} = \begin{cases} \vec{E}_0 + \beta_{21} r_p^3 \frac{3\vec{n}\vec{n} - \mathbf{I}}{r^3} \vec{E}_0, & \text{if } r > r_p, \\ \vec{E}_0 - \beta_{21} \vec{E}_0, & \text{if } r < r_p. \end{cases} \tag{3.6}$$

with $\vec{n}$ as radial unit normal and $\mathbf{I}$ as unity tensor. The field outside the sphere is equivalent to the applied field $\vec{E}_0$ plus the field of the dipole induced by the sphere with dipole moment $\beta_{21} r_p^3 E_0$, with E_0 as the absolute value of the homogeneous field $\vec{E}_0$.

Ongoing from the solution for a single spherical inclusion in a infinite matrix, the influence of an arbitrary number of small spherical inclusions—as sketched in Fig. 3.2—can be calculated. Therefore, the spherical inclusion is replaced by a composite sphere with radius r_e composed of N smaller spheres with conductivity κ_2 and a combined volume fraction ϕ_2 within the sphere r_e and matrix material with conductivity κ_1 (see Fig. 3.2). The disturbance of the intensity field at large

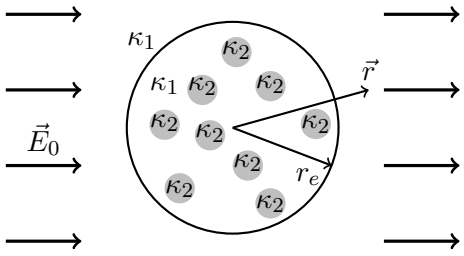

Figure 3.2.: Composite sphere of radius r_e, composed of spherical particles of conductivity κ_2 in matrix of conductivity κ_1, embedded in an infinite matrix with conductivity κ_1

distance of the composite sphere can be calculated from the superposition of the effect of each small sphere. When the large sphere with radius r_e is considered as homogeneous material with an effective conductivity κ_{eff}, it is assumed to have the same effect on the intensity field far from its origin. Thus, the polarizabilties can be related through the volume fractions of the smaller spheres as $\beta_{e1} = \phi_2\beta_{21}$ [67, 66], which allows to determine the effective conductivity of dilute dispersions as

$$\frac{\kappa_{\text{eff}} - \kappa_1}{\kappa_{\text{eff}} + 2\kappa_1} = \phi_2 \frac{\kappa_2 - \kappa_1}{\kappa_2 + 2\kappa_2}. \tag{3.7}$$

Based on this equation, different approximations can be derived to estimate the effective conductivity of composite materials. Two will be introduced here, as they are considered in the further course of this work. The first is the so-called *self-consistent approach*, which is assuming unbiased mixtures, in which both phases are added in such a way that the perturbation is zero on average. This approximation was used by Carson et al. [69] to determine the upper limit of the effective conductivity of granular materials with external porosity. The second, denoted as the *differential approximation*, is the mathematical derivation of the *Bruggeman equation*, which is widely used to determine the effective conductivity of LIB electrodes for cell level modeling.

Self-consistent effective-medium approximation

For the self-consistent approach, the composite at a certain, arbitrary mixing ratio is considered as a homogenized matrix phase with an effective conductivity $\kappa_{\text{eff},0}$. At first, a small amount $\Delta\phi$ of one phase is added to that mixture, and the new effective conductivity $\kappa_{\text{eff},\Delta\phi}$ is considered as the new matrix property. Next, such an amount of the other phase is added to this new matrix that the properties of the matrix are changed back to the initial value of $\kappa_{\text{eff},0}$. Supposing that thus little by little the mixing ratio of a given composite can be attained, the effective conductivity can be calculated implicitly from

$$\sum_i^M \phi_i \frac{\kappa_i - \kappa_{\text{eff}}}{\kappa_i + 2\kappa_{\text{eff}}} = 0, \tag{3.8}$$

as derived mathematically in Appendix A.1 for a binary mixture ($M = 2$). The derivation implies that this approach is only valid for symmetric composites. Symmetry in binary mixtures means in this context, that the results are invariant to the simultaneous exchange of the conductivities κ_1 and κ_2 plus the volume fractions ϕ_1 and ϕ_2. In binary mixtures of spherical particles, this is only valid for monosized assemblies. Further, the approximation yields unsatisfactory results for compositions with widely different conductivities: It predicts a spurious percolation threshold independent of microstructure. The percolation threshold is, however, strongly influenced by the microstructure, as will be discussed in section 3.1.2.

Differential effective-medium approximation

For the derivation of the differential approximation, on the other hand, an infinitesimal small amount of inclusion phase 1 is replaced by phase 2 in an arbitrary, homogenized mixture with phase 1 as matrix phase and phase 2 as inclusion phase. For the derivation, it is assumed that the effective conductivity $\kappa_{\text{eff}}(\phi_2)$ at one value of ϕ_2 is known. The calculation of $\kappa_{\text{eff}}(\phi_2 + \Delta\phi_2)$ leads to a differential equation of Eq. 3.7, as shown in Appendix A.2:

$$(1-\phi_2)\frac{d\kappa_{\text{eff}}}{d\phi_2} = 3\kappa_{\text{eff}}\frac{\kappa_2 - \kappa_{\text{eff}}}{\kappa_2 + 2\kappa_{\text{eff}}}. \tag{3.9}$$

Further, analytic integration (presented in Appendix A) leads to

$$(\frac{\kappa_2 - \kappa_{\text{eff}}}{\kappa_2 - \kappa_1})(\frac{\kappa_1}{\kappa_{\text{eff}}})^{1/3} = 1 - \phi_2. \tag{3.10}$$

Under the assumption, that the inclusion phase ϕ_2 is isolating[1], this can be reduced to

$$\frac{\kappa_{\text{eff}}}{\kappa_1} = \phi_1^{3/2}, \tag{3.11}$$

which is known as Bruggeman's equation. This equation is the equivalent of the experimentally found relationship known as Archie's law [71].

Effective medium theory (EMT) in electrochemical cell modeling

Assuming a binary mixture of active material and pore space in lithium ion battery (LIB), the Bruggeman equation (Eq. 3.11) is widely used to determine the effective transport properties of the microstructure. If, however, the heterogeneous material is composed of conducting material and quasi-isolating material—as the electrodes in consideration—then it is always possible that the conducting phase is not connected throughout the volume: As described in section 2.3, the conductivity drops drastically when the volume fraction of the conducting phase is below a certain volume fraction of the conducting phase; this was shown for example by Wilson et al. [54] for yttria-stabilized zirconia (YSZ) and strontium-doped lanthanum manganite (LSM) in SOFC cathodes or by Dominko et al. [59] for $Li_xMn_2O_4$ (LMO)-carbon black (CB) compositions. In solid oxide fuel cell (SOFC), both ions and electrons are transported within the solid phase, therefore it is essential to ensure the percolation of both ion conducting and electron conducting species. In LIB, the ion transport takes place in the electrolyte and the active material, and hence, it may not be a major issue [12]. To ensure electron conduction, however, a connected network of the CB phase is required.

In those studies, electron conduction was never an issue, as, the usually applied bulk properties are calculated based on conductivity values experimentally obtained for complete electrode structures as described in [72]. Neglecting the influence of the different phases, in particular the effect of carbon black, the electronic bulk conductivities obtained for the active material in this way are unrealistic high. For LMO as an example, electronic conductivities of 100 S/m [73] and 3.8 S/m [74] are used in cell modeling; in contrast, more realistic values for the bulk conductivity of LMO are in the range of 10^{-3} to $10^{-4} S/m$ [28, 75]. Most likely, cell modeling with the more realistic values should point out the impact of electron conduction.

[1] $\kappa_2 = 0$

As the different solid phases is in the models not resolved separately, the Bruggeman equation (Eq. 3.11) is applicable even though it does not consider percolation. For more detailed microstructural studies, however, percolation of CB has to be considered, as its relevance was experimentally demonstrated. Hence, the Bruggeman approach, or EMT, is not applicable to investigate morphological parameters such as mixing ratio or distribution of additives. The derivation of the probability P is described within the framework of percolation theory and is presented now.

3.1.2. Percolation theory

Percolation processes were first described by Flory (1941) and Stockmayer (1943) studying the reaction of small branching molecules to form very large macromolecules [76]. Formally introduced was the concept by Broadbent and Hammersley [77] in 1957; they demonstrated the existence of a threshold for flow of a fluid through a porous, random media, which depends on the amount of blocked pores. Percolation phenomena arise in a vast field of applications: besides transport properties, they can also be found in mechanical properties of composite materials, phase transition, fracture processes in heterogeneous rock formation, glass transition, spread of fire and diseases, etc. [67]. The exact determination of the percolation threshold has been possible to date only for one dimensional structures ($p_c = 1$) and few simple two dimensional lattices: for example, the critical volume fraction of a two-dimensional triangular lattice structure is 0.5 [78]. For more complicated cases, the percolation threshold has to be determined numerically [79]. A comprehensive introduction in the percolation theory was written for example by Stauffer and Aharony [76]. For similarity to the considered electrode microstructures, we focus on three-dimensional structures of binary mixtures with randomly distributed, spherical particles: for those, no analytic solution exists for the percolation probability.

Percolation in binary granular mixtures

Randomly packed powder structures can be generated numerically or built by filling hard spheres in a container. For details of the numerical packing algorithms see section 4.1.1. Translated to the language of percolation theory, spheres are equivalent to lattice sites and the contacts between spheres are bonds [80]. Typically in percolation theory, it is distinguished between occupied and unoccupied sites—this correlates to conducting and nonconducting particles in the electrode. The volume fraction ϕ_k of the conducting phase thus matches the probability that a site is occupied. With increasing volume fraction ϕ_k—starting from zero—the system properties segue at some point from non-conducting to conducting in a sharp transition, as was previously sketched in Fig. 2.2. That transition point is called the percolation threshold. The determination of the critical volume fraction $\phi_{k,c}$ of the conducting phase, for which the transition takes place, is an essential question of percolation theory. Mathematically, it is only precisely defined for an infinitely large system: only there do volume fractions larger than $\phi_{k,c}$ guarantee the existence of infinitely large clusters spanning the system, and volume fractions smaller than $\phi_{k,c}$ guarantee that no connection spans through the system [81]. As obviously the investigation of infinite lattice structures would require infinite time, finite structures have to be studied in the numerical approach. For volume elements smaller than infinity, the sharp transition at the percolation threshold becomes more diffuse—an effect, that becomes more pronounced with a decreasing ratio of particle size to volume element length. The impact of that ratio was thoroughly investigated by

Roussenq et al. [78] for two-dimensional lattice structures, as reprinted in Fig. 3.3: In Fig. 3.3a, the percolation probability in the transition range is shown for different lattice lengths n. Additionally, the percolation probabilities P of 0.1 and 0.9 are given in Fig. 3.3b as functions of volume fraction and lattice size. This illustrates clearly, how the accuracy of the determined percolation threshold

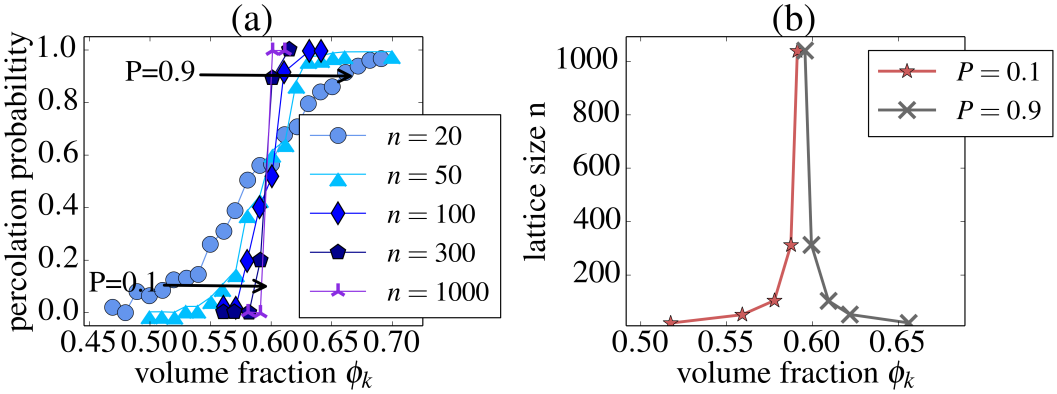

Figure 3.3.: (a) percolation probability against volume fraction for different lattice sizes and (b) lattice size vs volume fraction for percolation probabilities of 0.1 and 0.9 [78]

increases with increasing lattice size. Further, with regard to random structures, Powell [80] found that periodic boundary conditions reduce the size dependence of the percolation threshold, in his studies he recommended a volume element size of $10 \times 10 \times 10$ of particle diameter. Nevertheless, as even the biggest structure is smaller than infinity, the results will always entail some uncertainty. Therefore, it seems advisably to study always several configurations of the same composition.

Critical volume fraction in binary granular mixtures

In the following, findings relevant for the further course of the work—with no claim to be exhaustive—of the percolation threshold in random spherical structures are presented. Experimentally, the threshold can be determined via measuring the conductivity of various mixtures of conducting and isolating spheres [82, 83]. Oger et al. [83] apply small pressure repetitively, which leads to reproducible results after 15 cycles. They use roughly 50×10^6 particles per assembly, and study 10 assemblies per composition. Fitzpatrick et al. [82] test systems of 500, 2500 and 5000 spheres, which are shaken and compressed to reach a stable, dense configuration.

For numerical studies, random structures have to be generated at first and subsequently, connected clusters have to be determined in those structures. Those methods will be explained in detail in section 4.1 and 4.2, respectively. Finally, if a detected cluster spans from one boundary of the volume element to the opposite side, the structure is considered as percolated and the percolation probability can be determined from the fraction of conducting particles within the spanning cluster. The random structures are usually generated in such a way that they have a fixed number of particle contacts, referred to as overall coordination number Z_0, of 6 [84, 83, 80]. Based on their experimental findings, Oger et al. [85] noted, however, that a fixed coordination number of 6 is an artificial constraint inhibiting "real randomness", especially for larger size ratios. In their experiments, overall coordination numbers between 6.5 and 7 were reported. With the numerical approach, Bouvard and Lange [84] performed simulations with 10 000 particles to achieve a significant amount of large particles for the larger size ratios. For the largest size ratio,

they simulated several assemblies per composition. Further, Oger et al. [85] studied 10 assemblies per composition. In the monosized case, a box volume of $15 \times 15 \times 15$ of particles diameter was implemented. The maximum size ratio was chosen to be smaller than 4.45 in order to prevent segregation.

Fig. 3.4 summarizes the findings of numerical and experimental studies: For monosized assemblies and particle size ratios smaller than 1 the numerical results for the critical volume fraction are in good agreement with the experimental data. For larger size ratios, however, the values found by Bouvard and Lange [84] deviate significantly from the numerical and the experimental findings of Oger et al. [83]. To ascertain the tendency of the percolation threshold in that range, further studies would be required.

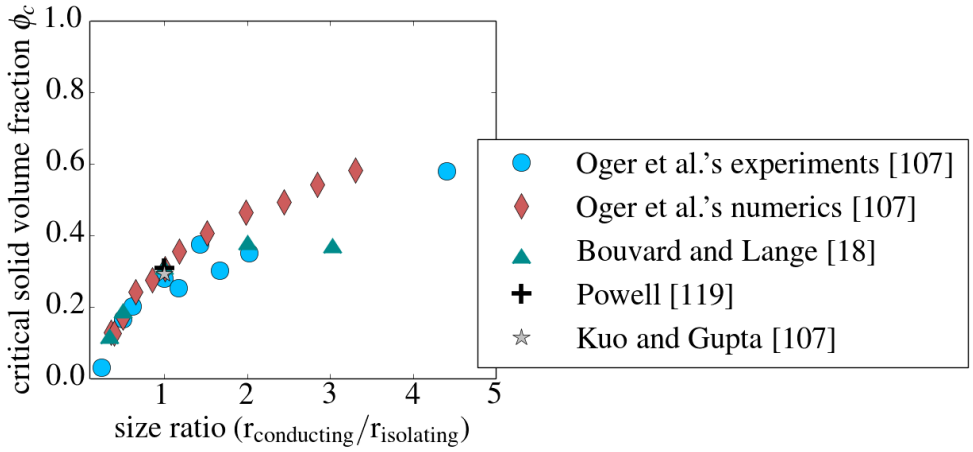

Figure 3.4.: Numerical and experimental data found in literature for the critical volume fraction at percolation threshold for several size ratios [84, 86, 83, 87]

Critical coordination number in binary granular mixtures

Ongoing from the pure determination of the critical volume fraction at percolation threshold, pioneering work was done by Bouvard and Lange [84]: They were the first to relate the percolation threshold to one certain coordination number $Z_{k,k}$ independent of the size ratios —the investigated range of size ratios was between 1/3 and 3. The coordination number $Z_{k,k}$ denotes in this the number of contacts a particle of species k has with particles of the same species. In [84], the percolation threshold was found for all size ratios for a coordination number $Z_{k,k}$ of 2. Based on that, they found the empirical formula for percolation probability

$$P = (1 - (\frac{4 - Z_{k,k}}{2})^{2.5})^{0.4} \tag{3.12}$$

to describe their results satisfactorily. For $Z_{k,k} < 2$ the equation has no solution in the realm of "real numbers", for $Z_{k,k} = 2$ the percolation probability equals zero, and P increases fast with increasing coordination number. The coordination number $Z_{k,k}$, for which the percolation threshold takes place, is denoted as critical coordination number Z_c in here. In order to determine the critical volume fraction in binary granular mixtures analytically, Eq. 3.12 can be combined with a description of the coordination number, which allows for the prediction of the the coordination

number $Z_{k,k}$ analytically from size ratio and volume fraction. An overview of the different approaches is given in [88]. As only the approach by Chen et al. [89] satisfies the contact number conservation requirement [34], only this approach is introduced.

Concept of coordination numbers

Assuming a binary mixture of spheres of either phase k or j, the contact number conservation principle means that the net contact between all k particles with j particles must be equal to the contact of j particles with k particles:

$$n_k Z_{k,j} = n_j Z_{j,k}, \tag{3.13}$$

where n_i is the number of particles of phase i. It is assumed that the coordination number $Z_{k,k}$ is proportional to the surface-area fraction ζ_k of all k particles and the overall coordination number Z_0 [90]

$$Z_{k,k} = \zeta_k Z_0. \tag{3.14}$$

Eq. 3.14 is equally applicable for k and j. The surface-area fraction ζ_k is defined in terms of the volume fractions ϕ:

$$\zeta_k = \frac{n_k 4\pi r_k^2}{\sum_i^M n_i 4\pi r_i^2} = \frac{\phi_k / r_k}{\sum_i^M \phi_i / r_i}, \tag{3.15}$$

with the volume fraction ϕ_k of phase k:

$$\phi_k = \frac{n_k 4/3\pi r_k^3}{\sum_i^M n_i 4/3\pi r_i^3} = \frac{n_k r_k^3}{\sum_i^M n_i r_i^3} \tag{3.16}$$

In a binary mixture, $\zeta_j + \zeta_k$=1 and $\phi_j + \phi_k$=1.

Combining Eqs. 3.14 and 3.15 leads to

$$Z_{k,k} = Z_0 \zeta_k = Z_0 \frac{\phi_k / r_k}{\sum_i^M \phi_i / r_i}. \tag{3.17}$$

$Z_{k,j}$ can be derived from the sum over all contacts:

$$n_{ges} Z_0 = n_k Z_{k,k} + n_k Z_{k,j} + n_j Z_{j,j} + n_j Z_{j,k}. \tag{3.18}$$

Under consideration of the contact number requirement (Eq. 3.13) and the derived expressions for $Z_{k,k}$ and $Z_{j,j}$, the coordination number $Z_{k,j}$ can be determined as described in appendix B in dependence of the volume fraction and particle radii as:

$$Z_{k,j} = 0.5 Z_0 (1 + \frac{r_k^2}{r_j^2}) \frac{\phi_j / r_j}{\sum_i^M \phi_i / r_i}. \tag{3.19}$$

The overall coordination number Z_0 of a particular composite electrode depends upon details of the fabrication process. Regardless of the fabrication process, Z_0 is widely assumed to be equal to 6 in accordance with the simulations of random structures [84, 85, 80]. Even though this is in good agreement with the experimentally determined coordination number of 6.24 for monosized hard spheres [91], the particle size ratio shows an effect on the overall coordination number [88, 91, 92]. Furthermore, different studies indicate that sintering and compression of the electrode

structures further influences the coordination number: Investigating the near contacts, Powell showed that with fixed particles centers and increasing radii (up to 1.9 times the initial radius) the overall coordination number increases from 6 to 30. Moreover, with increasing radii, the critical volume fraction at percolation threshold decreases from 0.183 to 0.051 [87]. This coincides with the more recent results of Bertei et al. [93]. Considering uniaxial compression, decreasing percolation threshold [83] and increasing coordination numbers [94] were found experimentally [94] and numerically [92].

Assuming a valid choice for Z_0, the concept of coordination numbers enables us to calculate the critical coordination number with Eq. 3.17 based on the critical volume fraction. Considering the results of different researchers, as summarized in Fig. 3.4, different values of the coordination number correlated to the percolation threshold have been found: The findings of Powell [80] lead to a critical coordination number Z_c of 1.86 for monosized assemblies. With a size scaling relationship, as introduced in [76], Kuo and Gupta [86] determine the percolation threshold for infinite random packings to be at volume fractions of 0.294 based on the experimental findings of Fitzpatrick et al. [82]. This is in good agreement with the threshold reported by Oger et al. [83]; it corresponds to a critical coordination number $Z_c = 1.764$. In contrast to those works, it was impossible to "establish any simple relationship between the values of the threshold and the co-ordinances of each type of spheres" for Oger et al.'s [83] results. Especially for large size ratios, the coordination numbers corresponding to the the critical volume fractions shown in Fig. 3.4 are ambiguous. Nevertheless, modifications of the approach of Bouvard and Lange (Eq. 3.12) are wildly used to determine the percolation probabilities of various compositions and morphologies in modeling SOFC electrodes [33, 89, 34, 95], whereas—to the best of my knowledge—it has not been applied to study LIBs.

3.2. Effective properties based on percolation theory

As described previously, the percolation probabilities of a binary granular mixture can be calculated based on volume fraction and size ratios of the particles. Subsequently, the effective conductivity of the phases as well as the reactive surface area can be determined based on the percolation probability. This approach, typically used in SOFC modeling, as well as the findings, based on it, are summarized in the following.

3.2.1. Percolation probability

For the calculation of the percolation probability, Eq. 3.12 was modified in order to reflect on the critical coordination number $Z_c = 1.764$, determined by Kuo and Gupta [86] as well as Oger et al. [83] in more recent research. In accordance with [89, 34], the slightly modified form will be used in the following to determine percolation probability P as

$$P = (1 - (\frac{3.764 - Z_{k,k)}}{2})^{2.5})^{0.4}. \tag{3.20}$$

For $Z_{k,k} = Z_c$, the percolation threshold is assumed to take place. In analogy to Eq. 3.12, Eq. 3.20 has no real solution for P when $Z_{k,k} < Z_c$. Further, P is zero for $Z_{k,k} = Z_c$ and increases with increasing coordination number $Z_{k,k}$. As was shown previously, Eq. 3.17 allows to express the coordination number as function of particle size ratio and volume fraction only. Thus, inserting

Eq. 3.17 in Eq. 3.20 allows for the determination of the percolation probability as a function of volume fraction and size ratio. Additionally, the critical volume fraction, at which the percolation threshold takes place, can be determined based on Eqs. 3.20 and 3.17 as a function of size ratio only.

SOFC electrodes, considered as binary mixture of ionic conducting and electronic conducting particles, require the connectivity of both phases. To obtain the range in which both electron conducting particles and ion conducting particles are percolating, the percolation probability P must be calculated for $Z_{k,k}$ and for $Z_{j,j}$ separately. Those probabilities, denoted P_k and P_j, are then multiplied. The percolation probability for the size ratios $r_k/r_j = 1$ and $r_k/r_j = 5$ are shown in Fig. 3.5a.

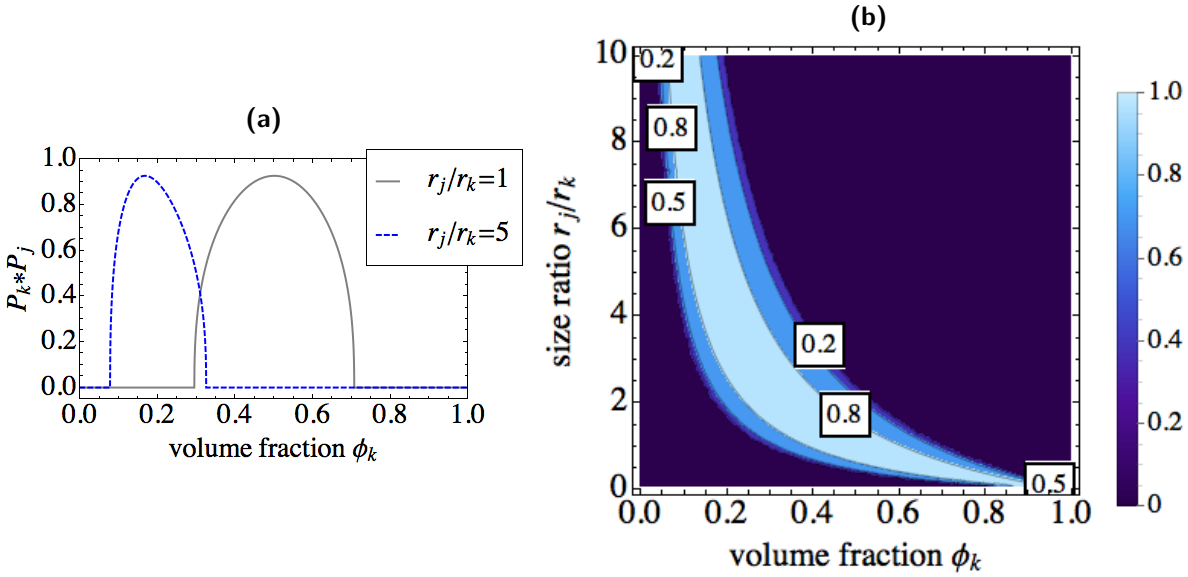

Figure 3.5.: Percolation probability P for (a) two size ratios and (b) as contour plot for size ratios from 0.1 to 10

For monosized assemblies, the maximum percolation probability is found for 50% volume fraction of both phases. For larger size ratios, the maximum is shifted towards smaller volume fractions of the smaller species [89, 34]. A valuable instrument to demonstrate the dependencies of the effective properties on volume fraction and size ratios are contour plots, as shown in Fig. 3.5b. There, the percolation probability is given for all volume fractions in the range from 0 to 1 and size ratios from 0.1 to 10. A general shift of percolation threshold to smaller volume fractions of the smaller species is found for all size ratios. This clearly demonstrates the need to adapt the used volume fractions under consideration of the size ratio.

3.2.2. Effective conductivity

To determine the effective conductivity under consideration of the connectivity within the phase, the Bruggeman equation (Eq. 3.11) is extended by the percolation probability P, which leads for an arbitrary phase k to [34]

$$\frac{\kappa_{\mathrm{eff,k}}}{\kappa_{\mathrm{bulk,k}}} = ((1-\epsilon)\phi_k P_k)^{1.5}. \tag{3.21}$$

Obviously, below the critical volume fraction no conductivity is found. Above the percolation threshold, the effective conductivity, plotted in Fig. 3.6, increases in general with volume fraction.

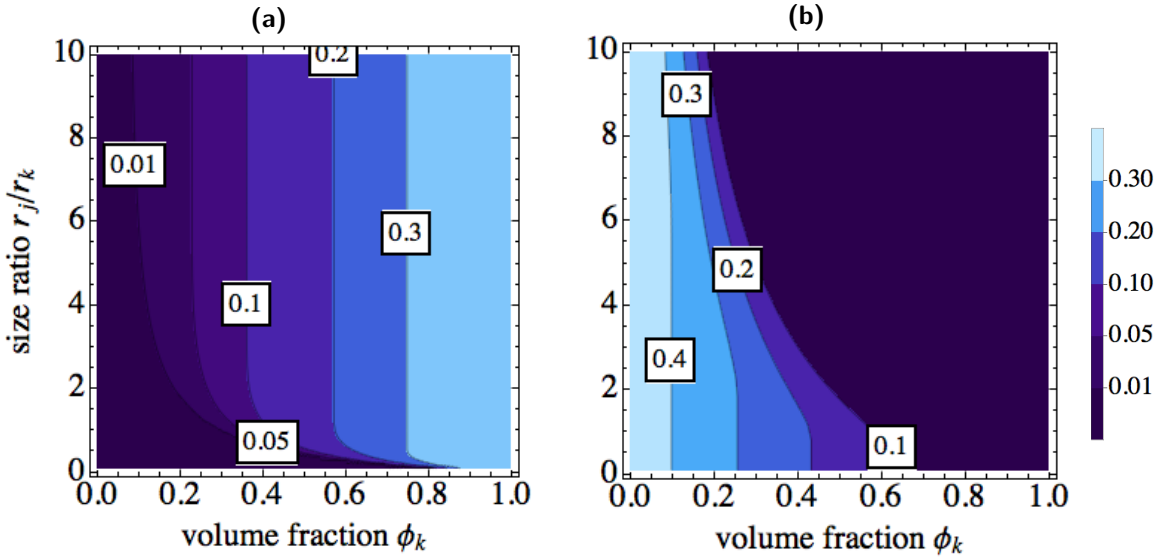

Figure 3.6.: Effective conductivity relative to bulk conductivity for (a) k and (b) j-type particles for size ratios from 0.1 to 10

Fig. 3.6a shows the effective conductivity of the particles k, whose size is kept the same for all calculations. For that phase, the influence of size ratio is negligible. For particles j, whose size is varied to obtain the different size ratios, there is a more noticeable influence of the size ratio (Fig. 3.6b). Furthermore, the effective conductivity of k increases with increasing volume fraction k, and the conductivity of j decreases with increasing volume fraction of k. This clearly leads to contrary improvement in effective electronic and ionic conductivity. As stated in section 2.3, the ion conductivity in SOFC is in general lower than the electron conductivity; therefore, this parameter is more critical in modeling SOFCs.

3.2.3. Active area

It was demonstrated experimentally, as described in section 2.3, that, besides transport in the solid phase, the size of the active area is relevant for the overall cell performance: in both, SOFC and LIB, a large active area reduces the activation losses. To identify the total active area per unit volume, the first step is to specify the active area for a single electrode-electrolyte contact. The

path of reactants, and thus, the active area differs significantly for cells with liquid electrolytes (LIB) and all-solid-state systems (SOFC).

Reaction path in LIB

In a liquid cell system, the Lithium is dissolved and oxidized at the surface of the positive electrode, transported as Li-ion within the electrolyte and absorbed and reduced in the negative electrode during charging and vice versa during discharging. As the electrolyte is usually both ionic conductor and solvent, the electrochemical reactions (Eqs. 1.3, 1.4) occur at the active material-electrolyte two-phase boundary [96]: The active area is the free surface area of the insertion material. The free surface area is assumed to be reduced during calendering [23]; and that is assumed to be accountable for increasing activation losses monitored during EIS experiments (see section 2.3). Nevertheless, to the best of my knowledge, in cell modeling the change of surface area during calendering or cell cycling was neglected so far.

Reaction path in SOFC

In contrast to liquid systems, in SOFCs, the electrolyte phase is usually no solvent of the gaseous oxygen (cathode) or the H_2 containing fuel (anode). A simple exchange reaction between the gaseous phase and the solid oxide ion conductor will hardly be found, as elementary oxygen or H_2 do not dissolve in most oxides [97]. As a consequence, the reaction can occur along different possible paths; those are sketched in Fig. 3.7.

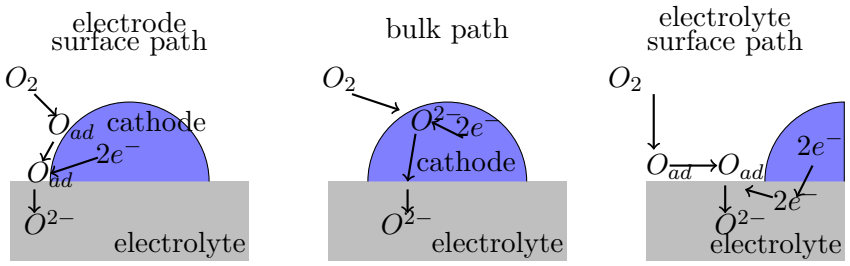

Figure 3.7.: Sketches of three possible reaction paths of the oxygen reduction and incorporation reaction and some possible rate-determining steps, redrawn from [98]

In general, it can be distinguished between surface and bulk path for the reaction; both are explained in detail in [96] for cathode materials and in [97] for anodes materials. The surface path includes adsorption the reactants—oxygen at the cathode and hydrogen at the anode—and diffusion along the surface of electrode material toward the three-phase boundary (TPB), where the reactants are ionized and incorporated into the electrolyte. Diffusion of the ionized species on the surface or within the interface could lead to a certain broadening of the active zone [98]. Considering the bulk path, the reactants are adsorbed into the electrode material and transported within the bulk to the contact zone. The ionization can take place either within the bulk or at the electrode-electrolyte interface followed by spillover to the electrolyte phase [96]. In LSM cathodes the bulk path dominates the reaction rate [98]; for anodes the reaction path seems less clear. Furthermore, even though one path is predominant, surface and bulk processes occur parallel. Finally, microstructural properties of the system (e.g. particle size, porosity and

electrode thickness) as well as the conditions in the cell (e.g. temperature, pressure, doping of material) significantly influences, which path is energetically favorable. Consequently, as the reactive zone depends on the reaction path, which is difficult to determine, the relation between contact geometry and the active area is hitherto poorly known.

Approximation of the active zone of one TPB contact

This uncertainties lead to different approaches found in cell modeling for the calculation of the reactive area a_x of a circular contact. Those are compared in [34]. For the geometric calculation of the contact area, overlapping spheres are assumed—usually with a contact angle θ of 15° for the smaller particle, as shown in Fig. 3.8. The contact radius r_c of two overlapping spheres can be calculated as $\min(r_j, r_k)\sin\theta$. Ongoing from the geometric description of the contact zone, the

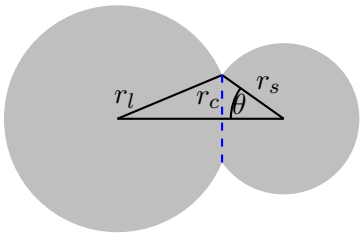

Figure 3.8.: Definition of contact angle θ for particles with different radii, of which the larger is denoted with r_l and the smaller with r_s

active zone can be determined with the following approaches: Considering the active zone to be one-dimensional, the TPB length is determined as the circumference of the contact [89, 95]

$$a_{\text{line}} = 2\pi r_c = 2\pi \min(r_j, r_k) sin\theta. \tag{3.22}$$

Further studies assume a two dimensional expansion of the active zone. The TPB area is calculated either considering the area within the contact [33]

$$a_{\text{bulk}} = \pi r_c^2 = \pi(\min(r_j, r_k) sin\theta)^2 \tag{3.23}$$

or a finite distance ψ from the contact on the surface [34] (sketched in Fig. 3.9)

$$a_{\text{surf}} = 2\pi r_j^2 (cos\theta_j - cos(\theta_j + \frac{\psi_j}{r_j})) + 2\pi r_k^2 (cos\theta_k - cos(\theta_k + \frac{\psi_k}{r_k})) \tag{3.24}$$

to be active. Considering these approaches, the first (Eq. 3.22) neglects any extension of the active

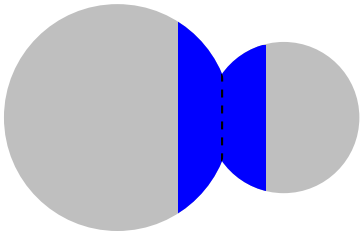

Figure 3.9.: Schematic of the active area (blue) of two contacting particles according to Eq. 3.24

zone around the direct contact zone of the three phases, Eq. 3.24 assumes a certain extension length ψ of the active surface zone, as it is found considering both electrolyte and electrode surface path for the reactions, as shown in Fig. 3.7. Moreover, Eq. 3.23 is based on the consideration of a bulk reaction path. Ge et al. [99] suggested even a three-dimensional expansion of the active zone, combining the different possibilities. As the true reaction path in the cells is not known, all approaches for the calculation of the active zone are justifiable, even though stated otherwise in [34].

Active zone within the microstructure

Based on the contact zone of a single contact, the total active zone is calculated by multiplying it with the average number of contacts $Z_{k,j}$ a k particle has with j particles (Eq. 3.19) and N_k, which is the number of k particles per unit volume. The total number n_k of particles can be determined as

$$n_k = \frac{(1-\epsilon)\phi_k \times L^3}{4/3\pi r_k^3}, \tag{3.25}$$

with L as length of the unit volume element. With $N_k = n_k/L^3$, the number of particles per unit volume can then be calculated. The porosity ϵ is usually assumed to be constant for all compositions—even though it is well known, that the packing density depends strongly on the size ratio [92]. As number conservation is satisfied, $n_k \times Z_{k,j}$ equals $n_j \times Z_{j,k}$. Further, for the three phase boundary to be active it is necessary that both ion and electron conducting phases are percolating. Therefore, the total active zone is multiplied by the probabilities that phase k and phase j are connected. This leads to an active TPB of

$$\mathrm{TPB} = a_x N_k Z_{k,j} P_k P_j, \tag{3.26}$$

where a_x stands for the active zone of two contacting spheres, determined with the different approaches, considering line (Eq. 3.22), bulk (Eq. 3.23) and surface (Eq. 3.24) reactions [34]. Considering the one-dimensional extension of the active zone of one contact, TPB is given in $\mathrm{m/m^3}$, and the two-dimensional extensions lead to $\mathrm{m^2/m^3}$.

Active area of monosized assemblies

For monosized assemblies, all studies agree on the beneficial effect of small particle sizes [95, 89, 33, 34], independent of the description of the TPB of one contact. Apart from that, the approaches lead to very different values for the extent of TPB, as shown in Table 3.1 for compositions of $\phi_l = \phi_k = 0.5$. For a radius of 500nm, Eq. 3.22 leads to a TPB length of several orders of magnitude larger than Eq. 3.23 and Eq. 3.24. Further, Eq. 3.24 strongly depends on the length of extension ψ of the reactive zone along the surface. ψ was determined in [34] from experimental values to be 30nm for r_p=500 nm.

Presumably, the general increase of TPB with decreasing particle size is related to the increase of the total surface area within a volume unit. To investigate this, we calculate the total surface area per unit volume S_{total}, assuming non-overlapping spheres in the microstructures for simplification, as

$$S_{\mathrm{total}} = \frac{n4\pi r^2}{L^3}, \tag{3.27}$$

	$\mathbf{TPB}_{\max}$	**unit**
a_{line}	1.296×10^{12}	$[m/m^3]$
a_{bulk}	8.38×10^{5}	$[m^2/m^3]$
a_{surf}, $\psi = 30nm$	8.64×10^{5}	$[m^2/m^3]$
a_{surf}, $\psi = 60nm$	18.99×10^{5}	$[m^2/m^3]$

Table 3.1.: Maximum of TPB for monosized particles with r_p=500 nm found for volume fractions of 50%:50% with the different approaches

with n as the total number of particles of radius r within a cubic volume of size length L. To estimate the number of particles in the volume element, we consider a simplified case of particles arranged on a cubic lattice. This allows to calculate the number of particles as $n = (L/2r)^3$, leading to

$$S_{\text{total}} = \frac{(\frac{L}{2r})^3 4\pi r^2}{L^3} \propto \frac{1}{r}. \tag{3.28}$$

this approximation demonstrates that the total surface area increases with decreasing particle radius. The reduction of particle size, however, is limited by production processes and pore size requirements—smaller particles lead to smaller pore sizes, and thus hinder the gas transport. Therefore, it is of large interest, to determine if the TPB can be increased by changing the size ratios while choosing the smallest still reasonable particle size as a lower radius limit.

Active area of binary sized assemblies

To study the impact of particle size ratios, the active TPB was calculated analytically with Eq. 3.26 for different ratios between 1 and 10, where 1 is assumed to be the smallest reasonable particle size. To obtain comparable results for the different definitions of the active zone, the values of the different approaches were normalized, as done by Völker and McMeeking [34]: The results of each TPB description were calculated relative to the maximum value found with this description; those values are given in Table 3.1. Thus, the monosized assemblies have the same normalized values, and the impact of size ratio can be determined regardless of the differences introduced by the approach. The results in Fig. 3.10 demonstrate for size ratios exceeding 1 that the normalized values differ only marginally for the methods, when the small particle is kept constant. The trends found for the extent of TPB are in good agreement with values found by [95, 34, 33]. Chen et al. [89] use normalized values of the TPB and show the result only in dependence of size ratio $r_{\min}/r_{\max}$. Therefore, the values are difficult to compare to the other studies, as it is not clear, whether the variation is done by keeping a mean radius fixed, or increasing one particle while the other is kept constant.

For monosized microstructures, we assumed that the total surface area is correlated to the active TPB. If this assumption is also valid for binary sized mixtures, the total surface area will decrease with increased size ratio. To assess this, we derived the dependence of surface area on particle size for binary mixtures. The surface area of a binary mixture can be determined from

$$S_{\text{total}} = \frac{n_j 4\pi r_j^2 + n_k 4\pi r_k^2}{L^3}, \tag{3.29}$$

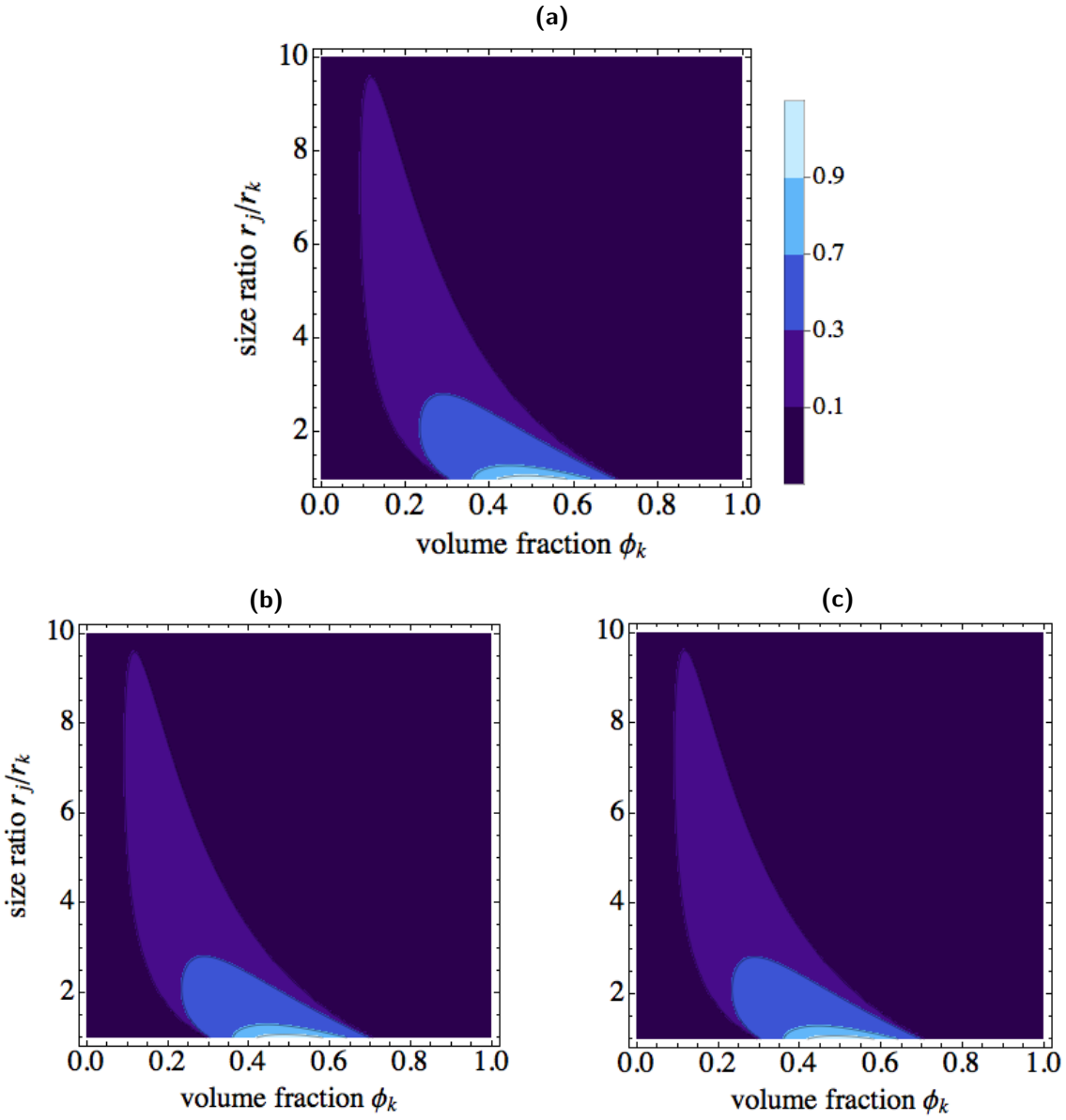

Figure 3.10.: Three-phase boundary length for different size ratios from 1 to 10 calculated from (a) a_{line} , (b)a_{bulk} and (c) a_{surf}. Normalization with the maximum value of monosized assemblies of each approach (see Table 3.1) allows the same legend for all calculations.

with n_i as the number of particles of the phase i. Using Eq. 3.25 leads to

$$S_{\text{total}} = \frac{\frac{(1-\epsilon)\phi_j L^3}{4\pi r_j^3/3} 4\pi r_j^2 + \frac{(1-\epsilon)\phi_k L^3}{4\pi r_k^3/3} 4\pi r_k^2}{L^3}, \tag{3.30}$$

which can be simplified to

$$S_{\text{total}} = 3(1-\epsilon)(\frac{\phi_j}{r_j} + \frac{\phi_k}{r_k}). \tag{3.31}$$

Assuming in accordance with the considered studies that the porosity ϵ is the same for all size ratios and applying $\phi_k = 1 - \phi_j$, this leads to

$$S_{\text{total}} \propto \frac{\phi_j}{r_j} + \frac{1-\phi_j}{r_k}. \tag{3.32}$$

Further, the size ratio χ relates the radii with $\chi r_j = r_k$. With a fixed radius r_k, the surface area is proportional to $\frac{\phi_j}{r_j} + \frac{1-\phi_j}{\chi r_j}$. Thus, with a size ratio $\chi > 1$, the total surface area decreases; and with $\chi < 1$ the surface area increases as shown in Fig. 3.11a. This explains the increasing TPB found with decreasing size ratio $\chi < 1$ in [34]. A monosized assembly with both particle sizes equal to the small particle would most likely still lead to better results.

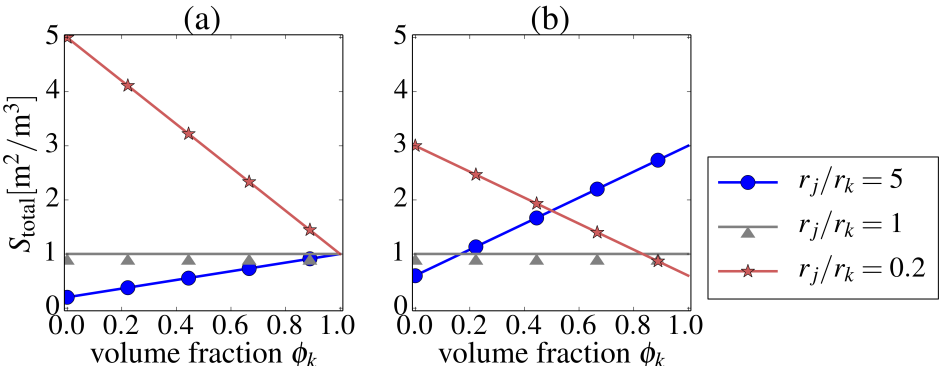

Figure 3.11.: Total surface area S_{total} calculated for particles without overlap for different particle size ratios with (a) the radius k kept constant (Eq. 3.32) and (b) the mean radius $(r_k + r_j)/2$ kept constant (Eq. 3.33)

In contrast to that, in the comparison of the different approaches for the active area of one contact in [34], the mean particle size was kept constant. This leads to largely different results for the extent of TPB: in particular, the previously shown trend of decreasing TPB with increasing size ratio (Fig. 3.10) is reversed, as shown in Fig. 3.12 exemplarily for the approach a_{line} for the active zone. To examine, if also this tendency is related to the overall surface area, S_{total} is recalculated with a constant mean radius $r_m = (r_j + r_k)/2$ and a size ratio $\chi = r_k/r_j$ as

$$S_{\text{total}} \propto \frac{\phi_j(1+\chi)}{2r_m} + \frac{(1-\phi_j)(1+\chi)}{2\chi r_m}, \tag{3.33}$$

As shown in Fig. 3.11b, this leads—regardless of the influence of percolation probability—to very different results for the total surface area, which influences the amount of TPB length.

This, in combination with the previous results obtained for e.g. the TPB length, is a strong

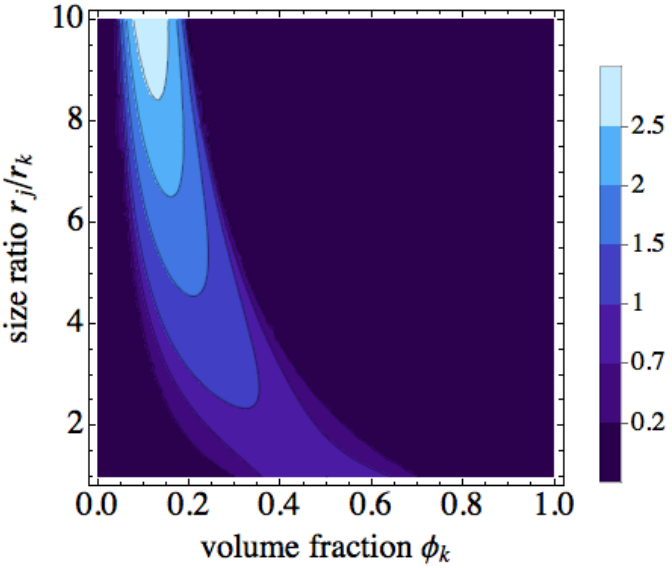

Figure 3.12.: Normalized three-phase boundary length for different size ratios from 1 to 10 calculated from a_{line} while mean radius kept constant

indication that the amount of total surface area is more relevant than the size ratio itself. For the interpretation and comparison of future results, this should be considered. Moreover, finding a correlation between free surface area and active area would be helpful—especially as it can be accessed more easily in experiments.

3.3. Resulting concerns investigated in this work

The most common estimations for the effective transport properties in LIB and SOFC—effective medium theory and percolation theory, respectively—have been introduced in this chapter; and the active zones of the two types of electrochemical cells were studied.

The Bruggeman approach, a variation of the EMT, is widely applied in LIB modeling—even though it neglects the impact of percolation; in contrast, percolation in the electron conducting phase was demonstrated experimentally to be relevant. Thus, the Bruggeman approach is considered as inapplicable for the modeling of the impact of composition and fabrication on effective transport properties; and thus, this method is unsuitable to study the parameters of interest. The question arising here is: would percolation theory, which is usually applied for SOFC modeling, lead to better results?

In combination with the concept of coordination number, the percolation theory considers connectivity within the phases; hence, it allows to reflect on the percolation thresholds found experimentally for both, LIB and SOFC. Nevertheless, due to simplifications made in this approach, further questions remain: While studying the influence of size ratio of electrode structures, porosity and the overall coordination number were assumed as fixed values—even though they most likely vary with size ratio [92]. This lead to the questions: How do those parameters vary for different compositions and fabrication processes? Is the variation marginal and therefore, negligible? Or, is

the variation more significant, but negligible as it has no influence on the parameters relevant for cell performance?

Further, the coordination number of $Z_c = 1.764$, as determined by Kuo and Gupta [86], is widely used to determine the percolation threshold regardless of the size ratio. Apart from the fact that several different values were found in literature for large size ratios, the value was determined for hard spheres in contact. It has not been investigated so far, if this approach is applicable to sintered or calendered microstructures without further amplifications. Those issues need to be addressed: Is a fixed Z_c valid for all size ratios? Is it applicable regardless of the fabrication process, or is it only valid for hard spheres?

The calculations of the the effective conductivity and TPB are based on the concept of coordination number and percolation probabilities as well. The concerns with regard to the percolation theory reflect on those values as well. Further, besides contact numbers, also contact areas, influenced by the fabrication process are most likely an impact factor. This poses the questions: In which way does the fabrication process affect the contact area and the free surface area? And how does that, in turn, affect the transport within the phase and the charge-transfer area?

To find answers to those questions, a vast number of numerically generated microstructures was studied in this work. Generation of the random mixtures of particles, and the possibilities to determine connectivity and effective transport properties of those, are introduced in the next chapter.

4. Monte-Carlo Method

Pioneering work in the investigation of electrochemical cells with Monte-Carlo methods was done by Sunde, who was the first to use random number generators in this field of work. As described in [100], he started to populate a cubic lattice with randomly placed electrode, electrolyte and pore space particles to mimic SOFC electrodes before he changed to random placement of spherical particles [101]. Comparison of his findings with percolation theory led him to recommend Monte-Carlo approaches as better suited for the investigation of electrode structures [102]. Especially for large size ratios, the two approaches show different results, indicating that the analytic determination of percolation might not be exact for larger particle size ratios. Further studies with Monte-Carlo methods on the effect of microstructure on parameters relevant for cell performance have been performed: general aspects [103], sintering conditions [104, 105], and polydispersity [106, 107] were investigated.

Different researchers studied the deviation between averaging methods and Monte-Carlo simulations: Sanyal et al. [105] as an example compared the effective parameters of monosized, sintered structures, generated with 2 different approaches to results obtained by percolation theory. With regard to the microstructure, they found a mean coordination number Z_0 of 6.7 for the numerically generated structures. This differs—already for monosized assemblies—from the assumed value of 6, the deviation is most likely caused by the simulated sintering process. Further, the numerically determined percolation threshold is found for smaller volume fractions than in the analytic approach.

Additionally, comparing volume averaging methods and Monte-Carlo methods in the investigation of LIB electrodes, Gupta et al. [103] found a significant difference between the results for the effective ion conductivity of the electrolyte and the active material: In the solid phase, the Bruggeman equation strongly overestimates the transport properties; in the electrolyte it underestimates it slightly. Sanyal et al. [105] determined numerically an effective conductivity which can be approximated with a Bruggeman approach weighted with percolation probability when a factor of 3.5 instead of 1.5 is used. In [104], the effect of porosity—which is in numerically generated assemblies correlated to the contact size—on effective transport properties as well as on the three-phase boundary (TPB) is pointed out. Further, Sanyal et al. [105] found a smaller amount of active TPB for the numerical generated structures in comparison to analytic results. Furthermore, the extent of TPB varies for two different packing methods, which were applied—this demonstrates the impact of microstructure and emphasizes the relevance of a realistic approximation of the microstructure to obtain meaningful results.

Those results provide a first picture on the deviation between numerically and analytically obtained results. In results found for microstructure, transport properties, and active area, the impact of manufacturing process becomes apparent; Monte-Carlo methods allow us to gain further insight into this influence factor. As, in general, a deviation between numerical and analytic results were determined, it is of interest to study causes of that. Further, it arises the question: can the analytic method be adapted to reflect better on the numerical results?

In order to further investigate the deviation and the applicability of analytic and numerical methods, a large number of Monte-Carlo simulations were performed in this work. Before those results are presented, the steps relevant for those simulations are introduced in this chapter: At first, assemblies with randomly distributed particles are generated; next, those are densified further with sintering or micromechanial simulations for solid oxide fuel cell (SOFC) and lithium ion battery (LIB), respectively. Subsequently, the effective properties are determined based on the densified structures and compared with results of previously introduced methods. As in both, SOFC and LIB, the methods for the initial microstructure generation and for the determination of effective transport properties are the same, I will introduce those here. Densification processes, however, differ for the two cell types; therefore, they are introduced in the respective sections.

4.1. Generation of initial microstructure

As seen in the FIB-SEM reconstructions, the particles of the electrodes have various shapes and are not ideally spherical. Although those structures provide very detailed descriptions of the electrode structure, they offer little predictive capabilities [105], which, contrarily, numerical generated structures can offer. Even simplified shapes allow already large insight into the influence of certain parameters on microstructure and characteristic parameters. Spheres are computational the least expensive 3D-shapes, as information on centers (coordinates) and radii are sufficient to describe the configuration.

For the generation of randomly packed microstructures exist several algorithms, which can be divided in (i) algorithms using sequential addition of particles [108] and (ii) algorithms starting from a random distribution of points [109, 110, 111, 108].

Widely used, especially in research on SOFC electrodes, is the first group in form of the drop-and-roll algorithm [104, 84, 107]. Particles are added one by one (droped), and moved until they build three contacts with the previously inserted ones (roll). This leads to microstructures with a defined coordination number of 6. As discussed by Oger et al. [85], this is an artificial constraint obstructing "real randomness"—that, in contrast, would imply varying coordination numbers, in particular with larger size ratios. Moreover, the drop-and-roll algorithm produces a weak anisotropy caused by the insertion direction; furthermore, the generated assemblies have a loose structure [104] with packing densities below 60% [112]. In addition, periodic boundary conditions can only be achieved in all three directions by removing several layers of wall boundary particles. As only periodic boundaries allow for modeling bulk material, the second type of methods is more suitable for this work.

Also a hard-sphere approach can be found in research for the generation of initial packings: Starting from randomly distributed particles, the particles are moved under the consideration of contact forces. At first, particle centers are randomly placed into the volume, and initial overlaps are removed by applying repulsive forces at the contact points. Afterwards, either the particle size is increased step-by-step [105], or the size of the container volume is reduced [113]. During both processes, repulsive forces are placed at the contact areas to prevent overlapping. The densification process is, in general, stopped, when (i) the forces exceed a certain limit or (ii) the predetermined box size is reached. The second stop criterion causes most likely a slight anisotropy in the packing as usually the box volume is reduced only in one direction. A comprehensive overview of this and further packing algorithm can be found in [114], chapter 7.

More effective than the above described approaches are mathematical algorithms like the one first suggested by Jodrey and Tory [109] for the generation of random close packings. Close packings have a higher density of around 64% [115]—this is comparable to packing densities achieved by shacking or mixing an assembly. In the electrode preparation process, the granular materials are mixed thoroughly before applied to the current collector to achieve homogeneous distribution of the different components. Hence, we assume that the manufacturing process generates close packings (unless purposely prevented). Among the mathematical algorithm, the algorithm described in [109] allows for controlling the packing factor (PF) by a single parameter [116]. We used in this work a version adjusted and implemented by Gan [117] for binary sized packings. The algorithm will be referred to as random close packing (RCP) algorithm in the following. The method is explained in detail in [116] and is introduced here only briefly.

4.1.1. Random Close Packing algorithm

Besides the PF, the solid volume fractions ϕ_i, particle size ratio and overall number of particles n are defined in advance. Then, in a first step, random values for the center coordinates of the n spherical particles are generated within a given volume of size $L_a \times L_b \times L_c$—this is often a cube with $L_a = L_b = L_c$. Two radii are assigned to each particle: an outer radius $\tilde{r}_{\text{out}}$, which is initially set to yield a nominal packing factor of 100%, and an inner radius $\tilde{r}_{\text{in}}$ defined by the worst overlap found within the assembly. For monosized assemblies, all particle radii correspond directly to the calculated values, whereas for binary packings the individual particle radii are scaled by a factor $h(I)$ in dependence of the size ratio. This results for a particle I in $r^I_{\text{out}} = h(I)\tilde{r}_{\text{out}}$ and $r^I_{\text{in}} = h(I)\tilde{r}_{\text{in}}$. To generate a microstructure from this initial distribution, two steps are carried out iteratively: First, the worst overlap is reduced by moving those two particles apart, who had it. This leads mostly to a smaller overlap elsewhere and therefore a larger inner radius. As a second step, all outer radii are reduced slightly with a contraction rate depending on the number of particles, the packing factors calculated with the actual inner and outer radii, and a predefined variable Q. The parameter Q is the only variable control-parameter of the contraction rate, and hence, the final packing factor can be influenced by changing Q [116]. The iteration process stops when the difference between outer and inner radius is smaller than a given tolerance. With the implementation of periodic boundary conditions (PBCs), the assemblies represent bulk regions inside the electrodes [118]. An exemplary microstructure with a particle size ratio of 3 and a solid volume fraction of 40% of small particles is shown in Fig. 4.1.

4.1.2. Densification process

As the RCP algorithm results in assemblies which, in an ideal case, just contain one contact, the structures need to be densified to a certain amount. This allows to form connected electrode structures and mimics sintering, calendering or intercalation. In the simplest case—geometric sintering—this is done by increasing the radii to a certain amount while the particle centers are kept fixed (section 5). More complicated approaches consider mechanical interaction between the particles, which is required to model calendering or the intercalation process (chapter 6). The densification leads to overlapping particles, and based on the overlap the contact between two particles can be described. As previously said, the densification process vary for the two cell types, and therefore, they are introduced in the respective chapters.

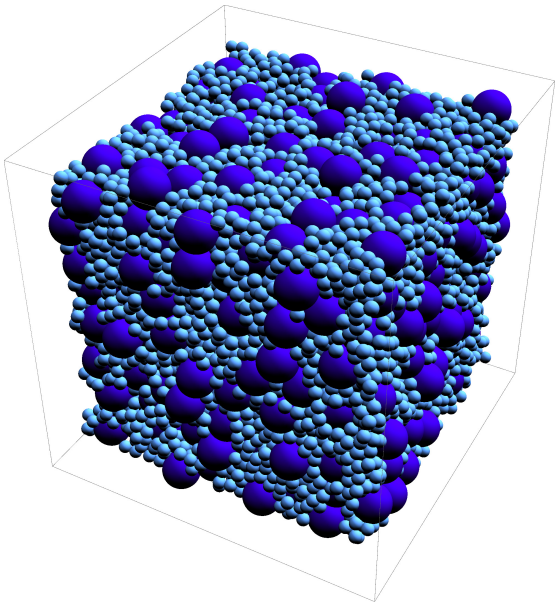

Figure 4.1.: Example for numerically generated structure with a particle size ratio of 3 and a solid volume fraction of 40% of small particles

4.2. Cluster detection for percolation studies

A complex step in the determination of effective transport properties in mixtures of orderless particles is to obtain information on the connectivity of the particles of each phase separately. Based on that information, the percolation probabilities and the effective conductivity can be determined. The importance of percolation probability P of electrode structures formed by a mixture of ion conducting and electron conducting particles was already discussed in detail in sections 2.3 and 3.1.2. To summarize this briefly: No percolation in one phase is synonymous for no conductivity of this phase within the electrode; and thus, it inhibits proper cell functionality.

4.2.1. Criteria for connectivity and percolation

For the determination of percolation probability P in arbitrary structures, we first need to define criteria for pairs of particles to be connected and for the volume to be percolating. For the description of the electrode microstructure in terms of percolation problems, particle centers are considered as sites, and their connection are the bonds. Each particle is assigned with certain bulk properties, e.g. a particle is either ion conducting or electron conducting. In the studies of this work, those properties were assigned to the particles based on their size, e.g. all large particles of a binary mixture are defined as ion conducting. Subsequently, a site is defined as occupied if the corresponding particle is either ion conducting or electron conducting, respective of whether ionic or electronic transport is studied. Further, two occupied sites are considered connected when the particles overlap, that is to say, if the Euclidian distance of their centers is smaller than the sum of their radii. Finally, two criteria for percolation can be distinguished: Isotropic percolation means that all boundaries are connected by one cluster; and directional percolation is given if there is a connecting cluster from one side of the box to the opposite side in each direction (x,y,z) separately. To investigate possible anisotropic characteristics, we applied the later definition.

4.2.2. Hoshen-Kopelman algorithm (HK)

The next step is to determine connected particles, referred to as a cluster, within the orderless microstructure. The straightforward way for this is to go from one particle directly to the next contacting neighbors and from there to the next contacts and so on. Algorithm based on this scheme are called Spanning-Tree algorithm, such as Depth-First- or Breadth-First-algorithm—they build, originating from the starting point, a tree-like construct [119]. As the effort raises linearly with the number of elements (and the proportionality coefficients are usually large), they are unsuited for large systems [120]. The Hoshen-Kopelman algorithm (HK), originally developed for lattice structures [121], is more adequate, as it is very low in memory usage and computation time.

For comprehensibility, the algorithm is first explained on lattice structures, before the details required for adaption to random systems are pointed out. Considering a lattice structure as shown

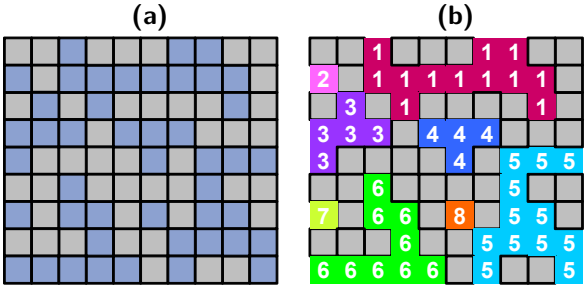

Figure 4.2.: (a) Lattice with randomly assigned occupation (dark) to each site (b) Cluster found with Hoshen-Kopelman algorithm considering the sites as connected if they share an edge

in (Fig. 4.2), a counter passes through the structure only once and assigns each occupied site (e.g. blue in Fig. 4.2) to a cluster. If thereby two yet existing clusters are found to be connected, this information is stored separately in a vector of much smaller size. After the run through the lattice is completed, the connected clusters are relabeled based on the information stored in the vector. Thus, as the relabeling operation is only performed on the much smaller sized vector, the time and memory space requirements are reduced in comparison to the other methods [118].

We extended the algorithm further to account for PBC, as they allow to eliminate wall effects and reduce volume size in the investigation of percolation probability as discussed in section 3.1.2. First, the extension of the lattice structure with PBC is explained, before the implementation of the extended HK for non-lattice structures is presented. Again, for illustration purpose only, the possible change in connectivity through periodic boundaries is explained on a lattice structure.

4.2.3. Extension of HK for periodic boundary conditions (PBC)

To illustrate the effect of periodic boundaries, those are generated by copying the original lattice structure in all directions (Fig. 4.3a). For the illustration, it is already labeled. Even though the copied lattice structure is cut off, e.g. as shown in Fig. 4.3a after the first layer, computational it is continued at the opposite side of the original lattice. Thus, it allows to mimic an infinite volume element. Too small original volume elements would, however, induce artificial patterns in the endless assembly. The copied versions of the cluster contain information of the position in

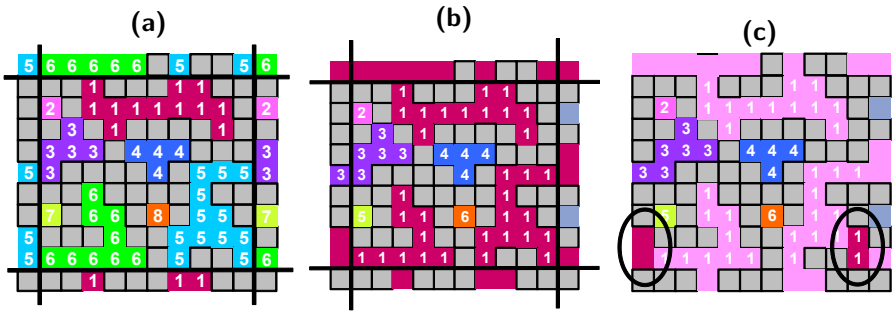

Figure 4.3.: Connectivity through periodic boundary conditions: (a) implementation of the periodic boundary conditions (PBC), (b) connectivity through the boundaries for cluster 1, (c) definition of percolation criterion for PBC

the original cluster additionally to its new location. The PBC lead to a state where lattice sites belonging originally to cluster 1 are in direct contact with cluster 5 or 6 and vice versa. Clearly these particles also belong to the clusters they are directly connected to. This leads to a combined cluster 1 containing the former cluster 5 and 6 (Fig. 4.3b). In contrast to cluster 1 found in the structure without PBC, now it connects the opposite edges horizontally. Based on this, we define an assembly to be percolating in one direction, when a cluster contains original sites on one side of the lattice and the periodic copies of these sites on the opposite side of the lattice as shown in Fig. 4.3c. This is done for all three directions separately.

4.2.4. Adaption of HK to non-lattice structures with PBC

The adaption of the original algorithm for non-lattice environments by [122, 123], was extended to account for PBC and implemented in C++ in order to investigate random electrode microstructures.

For adapting the algorithm to a non-lattice approach, the binary mixtures are first separated into the two phases, e.g. based on the particle size. Each phase is transformed in a random graph containing information on particle location (nodes) and contact information (links). The nodes are randomly numbered consecutively, and the algorithm runs once through this array of numbers sequentially, assigning each node to a certain cluster. After each particle within the assembly and the periodic boundaries is assigned to a certain cluster, the clusters connected through PBCs are merged. To do so, the periodic boundary particles perpendicular to the direction of examination (x, y, or z) are assigned to the cluster of the related original particles, which has the smallest number. Afterwards, the clusters have to be relabeled in order to consider all connections found after the first labeling, as explained previously. If a merged cluster now contains the original particle at on side of the box and the copy at the opposite side of the box in the direction of examination, the cluster is considered as percolating. Subsequently, the percolation probability is calculated from the ratio of percolated particles of one species to the overall number of this species within the assembly [84]. As we have chosen a directional definition of percolation, the probability is calculated separately for the different directions. Nevertheless, we also calculate an average probability: To do so, we mark particles, which are determined as being part of a percolating cluster when we determine the connectivity for each direction separately. Afterwards, we can identify all marked particles as part of one (or more) percolating cluster and obtain the ratio

of their sum over the overall number of particles of this species. In anisotropic assemblies, the directional percolation probabilities might deviate from the average one. In isotropic assemblies, on the other hand, no preferential direction is expected, and thus, both values should be similar.

4.3. Determination of effective transport properties

Based on the information of percolation probability, the effective ion and electron transport properties of a system can be determined. In the following, the different methods for this are introduced, before a more detailed description of the approach used within the scope of this work is given.

Only few studies exist, which solve the complete system of coupled partial differential equations given by the electrochemical processes and transport equations given in section 2.2 on artificial generated microstructures. As the field of variables, e.g. concentration of reactants, temperature etc. can be determined within the complete microstructure exactly, this approach allows to demonstrate, how inhomogeneities in geometry influence the field of variables and performance [57, 106, 124, 125, 105]. It is the most exact approach for static systems, however, different time- and length-scales have to be considered, which makes it computational most expensive, as discussed in section 2.3. Further, changes within the microstructure—either during calendering or operating life of the cell—are excluded. For this reasons, decoupled models, using parameters determined at the scale of the microstructure as input data for cell-level models, are an elegant alternative. Focusing on the determination of effective transport properties of porous composite electrodes in this section, the methods can be roughly divided into continuum theory, random-walk calculations and resistor-network approaches.

4.3.1. Continuum analysis

Continuum theoretical approaches usually use finite element simulations to determine the effective transport properties by solving the steady-state continuity equation

$$\nabla \vec{j} = 0 \tag{4.1}$$

on the discretizised microstructure with mostly commercial software, such as ABAQUS [75]. The required discretization and subsequent solving of the transport equation is computationally expensive for complex microstructures, such as the herein used electrode structures. The precision of the results strongly depends on the discretization, which, however, increases the computational time. Therefore, this method is usually applied to study assemblies with only few hundred particles [105, 113]. As for larger size ratios more particles are required to obtain representative results, this approach is disadvantageous.

4.3.2. Random-Walk simulation

Another method to determine transport coefficients of porous structures—in particular, diffusion coefficients—is the random-walk calculation. It is based on the measurement of distance traveled by tracer particles performing random movements within a phase of the structure [126]. The method is widely used in SOFC modeling, as it is applicable for investigations of both pore space

and solid phase. The mean square displacement $\langle u^2 \rangle$ of a large number of tracer particles in the relevant phase k is monitored over time. According to the basic principles of Brownian movement, as formulated by Einstein [127], the self-diffusivity D of a gas is related to the mean square displacement $\langle u^2 \rangle$ of a large number of gas particles. Assuming three dimensional space this is given by

$$D = \frac{\langle u^2 \rangle}{6t} \tag{4.2}$$

where t is the travel time. In a porous medium, the local microstructure causes the movement of gas particles to deviate from the straight path. To consider this in form of an effective diffusivity D_{eff}, the unimpeded diffusivity D_0 of a gas in a volume element with 100% porosity has to be corrected with the tortuosity. Theory suggests that D_0 scales with the tortuosity [29]:

$$D_{\text{eff}} = \frac{D_0 \epsilon}{\tau^2}. \tag{4.3}$$

A discussion of the different definitions of tortuosity can be found in [29]. It is assumed, that the tortuosity affects the effective conductivity with a similar functionality [32]:

$$\kappa_{\text{eff,k}} = \frac{\kappa_{\text{bulk,k}} \phi_k}{\tau^2}. \tag{4.4}$$

Additionally considering the connectivity within the phase, Tobochnik et al. [126] stated an effective conductivity scaled by P_k

$$\kappa_{\text{eff,k}} = \frac{\kappa_{\text{bulk,k}} \phi_k P_k}{\tau^2}. \tag{4.5}$$

This is a commonly used approach in SOFC, e.g. in [104], however, the discretization of the complex microstructure usually required for its application is computationally expensive. Also, the precision depends on the number of tracer particles and performed time steps, which additionally influences the computing effort. Moreover, to my knowledge, it has not been used to determine anisotropic transport properties without further adaption. LIB electrodes, however, are expected to have anisotropic microstructure after the calendering step. Thus, even though this approach is widely used, it is not completely suitable for the studies performed in this work. Nevertheless, as it is an established method, we used it for comparison of some exemplary results to validate our approach.

4.3.3. Resistor-Network approach

The resistor-network approach (RN) is a comparably fast and flexible approach, which can also be combined with changing electrode structures. It was used in this work to study effective transport properties in the electrodes. Thereby, the particle structure is converted in an electrical equivalent circuit by replacing particle-to-particle contacts with resistors R and particle centers with nodes [102]. A system of linear equations is then set up by using Kirchoff's current law [128] in combination with Ohm's law, which can be solved with the node potential method [129]. As no discretization is required with this approach, it is computational less expensive, and therefore, it is more suitable for systematic studies of the influence of microstructure. The downside of this approach is that for densities exceeding 85% the effective conductivity is overestimates, as discussed in [118]. As both, SOFC and LIB, require connected pore space to sustain transport in the fluid phase, we only consider structures with porosities $> 15\%$ in order to ensure this. Thus, the application of the RN approach is justified. The individual steps are explained in detail next, starting with the conversion of particle contacts in resistors.

Resistance between two contacting particles

As previously mentioned, the microstructures generated with the RCP algorithm are densified in order to form a connected electrode structure—this leads to overlapping particles. The densification process applied for SOFC electrodes is purely geometric. Therefore, it is used here for the derivation of a fit law for the resistance between two contacting particles. Determination of the conductivity between particles under mechanical load, as found in LIB electrodes, requires the consideration of deformation. Therefore, the calculation of the inter-particle resistance in LIB electrodes will be explained in chapter 6 in connection with the considered force law.

A numerical approach similar to Argento and Bouvard's [130] was chosen to calculate the one-dimensional resistance of two overlapping, equal-sized particles of the same material. The ohmic resistance $R_{\iota,\Upsilon}$ between two contacting spheres ι and Υ can be determined in analogy to its thermal resistance, which is defined as

$$R_{\iota,\Upsilon} = \frac{T_\iota - T_\Upsilon}{I} \tag{4.6}$$

with T_ι and T_Υ as temperatures at the extremities of the volume and I as the resulting flux. The steady state calculations of the thermal resistance were performed with Ansys CFX. Because of periodicity, the FE-calculations need only to be performed for two half spheres, as sketched in Fig. 4.4a. The resistance $R_{\iota,\Upsilon}$ was determined for several particle radii r_p, while the extremities were kept as a constant distance $d^{\iota,\Upsilon}$.

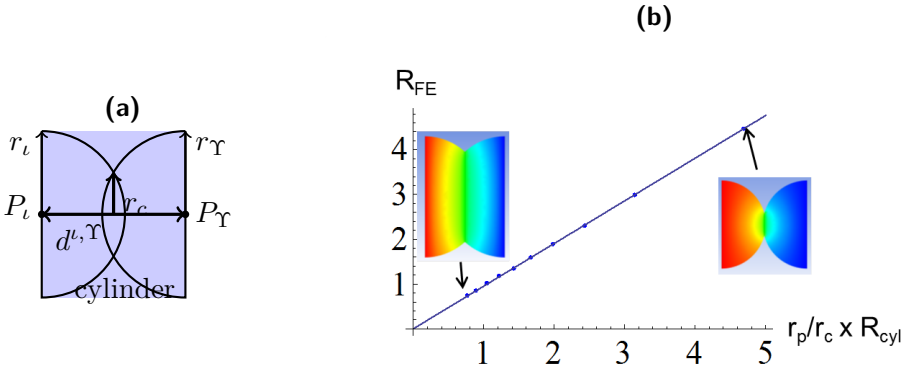

Figure 4.4.: (a) Sketch of the model of two overlapping spheres with the reference cylinder in light blue (b) Fit found for several contact configuration with increasing particle radius size. Two of the configurations are shown as example

In analogy to [130], the following linear relation was found to calculate the resistance between two particles relative to the resistance of a cylinder R_{cyl} of radius r_p and length $d^{\iota,\Upsilon}$ (light blue in Fig. 4.4a) in dependence of the contact geometry:

$$\frac{R_{\iota,\Upsilon}}{R_{\text{cyl}}} = 0.952 \frac{r_p}{r_c^{\text{SOFC}}}, \tag{4.7}$$

with the contact radius r_c^{SOFC} of the two overlapping spheres equal to

$$r_c^{\text{SOFC}} = \sqrt{r_p^2 - \frac{d^2}{4}}. \tag{4.8}$$

Two exemplary configuration for different particle radii and constant delta are shown in Fig. 4.4b in addition to the linear relation obtained by fitting the obtained data.

Network and node-potential method

Based on the fit law, the particle contacts can be converted into resistors $R_{\iota,\Upsilon}$ in accordance with the geometry of the contact. The centers of neighboring particles ι and Υ are considered as nodes in the following. After the particle assembly is converted in a resistor network, the node-potential method is used to calculate the overall conductivity of this network.

The node-potential method transforms electric circuits according to a well defined pattern into a system of linear equations; therefore it is well suited for software solutions. Detailed explanation can be found in e.g. [129]. It's derivation and implementation will be demonstrated on a small example for the circuit given in Fig. 4.5.

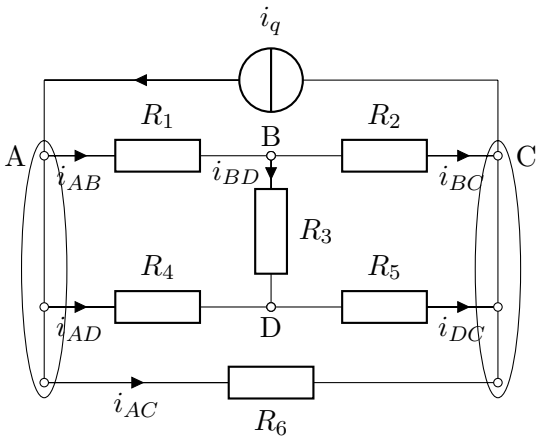

Figure 4.5.: Electric circuit of the exemplary calculation

First, the potentials of each node are calculated relatively to an arbitrary chosen node, whose potential is set to zero. To do so, a system of linear equations is set up using Kirchhoff's current law and Ohm's law. Thus, for node ι, we obtain

$$I_\iota = \sum_{\Upsilon} I_{\iota,i} = \sum_{i} \frac{\varphi_i - \varphi_\iota}{R_{\iota,i}}, \tag{4.9}$$

with I_ι as the sum of currents at node ι, $I_{\iota,i}$ the current in a branch between node ι and i caused by the difference in φ_ι and φ_i, which are the potentials at site ι and i, respectively, and $R_{\iota,i}$ is the resistance between nodes ι and i. The sum of currents is zero for all internal nodes. Replacing the resistance with conductivity values $G_{\iota,\Upsilon} = 1/R_{\iota,\Upsilon}$ this leads in the here considered example to

$$\begin{aligned}
\text{B}: &\quad (\varphi_B - \varphi_A)G_1 + (\varphi_B - \varphi_C)G_2 + (\varphi_B - \varphi_D)G_3 = &0\\
\text{C}: &\quad (\varphi_C - \varphi_A)G_6 + (\varphi_C - \varphi_B)G_2 + (\varphi_C - \varphi_D)G_5 = &I_q\\
\text{D}: &\quad (\varphi_D - \varphi_A)G_4 + (\varphi_D - \varphi_B)G_3 + (\varphi_D - \varphi_C)G_5 = &0
\end{aligned}$$

for the nodes B, C and D relative to the reference node A with the potential $\varphi_A = 0$. This can be rewritten in matrix form $[G][V] = [I]$, where $[G]$ is a symmetric matrix containing the

conductivities between percolated particles in contact, vector $[V]$ the unknown particle potentials and the vector $[I]$ the sum of currents for each particle—including the source terms.

$$\begin{bmatrix} G_1+G_2+G_3 & -G_2 & -G_3 \\ -G_2 & G_2+G_5+G_6 & -G_5 \\ -G_3 & -G_5 & G_3+G_4+G_5 \end{bmatrix} \begin{bmatrix} \varphi_B \\ \varphi_C \\ \varphi_D \end{bmatrix} = \begin{bmatrix} 0 \\ I_q \\ 0 \end{bmatrix}. \tag{4.10}$$

In general, the conductivity matrix $[G]$ can be determined for an arbitrary system with k nodes as

$$\begin{bmatrix} G_{11} & G_{12} & \dots & G_{1(k-1)} \\ -G_{21} & G_{22} & \dots & G_{2(k-1)} \\ \vdots & & & \\ -G_{(k-1)1} & -G_{(k-1)2} & \dots & G_{(k-1)(k-1)} \end{bmatrix} \tag{4.11}$$

with $G_{\iota,\iota}$ as the sum of the conductivities to all neighboring nodes and $G_{\iota,i}$ as the negative conductivity between node ι and node i. When there is no direct contact between two nodes, the conductivity is set to zero.

By considering the particles centers as nodes and calculating the resistance between two particles determined as described in section 4.3.3, every assembly can be transformed into an equivalent circuit; and then, based on this scheme it can be transformed into matrix form. As a particle has only few contacting particles in the assembly compared to the total amount of particles, the matrix contains a lot of elements that are zero; and therefore, $[G]$ is best saved in sparse form to reduce memory space.

To solve the complete system, potentials φ_1 and φ_2 are imposed on the opposing sides in the considered direction as boundary conditions. Thus, $[G]$ and the $[I]$ are known, which allows $[V]$ to be calculated. This is done with an iterative stabilized bi-conjugated gradient method (BICGSTAB) of EIGEN [131]. The potential distribution for one phase of an exemplary microstructure is shown in Fig. 4.6.

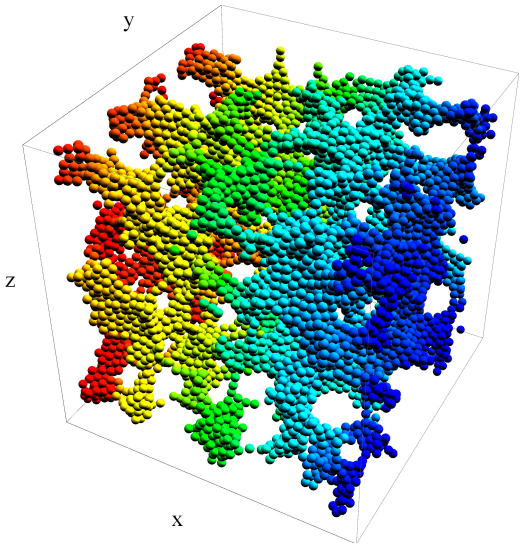

Figure 4.6.: Potential distribution of one phase with an applied potential difference in x-direction, particles colored according to their potential

The currents within the network can be found from back substituting particle potentials and solving Ohm's law for each contact. The total current I entering or leaving the network is then calculated by adding all currents of the boundaries. Finally, the effective conductivity $\kappa_{\mathrm{eff,k}}$ of phase k can then be calculated in S/m

$$\kappa_{\mathrm{eff,k}} = \frac{I}{\varphi_1 - \varphi_2}\frac{L}{A}, \tag{4.12}$$

with L as the box length in the considered direction and A as the area of the cross section perpendicular to the considered direction. In the numeric calculation of the current I through the system, the bulk conductivity $\kappa_{\mathrm{bulk,k}}$ of the particle bulk material is applied. Due to the linearity of Ohm's law, the effective conductivity can be normalized by the bulk conductivity $\kappa_{\mathrm{bulk,k}}$ to obtain material independent results:

$$\frac{\kappa_{\mathrm{eff,k}}}{\kappa_{\mathrm{bulk,k}}} = \frac{1}{\kappa_{\mathrm{bulk,k}}}\frac{I}{\varphi_1 - \varphi_2}\frac{L}{A}. \tag{4.13}$$

4.3.4. Validation of the RN approach

As already published in [118], the RN method was compared with calculations performed with an established Random-Walk simulation (RW) (section 4.3.2) and effective media theory (EMT) (section 3.1.1).

Therefore, a cubic lattice structure of $5 \times 5 \times 5$ equally sized particles was densified by uniformly increasing the particle size. The self-consistent approach of the effective medium approximation used here, can be simplified for composites with only one conducting phase to $\kappa_{\mathrm{eff,k}}/\kappa_{\mathrm{bulk,k}} = 1.5\phi_k - 0.5$. The effective conductivities normalized to the bulk conductivity obtained with the different methods for several stages of densification is shown in Fig. 4.7. Below densities of 80%,

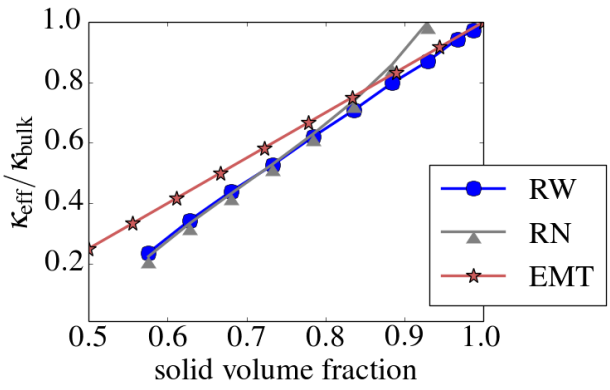

Figure 4.7.: Comparison of effective conductivity from different approaches, RW: Random-Walk (section 4.3.2), RN: resistor network (section 4.3.3), EMT: effective medium theory (section 3.1.1)

the difference of the results between RW and RN is marginal, rendering the RN approach suitable. For densities exceeding 85%, RN overestimates conductivity with respect to RW, and also exceeds the values of EMT.

As described in [130], the notion of touching particles is no longer valid at densities approaching a packing factor of 100% due to interaction of the multiple contacts. Such structures rather should

be modeled as a dense matrix with distributed pores. According to Carson et al. [69], the effective conductivity of material with open, continuous pore-space, as required in the electrode structures, is bounded above by the self-consistent effective-medium approximation. The results found with the RN approach exceed this upper bound already for densities of 85% (Fig 4.7)—this indicates that already for that amount of densification the notion of touching particles is no longer valid. The resistor network approach (RN) therefore overestimates the effective conductivity for high packing factors as the particle overlaps intersect. Nevertheless, as both, LIB and SOFC, require connected pore space to sustain electrolyte or gas transport, it is justified to investigate their structures with RN as we only consider assemblies with densities below 85%.

As an further example, the effective conductivities of the two phases of numerically generated, binary structures with a size ratio of 5 are shown in Fig. 4.8. Ten assemblies of each volume fraction were analyzed for statistical purpose, and the mean values of the conductivity of the large and small particles (referred to as l and s, respectively, in the following) were calculated. Let us first compare in Fig. 4.8a and 4.8b the mean conductivities found with RW and RN approach to assess the systematic deviation due to methodical differences. The predicted tendency

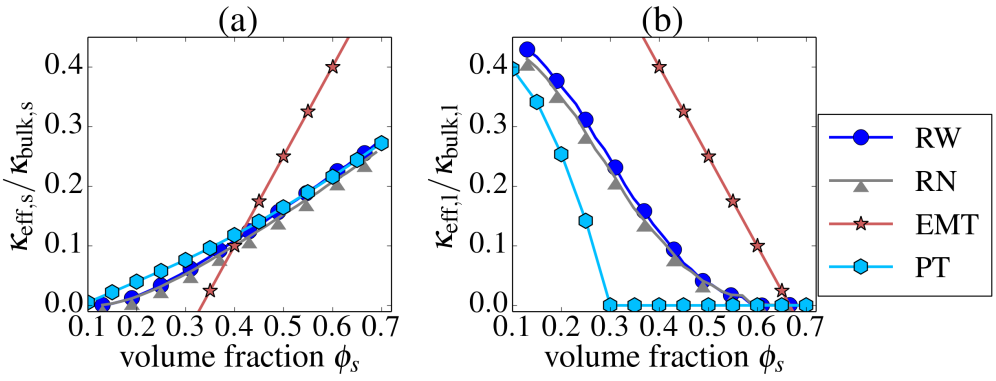

Figure 4.8.: Effective conductivity calculated with resistor network approach (RN) compared to results from a Random-Walk (RW) approach, effective medium approximation (EMT) and an adjusted Brueggeman equation (PT) for (a) small and (b) large particles for assemblies with a size ratio of 5

of increasing conductivity with increasing volume fraction is similar. The relative deviation $|k_{\text{eff,RN}} - k_{\text{eff,RW}}|/k_{\text{eff,RW}}$ is 5 to 9% for the large particles and 5 to 7% for the small ones. Such a small deviation between the mean values of the two approaches confirms that the results found are in reasonable agreement. Thus, RN is suitable for the determination of the effective conductivities of separate phases in densified structures. Additionally, the results are compared to values obtained with EMT (Eq. 3.8, EMT) and the Bruggeman equation, adjusted with the percolation probability [84] (Eq. 3.21, PT). As expected, the EMT approach is not well suited to determine the effective properties of non-symmetric assemblies, like it is here because of the size ratio. The adjusted Bruggeman approach (PT), on the other hand, predicts the effective conductivity adequately for the small particle phase s; however, it underestimates the percolation threshold and the effective conductivity for large particles significantly. The possible causes of the large deviation will be discussed in detail in section 5.3. But even now, the large deviation shows the relevance of choosing an appropriate approach to achieve meaningful results and understanding of the microstructure's impact on effective transport properties.

In Fig. 4.9, the variations of the results calculated from the maximum and minimum value of the 10 assemblies of each composition are illustrated. The deviation obtained for the RN method is slightly shifted to the right for better visibility. The deviation in the conductivities of the same composition is due to the variation in microstructure of the randomly generated distributions. The standard deviation for RW is in most cases insignificantly larger than the values of the RN approach. That difference might be caused by the averaging over a certain number of time steps in RW, and we assumed it would vanish with increasing time. For the large particles, the error is below 2% for most compositions; for few errors up to 5% were found. For the small particles, it is an order of magnitude smaller. The difference between the deviation of large and small particles is due to the fact that the amount of small particles is large in comparison to the number of large particles within the structure. As, however, the error is reasonably small for both species, the assembly size in terms of number of particles can be considered to be sufficient.

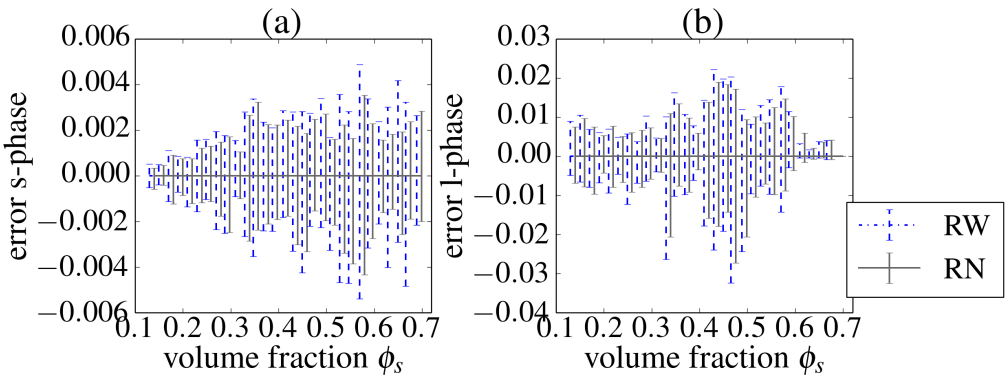

Figure 4.9.: Deviation in the results found for different microstructures with RW and RN approach for (a) small and (b) large particle phase

5. Modeling SOFC Electrodes

Based on the previously described methods, the impact of size ratio, volume fraction, and sintering on effective properties in solid oxide fuel cells (SOFCs) is studied in this chapter. Under consideration of the questions in section 3.3, the numerically obtained results are compared to the analytic ones. As described, SOFC electrodes are considered in this work as a mixture of ion and electron conducting spheres, which are randomly distributed in a volume element. The most common materials for the cells are yttria-stabilized zirconia (YSZ) as ion conducting phase and nickel (Ni) and strontium-doped lanthanum manganite (LSM) as electron conducting phase of anode and cathode, respectively. We will focus on the anode in the following; nevertheless, the findings are also applicable for cathodes when densified to the same amount.

For the systematic investigation of the microstructures, a multitude of assemblies is generated for size ratios from 1 to 10 and solid volume fractions of small particles between 0 and 1. For statistics, 10 assemblies per composition, with 10 000 particles each, are set up. First, we will describe the densification step, and then, study percolation probability and effective properties for different mixtures. For generality, the properties of small particles will be referred to with a subscript s and these of large particles with a subscript l. Obviously, small and large particles can be electron conducting and ionic conducting, respectively—or vice versa.

5.1. Sintering in SOFC

As described in [17], the anodes are first sintered to nearly 100% density and subsequently, the nickel oxide (NiO) within is reduced, creating sufficient porosity to enable gas transport. Starting with mixtures of 65:35 vol.% NiO:YSZ leads to porosities around 25.6% and solid volume fractions of 50:50 vol.% Ni:YSZ. The sintering process itself can best be simulated with a diffusion based discrete element model, as used e.g. by Schneider et al. [132]. The reduction of NiO, however, is not considered in those approaches. Due to the many unknown quantities in sintering and reduction, even complicated models do not exactly reflect the microstructure. Therefore, we consider a purely geometric approach to be sufficiently exact for the densification. In accordance with [107, 105, 104], the densification is done by increasing the radii to a certain amount, and the particle centers are kept fixed. In those studies, different contact angles between two contacting particles represent different sintering stages [107] and allow to adjust the porosity [104]. Typical values of the contact angle used in percolation approaches are around 15° for the smaller particle [89] (see Fig. 3.8). As in Monte-Carlo structures the contact situation depends upon the local configuration, Sanyal et al. [105] allowed contact angles between 0 and 30°.

5.1.1. Stop criteria for densification

In the implementation of densification, the selection of a stop criterion that allows for modeling realistic properties of the electrode structure is necessary. Besides a given contact angle, packing factor (PF) or densification rates can be chosen. The packing factor allows to easily compare modeled parameters to values found for real microstructures in focused ion beam scanning electron microscopy (FIB-SEM). But, for size ratios unequal to one, the PF of uncompacted assemblies generated with random close packing (RCP) algorithm varies significantly, as shown in Fig. 5.1. Within an arbitrary size ratio, the packing factor is dependent on the volume fraction. Usually,

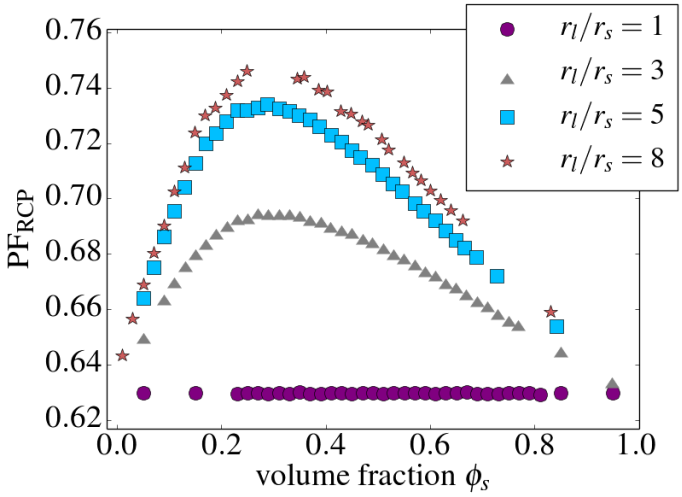

Figure 5.1.: Packing factor of undensified random close packings vs. solid volume fraction of small particles for different size ratios

the maximum PF of a certain size ratio is found between 25 and 30% solid volume fraction of small spheres ϕ_s [133], which is in good agreement with the results shown in Fig. 5.1. Up to this value, the small amount of smaller particles is filled into the interstices of the mechanical stable network of larger particles. Thus, they are just added to the packing factor of a stable, monosized assembly. Above the maximum value, on the other hand, the amount of small particles becomes so large that the network of large particles is destructed.

Since a fixed PF as densification criterion neglects this variation in the initial PF, it is unsuitable for the investigation of the influence of size ratio. As the internal processes during sintering and subsequent reduction in the electrode fabrication are not yet fully understood, two different densification approaches will be investigated.

Densification ratio

First, assuming that the densification rate is independent of the composition, a densification ratio, which is always the same, is applied in form of Δ PF to the different assemblies. In [54], the packing factor $\mathrm{PF}_{\mathrm{exp}}$ is experimentally determined as 74%, the numerically generated structures with monosized spheres, on the other hand, have a packing factor $\mathrm{PF}_{\mathrm{RCP}}$ of 63%. We determined the amount of densification from the ratio of those two values to be $\Delta PF = \frac{PF_{\mathrm{exp}}}{PF_{\mathrm{RCP}}} = 1.175$.

With this, the radii within the assembly are increased step-by-step; and the new packing factor is calculated under consideration of the new particle radii minus the volume of the spherical caps in overlapping regions. Several structures with different size ratios are densified by the determined ΔPF, which leads to packing factors between 74% for monosized and around 86% solid fraction for a large size ratio of 8. As, according to Bertei et al. [104], a porosity of 10% is sufficient to ensure a connected gas phase, the packing factor of large size ratio are still in a suitable range.

Mean contact angle

Second, assuming that contacting during sintering is independent of the composition, a specified mean contact angle θ will be applied as stop criterion. In contrast to the value usually used in the analytic percolation studies, the mean contact angle of monosized assemblies densified to 74% is 17.9°. A mean contact angle of 15°, on the other hand, leads to a packing factor of 70.8% for monosized structures. The different packing factors due to the different mean contact angles mimic different sinter conditions, which cause different amount of densification. In order to have the same conditions for monosized assemblies, a mean contact angle of 17.9° is chosen as further stop criterion for different size ratios. Following the analytic approach in section 3.2, the contact angle of the smaller particle is taken into consideration for the calculation (Fig. 3.8). Additionally, results for a mean contact angle of 15° are given to study the influence of densification and enable the comparison to the analytic approach.

5.1.2. Microstructure of densified structures

The influence of the two criteria, ΔPF and mean contact angle θ, on the respective value is shown in Fig. 5.2. Applying the first approach leads to a variation of the mean contact angle in binary

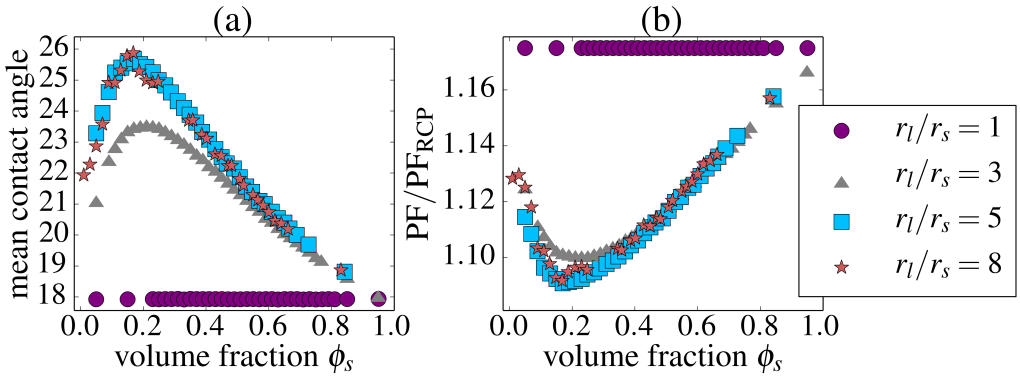

Figure 5.2.: (a) Mean contact angle for assemblies densified with a PF ratio of 1.175 and (b) ratio of packing factor to initial packing factor for assemblies densified to a mean contact angle of 17.9°

sized mixtures with volume fraction and size ratio, as shown in Fig. 5.2a. The second approach leads to a variation in $\Delta\text{PF} = \text{PF}/\text{PF}_{\text{RCP}}$ with volume fraction and size ratio (see Fig. 5.2b). This shows that the second approach leads to less densification for binary sized mixtures. Further, the mean contact angle of binary mixtures densified with constant ΔPF is higher than in monosized assemblies (Fig. 5.2a).

Contact angles

To examine the difference in contact angle between monosized and binary sized assemblies, we calculated the probability distribution of contact angles, determined for the small particles in the microstructures. This is shown exemplary in Fig. 5.3 for a monosized and a binary sized assembly of size ratio 8 with solid volume fraction of 50:50%.

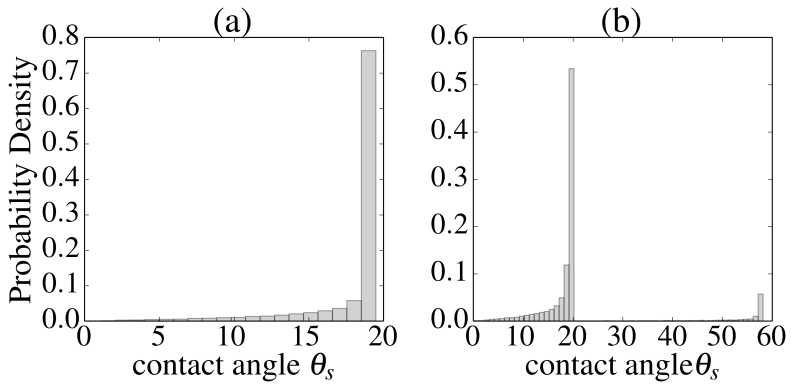

Figure 5.3.: Probability of the contact angles θ of the small particles of an assembly of solid volume fractions of 50:50 for (a) a monosized assembly and (b) a assembly with size ratio of 8

The probability distribution is very similar for all 10 generated structures of the same composition. To calculate the contact angle of two overlapping, equal sized particles, one particle of the contact pair is randomly assigned as small and the other as large particle. Comparison of the probability distribution within the binary and the monosized assemblies shows that the small particles have a very similar probability distribution for the range of contact angles smaller than 20°. Additionally, a certain amount of significantly larger angles is found for the binary sized structures. Most probably, the smaller angles are found for small particles in contact with small particles—equivalent to a monosized structure—the large contact angles, in contrast, are found for small particles in contact with large ones.

As illustrated in Fig. 5.4, the maximum contact angle, correlating to the second peak in Fig. 5.3b, is dependent on size ratio and mean contact angle. The ratio of maximum contact angle to mean contact angle of the assemblies, on the other hand, is independent of the densification approach. An maximum $\theta_{\max}$ of 58° is found for a size ratio of 8. This greatly exceeds the maximum allowable contact angle suggested by Sanyal et al. [105] of 30°; however, that value would led to porosities of 47%. As those porosities are much higher than the experimentally determined values [54], we consider this as too little densification. Finally, as only for a maximum contact angle above 90°, absorption of small particles by the large ones is expected—causing physically not sound structures and numerical difficulties—values around 60° are still acceptable.

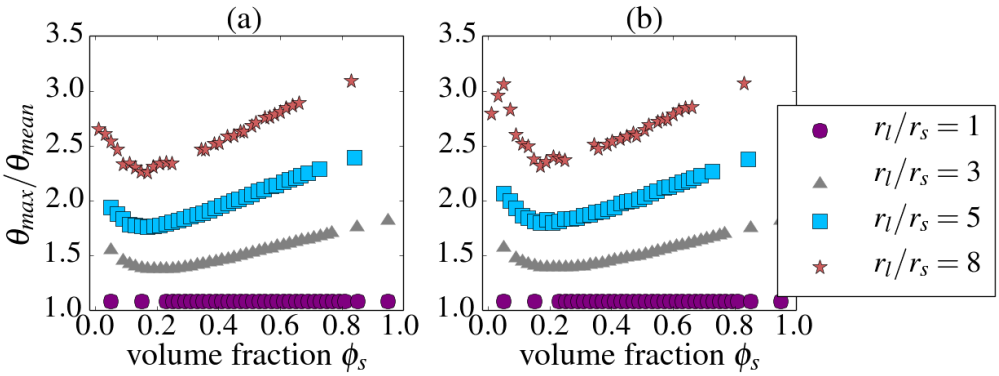

Figure 5.4.: Maximum contact angle divided by the mean contact angle θ found in the assemblies, which are densified (a) with a PF ratio of 1.175 and (b) to a mean contact angle of 17.9°

Coordination Numbers

As described in section 3.1.2, the overall coordination number Z_0 is expected to affect the relevant effective cell properties, such as percolation probability, effective conductivity and reactive area. Consequently, it is significant for the analytic determination of those parameters. As the drop-and-roll algorithm (section 4.1) specifies a constant overall coordination number of 6 in advance, this value is usually used in analytic studies. Such a target value, however, reduces the degree of freedom in the "randomness" of the microstructure. In contrast to this, the RCP algorithm, in combination with the densification, does not specify Z_0 in advance. As shown in Fig 5.5, an overall coordination number of Z_0= 6 is only found for very few compositions. In monosized assemblies, the values are found to be around 7.8 contacts per particle, regardless of the composition. For binary sized mixtures, on the other hand, Z_0 depends on the volume fraction, as was also reported by Bertei and Nicolella [88].

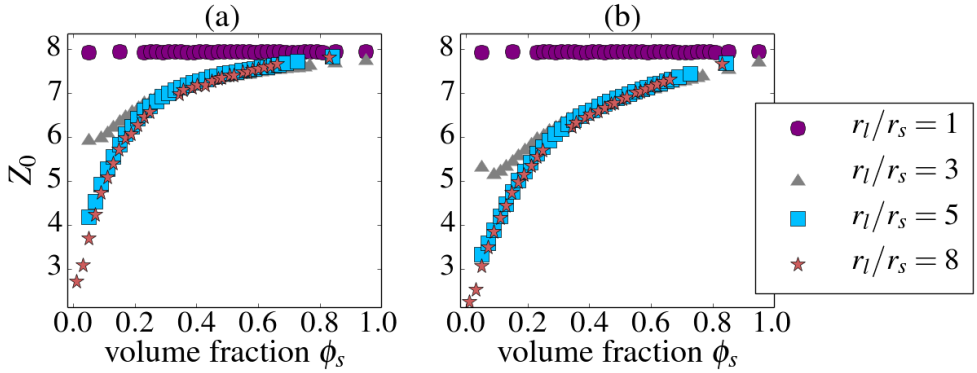

Figure 5.5.: Overall coordination number Z_0 in assemblies, which are densified (a) with a PF ratio of 1.175 and (b) to a mean contact angle of 17.9°

Both densification approaches lead to similar results: binary sized mixtures with large amounts of small particles ($\phi_s \to 1$) have overall coordination numbers like monosized assemblies. From there, the coordination number decreases slowly with decreasing amount of small particles until it

starts dropping more drastically in the range of 25 to 30%—this is similar to the range of the maximum packing factor (Fig. 5.1). The drop is more drastically for a larger size ratio. Probably, the drop in coordination number is induced by the small particles: ongoing from the point of maximum packing factor down to lower volume fractions, the small particles are no longer part of the mechanical stable network. They rather fill the interstices in form of so-called rattlers, which have less than three contacts. Therefore, the amount of particles with a low number of contacts increases. The larger amount of small particles in larger size ratios intensifies this effect. To verify this, the number of contacts the particles have with particles of the same species k divided by the amount of particles of this species (i.e. $Z_{k,k}$) is presented in Fig. 5.6. For small volume fractions ϕ_s, the large particles in binary mixtures have an internal coordination number of 5 and higher. Thus, they form a mechanical stable network. The decreasing amount of contacts within the smaller species confirm that these are loosely filling the interstices. That tendency is reversed for large volume fractions of ϕ_s. Further, at the threshold from a mechanical stable network of large particles to a network of small particles, both species have a similar amount of contacts with themselves.

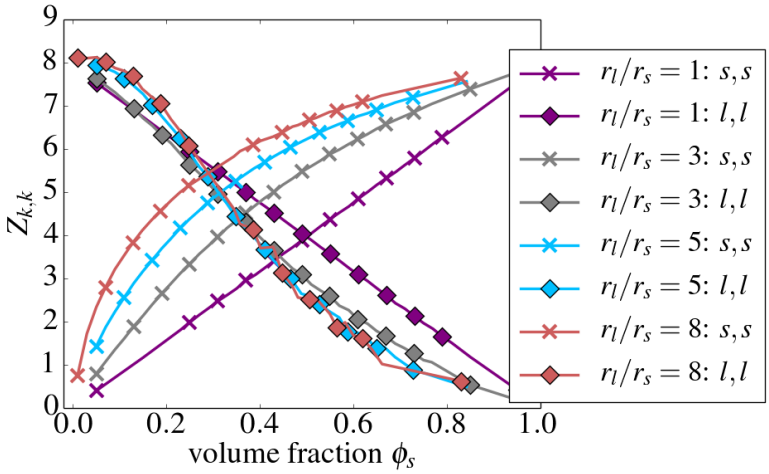

Figure 5.6.: Number of contacts of particles of the same species divided by the number of particles of this species for different size ratios

A comparison of the numerically found values for $Z_{k,k}$ to the analytically determined values (Eq. 3.17) is given exemplary for the size ratio of 8 in Fig. 5.7. As the original assumption—Z_0 equals 6, regardless of size ratio and volume fraction—does not reflect on the conditions in the numerically generated microstructures, we adjusted Eq. 3.17 with numerically determined parameters and compare the different results in Fig. 5.7. First, the value of $Z_0 = 7.8$, as found for monosized particles, was considered in Eq. 3.17 (denoted as $Z_0 = 7.8$ in Fig. 5.7). That leads to relatively good agreement for the contacts within the small particles $Z_{s,s}$; in contrast, a significant deviation is found for the large particle contacts $Z_{l,l}$. Also using the numerically determined values Z_0 found for the size ratio of 8 in Eq. 3.17 ($Z_{0,num}$) leads to good agreement for the small particle contacts $Z_{s,s}$; however, for the large particles a significant variation between numerically determined and analytic results is found as well. The curvature of the function $Z_{0,num:l,l}$, on the other hand, shows similarity to the numerically determined values (num: l,l). This indicates that scaling of $Z_{0,num:l,l}$ allows to approximate the numerical results. Indeed, a relative close

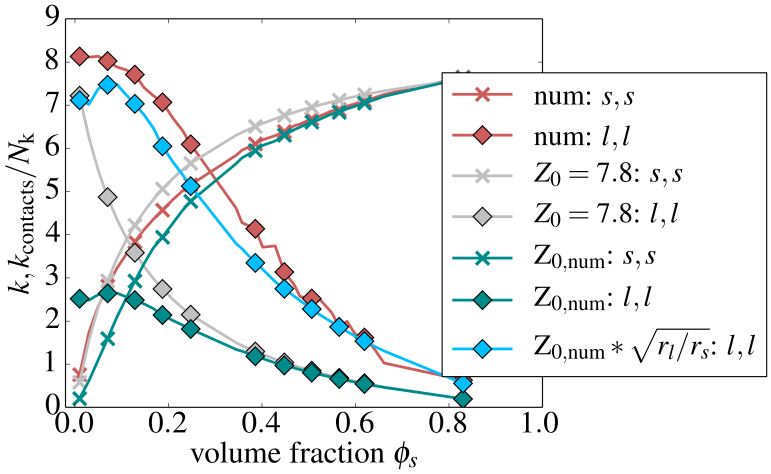

Figure 5.7.: Number of contacts of particles of the same species divided by the number of particles of this species for a size ratio of 8

approximation of the numerically found values is obtained by scaling $Z_{0,num:l,l}$ with the square root of the size ratio $\sqrt{r_l/r_s}$. This holds true for the large particles of different size ratios as well. Thus, such a scaling should be considered for further adaption of the concept of coordination number: it represents a possibility to analytically predict the coordination number $Z_{l,l}$ of large particles more accurate, taking size ratio and an overall coordination number dependent on volume fraction into account.

Free surface area and contact area

Another relevant parameter for cell performance is the amount of specific surface area S of a porous structure, as was indicated in section 3.2. Most likely, S influences the total extent of three-phase boundary (TPB) within an electrode structure and also contains information on the amount of connected area within the electrode. Therefore, it is assumed that a large specific surface area is beneficial for cell performance, which will be investigated in the following sections. Further, calculating S for the numerically generated structures enables us to examine to which part the analytic approximations in section 3.2 predict the numerical calculated values (Eq. 3.28 for monosized and Eq. 3.32 for binary sized structures).

The surface area per unit box volume S_{RCP} of the undensified structures generated with the RCP algorithm is largest for the monosized assemblies and decreases with size ratio, as shown in Fig. 5.8a. For different size ratios, the minimum moves to smaller values of ϕ_s, in a similar range as the maximum of the initial packing factor is. The analytic approximation, derived in section 3.2 (see Fig. 3.11), predicts a decrease of surface area in comparison to monosized assemblies; it does, however, does not show that minimum.

During densification, two contradicting effects influence the surface area: on the one hand, the free specific surface area is assumed to decrease due to the contact zone between the increasing particles; on the other hand, the particle radii increase, and thus, the total surface of the particles. Calculating the free surface area of densified structure shows a reduction of around 30% for

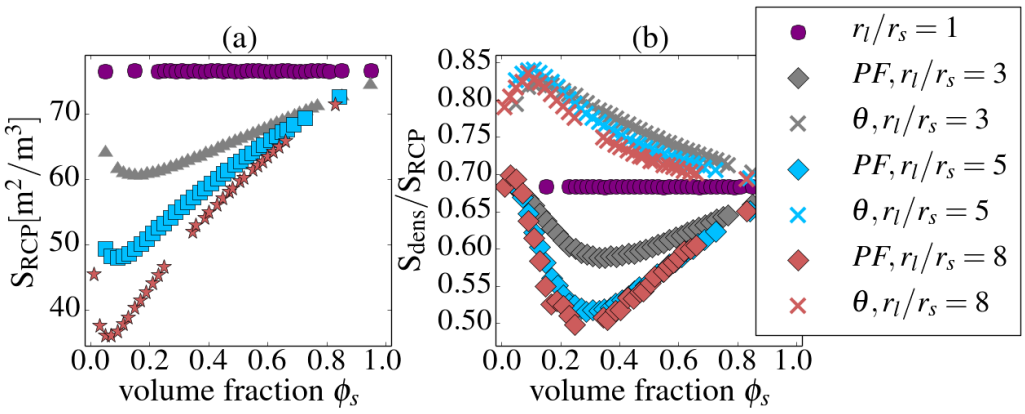

Figure 5.8.: (a) Specific surface area S_{RCP} of the initial, non-densified packings and (b) specific surface area of the different densified packings relative to their initial values S_{RCP}

monosized structures in Fig. 5.8b for the free specific surface area of the densified packings relative to its initial value. For the constant packing factor ratio ΔPF approach, the reduction is more severe for larger size ratios. In contrast, in comparison to the monosized values, the binary mixtures densified with the mean angle approach undergo less reduction during the densification. Nevertheless, comparing the total numbers instead of the relative ones, the largest amount of free surface area is achieved with monosized assemblies. A smaller mean contact angle of 15° reduces the reduction of the specific surface area due to the densification process. As previous considerations suggested a correlation between TPB and specific surface area S, we expect the largest extent of TPB for monosized assemblies with a low densification rate. This is further examined in section 5.4.

Additionally, based on the previous results, the total contact area can be calculated approximately from the difference of initial free surface area S_{RCP} minus the free surface area of the densified structures (see Fig. 5.9a).

As expected, the tendency found for the specific surface area, is reversed for the contact area: In comparison to the values found for monosized assemblies, a constant densification rate ΔPF leads to larger contact areas relative to the initial specific surface area; the constant mean contact angle approach, on the other hand, causes a smaller area relative to S_{RCP}. Looking at the total size of contact area per box volume, the highest one is found for the binary structures densified with the ΔPF approach. Assuming that the effective conductivity is correlated to the overall contact area, those results predict improved effective conductivities with higher densification.

Further, one might assume that the contact area of a structure is correlated to its overall coordination number Z_0 and mean contact angle θ. To study that, we calculated the mean contact area per particle surface by

$$A_c = \frac{\pi r_c^2 Z_0}{4\pi r_p^2} = \frac{sin^2(\theta) Z_0}{4}, \tag{5.1}$$

which is presented in Fig. 5.9b. Comparing these results to the numerically determined contact area shows that the approximated results underestimate the relative contact area in general. Further, for the constant mean contact angle approach, the results are dominated by the overall coordination number. Nevertheless, the predicted tendency for the contact area is correct for

most compositions. Thus, this simplification is applicable to obtain a rough estimation, but it is invalid to approximate the contact area properly.

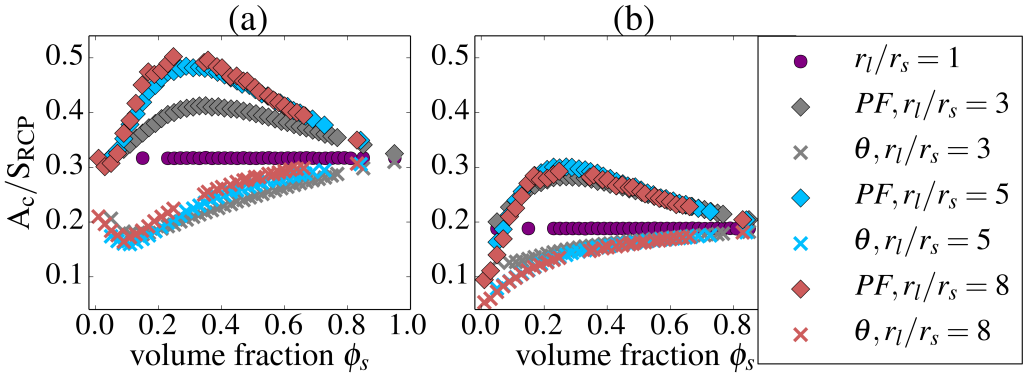

Figure 5.9.: (a) Contact area per box volume within the different assemblies, normalized to the specific surface area S_{RCP} of the initial packing, which is shown in Fig. 5.8(a); (b) mean contact area per particle surface, calculated by Eq. 5.1

Summary

Comparing the basic geometrical parameters obtained from the numerically generated structures to the analytic assumptions and findings, described in section 3.1.2, we already found significant discrepancies:

- In undensified structures, the PF varies significantly with size ratio; however, in the analytic approach the porosity $\epsilon = 1 - PF$ is usually assumed to be constant.
- Experimentally determined and thus numerically generated PF of monosized structures are 74%; this is contrasted by 60% PF in the analytic approach.
- A mean contact angle of 15°, widely used in literature, leads to a PF of 70.8% for monosized microstructures.
- The overall coordination number Z_0 is dependent on size ratio and volume fraction. Only for monosized assemblies, a constant value of 7.8 was found. Conversely, the analytic approach is based on the assumption of a constant value of 6 for all structures.
- The numerically found coordination number $Z_{k,k}$ differs significantly from the analytic values, in particular for the large particles. For those, the best fit was found by adapting Eq. 3.17 with the numerically found values of $Z_{0,num} \times \sqrt{r_l/r_s}$. $Z_{s,s}$, on the other hand, can be approximated based on $Z_{0,num}$.
- The analytic solution of the specific surface area predicts the same trend as the numerical one, however, deviates in some details.
- The contact area found numerically is larger than the one found with an analytic approximation under consideration of numerically determined coordination numbers Z_0 and mean contact angle θ.

These discrepancies provoke the assumption that predictions made based on the analytic approach might be inaccurate; and thus, they result in inaccurate predictions of the effective properties. To investigate this further, we determined the percolation probability and the effective conductivity as well as the TPB; those are presented in the next steps.

5.2. Percolation probability

The importance of percolation in SOFC electrode structures was described in section 3.1.2: only when both, electron conducting and ion conducting phases, are connected sufficiently, the cell can function properly. Information on the connectivity of particles within the numerically generated microstructures was obtained with the adapted Hoshen-Kopelman algorithm (HK) algorithm described in section 4.2. Based on this information, the percolation probability is calculated as the ratio of percolated particles of one phase k to the overall number of k particles within the assembly [84]. In order to consider both phases, the overall percolation probability P is calculated by multiplying the probabilities of both phases, as it is done in the analytic investigations of P. We continue to distinguish between small and large particles, assuming that one size is either ion conducting or electron conducting.

5.2.1. Percolation for different densification approaches

First, the percolation probabilities obtained for the different densification steps are compared. As shown in Fig. 5.10a, the percolation probability of monosized assemblies is independent of the densification approach. This also holds true for size ratios up to 5. For larger size ratios the low densification with a constant mean contact angle of 15° reduces the range of percolating compositions slightly, as can be seen in Fig. 5.10b for a size ratio of 8. the difference in the percolation probability for the two other approaches is marginal.

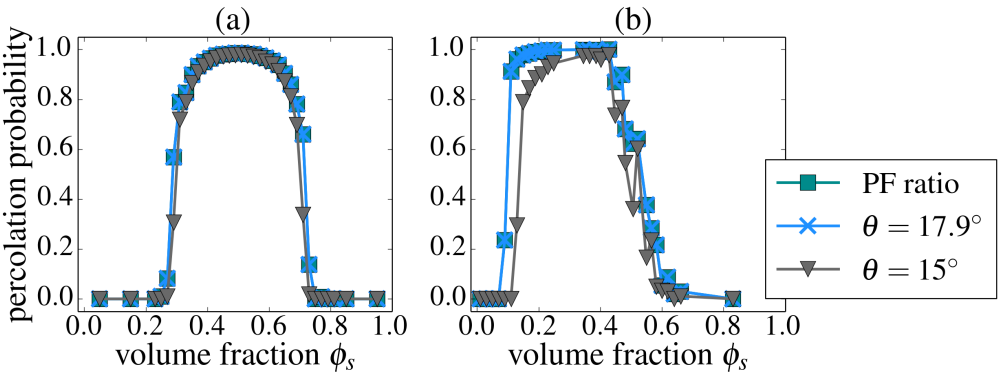

Figure 5.10.: Percolation probability P obtained for (a) monosized structures and (b) binary sized structures with a size ratio of 8 for all three densification approaches

Comparing the percolation threshold in Fig. 5.10a and 5.10b shows the influence of size ratio on the percolation probability: similar to the analytic findings, the percolated region between upper and lower limit moves with increasing size ratios r_l/r_s to smaller volume fractions ϕ_s. For better insight, the volume fractions of the percolation threshold, denoted as critical volume fraction

$\phi_{c,i}$ with i as percolating phase, are given in Tables 5.1 and 5.2 in comparison to analytically determined values for different size ratios. Since the critical volume fraction $\phi_{c,i}$ is given as the volume fraction of small particles ϕ_s, $\phi_{c,s}$ is the volume fraction of small particles above which percolation of the small particles is most likely (Table 5.1), and $\phi_{c,l}$ denotes the volume fraction of small particles above which the large particle are no longer percolating (Table 5.2). The finite size of the volume element most likely broadens the percolation threshold to a threshold range, as discussed in section 3.1.2 (Fig. 3.3) [78]. Therefore, we did not consider the volume fraction of the first percolated assembly but a percolation probability of 50%. The analytic values are exact solutions of Eq. 3.20 for P=0.5. For the numerical solutions, in contrast, only a number of discrete values of ϕ_s were investigated. Hence, most likely none of the compositions has a percolation probability of exactly 50%; and thus, the volume fraction of the first mixture with a percolation probability higher than 50% will be considered here.

	P_{ratio}	P_{angle}	P_{analytic}
$\phi_{c,s}(r_l/r_s = 1)$	0.29	0.29	0.319
$\phi_{c,s}(r_l/r_s = 3)$	0.19	0.19	0.135
$\phi_{c,s}(r_l/r_s = 5)$	0.15	0.15	0.086
$\phi_{c,s}(r_l/r_s = 8)$	0.11	0.11	0.055

Table 5.1.: Volume fraction $\phi_{c,s}$ at the percolation threshold of the the small particles r_s for the different densification approaches. For volume fractions ϕ_s smaller than this value, no percolation is found in the s phase.

	P_{ratio}	P_{angle}	P_{analytic}
$\phi_{c,l}(r_l/r_s = 1)$	0.71	0.71	0.681
$\phi_{c,l}(r_l/r_s = 3)$	0.59	0.59	0.416
$\phi_{c,l}(r_l/r_s = 5)$	0.53	0.53	0.299
$\phi_{c,l}(r_l/r_s = 8)$	0.51	0.51	0.211

Table 5.2.: Volume fractions $\phi_{c,l}$ at the percolation threshold of the large particles r_l for the different densification approaches. For volume fractions ϕ_s larger than this value, no percolation is found in the l phase.

The numerical results for the critical volume fraction coincide for the two densification approaches, as demonstrated in Table 5.1 and 5.2. This allows to consider only one densification approach in the further discussion on percolation probability. Comparison to the analytic values, derived with Eq. 3.20, shows a significant deviation in the results. To emphasize those differences, in Fig. 5.11

the numerical results obtained with the densification approach ΔPF for size ratios from 0.1 to 10 (Fig. 5.11a) are compared to the contour plot of the analytic solutions in Fig. 3.5b, depicted here again for the readers convenience. With increasing size ratio, the difference between the two solutions becomes more pronounced; especially the percolation threshold of the large particles r_l is moved to larger volume fractions ϕ_s.

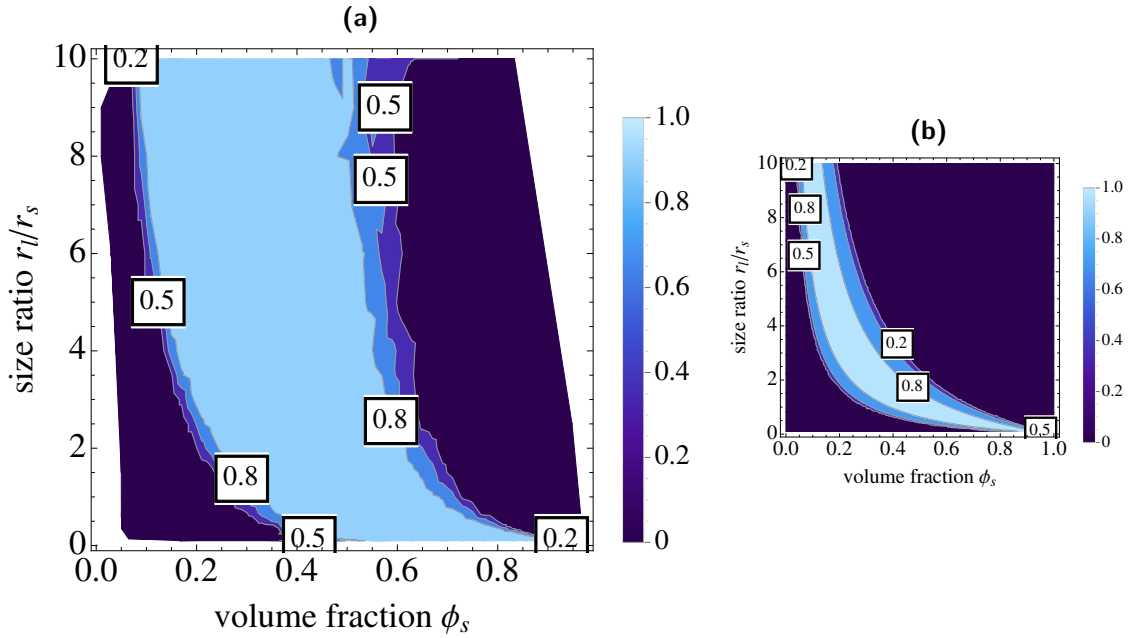

Figure 5.11.: Percolation probability for (a) numerically generated microstructures and (b) for comparison the analytic derived solution as already shown in Fig. 3.5b for size ratios from 0.1 to 10

5.2.2. Analysis of the deviation from analytic results

The deviation of the numerical results from the analytically determined, as shown in Fig. 5.11, can be caused by different factors, which are discussed in this section. The possible influence factors are (i) inappropriate assumptions made in the analytic approach and (ii) insufficient size of the numerically generated structures. The differences between the assumptions made in the analytic approach and the geometrical parameters of the numerically generated structures were already discussed in section 5.1.2. It was shown in Fig. 5.1 and Fig 5.5 that the packing factor as well as the overall coordination numbers Z_0 deviate even for monosized assemblies from the assumptions made in the analytic solution. Furthermore, the numerical values are strongly dependent on the size ratio and volume fraction of the composition. Also, the numerically determined coordination number $Z_{k,k}$ varies significantly from the analytic solution. To assess those factors, the influence of an adapted Z_0 on the percolation probability is studied next. Further, the relationship between $Z_{k,k}$ and the percolation threshold is examined next. Additionally, the influence of the finite size of the modeled structure is investigated.

Influence of the coordination number Z_0 on the percolation probability

To examine the impact of an adapted coordination number Z_0, we first use the numerically derived constant value $Z_0 = 7.8$ of monosized assemblies in the analytic approach (Eq. 3.17) to determine an adapted threshold $P_{\mathrm{Z_0=7.8}}$. The resulting values of $P_{\mathrm{Z_0=7.8}}$ show a shift of $\phi_{c,s}$ to smaller volume fractions ϕ_s, and of $\phi_{c,l}$ to larger ϕ_s (Table 5.3 and 5.4). This induces a broadening of the percolated area, as it is seen with the numerically generated assemblies. Nevertheless, the agreement between numerical and analytic results has barely improved, as now $\phi_{c,s}$ is even lower than the numerical values, and the $\phi_{c,l}$ remains below the numeric value.

	P_{ratio}	$P_{\mathrm{Z_0=7.8}}$	P_{analytic}
$\phi_{c,s}(r_l/r_s = 1)$	0.29	0.243	0.319
$\phi_{c,s}(r_l/r_s = 3)$	0.19	0.097	0.135
$\phi_{c,s}(r_l/r_s = 5)$	0.15	0.060	0.086
$\phi_{c,s}(r_l/r_s = 8)$	0.11	0.038	0.055

Table 5.3.: Volume fractions $\phi_{c,s}$ at the percolation threshold of the small particles r_s for the adapted analytic approach in comparison to the previous values. For volume fractions smaller than this value, no percolation is found in the s phase.

	P_{ratio}	$P_{\mathrm{Z_0=7.8}}$	P_{analytic}
$\phi_{c,l}(r_l/r_s = 1)$	0.71	0.757	0.681
$\phi_{c,l}(r_l/r_s = 3)$	0.59	0.509	0.416
$\phi_{c,l}(r_l/r_s = 5)$	0.53	0.384	0.299
$\phi_{c,l}(r_l/r_s = 8)$	0.51	0.280	0.211

Table 5.4.: Volume fractions $\phi_{c,l}$ at the percolation threshold of the large particles r_l for the adapted analytic approach in comparison to the previous values. For volume fractions ϕ_s larger than this value, no percolation is found in the l phase.

In that, the dependence of Z_0 on size ratio and volume fraction was neglected—even though the coordination number varies significantly. In particular for large size ratio and small volume fractions of ϕ_s ($\phi_s \to 0$), the coordination number decreases substantially. To estimate the influence of the numerically determined coordination numbers, we applied values more adequate for the expected volume fraction of the percolation threshold in Eq. 3.17: for $\phi_{c,s}$, Z_0 equals approximately 4 and for $\phi_{c,l}$, Z_0 is 7. The results for the percolation threshold based on those coordination numbers are given in Table 5.5 and 5.6 for $\phi_{c,s}$ and $\phi_{c,l}$, respectively.

	P_{ratio}	$P_{\mathrm{Z_0=4}}$	$P_{\mathrm{Z_0=7.8}}$	P_{analytic}
$\phi_{c,s}(r_l/r_s = 5)$	0.15	0.155	0.060	0.086
$\phi_{c,s}(r_l/r_s = 8)$	0.11	0.103	0.038	0.055

Table 5.5.: Volume fractions $\phi_{c,s}$ at the percolation threshold of the small particles r_s for $Z = 4$ in comparison to the previous values. For volume fractions smaller than this value, no percolation is found in the s phase.

	P_{ratio}	$P_{Z_0=7}$	$P_{Z_0=7.8}$	P_{analytic}
$\phi_{c,l}(r_l/r_s = 5)$	0.53	0.347	0.384	0.299
$\phi_{c,l}(r_l/r_s = 8)$	0.51	0.250	0.280	0.211

Table 5.6.: Volume fractions $\phi_{c,l}$ at the percolation threshold of the large particles r_l for $Z = 7$ in comparison to the previous values. For volume fractions ϕ_s larger than this value, no percolation is found in the l phase.

Applying those values, leads to good agreement with the numerical found threshold values for $\phi_{c,s}$. Conversely, the new adaption impairs the agreement further for $\phi_{c,l}$.

Those adaptions demonstrate the effect of a size ratio dependent coordination number Z_0 on the percolation threshold. The large deviation for $\phi_{c,l}$ at large size ratios between the numerically and analytically determined percolation thresholds, however, remains.

Critical coordination number Z_c

Further, the analytic approach is based on the assumption that the percolation threshold is—independent of size ratio—correlated to a certain coordination number $Z_{k,k}$, denoted as critical coordination number Z_c. As discussed in section 3.1.2, there is, however, no consensus on a threshold values, especially for size ratios larger than 1. Nevertheless, in the analytic investigation of SOFC percolation, the value of $Z_c = 1.764$, as determined by Kuo and Gupta [86], is widely applied.

To examine this relationship, the percolation probabilities found for the numerical assemblies in this work are plotted versus the coordination number $Z_{k,k}$ in Fig. 5.12 for several size ratios. For the small particles s, the percolation threshold correlates to critical coordination numbers

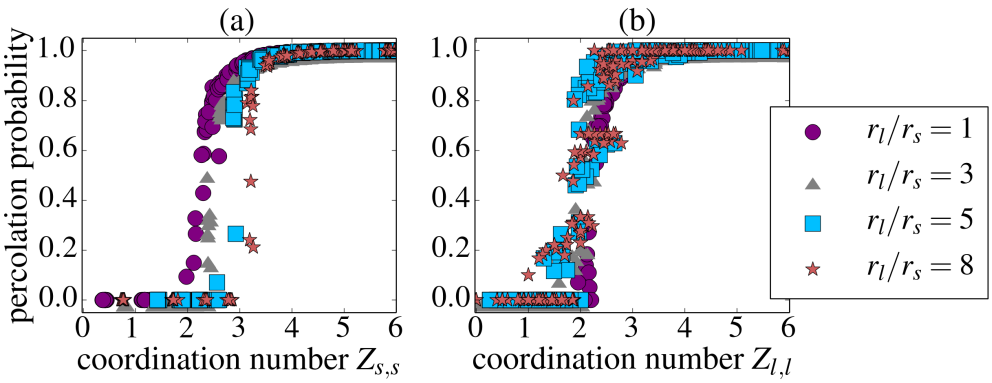

Figure 5.12.: Percolation probability P versus coordination number (a) $Z_{s,s}$ and (b) $Z_{l,l}$ for several size ratios from $r_l/r_s = 1$ to $r_l/r_s = 8$

$Z_{c,s}$ between 2 and 3, whereby the value distinctly increases with size ratio. In contrast to that, the critical coordination number for larger particles $Z_{c,l}$ scatters diffusely around 2— with a significant spread for larger size ratios. This indicates that the assemblies contain too few large particles for higher size ratios. At a radius ratio of 8, for example, the assemblies contain 156 large particles at the critical solid volume fraction of 0.1 for percolation of the small particles, and only

16 large particles at the critical volume fraction of 0.55 for percolation of the l phase. Comparing the results to the findings of Roussenq et al. [78] with regard to lattice size, shown in Fig. 3.3a, corroborates this. The possible effect of the investigated volume element size should also be considered for small particles: with increasing size ratio, the number of small particles within the assembly increases and thus, the ratio of particles per box length as well. Nevertheless, the distinct increase of percolation threshold with size ratio suggests that the correlation of the percolation threshold to a single coordination number Z_c, as done so far, is an oversimplification. Rather, a dependence on further parameters such as size ratio, method for generation, and densification should be taken into account in future studies of effective properties.

Influence of the finite size of volume element

In order to compensate the finite size of the structures, 10 assemblies of each composition were generated. So far, we only examined the mean of the 10 assemblies for each composition. The deviation in the results helps to further examine the effect of size on the results: In infinite volume elements, the percolation threshold takes place at one critical volume fraction ϕ_c; below, no connectivity is found (percolation probability = 0), and above, the percolation probability is 1. At the critical volume fraction itself, a large deviation within the percolation probability of the 10 different assemblies of that composition is most likely. When the volume element size becomes smaller, the percolation threshold is no longer a peak—rather, it is broadened to a range.

To study this, in Fig. 5.13, the standard deviation of the percolation probability for all 10 assemblies of the same composition is shown—for all volume fractions for radius ratio 1 and radius ratio 8. Within the range of percolation threshold, the percolation probabilities of the 10 different

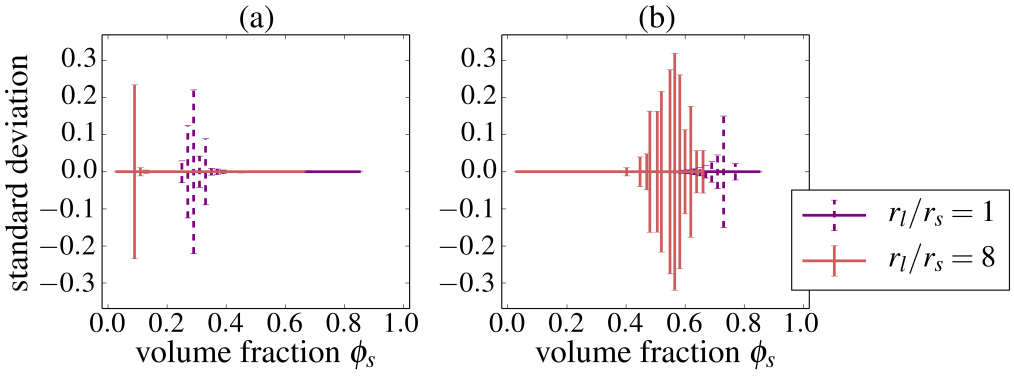

Figure 5.13.: Standard deviation in percolation probability versus volume fraction for (a) small and (b) large particles for two size ratios $r_\mathrm{l}/r_\mathrm{s} = 1$ and $r_\mathrm{l}/r_\mathrm{s} = 8$

assemblies of each composition deviates significantly. A single peak in the standard deviation of percolation probability, as found for the small particles in $r_l/r_s = 8$ (Fig. 5.13a), indicates a high accuracy of the determined percolation threshold. For the other cases in the example, the values scatter about a median. In an infinite volume, the percolation threshold for monosized assemblies is expected to be symmetric, when the particles are randomly assigned as large or small in order to achieve the target volume fraction of each composition. Due to the finite size of the volume element—in combination with the random nature of the structures—the standard deviation differs at the upper and lower limit of the percolation range. Further, for the large particles in $r_l/r_s = 8$

(Fig. 5.13b), the dispersion with respect to the volume fraction is wide. Although the dispersion could be reduced with larger assemblies, 10 assemblies of 10,000 particles were considered to be sufficient as a trade of between accuracy and computational costs. The standard deviation of the percolation probability is very similar for the mean contact angle approach. For 15° slightly larger values are found.

In conclusion, all of the three studied parameters have an impact on the deviation between numerically and analytically determined values of the percolation probability. Consideration of numerical coordination numbers Z_0 positively influenced the accuracy of the analytic solution at the lower limit $\phi_{c,s}$. It seems, however, that for a higher accuracy of the upper limit $\phi_{c,l}$, the correlation of critical coordination number Z_c and percolation threshold must be revaluated. The numerical results indicate a dependence of Z_c on the size ratio. Additionally, the influence of the ratio of particle size to box volume size on the percolation threshold could not be ruled out. As the effective conductivity and the TPB are determined under consideration of the percolation probability, the scattering of the numerical results should be kept in mind—in particular for larger size ratios.

5.3. Effective conductivity

The effective conductivities κ_{eff} of the assemblies was determined with the resistor-network approach (RN) approach, as introduced in section 4.3.3, based on the information on connectivity within the clusters. For generality, the effective properties, indexed with eff, are given relative to the bulk values, which are indexed with bulk.

5.3.1. Comparison of numerical and analytic results

Comparing monosized assemblies (Fig. 5.14), and the ones with a large size ratio of 8, (Fig. 5.15) to the averaging approaches—introduced in section 3.1—clearly demonstrates the necessity of explicit consideration of the microstructure to obtain reliable results for cell modeling:

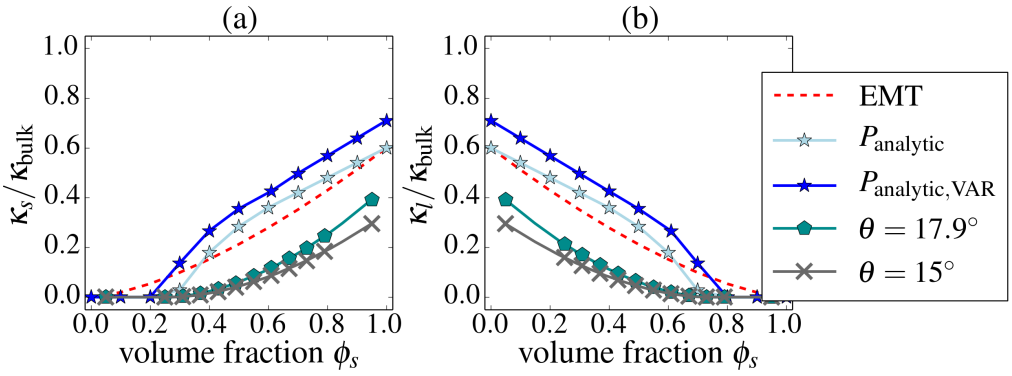

Figure 5.14.: Effective conductivity relative to the bulk conductivity for size ratio 1 with averaging theories from section 3 and the different densification approaches for phase s and its complementary phase l

As shown in Fig. 5.14, the averaging methods overestimate the effective conductivity already for monosized assemblies. While the effective conductivity based on the analytic determination of percolation probability P_{analytic} (Eq. 3.21) shows a similar onset of conductivity, the curve of the effective medium approach EMT (Eq. 3.11) reflects better on the conductivity found in the densified microstructures - except for the percolation threshold. Adapting the analytic percolation approach with the microstructural parameters $Z_0 = 7.8$ and $PF = 0.74$, as determined in section 5.1.2, further worsens the agreement between the averaging approach and the results of the densified microstructures ($P_{\text{analytic,VAR}}$). Furthermore, the impact of the degree of densification—symbolic for different sinter conditions—can be seen: with increasing volume fraction of the conducting phase, the conductivity of the differently densified assemblies varies more. This supports the assumption that a larger contact area, which is equivalent to larger mean contact angles, is correlated to elevated conductivity. The averaging approaches neglect the impact of fabrication process so far.

For assemblies with a large size ratio of 8, presented in Fig. 5.15, the effect of different mean contact angles increases further. Also a deviation between the mean contact angle of 17.9° and the ΔPF ratio densification can be seen, which, however, is less significant. This affirms the assumption of a correlation between mean contact angle and effective conductivity. In contrast to

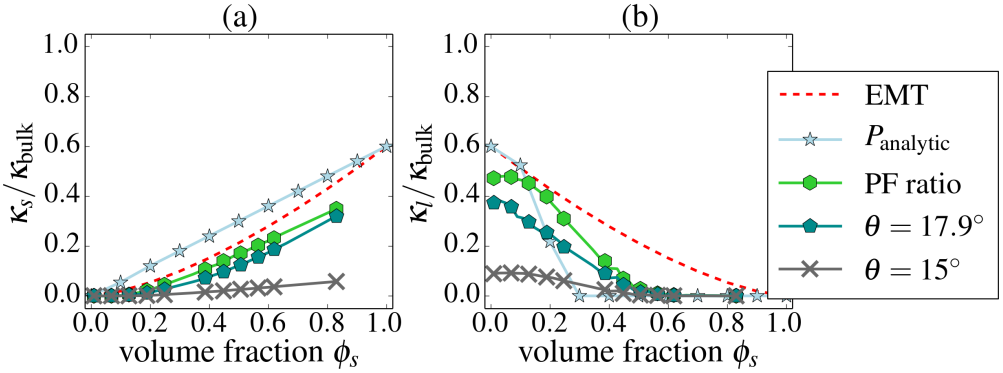

Figure 5.15.: Effective conductivity relative to the bulk conductivity for size ratio 8 with averaging theories from section 3.2 and the different densification approaches for phase s and its complementary phase l

the results for monosized structures, the conductivities found for binary sized assemblies vary for the small and the large phase for the analytic percolation approach as well as for all densification methods. The conductivities of the small phase are in relatively good agreement with EMT for the higher amounts of densification; the curves of the large phase rather show similarities with the analytic percolation approach for those two densification approaches. The percolation threshold, however, varies significantly—the possible causes for that were already discussed in the previous section. The values found for the smaller mean contact angle of 15° are significantly lower for both phases; this emphasizes the relevance of the process conditions.

5.3.2. Influence of the size ratio

Further, to study the influence of size ratio, the effective conductivities of microstructures with different size ratios are compared in Fig. 5.16. In the left column (Fig. 5.16a and 5.16c) results

for assemblies densified with constant ΔPF as stop criterion are shown, while in the right column (Fig. 5.16b and 5.16d) the mean contact angle approach was used. The upper row shows the effective conductivities κ_{eff} of the small phase s and the lower row the values of large phase l. All show the same—and expected—trend of increasing conductivity with increasing volume fraction of the respective phase. For all but the large phase in the mean contact angle approach, shown in Fig. 5.16d, the effective conductivity improves with larger size ratio. In the mean contact angle approach, however, the monosized assembly leads to highest conductivities for the large particles; and the size ratio of 3 provides the lowest values. Apparently the smaller densification of this approach significantly effect the contacts within the large particle phase.

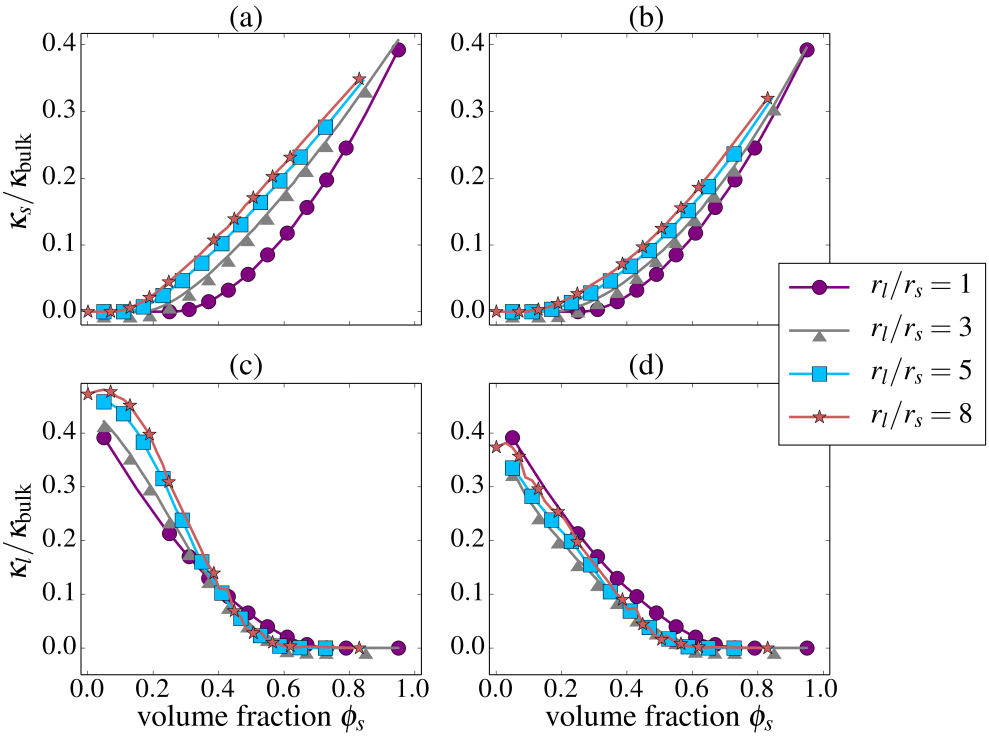

Figure 5.16.: Effective conductivity relative to the bulk conductivity found in assemblies, which are densified with a PF ratio of 1.175 ((a), (c)) and with a mean contact angle of 17.5° ((b),(d)) for several size ratios. The upper row shows the results for the smaller particles, while the lower contains the larger particles.

Considering the relevant range of volume fraction, in which both phases are conducting ($0.11 < \phi_s < 0.71$), given in Table 5.1 and 5.2 for the different size ratios, the effective conductivities obtained for the large sized particle phase l are larger than the values found for small particles. In the experimental studies (section 2.3), it was suggested that the effective conductivity of YSZ is more critical for cell performance since the bulk value of the ion conductivity is small in comparison to the electron conductivity. Based on this, it is reasonable to choose a configuration, which achieves optimized transport properties for the YSZ phase, while the Ni phase is still sufficiently connected to sustain electron transport. As the bulk values of the electron conductivity are high in comparison to the ionic bulk values, a smaller ratio of effective conductivity to bulk conductivity is tolerable. As the first approach achieves higher effective values (Fig. 5.16a and 5.16c), it is considered in the following. Thus, the requirements are best met when small sized Ni-particles are

combined with large sized YSZ particles: The highest effective conductivity relative to the bulk conductivity is achieved for large particles in compositions with large size ratios and small volume fractions of small particles. Thus, large sized YSZ particle allow to optimize the ionic transport. Furthermore, a small volume fraction of small particles is sufficient in such compositions to allow for a connected pathway through the volume.

5.4. Three-Phase boundary

In addition to sufficient transport in all phases, the three reaction components, which are oxygen ions, electrons, and gas molecules, need to be in contact to allow for the energy releasing reactions to take place, as described in section 3.2. Besides geometrical information on the contact, the connectivity of the three phases has to be taken into account to distinguish between the overall contact area and the electrochemical active region. In literature [95, 89, 33, 34], both the circumference and the area of the triple contacts are denoted as TPB. As was shown in Fig. 3.10, the different approaches for the calculation of the extent of the TPB of a single contact predict the same impact of morphology on the overall TPB. When normalized to the respective maximum extent of TPB determined for the monosized mixtures, the variation of the results is negligible for the three descriptions of TPB. Therefore, we consider it sufficient to calculate only the TPB length given by Eq. 3.22 for the numerically generated assemblies. In the numerical calculations, only particles connected to a percolating cluster were considered; this means that only the active amount of TPB was determined.

To enable comparison with the analytic results found in section 3.2 with Eq. 3.26, the numerical results shown in the following are normalized with $a_{\text{line}} = 1.296 \times 10^{12}$ m/m^3; this is the maximum value found for monosized assemblies in section 3.2. In Fig. 5.17, the results determined with the different approaches are given for monosized (Fig. 5.17a) and binary sized assemblies with a size ratio of 8 (Fig. 5.17b). First, comparing the different densification approaches to the analytic approach shows that—even though predicting the same tendencies—the analytic approach underestimates the extent of TPB significantly for monosized assemblies. In binary sized assemblies with a size ratio of 8, the amount of active TPB found for the mean contact angle of 15° is in good agreement with the analytic results. The differences of the volume fractions, for

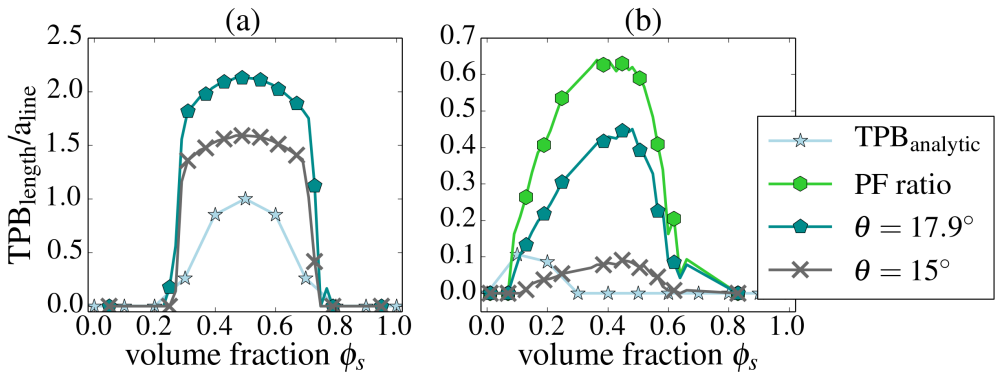

Figure 5.17.: Comparison of the three phase boundary length normalized with TPB length introduced in section 3.2 of the different approaches for (a) monosized and (b) binary sized assemblies with size ratio $r_l/r_s = 8$.

which active TPB is detected, is caused by the deviation between the numerically and analytically determined percolation thresholds. Further, comparing the results of the different densification approaches at an arbitrary size ratio, it indicates that a higher degree of densification is correlated to a larger active TPB. Finally, comparing the extent of TPB for monosized assemblies and the assemblies with a size ratio of 8, it shows that the TPB decreases substantially with increasing size ratio.

In order to predict the extension of the active TPB, the assumption was made that, in general,a larger extent of active TPB is obtained for larger free surface area (section 3.2). The examination of the specific surface area S in section 5.1.2, Fig. 5.8, showed that a larger size ratio leads to a smaller free surface area. As also the active TPB decreases significantly with size ratio, this supports the assumption. Conversely, within an arbitrary size ratio, a higher amount of densification corresponds to a lower specific surface area—and to a larger extension of TPB. As this contradicts the assumption, we revaluate the correlation, which only seems partially true. It appears that the initial free surface area allows to predict the tendency—or potential—a microstructure has for the formation of active TPB. In an undensified structure, a large free surface area offers the possibility to form a large number of contacts, and thus, a large active TPB. The actual extension of the TPB is then correlated to the densification process, which emulates the degree of sintering: with large contact radii (i.e. higher densification), the extent of TPB per contact is enlarged as well.

5.5. Effective electrode resistance

As stated in section 2.3, the two effective parameters $\kappa_{\text{eff,YSZ}}$ and TPB were experimentally identified to be mainly responsible for cell performance. Both, high effective ionic conductivity and large TPB lead to improvements in cell performance [134]. Investigating the two parameters separately led to contradicting recommendation for an improved microstructure: For an optimized effective conductivity $\kappa_{\text{eff,YSZ}}$, large size ratios and small volume fractions of the electron conducting phase are beneficial; however, for large TPB monosized composition with 50:50% of solid volume fraction are advantageous.

To predict a tendency for an optimized overall cell performance, the combined effect of the two parameters on the effective cell resistance has to be considered. This can be done with a modified Tanner-Fung-Virkar (TFV) model, which was shown e.g. in [54, 134] to be in good agreement with the experimentally determined overall cell resistance. The TFV model [135] is based on a simplified geometry, illustrated in Fig. 5.18, for which an analytic solution for the cell resistance can be derived. Further, considering the effective conductivity $\kappa_{\text{eff,YSZ}}$, as determined in section 5.3, as bulk conductivity and the active TPB (section 5.4) to scale the activation polarization at the surface, allows to adapt the model in such a way that it takes the microstructure into account. First, I briefly explain the derivation of the original model, for which a more comprehensive explanation can be found in [134, 136]. Subsequently, the different adaptions are introduced, and the influence of the two parameters is assessed.

5.5.1. The Tanner-Fung-Virkar model

For the derivation of the analytic solution of the cell resistance R_{cell}, several assumptions were made regarding the electrode structure and the relevant transport processes [136, 135]; those are introduced next.

Simplified electrode structure

The simplified electrode structure (Fig. 5.18) approximates the randomly distributed ion conducting phase of the electrodes as columns. Important geometric electrode parameter, such as porosity, electrode thickness and YSZ particle size are still considered in the calculation. In this work, the

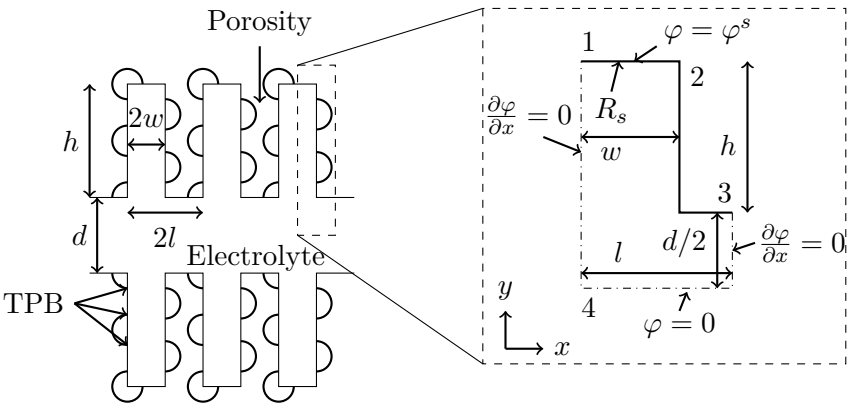

Figure 5.18.: Simplified electrode structure of the TFV model [135] with the repeat-unit, which is considered in the derivation of the model, on the right

heights of the dense electrolyte layer is denoted as d, and the heights of the electrode as h. The thickness of the cell is obtained by extending Fig. 5.18 into and out of the page by a constant distance t. Further, the YSZ columns, normal to the dense electrolyte layer, are of width $2w$. A reasonable choice for the width w is the mean radius of YSZ particles [135]. The corrugation length l of a characteristic element of the structure can be calculated from $l = w/(1-\epsilon)$, with ϵ the porosity of the system. The electron conducting phase is represented in the left part of the picture as spheres on the surface.

Taking the symmetry of the structure into account allows to further simplify the geometry to a single repeat-unit of length l, which is shown in the dashed clipping in Fig 5.18. The electrode area normal to the column is then given by lt and wt for electrolyte and electrode, respectively.

Transport properties

Besides the simplifications of the geometry, several assumptions are made for the transport properties: Full connectivity of all three phases is implied tacitly. Further, the resistance to electron transport is comparably small, and therefore, neglected. Additionally, the concentration polarization (section 2.2.3), associated with gas transport, is neglected, which is consistent with the assumptions made in this work. Hence, the influence of the ion transport and the charge

transfer reactions at the TPB are considered as the relevant parameters. Both are approximated by ohmic behavior, as given in Eq. 2.3.

The charge transfer reaction, or activation polarization (described in section 2.2.2), usually is not ohmic, it behavior can be described by the more complicated Butler-Volmer equation (Eq. 2.5). For low current densities, however, Eq. 2.5 predicts ohmic behavior [8, 135], which can be described by a charge transfer resistance R_{ct} for the electrode surface with

$$R_{ct} = \frac{U_s - U_{oc}}{j} = \frac{(U_s - U_{oc})A}{I}. \tag{5.2}$$

Therein, $U_s - U_{oc}$ is the overpotential at the surface and j the current density normal to the surface. It should be noted that the charge transfer resistance of a surface is given as an area specific resistance in $\Omega\mathrm{m}^2$. Generally, the resistance of an arbitrary body of length Λ and cross-section area A can be calculated as

$$R = \rho\Lambda/A, \tag{5.3}$$

with ρ as the material specific resistivity. For measured values of the resistance across a surface, the variables ρ and Λ are both unknown, and therefore, can not be obtained separately. To work around the problem, an area specific resistance R_{ct} is determined by multiplication with the area A in form of $R_{ct} = RA = \rho\Lambda$ [136]. In [135], R_{ct} is given as 0.00012 $\Omega\mathrm{m}^2$ at $800°C$; this value was used in here as well.

For the YSZ transport, it was demonstrated in [136] that ohmic behavior is a valid description for the oxygen transport through the YSZ scaffold. Additionally, as demonstrated by Tanner et al. [135], the potential distribution φ can be approximated as invariant in x-direction, which allows to reduce Ohm's law (Eq. 2.3) to

$$j_y = -\kappa_{\mathrm{bulk,YSZ}} \frac{d\varphi(y)}{dy}. \tag{5.4}$$

with j_y as the current density in y-direction of the electrode. Finally, as the resistance to electron transport is neglected, the potential at the electrode surface φ^s is the same at all surfaces of the electrode.

Boundary conditions

The spatial boundary conditions of the repeat-unit are given in Fig. 5.18: At facets 1, 2 and 3, the potential φ is defined by an arbitrary potential φ^s, which is the same at all surfaces, as explained previously. For simplicity, the potential at facet 4 was chosen to be 0. The boundary conditions of the additional facets are defined by the invariance of of the potential in x-direction.

Further, steady-state conditions are applied[1], which lead to

$$\sum I = 0. \tag{5.5}$$

This is valid for an arbitrary volume within the repeat unit, as well as for entire unit. For the repeat-unit element, this can be written as

$$I_1 + I_2 + I_3 = I_4, \tag{5.6}$$

[1] As mentioned in section 2.2, this is valid in SOFC after start up.

with the subscripts indicating the boundaries through which the currents enter or leave the electrode, as shown in Fig. 5.18 [135]. Additionally, it is stated that the current across facet 1 is equal to the one immediately inside the column:

$$I_1 = I\,|_{y=h+\frac{d}{2}}\,. \tag{5.7}$$

Derivation of the electrode resistance

In general, the resistance of the repeat-unit, R_{RU}, consists of the resistance of the electrode column R_{c} and the resistance of the dense electrolyte layer R_{el}

$$R_{\mathrm{RU}} = R_{\mathrm{c}} + \frac{1}{2}R_{el}. \tag{5.8}$$

Multiplication with the geometric electrode area A turns each resistances into an area specific resistance (ASR), in accordance with the surface resistance previously introduced. Assuming a rectangular geometric cell with depth t and length l leads to an area for the repeat unit of lt, and thus,

$$R_{\mathrm{RU}}lt = R_{\mathrm{c}}lt + \frac{1}{2}R_{el}lt. \tag{5.9}$$

By defining the area specific resistance of the electrode as R_{eff}, and rearranging the equation, this can be rewritten as

$$R_{\mathrm{eff}} = R_{\mathrm{RU}}lt - \frac{1}{2}R_{el}lt. \tag{5.10}$$

For the dense solid electrolyte layer, the definition of resistance (Eq. 5.3) can be applied

$$R_{el} = \frac{d}{\kappa_{\mathrm{bulk,YSZ}}lt}, \tag{5.11}$$

with d as heights of the electrolyte layer. By inserting R_{el}, Eq. 5.10 becomes

$$R_{\mathrm{eff}} = ltR_{\mathrm{RU}} - \frac{d}{2\kappa_{\mathrm{bulk,YSZ}}}. \tag{5.12}$$

Next, R_{RU} can be calculated based on Ohm's law as

$$R_{\mathrm{RU}} = \frac{\varphi^s - \varphi\,|_{y=0}}{I_4} = \frac{\varphi^s}{jlt} \tag{5.13}$$

In order to determine I_4, the currents through facets 1 to 3 must be known. The derivation of the current components, depending on potential distribution, geometric properties and R_{ct}, is given in appendix C. Finally, substituting I_4 in Eq. 5.13 and with this expression R_{RU} in Eq.5.12 leads to the area specific resistance of the electrode R_{eff}

$$R_{\mathrm{eff}} = \frac{lR_{ct}}{w\frac{1+\beta}{1+\beta e^{-2\frac{h}{a}}}e^{-\frac{h}{a}} + \frac{1+\beta e^{-\frac{h}{a}}}{1+\beta e^{-2\frac{h}{a}}}a(1-e^{-\frac{h}{a}}) + \epsilon l} \tag{5.14}$$

with ϵ as porosity,

$$a = \sqrt{\kappa_{\mathrm{bulk,YSZ}}wR_{ct}} \tag{5.15}$$

and

$$\beta = \frac{\kappa_{\mathrm{bulk,YSZ}}R_{ct} - a}{\kappa_{\mathrm{bulk,YSZ}}R_{ct} + a}. \tag{5.16}$$

This expression allows to estimate the overall electrode resistivity based on easily accessible, geometrical properties only.

5.5.2. Adaption of TFV with effective properties

In order to estimate the area specific resistance of an electrode, R_{eff} (Eq. 5.14), we started by using the original TFV model, as derived in the previous section. Subsequently, the constant input parameters $\kappa_{\text{bulk,YSZ}}$ and R_{ct} are replaced under consideration of the effective properties, calculated in section 5.3 and 5.4, in order to reflect on electrode microstructure. The results are summarized in Fig. 5.19.

The geometric parameters of the repeat-unit, summarized in Table 5.7, were chosen in accordance with the microstructural parameters of Wilson et al. [54]. The electrode thickness h is 10 μm, and the column width w is set to match the YSZ particle size of 0.5 μm for monosized structures. The porosity ϵ of the electrode structure is calculated by $1 - \text{PF}$, considering the PF of the densified structures (section 5.1.2). In monosized assemblies, which were studied first, the PF is 74% for all compositions. Based on this, the length l of a repeat unit is calculated as $l = w/(1-\epsilon)$. For the bulk properties $\kappa_{\text{bulk,YSZ}}$ and R_{ct}, the values used by Tanner et al. [135] were applied (Table 5.7).

	value	**unit**	
h	10	μm	[54]
w	0.5	μm	[54]
ϵ	1-PF	-	
l	$w/(1-\epsilon)$	-	
$\kappa_{\text{bulk,YSZ}}$	2.1	S/m	[135, 54]
R_{ct}	0.00012	Ωm^2	[135]

Table 5.7.: Parameters used in the calculation of the specific area resistance R_{eff} (Eq. 5.14) of the electrode

The resulting area specific resistance R_{eff}, calculated with the original TFV model in the percolating range only, is shown in Fig. 5.19 as TFV_{ori}. With the original model, the calculated resistance is found to be the same for all volume fractions ϕ_{el} of the electron conducting phase. This is in contrast to the experimental findings, e.g. [54], reported in section 2.3. As, however, the model so far only considers the simplified microstructure and neglects the influence of effective transport parameters, this kind of results was expected. It clearly demonstrates the need for further adaptions, which are introduced next one by one. The applied effective properties were gained for monosized assemblies, unless stated otherwise.

Influence of the effective conductivity

The effective conductivity, determined in section 5.3 for varying compositions, can be employed by replacing $\kappa_{\text{bulk,YSZ}}$ in Eq. 5.14 with $\kappa_{\text{eff,YSZ}}$, as done in [54]. As the values given in section 5.3 were normalized by its bulk value, the effective conductivity $\kappa_{\text{eff,YSZ}}$ was determined by multiplying those values with the bulk conductivity $\kappa_{\text{bulk,YSZ}}$. That straightforward adaption is referred to as TFV_{keff} in Fig. 5.19a.

As the effective conductivity is always smaller than the bulk conductivity, the increase of the resistance R_{eff} for all percolating volume fractions is reasonable. Additionally, a dependence of

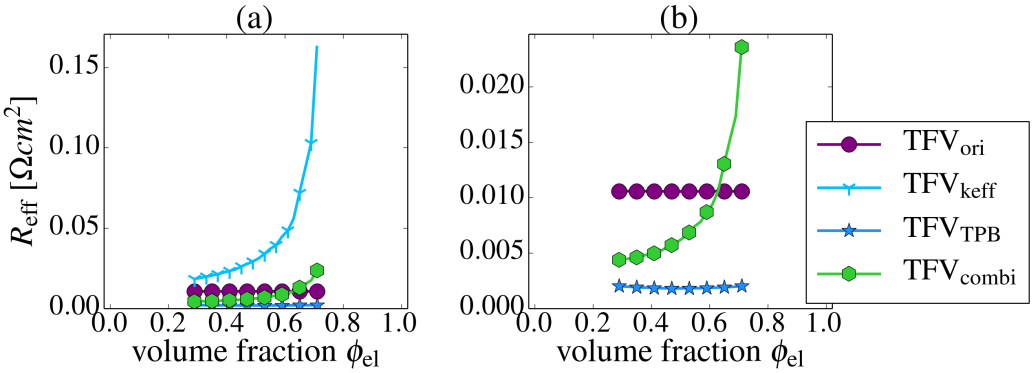

Figure 5.19.: (a) Overall area specific electrode resistivity R_{eff} determined with different adaption of the TFV-model for monosized structures, with the lower section replotted in (b) for better visibility

volume fraction is introduced due to the consideration of $\kappa_{\text{eff,YSZ}}$: With an increasing volume fraction of the electron conducting phase, the effective ionic conductivity decreases and thus, the cell resistance R_{eff} increases significantly.

Influence of the active TPB

As previously explained, the simplification of the Butler-Volmer equation (Eq. 2.5) allows to describe the charge transfer at a reactive surface as ohmic with a resistance R_{ct}. In SOFC, the charge transfer takes place at the active TPB (section 3.2). Thus, to consider the influence of microstructure on the active TPB length, R_{ct} needs to be adapted in order to account for the extent of TPB in the electrode structure. In the original TFV model, the active surface is only at the facets 1, 2 and 3 of the column, with a combined length of $l + h$. Taking the originally porous electrode structure into account, the active area is enlarged in comparison to the active area of the columnar structure. To consider this, the length of the columnar surface is scaled accordingly. To do so, we replace R_{ct} in Eq. 5.14 with an effective area specific resistance $R_{\text{ct,eff}}$, defined as

$$R_{\text{ct,eff}} = \frac{R_{ct}}{l_s t} A \tag{5.17}$$

with l_s as the active surface length, t the electrode thickness and A the column surface area. Considering the simplified structure exemplarily, this leads to

$$R_{\text{ct,eff}} = \frac{R_{ct}}{(l+h)t}(l+h)t = R_{ct}. \tag{5.18}$$

For an active TPB of total length l_s, the effective area specific resistance is

$$R_{\text{ct,eff}} = \frac{R_{ct}}{l_s}(l+h). \tag{5.19}$$

As the TPB lengths calculated in section 5.4 were determined as length per volume, the TPB per volume of column ($V_c = l \times h \times t$) has to be considered in form of $l_s = TPB \times V_c$. Therefore, the column thickness is assumed as 10 μm, equal to the column heights.

In Fig. 5.19, the results calculated with an adapted charge transfer resistance $R_{\mathrm{ct,eff}}$ in combination with the bulk conductivity $\kappa_{\mathrm{bulk,YSZ}}$ are denoted as $\mathrm{TFV_{TPB}}$. Fig. 5.19b depicts a lower section of Fig. 5.19a for better visibility, in particular for $\mathrm{TFV_{TPB}}$. The enlarged active surface due to the numerical obtained values, considered in $R_{\mathrm{ct,eff}}$, reduces the effective cell resistance. Even though the extent of the active TPB depends on the volume fraction (Fig. 5.17), the effective cell resistance ($\mathrm{TFV_{TPB}}$) changes little with varying different microstructures.

Combined consideration of κ_{eff} and TPB

Finally, in a combined approach ($\mathrm{TFV_{combi}}$ in Fig. 5.19), both parameters, $R_{\mathrm{ct,eff}}$ and κ_{eff}, were applied for the calculation of R_{eff}. This allows to estimate how the cell efficiency is affected by the contradicting parameters.

It indicates that considering only the effective conductivity overestimates the electrode resistance significantly. Conversely, the separate implementation of the effective charge transfer resistance underestimates the cell resistance. Additionally, the second adaption lacks the influence of the varying composition, which, however, was observed experimentally [54]. Based on the combined approach, a composition at the percolation threshold of the electron conducting phase ($\phi_{el} \rightarrow 0.29$, compare Table 5.1) appears favorable in terms of cell efficiency.

5.5.3. Influence of the composition on R_{eff}

With the combined TFV model ($\mathrm{TFV_{combi}}$), derived in the previous section, the influence of densification approach and size ratio were studied next. As the column width w reflects on the particle size of the YSZ phase, the initial value of w_1=5μm is changed in accordance with the size ratio: $w = w_1 r_{\mathrm{YSZ}}/r_{el}$. As discussed, a size ratio larger 1 is beneficial for the effective ionic conductivity of the structure. Therefore, compositions with size ratio of $r_{\mathrm{YSZ}}/r_{el} = 8$ are compared to the monosized assemblies.

The resulting effective electrode resistance is given for the different densification approaches for monosized assemblies in Fig. 5.20a, and for the binary sized assemblies in Fig. 5.20b. In both

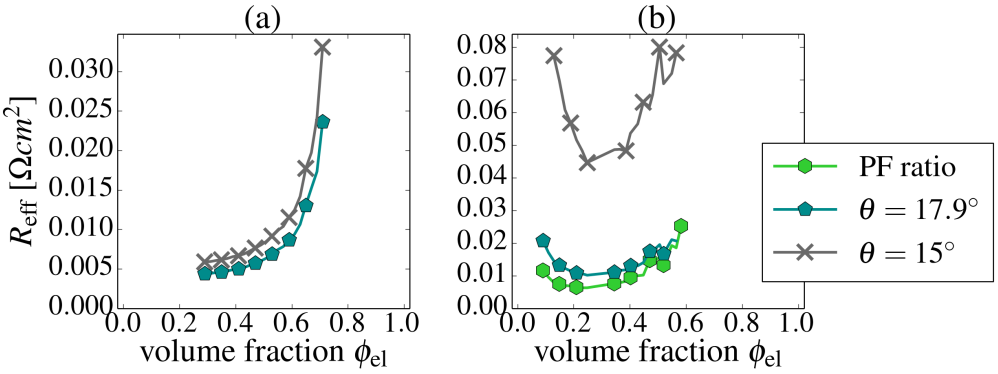

Figure 5.20.: Overall electrode resistivity determined with combined adaption of the TFV-model (a) monosized assemblies and (b) a size ratio of 8 for the different densification approches

cases, a reduction of electrode resistivity can be observed for higher densification, which is more

pronounced for the large size ratios. For monosized assemblies, the densification had very little influence on the effective conductivity in the here considered range of volume fractions. (Fig. 5.14). Thus, the—only slightly—higher electrode resistance of the less densified structures is due to the differences in active TPB (Fig. 5.17a). For the binary sized assemblies, both, effective conductivity (Fig. 5.15) and active TPB (Fig. 5.17b), differed significantly with the degree of densification. This explains the much higher electrode resistance for θ=15°. In contrast to the monosized assemblies, in binary assemblies the curvature of the electrode resistance reflects more on the curvature of the active TPB (or, to be exact 1/TPB) and less on the effective conductivity. Further, even though the active TPB found for monosized structures was more than twice the size compared to the binary assemblies, the effective electrode resistivities of the higher densified structures are similar for both size ratios. Generating structures in an optimized range, concededly, allows to obtain slightly better results for monosized structures.

5.6. Conclusion

In this chapter, the SOFC microstructure and its influence on effective transport properties relevant for cell performance were studied based on numerically generated microstructures. First, it was shown that the geometric characteristics of the numerically generated microstructure deviate significantly from the assumptions made in the analytic approaches (section 5.1.2).

Further, as shown in section 5.2, the numerically determined percolation probability deviates significantly from the analytic findings based on the assumed values: the percolation area determined numerically was larger, especially for large size ratios. Application of numerically determined, geometric characteristics in the analytic solution had little influence on that deviation. The findings of this section led to reasonable doubt regarding the correlation between coordination number $Z_{k,k}$ and the percolation threshold. Concededly, the ratio of particle size to volume element size should be studied additionally, in the future, to rule out its impact on the percolation threshold.

As stated in section 2.3, the two effective parameters, $\kappa_{\text{eff,YSZ}}$ and active TPB, were experimentally identified to be mainly responsible for cell performance. Based on the percolation probability of the structures, these values were determined numerically in section 5.3 and section 5.4. We found significant deviation between the numeric and the analytic results for those calculations as well: the numerically determined effective conductivities were in general lower than predicted by the analytic approaches. Conversely, the active TPB length found numerically was larger than the one found for the analytic approach. Nevertheless, the tendencies of increase with volume fraction (κ_{eff}) and decrease with size ratio (TPB) were predicted correctly with the analytic approach.

Both effective parameters, $\kappa_{\text{eff,YSZ}}$ and TPB, improve—independent of size ratio—with increasing densification, which is a measure for the degree of sintering. But, due to the necessity of a connected pore space, the densification is restricted. Assuming a minimal pore space of 15% as required, the monosized assemblies offer more potential for densification, as their initial PF is lower than the one of binary sized assemblies (see Fig. 5.1). Further, compositions with a large size ratio and large YSZ particles, in combination with small volume fractions of the electron conducting phase, are favorable in order to achieve high ionic conductivity of the structure. Conversely, the largest extent of active TPB was found for monosized assemblies with a mixture of 50:50% volume fraction; and, a large size ratio reduces the extent of active TPB significantly.

In order to assess those contradicting trends, an adapted TFV model was implemented, which allows to assess the combined effect of those two parameters on the effective cell resistance. With this model, the positive influence of densification on the cell efficiency is pointed out as well. Additionally, the negative influence of size ratio on the cell resistance seems less pronounced as it was assumed based on the results for active TPB. Those result indicate that an appropriate combination of volume fraction and size ratio is much more relevant than the size ratio or the volume fraction itself. Considering an optimized mixture for each size ratio, monosized assemblies with a volume fraction of the electron conducting phase slightly above 30% are the most promising. Clearly, the TFV model is a very simplified approach, and thus, the revaluation of these findings with more advanced cell level models is recommendable. Additionally, the implementation of numerically determined effective transport properties in advanced cell level models implies the possibility to obtain enhanced insight in the absolute effect of morphological variations. The studies based on the analytically determined effective properties, as usually found in the literature, might be influenced by the overestimation of the effective conductivity and the underestimation of the active TPB.

6. Micromechanical Modeling of Electrode Structures

As explained in section 2.3, lithium ion battery (LIB) electrodes are influenced by composition and morphology. Additionally, mechanical loads during cell fabrication and cycling play an important role in cell optimization and degradation: In the course of cell manufacturing, porosity and inter-particle contacts are adjusted mechanically with a calendering process. Subsequently, while charging and discharge the cell, the intercalation process leads to volume change of the particles, inducing stress within the electrode. Both processes influence the electrode microstructure mechanically; and they cause rearrangement of the particles, which is coupled with the formation and the loss of contacts. As discussed in sections 2.3 and 3.2, the internal surface and the contact area strongly influence the performance due to its effects on conductivity and surface reactions. Thus, the mechanically caused changes in the microstructure are relevant for the investigation of cell performance. To consider those changes, we chose a densification step reflecting on the inter-particle mechanics to model the LIB electrode structures based on the assemblies generated with the random close packing (RCP) algorithm (section 4.1.1). Due to the granular nature of the electrodes, this can best be done with a discrete element approach, which will be introduced next.

6.1. Discrete Element Modeling

Continuum modeling of the described mechanical processes would require sophisticated constitutive models to capture the complexity of the granular material behavior to some extent. Discrete element modeling (DEM), on the other hand, has the unique feature that it considers the individual particles, their interactions and contact formation or dissolution explicitly. Thus, many of the mechanical response features associated with the granular nature of the material can be covered more accurately than with continuum approaches, even if only simplified contact laws are adopted. Originally described by Cundall and Strack [137] in the field of geomechanics, the method is nowadays used in various disciplines. I will briefly describe here the basic principles of a DEM simulation. A more comprehensive introduction to the topic can be found in [114]. Prior to modeling the mechanical response, the microstructures, generated as described in section 4.1.1, loading and boundary conditions, and inter-particle force laws have to be defined. Further, in dependence of the force law, either a quasi-static approach[1] or a time-dependent[2] discrete element approach has to be choosen.

After initial set-up of the simulation, the load is applied incrementally. In each loading step Δt a sequence of calculations has to be performed, as shown schematically in Fig. 6.1: First, a contact search is performed to determine all contacting particles within the assembly. The repetition

[1] equivalent to stationary simulation in FEM
[2] equivalent to dynamic simulations in FEM

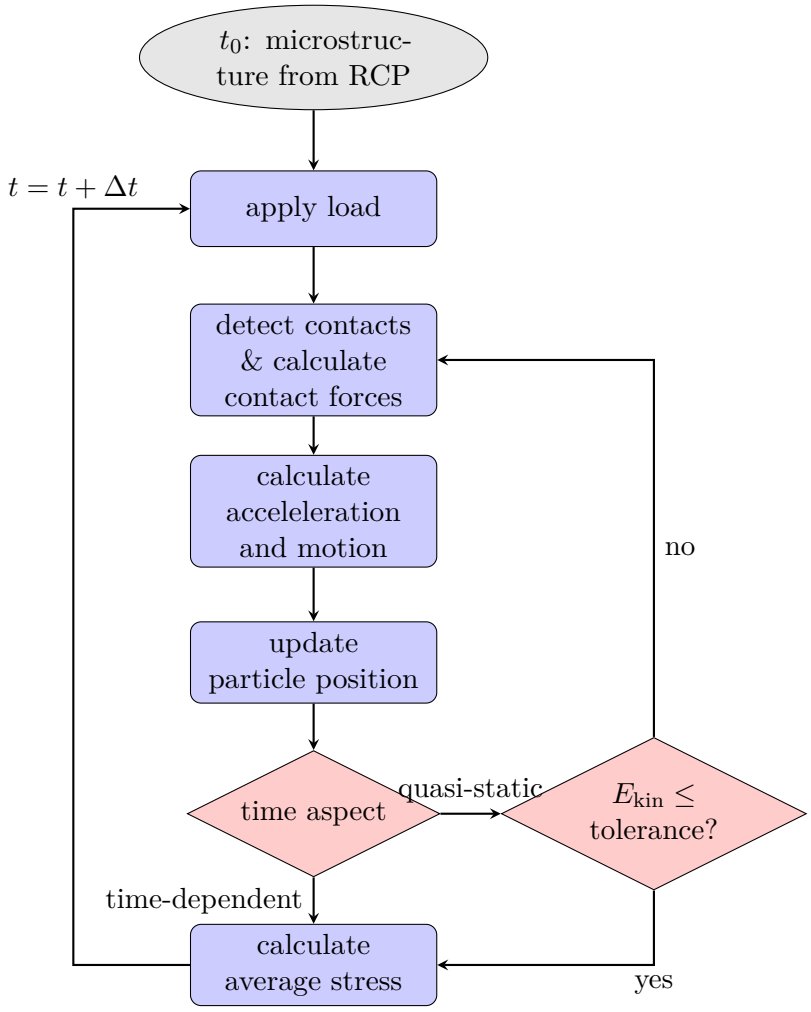

Figure 6.1.: Schematic diagram of sequences of calculations in DEM

of this step for each loading step allows to consider the changes in contact situation. Then, in accordance with the defined contact law, the contact forces $\vec{f}^{\iota,\Upsilon}$ between all particles ι and their contacting particles Υ are calculated based on the distance $d^{\iota,\Upsilon}$ between the particles and their material properties. The particles itself do not deform during the loading, only the contact law $\vec{f}^{\iota,\Upsilon}$ reflects the material behavior of the particles' bulk material, e.g. whether it is considered as elastic, viscous or elastic-plastic. Subsequently, based on the inter-particle forces $\vec{f}$ and moments $\vec{\Gamma}$, the acceleration $\vec{a}$ and angular acceleration $\dot{\vec{\omega}}$ of each particle ι with mass m and moment of inertia J can be calculated with Newtons law of motion

$$\sum_{\Upsilon} \vec{f}^{\iota,\Upsilon} = m^{\iota}\vec{a}^{\iota}, \qquad \sum_{\Upsilon} \vec{\Gamma}^{\iota,\Upsilon} = J^{\iota}\dot{\vec{\omega}}^{iota}. \tag{6.1}$$

Motion integration leads to translational velocities $\dot{\vec{x}}$ and rotational velocities $\vec{\omega}$ and displacements, and thus, to updated particle positions $\vec{x}^{\iota}$ depending on the time-step size.

For the quasi-static approach, the kinetic energy is minimized for each loading step by repeated rearranging of the particles before the loading continues, as indicated in Fig. 6.1. For the time-dependent approach, such a loop is not practical, as the loading history is considered to determine

damping, which is necessary for modeling of time-dependent forces, e.g. visco-elasticity. For each time step, the average stress σ_{ij} developed in the microstructure can be calculated by summing up the forces of all existing contact pairs

$$\sigma_{ij} = \frac{1}{L_x L_y L_z}(\sum_{\iota<\Upsilon} d^{\iota,\Upsilon} f_N^{\iota,\Upsilon} n_i n_j + \sum_{\iota<\Upsilon} \delta^{\iota,\Upsilon} f_T^{\iota,\Upsilon} n_i t_j). \tag{6.2}$$

Here, $f_N^{\iota,\Upsilon}$ and $f_T^{\iota,\Upsilon}$ are the magnitude of normal and tangential forces applied from particle Υ on particle ι, as shown in Fig. 6.2, $d^{\iota,\Upsilon}$ denotes the distance between the centers of the particles and the unit vectors n_i and t_j are the normal and tangential unit vectors of the contact, respectively.

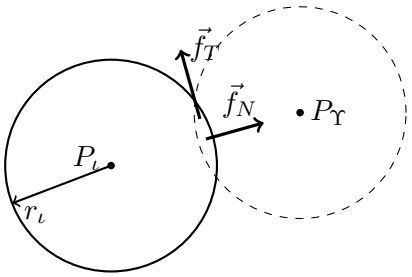

Figure 6.2.: Contacting particle

Even with simplified contact laws the mechanical response features, associated with the granular nature of the material, can be captured more accurate with DEM than with continuum models. Hence, the particle contacts are often represented with basic rheological models, which contain various combinations of spring and dashpot elements to represent the material behavior; and they relate a contact displacement to a contact force $\vec{f}$ in DEM. Unless stated otherwise, we used a classic Hertz-Mindlin contact law for spherical particles [138, 139], assuming nonlinear elastic material behavior. The normal contact force $\vec{f_N}$ between two arbitrary sized particles ι and Υ can be calculated as

$$\vec{f_N} = \frac{4}{3} E^* \delta \sqrt{r^* \delta} \vec{n}^{\iota,\Upsilon} \tag{6.3}$$

with $\vec{n}$ as contact normal, δ as overlap ($\delta = d^{\iota,\Upsilon} - (r_\iota + r_\Upsilon)$), E^* defined by

$$\frac{1}{E^*} = \frac{1-\nu_\iota^2}{E_\iota} + \frac{1-\nu_\Upsilon^2}{E_\Upsilon} \tag{6.4}$$

where E_i is the Young's Modulus and ν_i the Poisson's ratio of the i particle, and r^*:

$$\frac{1}{r^*} = \frac{1}{r_\iota} + \frac{1}{r_\Upsilon}. \tag{6.5}$$

The tangential force $\vec{f_T} = \mu \vec{f_N}$, with μ as friction coefficient, has to be smoothed to avoid a singularity for sliding velocities of zero. This leads to a tangential contact force of

$$\vec{f_T} = -\frac{\Delta \vec{v}_T}{\mid \Delta \vec{v}_T \mid} min(\mu f_N, k_s r_c \mid \Delta x_T \mid) \tag{6.6}$$

with $\vec{v}_T$ as sliding velocity, k_s as shear stiffness and r_c as contact radius.

For the simulations in this work, the DEM code developed by Gan [116, 138] was used. As we are only modeling a segment of the electrode's inner microstructure, we always applied periodic

boundary conditions. Periodic boundary conditions are obtained by copying the assembly and arranging these copies in all directions around the volume element. Further, a particle that leaves the original box volume due to its displacement enters the box on the opposite side again in form of its copied version [116].

6.2. Calendering of LIB electrodes

Similar to solid oxide fuel cell (SOFC), the microstructure and composition of LIB electrodes is important for cell performance. Hutzenlaub et al. [124], for example, demonstrated the influence of the different phases on the electric potential, based on three-dimensional cell reconstructions coupled with numerical investigations. In contrast to that, the often applied effective media approach considers neither the different phases nor their distribution. Especially the widely used effective conductivity values, which had been derived based on complete electrodes as described in [72], are unfit to investigate effects of composition.

Only few Monte-Carlo simulations exist, which study the influence of composition and compaction on the effective transport parameters: Sastry et al. [75, 57, 103, 113] used an event-driven hard sphere approach[3], as described in section 4.1 and [113], to generate initial microstructures. The electrode structure contains active material (AM) coated with a conducting layer, composed of carbon black (CB) and binder, and graphite as additional conduction aid. Investigating different compositions and surface coatings, they found the ratio of CB to binder within the coating to be the most important influence parameter on the overall electron transport properties of the cell [75]. Studying different porosities [57], under consideration of the effect on electron conductivity in the solid phase as well as the effect on ion conductivity in the liquid electrolyte, demonstrates that a trade-off is required for a maximum of specific energy. They found a composition of 36.2% AM with 10% surface coating as optimal. This indicates, however, a packing factor below 50%, which is too low to be mechanically stable. Further, Gupta et al. [103] compared the values of ionic conductivity in the solid and the liquid phase, found with Monte-Carlo simulations, to the widely used Bruggeman's equation (section 3.1.1, Eq. 3.11). They showed that the Bruggeman's equation overestimates the conductivity in the solid phase, and it underestimates it in the liquid phase. Thus, using this equation in macroscale simulations might lead to inaccurate results.

A similar packing approach is implemented by Awarke et al. [140] to study different size ratio's of AM to CB in assemblies with either bare or coated active material particles in combination with CB particles. For the bare particles, the size ratio is found to be important as it influences the percolation threshold: In monosized assemblies, percolation is only achieved for a solid volume fraction of CB of 15%, while for larger size ratios percolation can already be found for 10% of CB. A uniform coating of the particles, on the other hand, enables sufficient electron transport already for 1% solid volume fraction of CB for all particles sizes. In real electrode structures, however, such a distribution is improbable, unless the electrode production process is adapted. A further drawback is, as stated by Hutzenlaub et al. [124], that a uniform coating might hinder the Li^+-ion transfer from the liquid electrolyte to the active material; thus, it drastically reduces cell performance.

[3] A hard-sphere approach does not allow overlap of the particle, hard refers to the neglect of deformation during the impact of particles. The contact itself is not necessarily of interest, the collision may be assumed to be instantaneous, and just the change in velocity is considered [114].

In summary, those studies demonstrated the importance of considering the effect of microstructure, particle size ratio, packing factor, and composition on the overall transport properties relevant for cell performance. None of those, however, investigates the effect of calendering on the microstructure and the related changes in electrode parameters relevant for cell performance.

Due to the material components studied in here, the size ratio of electron to ion conducting particles is considered as a fixed parameter in the following: For high rate applications, a particle size of several 100 nm is recommended for AM [140], and CB is usually fabricated in a size of about 40 nm. Therefore, we chose a radius ratio of 10 for AM to CB, bearing in mind, that for other applications and material compositions the active material particles may be in a different size range. Knowledge on the influence of size ratio on the properties can be gained from section 5.3 for SOFC materials.

Additionally, the calendering process during cell fabrication affects the cell microstructure—therefore, it should be considered in those investigations. The calendering step—the thin cells with a thickness between 50 and 300 μm passes through pairs of rolls in the assembled state— is performed to obtain homogeneous thickness and to improve particle-to-particle contact [11, 21]. In experimental investigations of calendering, the cells are usually compressed uni-axially [22]. It is assumed that with decreasing porosity the contact resistance decreases, due to increasing contact area; at the same time the charge transfer resistance increases, most probably resulting from a decreasing free surface [46, 56, 23], as discussed in section 2.3. There is, however, no consensus about the effect of calendering on effective conductivity and the trade-off point [22, 55].

6.2.1. Micromechanics of calendering

To study the effect of calendering on the microstructure and the effective transport properties in this work, the assemblies, generated with RCP, are compressed uni-axially in DEM simulations. To do so, a strain ε_{xx}, 2.5% in total,is applied gradually by moving each particle at the beginning of each loading step by

$$\Delta x_x = \Delta \varepsilon_{xx} x_x, \tag{6.7}$$

with x_x as the x-component of the position of the particle center [138]. The box size is adapted according to the applied strain, and the periodic boundaries are regenerated. In the directions perpendicular to the loading direction the periodic boundaries are kept fixed for uni-axial loading.

In the following sections, the influence of mechanical properties, initial packing factor, and composition of the assemblies on the mechanical response during calendering and its effect on transport properties will be studied.

Material properties

First, we will examine the influence of mechanical properties of the bulk material on the micromechanical response for assemblies of pure active material, as well as for compositions containing AM and CB. Reviewing literature, a large amount of different mechanical bulk properties of AM is found. Especially for $Li_xMn_2O_4$ (LMO), the values found for the Young's modulus E range from 10 GPa [141] to 200 GPa [142]. The lower values of 10 GPa [141] and of 25 GPa have been found for blocks of polycrystalline, sintered structures in the size range of mm with porosities around 40%. Even though these values are widely used in simulations of mechanical stress in

single-particle models (e.g. [103, 143, 75, 144]), it was discussed in [145] that the values deviate largely from values found for materials of the same kind (spinels), presumably due to microcracks in the large, sintered samples. Values around 100 GPa were determined by nanoindentation for particles embedded in real electrode structures [146, 147, 148], whereas a Young's Modulus of up to 200 GPa [142] was measured for large, electrodeposited structures. As the values in [148] were identified in conditions relevant for LIB, these values are assumed to be the most realistic mechanical properties of LMO. To better illustrate the influence of Young's Modulus on macroscopic stress and effective transport parameters, we started by using additional values as well, which are summarized in Table 6.1.

	Young's modulus E [GPa]	**Poisson's ratio ν**
LMO_{low}	10 [141]	0.3 [141]
LMO	93 [148]	0.3 [145]
LFP	125 [149]	0.22 [149]
Graphite	32.5 [150]	0.315 [150]
CB	6 [146]	0.3

Table 6.1.: Material properties used in the DEM simulation of LIB electrodes

In the first instance, we conducted simulations with structures containing active material only. The active material of the electrode is represented by same sized particles, thus, we generated three different assemblies with 5,000 monosized particles each. To choose a suitable packing factor for those monosized assemblies, we have to calculate the volume occupied by active material in composite electrodes, as information on the packing factor is only available for complete electrodes: based on experimental investigations on the effect of the electrode porosity, a value of about 70% was recommended as packing factor for electrode structures [22]. Due to restrictions of the RCP algorithm, this PF was not exactly matched by the numerically generated assemblies of the electrode composite. In those, which represent the composite as a binary mixture of spheres, the medium packing factor is of about 69.4% for assemblies containing a solid volume fraction of 12.5% CB (see Table 6.2). Applying the relationship introduced by Kyrylyuk et al. [133] for the packing factor (PF) of binary sized packings

$$PF = \phi_{AM} + \phi_{CB} \tag{6.8}$$

allows to calculate the remaining PF after removing the volume fraction ϕ_{CB} of CB from the existing assemblies. A solid volume fraction of 12.5% CB corresponds to a total volume fraction of 8.7% CB which leads to a packing factor of approximately 60.73% for the monosized assemblies. This led to packing factors in the range of 60.73% to 60.81% for the three assemblies, with the deviation caused by the random nature of the granular structures.

The macroscopic stress induced by the calendering process was calculated for different material properties, as given in Table 6.1. The stress components in the main directions x, y, and z are shown in Fig. 6.3 for the smallest and the highest considered Young's Modulus (LMO_{low} and Li_xFePO_4 (LFP) respectively). Obviously, the stress is strongly dependent on the material properties: the assemblies composed of LFP show a ten times larger stress at the end of the calendering process than the once with LMO. Further, the uni-axial compression in x-direction leads to anisotropic material response: as expected, the stresses in loading direction are much

higher than the stresses perpendicular to it. We assume that the mechanically induced anisotropy will affect the anisotropy of the transport properties.

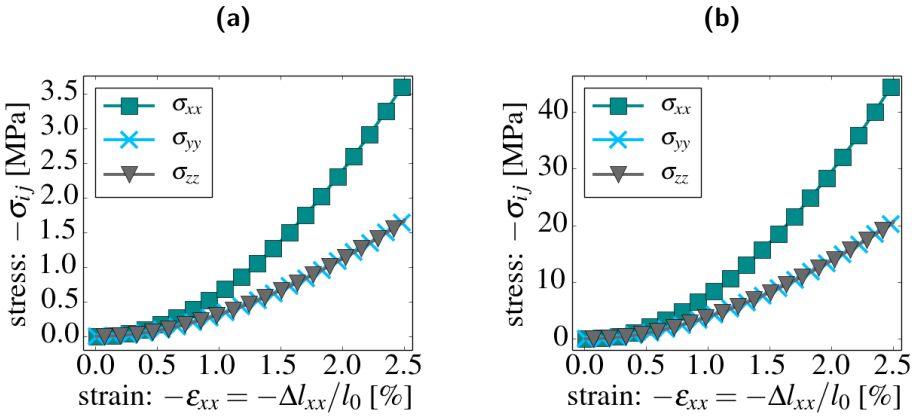

Figure 6.3.: Macroscopic stress components of monosized assemblies during uni-axial compression for (a) Young's Modulus =10GPa and (b) Young's Modulus =125GPa

Next, to determine the effect of CB on the mechanical response, the calendering process is simulated with binary assemblies (PF: 69,4%, CB: 12.5% vol. frac). As discussed in section 5.1.1, adding CB to the mechanically stable monosized assemblies of active material leads to an increasing PF, as the much smaller CB particles are filled into the interstices of the AM network [92]. The influence of size ratio on initial packing factor was shown in section 5.1.1. The CB phase is assigned with a Young's Modulus of 6 GPa (see Table 6.1). Also for the binary assemblies, three different assemblies, each containing 10,000 particles, were generated per composition.

To compare binary and monosized assemblies, the mean hydrostatic macroscopic stresses σ_h are shown in Fig. 6.4 for different material properties. The binary mixture induces a significant increase of the average macroscopic stress σ_h for all materials (Fig. 6.4b). For the LFP material, the relative difference $(\sigma_{\text{binary}} - \sigma_{\text{mono}})/\sigma_{\text{binary}}$ is 28.54% for a strain of 2.5%; for a Young's Modulus of 10 GPa, the difference is 36.26%. The error bars indicate the range of the results

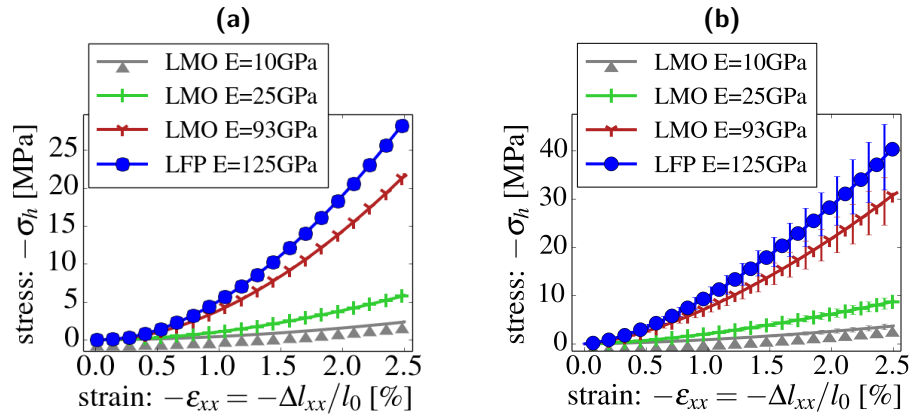

Figure 6.4.: Hydrostratic macroscopic stress for different active material properties in (a) monosized, one-component materials and (b) binary composites with 12.5% solid volume fraction CB during uni-axial compression

found for the three different structures, which can vary due to the random distribution of particles. The variation is small for the monosized (Fig. 6.4a) and increases for binary mixtures (Fig. 6.4b). The larger error bars found for binary mixtures demonstrate the importance to study several microstructures per composition.

As derived by Zhao [139](p.74), the hydrostatic stress σ_h of structures with two different material properties E_1 and E_2 is related via

$$\sigma_h(E_1) = \frac{E_1}{E_2}\sigma_h(E_2), \tag{6.9}$$

with $\sigma_h(E_1)$ as the hydrostatic stress found for material 1. This could be validated for the monosized assemblies; however, it does not hold true exactly for the binary composite. The discrepancy of the normalized stresses, obtained for binary assemblies with different material parameters, can be seen in Fig. 6.5. Most likely this deviation is due the different material parameters used for CB and AM. Nevertheless, the difference between the normalized stresses is small in comparison to the deviation between the three different assemblies, induced by the random distribution of the particles. Thus, also for binary mixtures, the stress in assemblies with different material parameters can be estimated relatively accurate with Eq. 6.9. Therefore, we will focus on one set of material parameters in the following.

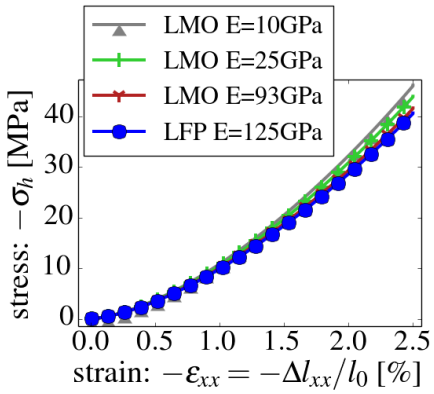

Figure 6.5.: Average macroscopic stress of binary composite electrodes normalized to a Young's Modulus of 125GPa in accordance with relation 6.9

In addition to the hydrostatic stress, the anisotropy, induced by the calendering process, might influence the effective transport parameters of the electrodes. To assess it, a degree of anisotropy can be determined as σ_{ii}/σ_h. For both, monosized and binary assemblies, the influence of material properties on the anisotropy is negligible (Fig. 6.6). In comparison with monosized assemblies, binary compositions (Fig. 6.6b) lead to an increased degree of anisotropy.

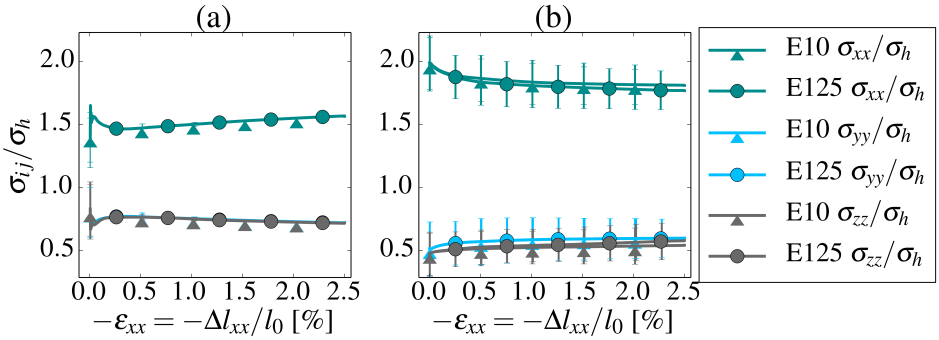

Figure 6.6.: Degree of anisotropy during uni-axial compression of (a) monosized, one-component materials and (b) binary composites with 12.5% solid volume fraction CB

Packing Factor

Further, the influence of packing factor on the mechanical response of the system is investigated. Therefore, further assemblies with lower and higher packing factor are generated with the same composition (CB: 12.5%). Again, three assemblies per group will be studied. Due to the random structure, the PF of two packings are never exactly the same. Hence, the assemblies are classified in groups of low, medium and high PF; the deviation of the PF can be seen in Table 6.2.

No	**low PF**$_{\text{ini}}$ [%]	**medium PF**$_{\text{ini}}$ [%]	**high PF**$_{\text{ini}}$ [%]
1	67.32	69.36	71.01
2	67.31	69.49	70.87
3	67.23	69.41	70.88

Table 6.2.: Initial packing factor of the different assemblies divided into three groups.

The average hydrostatic stress of the different PFs is shown in Fig. 6.7a. As expected, a higher packing factor leads on average to a higher stress. The difference between the maximum and minimum values of the assemblies of a group of PFs—indicated by the errorbars—is, however, larger than the difference between mean values of the different groups. Thus, even though a general trend is shown in Fig. 6.7a, an assembly with high packing factor can still be found with less stress than an assembly with medium packing factor.

Composition

Finally, we analyze the influence of different solid volume fractions of CB on the overall macroscopic stress. For better comparability, assemblies with similar—medium—packing factors are generated, three for each composition. This leads—in accordance with Eq. 6.8—to different amounts of active material within the assembly. The hydrostatic stress decreases with increasing solid volume fraction of CB, as shown in Fig. 6.7b for LFP as active material.

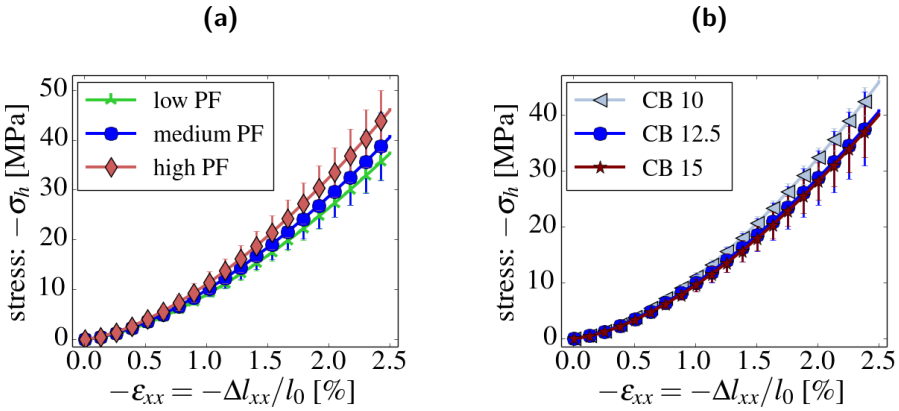

Figure 6.7.: Hydrostratic macroscopic stress for (a) different initial packing factor and (b) different solid volume fractions of carbon black (CB) during uni-axial compression

The decrease, however, is nonlinear: While the difference between assemblies with 12.5% and 15% is negligible, the difference between assemblies with 10% CB and 12.5% is more significant. Again, the deviation between the assemblies of one composition is large in comparison to the deviation between the mean values.

In summary, the addition of CB to monosized assemblies of pure active material leads to a significant increase in stress and anisotropy. Additionally, the binary assemblies show larger deviation between the three assemblies of a composition, most likely due to the random structure of the assemblies. The influence of further variations of packing factor and composition on the macroscopic stress is negligible in comparison to that.

6.2.2. Influence of calendering on connectivity

As discussed in 2.3, the percolation of the CB phase and connection of AM particles to a percolated CB network affect the cell performance significantly. Both are expected to be changed by the mechanical calendering process and by the rearrangement of particles in the microstructure resulting from the applied load. The percolation of microstructures at different stages of compression was determined with the methods described in section 4.3. The percolation probabilities P was calculated from the number of percolating CB particles to the total number of CB particles. Subsequently, based on the connectivity of the CB network, the amount of AM particles connected to a percolating CB network can be determined. This is of importance as only sufficiently connected AM particles take part in the overall cell reaction. If a AM particle is isolated from the electron transport, no energy releasing reactions can take place. Thus, the particle is "dead weight". Ion transport, on the other hand, mainly takes places in the liquid electrolyte within the pore space. Even though the pore space will change during calendering, it can be assumed that concentration losses are not significantly influenced when the porosity is kept larger than 20% (section 2.3). Therefore, in this chapter, we focus on the electron transport only.

As shown in the previous section 6.2.1, the influence of the Young's Modulus on the overall mechanics is assessable from relation 6.9 for the considered mixtures. Thus, the more interesting question is: how do the different mechanical properties of AM affect the microstructure, percolation, and effective conductivity of the CB phase? To evaluate this, the percolation probabilities P of

the lowest and highest of Young's Modulus are compared in Fig 6.8a: the percolation probability during the calendering process is not significantly influenced by the elastic properties of the active material. The percolation threshold, defined as 50% percolating CB particles, takes place for 1.0% of compression for both compositions. This strain corresponds to hydrostatic stresses σ_h of -0.43MPa and -5.3MPa for the lowest and highest value of Young's Modulus, respectively. This indicates that the percolation probability is independent of the average mechanical stress within the assembly.

Additionally, for percolating CB clusters, the amount of AM particles connected to percolating CB networks was determined. As can be seen in Fig. 6.8b, the amount of connected AM particles increases drastically for a compression of 1.0%. Comparing the change of percolation probability and the amount of connected AM during calendering, it demonstrates the correlation of those parameters very clearly. This emphasizes the importance of percolation within CB for LIB electrodes—especially for badly electron conducting active material—for proper cell performance.

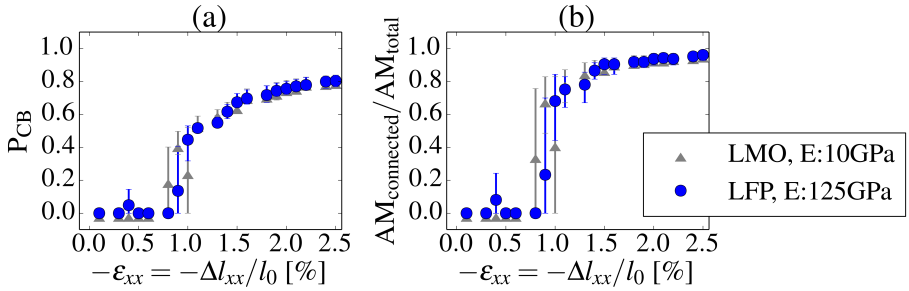

Figure 6.8.: (a) percolation probability of CB phase and (b) the fraction of AM particle connected to a percolating CB network for the lowest and highest value of Young's Modulus during calendering

Next, the influence of different initial packing factors is studied for compositions with a solid volume fraction of 12.5%. The different packing factors are given in Table 6.2. The variation in PF leads for both low and high PF to a broad range with large differences between the individual assemblies as can be seen in Fig. 6.9a. Thus, no clear percolation threshold can be determined in those cases. This behavior is reflected in the amount of AM connected to the percolating CB

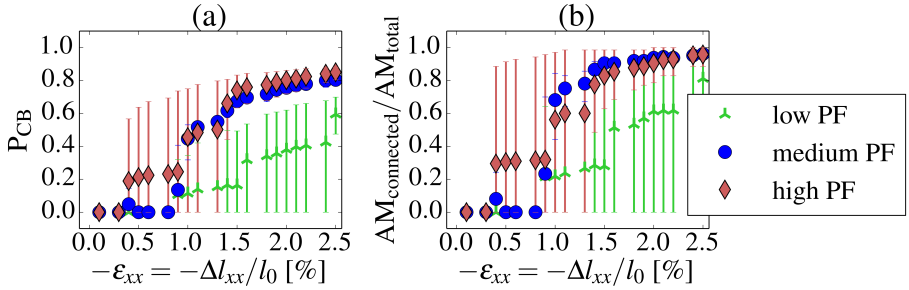

Figure 6.9.: (a) percolation probability of CB phase and (b) the fraction of AM particle connected to a percolating CB network for different packing factors

network, shown in Fig. 6.9b: a large difference between the individual assemblies over a broad range is found for that as well.

Finally, the effect of different volume fractions of CB on the connectivity is examined. As described previously, the PF is kept constant—this leads to an amount of active material varying relative to the amount of CB. As can be seen in Fig. 6.10, the percolation threshold clearly depends on the composition: For 15% solid volume fraction of CB, the percolation threshold already takes place for 0.5% compression. In contrast, for 10%, a large deviation between the different assemblies is found, and only for 2.5% of strain the percolation probability of 50% is surpassed on average. In contrast to the sudden increase of percolation probability—found for 12.5% and 15%—a broad range with undefined behavior can be seen for 10% CB. The same correlation as seen in Fig. 6.8b and Fig. 6.9b for the connectivity of active material to a percolating CB network can be found for 10% and 15% of CB in Fig. 6.10b.

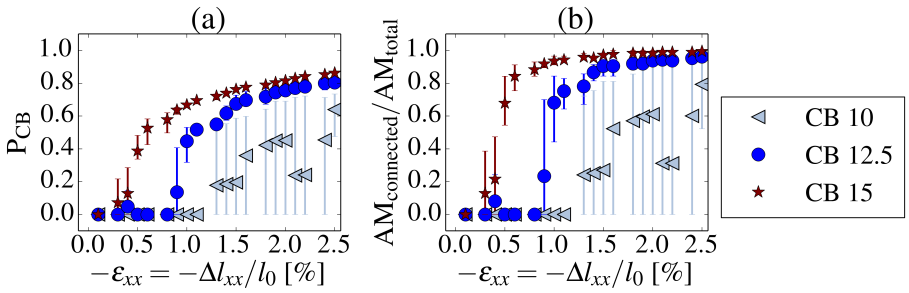

Figure 6.10.: (a) Percolation probability of CB phase and (b) the fraction of AM particle connected to a percolating CB network for different solid volume fractions of CB

Critical coordination number Z_c

As suggested in the analytic approach of the percolation theory described in section 3.1.2, the percolation threshold is correlated the coordination number $Z_{\mathrm{CB,CB}}$, which describes the number of contacts a CB particle has with other CB particles. Additionally, the overall coordination number Z_0, which is relevant for the analytic derivation of $Z_{\mathrm{CB,CB}}$, was assumed to be 6 It was shown in section 5.2.2 for SOFC that the theoretic assumptions do not hold true for sintered structures. To examine the relation of percolation threshold and coordination number during mechanical loading, first the coordination numbers Z_0 and $Z_{\mathrm{CB,CB}}$ are considered. In contrast to the sintering approach, with constant coordination numbers for each assembly, here they change with the load: Starting from the undensified structure, Z_0 and $Z_{\mathrm{CB,CB}}$ increase steadily with the applied strain up to 2.5 and 2, respectively, as shown exemplarily in Fig. 6.11 for the different compositions. The overall coordination number Z_0 is too low to be considered as a mechanically stable.Thus, we assume that the active material is load carrying throughout the process. This is supported by the coordination number $Z_{\mathrm{AM,AM}}$[4], which increases, e.g. for 12.5% CB from 4.8 to 5.5, during the calendering process (Fig. 6.12). The overall coordination number, however, is strongly influenced by the low values of $Z_{\mathrm{CB,CB}}$, as the amount of CB particles is dominant[5].

[4] In analogy to $Z_{\mathrm{CB,CB}}$, $Z_{\mathrm{AM,AM}}$ is the number of contacts an AM particle has with further AM particles.
[5] e.g. an assembly of 12.5% CB contains only 70 AM particles and 9930 CB particles

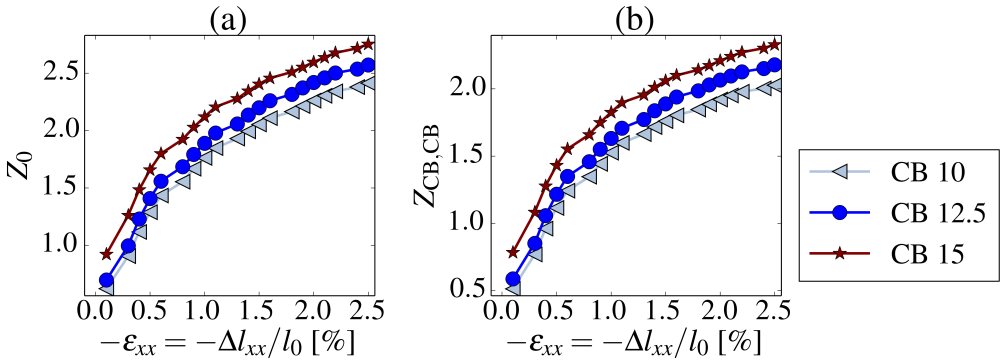

Figure 6.11.: (a) overall coordination number Z_0 and (b) coordination number $Z_{\mathrm{CB,CB}}$ versus compression for different solid volume fractions of CB

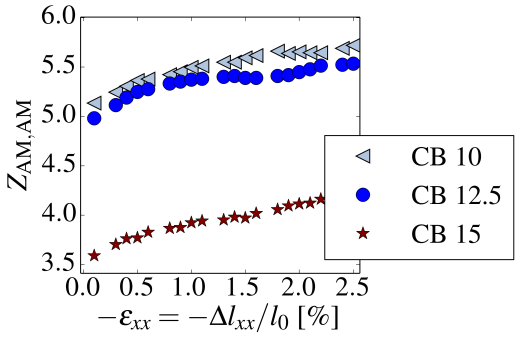

Figure 6.12.: Coordination number $Z_{\mathrm{AM,AM}}$ for different composition

The low number $Z_{\mathrm{CB,CB}}$ is mostly caused by a large amount of so-called rattlers, i.e. particles with only 1 or 2 contacts. The analysis of further microstructures showed that the coordination numbers are independent of the elastic properties, whereas an increase with increasing PF could be seen.

Looking at the correlation between coordination number and percolation probability for different initial packing factors (Fig. 6.13a) and different solid volume fractions of CB (Fig. 6.13b) does

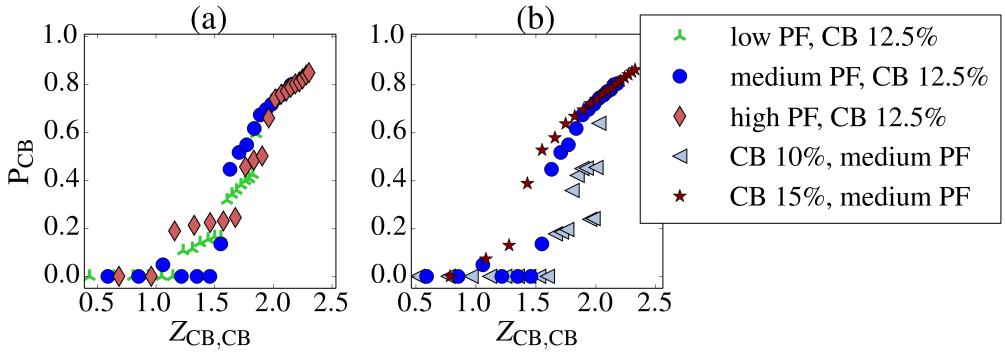

Figure 6.13.: Percolation probability P_{CB} versus coordination number $Z_{\mathrm{CB,CB}}$ for (a) different packing factors and (b) different solid volume fractions of CB

not allow to correlate a single critical coordination number to the percolation threshold. This indicates that the percolation theory as described in section 3.1.2 is inapplicable for structures under mechanical loading.

Free surface area

In analogy to the active three-phase boundary (TPB) area of the SOFC electrodes, the energy releasing reactions take place at the surface between active material and electrolyte, as discussed in section 3.2. Thus, it is beneficial for cell performance to maintain a large free surface area during cell production: a larger surface area allows to maintain a small local overpotential at higher charging and discharging rates. A small local overpotential, in turn, is beneficial in terms of activation polarization (section **??**). In analogy to the active TPB in SOFC, only the section of the surface area, where all reactive species come into contact, takes part in the cell reaction. Thus, only when the active material is electronically connected to the current collector, it is part of the active free surface area (FSA) of the cell. Therefore, we assume that the FSA is directly correlated to the amount of connected AM phase. Further, it was assumed (section 2.3) that an increase in cell resistance—observed with electrochemical impedance spectroscopy (EIS) during calendering—is caused by a decrease of free surface area, as sketched in Fig. 2.4.

To investigate this, the free surface area was calculated as the surface area of the active material, considering only the particles connected to a percolated CB cluster, minus the contact area within the solid phase. Packing factor and composition affect the FSA significantly, whereas the influence of mechanical properties is negligible. As shown in Fig. 6.14, the active surface area increases drastically at the percolation threshold—this is correlated to the amount of active material connected to the percolating CB network. The increase in FSA, as seen e.g. for low PF in Fig. 6.14a, with further compression is due to a higher amount of connected AM particles. Its decrease, found e.g. for the high PF at around 1.7% of compression, however, is not correlated to a reduced amount of connected AM. Thus, it might indicate a significant increase of contact area within the solid phase. Decreasing FSA with increasing compression can also be seen for assemblies of medium PF with 12.5% and 15% solid volume fraction of CB in Fig. 6.14b. In accordance with the decrease for the high PF, the amount of connected AM remains unchanged. This corroborates the hypothesis of an increasing solid contact area, as predicted in the experimental studies [56, 46, 23].

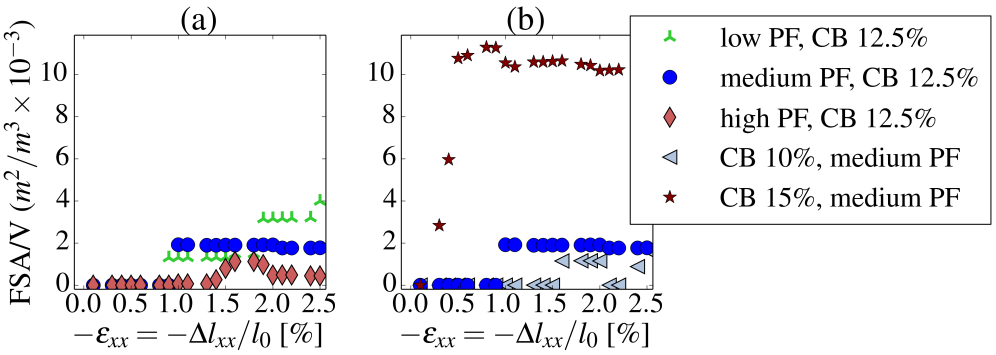

Figure 6.14.: Change in free surface area per volume during calendering for assemblies with (a) different packing factors and (b) different solid volume fractions

Of particular interest in the investigation of FSA is the—unexpected—significant larger amount of active free surface area found for 15% of CB. As the solid volume fraction of AM material is low in comparison to the other mixtures, a possible reason for the large FSA is a small inter-particle contact area. To estimate the solid-solid contact area, the coordination numbers as well as the mean contact radii of the different compositions have to be considered. The mean contact radii are given in Table 6.3 for the maximum strain of 2.5%. Obviously, the contact radii of AM-AM contacts $r_c(\mathrm{AM},\mathrm{AM})$ dominate the overall solid-solid contact area, as they are one order of magnitude larger than $r_c(\mathrm{AM},\mathrm{CB})$ and two orders of magnitude larger than $r_c(\mathrm{CB},\mathrm{CB})$. The radii $r_c(\mathrm{AM},\mathrm{AM})$ themselves show no significant deviation for the different assemblies. Thus, the difference in FSA is most likely due different coordination numbers $Z_{\mathrm{AM,AM}}$, which are shown in Fig. 6.12 for the varying volume fractions of CB. As the larger amount of CB reduces the number of AM-AM contacts, it also reduces the solid-solid contact area. This, in turn, can be correlated to a bigger free surface area, and finally, to lower activation polarization.

	$r_c(\mathrm{AM},\mathrm{AM})$	$r_c(\mathrm{CB},\mathrm{CB})$	$r_c(\mathrm{AM},\mathrm{CB})$
LFP (125 GPa)	0.0109	0.00052	0.0013
LMO (10 GPa)	0.0110	0.00034	0.0010
PF low	0.0108	0.00045	0.0011
PF high	0.0108	0.00050	0.0012
10% CB	0.0101	0.00044	0.0011
15% CB	0.0117	0.00060	0.0014

Table 6.3.: Mean contact radius of AM-AM, CB-CB and AM-CB contacts normalized to a box length of 1

6.2.3. Influence of calendering on effective conductivity

Besides the percolation of the CB phase and its connectivity to the active material, the effective electron conductivity within the CB network is relevant for the overall cell performance. Based on the information on connectivity, it was determined via the node-potential method, as described in section 4.3.3.

Inter-particle resistance

The contact resistance between two particles is so far only derived for geometrically overlapping particles (section 4.3.3). To perform similar calculations of the conductivity with two elastically deformed particles in contact, a different geometry is required. The deviation of the particles from the completely spherical shape is described with Hertz theory [151]. The Hertzian contact radius r_c can be determined in dependence of the overlap δ

$$r_c = \sqrt{r^*\delta}. \tag{6.10}$$

with the reduced radius r^*, as given in Eq. 6.5. Computing the displacement of Hertz contact showed that the deformation only takes place in the direct contact zone without any pile up [151]. Therefore, we approximate the deformed spheres in numerical calculations of the conductivity as

ellipsoids— with the axis vertical to the contact normal equal to the undistorted particle radii r_ι and r_Υ, respectively (Fig. 6.15). The second radius of the ellipsoid, r_{Hertz}, is calculated based on the contact radius r_c and the distance between the particle centers of the two ellipsoids. For this geometry, the ohmic resistance $R_{\iota\Upsilon}$ between the deformed spheres ι and Υ can be determined as described section 4.3.3 via

$$R_{\iota\Upsilon} = \frac{T_\iota - T_\Upsilon}{I} \tag{6.11}$$

with T_ι and T_Υ as temperatures at the extremities of the volume and I as the resulting flux. The calculations for the ellipsoids were also performed with Ansys CFX for a variety of overlaps. Fitting the data leads to the following relationship for the contact resistance $R_{\iota\Upsilon}$:

$$\frac{R_{\iota\Upsilon}}{R_{\text{cyl}}} = 0.821\frac{r^*}{r_c} \tag{6.12}$$

with

$$R_{\text{cyl}} = \frac{1}{k_{bulk}}\frac{d}{\pi r^{*2}}. \tag{6.13}$$

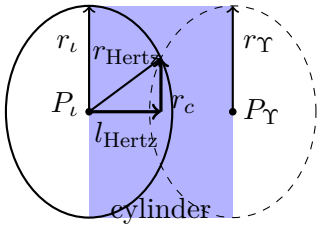

Figure 6.15.: Exaggerated drawing of the deformed spheres in contact, with the blue shape as reference cylinder

Evolution during calendering

With the relationship developed in Eq. 6.12, the conductivity of the electrode structures during calendering can be calculated based on the previous determined information of connectivity with the node-potential approach (section 4.3.3). As the uni-axial compression leads to anisotropy in stress tensor, microstructure, and densification of the structure, the directional information of conductivity is of importance. To study this, the conductivities of the three main directions are shown in Figs. 6.16, 6.17, and 6.18.

First, the influence of material properties on the effective conductivity is examined, considering the lowest and highest Young's Modulus given in Table 6.1. As can be seen in Fig. 6.16, the effective conductivity of both compositions increase steadily with increasing strain—for values larger than the strain at the percolation threshold. Comparing the effective conductivity of assemblies with the low Young's Modulus in Fig. 6.16a and the high Young's Modulus in Fig. 6.16b shows that a higher Young's modulus of the active material leads to higher effective conductivity within the CB phase, even though the material properties of CB are the same for all calculations. As the percolation probability was shown to be independent of the elastic properties, a higher conductivity due to an increasing number of conducting paths within the assembly can be ruled out. Thus, this indicates an influence of the overall macroscopic stress. Presumably, the higher stress (Fig. 6.4) leads to larger contact forces between CB particles, which are correlated to increased inter-particle

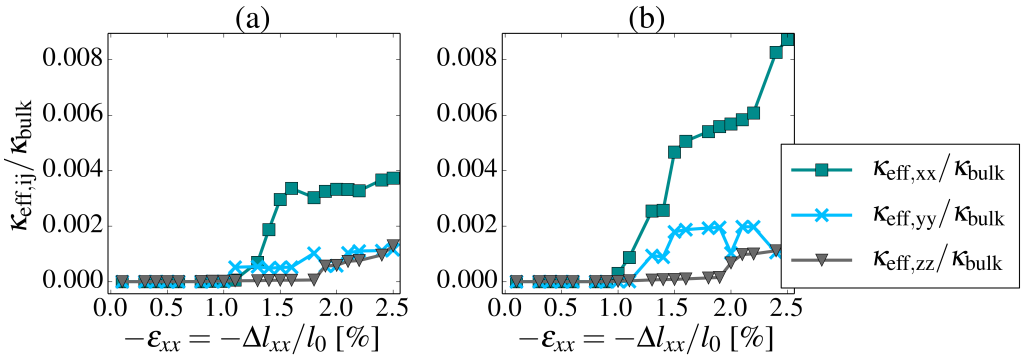

Figure 6.16.: Directional effective conductivity for Young's Modulus of (a) 10GPa and (b) 125GPa with medium PF and a solid volume fraction of 12.5% CB

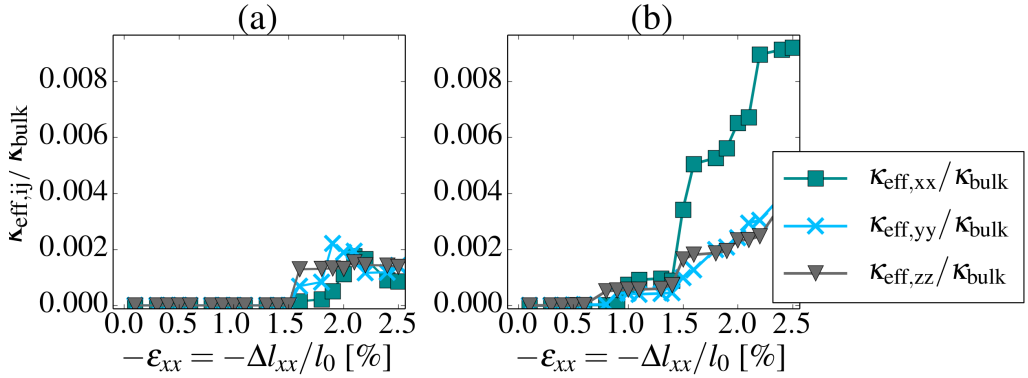

Figure 6.17.: Directional effective conductivity for (a) low initial PF and (b) high initial PF for comparison to medium PF see Fig. 6.16(b)

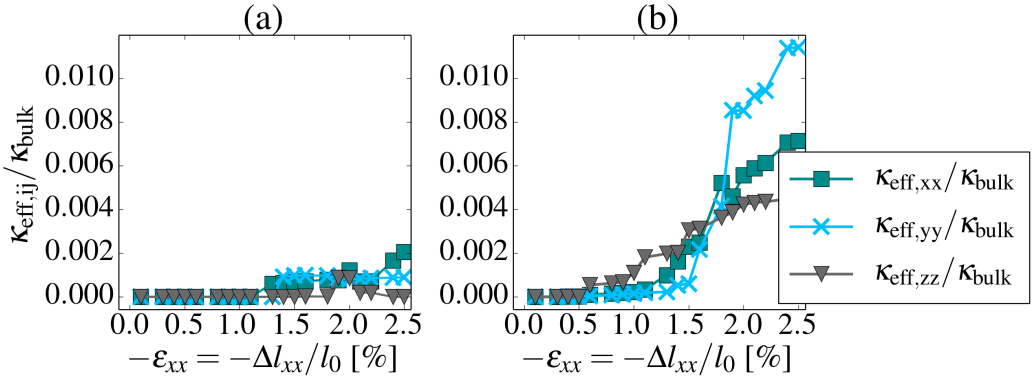

Figure 6.18.: Directional effective conductivity for (a) 10% CB and (b) 15% CB for comparison to 12.5% CB see Fig. 6.16(b)

contacts. The mean contact radius between two CB particles $r_c(\mathrm{CB}, \mathrm{CB})$ is, e.g. for the maximum load, slightly smaller for the lower Young's Modulus, whereas the contact radius between two AM particles $r_c(\mathrm{AM}, \mathrm{AM})$ is almost the same (Table 6.3). As the resistivity between two particles is inversely proportional to the contact radius (see Eq. 6.12), an increasing inter-particle contact area is correlated to an increasing effective conductivity. This most likely also explains the anisoptropy in the effective conductivity: The calendering leads to higher stress in loading direction (Fig. 6.3) as well as higher effective conductivity in this direction, as can be seen in Fig. 6.16; the two effective conductivities in the directions perpendicular to the loading direction are both smaller and similar. The conductivity-strain relationships, however, show significantly different behavior for the two compositions. In contrast to the stress-strain relationship, which can be scaled by the elastic properties, a normalization seems impossible.

Comparison of the influence of different packing factors in Fig. 6.17—calculated for LFP—shows that the high PF (Fig. 6.17b) leads to higher conductivities than the low PF (Fig. 6.17a). This might correlate to the increasing macroscopic stress with increasing PF, as was shown in Fig. 6.7a, or to a larger total amount of CB for a constant solid volume fraction. The mean contact radius between two CB particles $r_c(\mathrm{CB}, \mathrm{CB})$ of the high PF is similar to the medium PF and smaller for the low PF—as shown in Table 6.3. Further, the low PF shows no preferential direction for the effective conductivity during calendering, whereas a clear anisotropy can be found for the high PF. Considering the previously described concept of the filled interstitial spaces leads to the following interpretation: The lower packing factor is further away from the jammed state; thus, more rearrangement in the microstructure is possible. As the CB particles are not part of the force carrying mechanical stable network, they are more likely to rearrange. Calculation of the mean displacement of the small particles, however, showed that the displacement is similar for the assemblies with low and high PF. The large particles of assemblies with low PF, on the other hand, show larger displacement. Further comparison to the medium PF showed similar displacement in all cases; hence, this is insufficient to explain the directional variation.

Furthermore, the results of the different mixtures are in contrast to the previous findings for correlation of stress and effective conductivity: Even though the highest stress is found for compositions with 10% of CB (Fig. 6.7b), the according effective conductivity is the lowest and vice versa for 15%, as can be seen in Fig. 6.18. This can be explained as follows: The higher amount of the soft CB in the compositions of 15% solid volume fraction CB softens the mechanical response during loading; additionally, it increases the amount of conducting paths within the assembly, resulting in improved effective conductivity. Similar to the results for low PF, no clear preferential direction is found for the effective conductivity of the different compositions (Fig. 6.18). The mean displacement of the different compositions, however, is as inconclusive as the displacement of the low PF: all structures have very similar displacement in loading direction. In the directions perpendicular to the loading direction only for composition of 15% CB the displacement is significant larger in comparison to the reference case of 12.5% CB: The difference $\Delta x - \Delta x_{\mathrm{ref}}/\Delta x_{\mathrm{ref}}$ is around 40%, while the other compositions show deviations of around 5%. This might be reason for the larger deviation in the directional components of the effective conductivity.

Subsuming, it appears that a higher Young's Modulus of the active material, higher PF, and also a higher amount of CB is beneficial for the effective conductivity of structure. Concededly, the mean effective conductivities, relative to the material's bulk value, are all in the range of 0.001 to 0.008 for a strain of 2.5%, i.e. they all have the same order of magnitude. Considering the total volume fractions of the compositions, the Bruggeman approach would lead to relative

effective conductivities in a range from 0.018 (for 10% CB) to 0.033 (for 15% CB). Those approximations strongly overestimate the effective conductivities found with the RN-approach. Furthermore, the conflicting results of this section demonstrated the difficulties in finding a direct correlation to predict the effective conductivity during mechanical loading. Apparently, only the explicit consideration of rearrangement in the microstructure allows to predict the conductivities properly.

6.2.4. Summary

In this section was shown that DEM is a appropriate tool to predict the microstructural rearrangement due to mechanical loading. It allows to reproduce the anisotropy induced by the calendering process— simulated as uni-axial compression. The macroscopic stress in binary microstructures—representing compositions of AM and CB—varies significantly for the three different assemblies generated per composition. Its dependence on material properties was shown to be described quite accurately by Eq. 6.9 for the mixtures. The variation in stress found for the different groups of PF and the different compositions is small in comparison to the variation due to the random nature of the assemblies—at least in the here considered range.

The percolation probability and other relevant transport properties in this section were given as function of strain, not as function of the solid volume fraction—as it was done in the previous section. It was shown that the percolation threshold is independent of the elastic material properties; yet it is reduced to lower strain values for increasing amount of CB as well as for increasing packing factor. Studying the coordination numbers during loading showed that the concept of coordination number is inapplicable for the here considered systems: no critical coordination Z_c could be identified. Further, a direct correlation between the percolation probability of CB and the amount of connected active material was found. This demonstrates how important a connected CB network is for proper cell function. Not only the amount of connected AM, but also the free surface area—relevant for the reaction rates—was shown to be dependent on the percolation threshold. A decrease of the free surface area with compression, suggested in experimental studies [23], was only found in some cases. It should be noted that the highest values of connectivity and of active free surface area were found for the highest amount of CB. Hence, a lower amount of AM seems to be beneficial for cell performance in terms of connectivity as well as in terms of possible charge rates.

In contrast to the percolation probability, the effective conductivity seems to depend on the overall state of stress—reflecting on the contact forces. The mechanically induced anisotropy, however, is not consistently transferred to the effective conductivity. Increased rearrangement of the CB particles might influence the deviations in anisotropy; however, the displacement could not explain all preferential directions found for the effective conductivity. Additionally, it was shown that the Bruggeman equation overestimates the effective conductivity. Thus, further insight in the effective transport properties can best be obtained with a coupled approach of DEM and RN-models, as implemented here.

6.3. Cell operation of LIB

Applying LIB as power sources for electric vehicles or stationary energy storage, requires improved long-term properties of the cells: In terms of cycle life, a life-time up to 1000 cycles at 80% depth-of-discharge (DOD) is demanded [24]. Capacity decrease and power fading with each loading cycle[6] are, however, often observed. Due to the complexity of the system, ageing does not originate from a single cause but from a number of processes and their interaction. This includes processes like electrolyte decomposition, solid-electrolyte interface conversion and growth, side reactions, and mechanical degradation. A comprehensive overview of those different ageing mechanism can be found in [24]. Even though most of the processes are largely coupled in the cell, and thus, can not be studied independently in experiments, it is important to decouple them in numeric investigations to obtain a general understanding.

6.3.1. Intercalation and degradation

In this work, we focus on mechanical aspects of material degradation in the electrode. The intercalation-deintercalation of Li-ions in the host structure is accompanied by local volume changes due to changes in lattice parameters and due to changes in crystal structure caused by phase change. Thus, concentration gradients result in stress within the particle [152]. The volume change is additionally constrained by neighboring particles and non-active cell components such as additives, current collector, and cell housing [26]. Mechanical degradation is often manifested in fracture and disintegration [153, 154, 155], as shown in Fig. 6.19 exemplary for two different active materials.

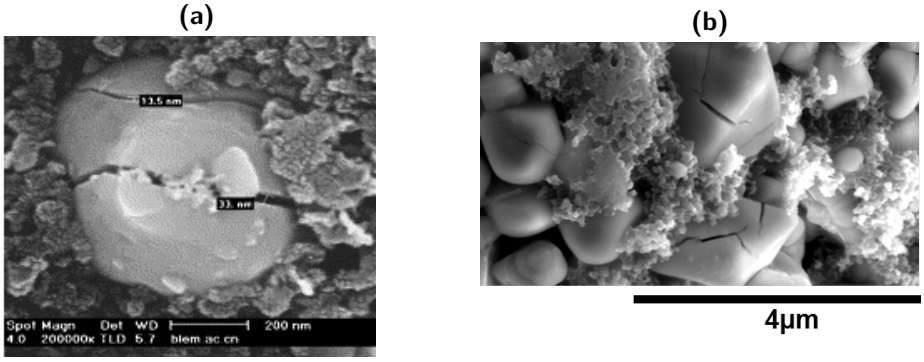

Figure 6.19.: Crack formation in (a) LFP particle after 60 cycles [64] and (b) LMO particles by courtesy of R. Moenig [156]

In combination with loss of contact to the current collector or the electron conducting network, a part of the the host material might become isolated. Additionally, particle fracture results in solid-electrolyte interface (SEI)[7] formation on the newly build surface, consuming Li-ions irreversibly. Both aspects reduce the amount of active material and thus, decrease cell capacity [26].

[6] charge and discharge

[7] SEI is a passivation layer that forms on the free surface of the electrode material in contact with the electrolyte, usually during the first cycle [24].

Intercalation induced stress

Besides monitoring the crack growth during cycling, only few experimental studies exist on the intercalation induced stress in the electrodes. Substrate curvature tests have been used to determine the macroscopic stress in simplified thin film electrodes [157] or porous composite electrode materials [158, 159]. To do so, the electrode material is deposited on a stiff substrate and then cycled. The deflection of the stiff substrate—caused by constraining dimensional changes of the active film during cycling—is measured in order to determine the overall stress level. For thin film graphite electrodes, a maximum stress up to -1 GPa was reported [157]; and for composite electrodes of the same material, the maximum stress was reduced to -10 MPa [159]. This indicates the effective role of the binder phase on buffering stress development.

Besides the experimental studies of the intercalation induced stress, several numerical investigations have been performed. So far, mostly single particle models exist, which determine the stress distribution due to concentration gradients [144] and phase change [143] within the particle. Only few consider a 2 or 3 dimensional distribution of the particles within the cell; and those state that particles close to the electrolyte layer undergo more severe mechanical loading [73, 160, 161]. Of those, only Wu et al. [161], and Rahini and Shenoy [160] take the interaction of particles in form of mechanical constraints into account. They considered the interactions of active material particles with each other as well as their interaction with binder as mechanical constraints. Resulting inhomogeneous stress profiles within the particles are caused by inhomogeneous contact distribution. This indicates that—for the determination of a realistic stress profile—knowledge of the contact distribution is of importance. Nevertheless, they used finite element modeling (FEM) and studied the stress development for geometrical fixed microstructures. Further, Awarke et al. [162] consider the effect of microstructural changes during cycling on effective conductivity and mechanical properties as input parameters for mechanical continuum cell modeling. Particle rearrangements, contact losses, and contact formations, however, have not been considered so far.

6.3.2. Micromechanics of intercalation

As discussed in section 6.1, DEM is ideally suited to consider the particle rearrangement, changing contact forces, and the influence of that on macroscopic cell stress.

To simulate the intercalation process, the radii of AM particles within the electrode structure have to be correlated to the lithium-concentration c_x (in mol/m^3). This correlation can be determined based on the relationship of particle strain and concentration [152, 144]

$$\varepsilon_{ij} = \frac{c_x - c_0}{c_{\max}} \frac{\overline{\Omega}}{3} \delta_{ij}. \tag{6.14}$$

In this, the concentration c_0 is the concentration at the low-concentration state, $c_{\max}$ is the maximum allowed lithium concentration; $\overline{\Omega}$ is the dimensionless partial molar volume, which can be approximated linearly as [152]:

$$\overline{\Omega} = \frac{1}{a_{\max}^3} \frac{a_f^3 - a_0^3}{(c_f - c_0)/c_{\max}}. \tag{6.15}$$

In there, a_f and a_0 are the lattice parameter of the low and the high lithium-concentration state, respectively, and $a_{\max}^3$ denotes the lattice parameter of the maximum allowable lithium

concentration. By relating the lattice parameter directly to the volume changes, Eq. 6.15 can be calculated based on measured volume changes as

$$\overline{\Omega} = \frac{\frac{\Delta V}{V_{\max}}}{\frac{c_f - c_0}{c_{\max}}}. \tag{6.16}$$

Assuming in the definition of $\overline{\Omega}$—as a simplification—c_f equal to $c_{\max}$ and c_0 as zero[8], allows to define the partial molar volume based on the volume change only.

The present volume change ε_V of the particles for a certain intercalation state can be calculated from the tensor trace of ε_{ij}

$$\varepsilon_V = Sp\varepsilon_{ij} = \frac{c_x - c_0}{c_{\max}}\overline{\Omega} = \frac{V_x - V_0}{V_0} \tag{6.17}$$

with V_x as the current volume and V_0 the volume before intercalation. This can be rewritten as

$$\begin{aligned} V_x - V_0 &= V_0 \frac{c_x - c_0}{c_{\max}}\overline{\Omega}, \\ V_x &= V_0 + V_0 \frac{c_x - c_0}{c_{\max}}\overline{\Omega} = V_0(1 + \frac{c_x - c_0}{c_{\max}}\overline{\Omega}). \end{aligned} \tag{6.18}$$

With the volume of a sphere V as $4/3\pi r^3$, this leads to

$$r_x^3 = r_0^3(1 + \frac{c_x - c_0}{c_{\max}}\overline{\Omega}). \tag{6.19}$$

Hence, the present radius r_x can be calculated as

$$r_x = r_0 \sqrt[3]{1 + \frac{c_x - c_0}{c_{\max}}\overline{\Omega}}, \tag{6.20}$$

which can be simplified by series expansion to

$$r_x = r_0(1 + \frac{1}{3}\frac{c_x - c_0}{c_{\max}}\overline{\Omega}). \tag{6.21}$$

Following from that, the radius increase can correlated to the current Li concentration by

$$\frac{r_x - r_0}{r_0} = \frac{1}{3}\frac{c_x - c_0}{c_{\max}}\overline{\Omega}. \tag{6.22}$$

An overview of the relative volume change and the related radius change is given in Table 6.4 for the standard electrode materials.

During operation, the intercalation and deintercalation process is mostly restricted from complete charge or discharge in order to maintain the material's integrity. Therefore, we conducted the calculations considering a volume increase of 6% (=2% radius increase), which is slightly below the given values. In order to keep the results universal, they are given in dependence of c_0 and $c_{\max}$ rather then in terms of the actual Li-concentration.

[8] For LMO, this is a deviation from the actual values of $c_f = 0.995 c_{\max}$ and $c_0 = 0.2$; however, for the given volume changes of LFP and graphite, determined for $c_0 = 0$ and $c_f = c_{\max}$, this is valid.

	Δ V/V$_{max}$ [%]	Δ r/r$_{max}$
LMO [144]	6.5	0.0212
LFP [163]	6.5	0.0212
Graphite [150]	9	0.03

Table 6.4.: Volume change during Li^+-ion intercalation

Material properties

The material properties of LMO and LFP are assumed to be constant during the intercalation process, as they only undergo insignificant changes with lithium concentration [149, 150]. For the standard anode material—graphite—on the other hand, a threefold increase of the Young's Modulus with Li-intercalation is reported in [150]. The Young's modulus changes from 32.47 GPa for graphite to 108.67 GPa for LiC_6, and the Poisson's ratio changes from ν=0.315 to ν=0.24, respectively.

In the simulation of the intercalation process, the boundaries of the volume element are constrained by $\varepsilon_{ij} = 0$. Thus, the swelling of the particles is constrained by the surrounding particles, which themselves are swelling, too. Those constraints cause macroscopic stress in the volume element, which was calculated first for monosized assemblies of pure AM. Additionally, the macroscopic stress was calculated for a binary mixture with medium PF, containing 12.5% solid volume fraction of CB. The compositions were chosen in analogy to the assemblies used in the simulations of the calendering process. The PF of the binary mixture was chosen based on the findings of Zheng et al. [22], and the PF for monosized assemblies was calculated accordingly.

The components of the macroscopic stress, developing during the intercalation process, are shown in Fig. 6.20a for monosized and in Fig. 6.20b for binary assemblies of LFP electrodes. The volume increase of active material during intercalation leads to an isotropic stress distribution. The addition of CB to the monosized assembly of pure AM induces a stress increase of 24.2% for the maximum Li-concentration. The significant deviation, found for the three different assemblies of

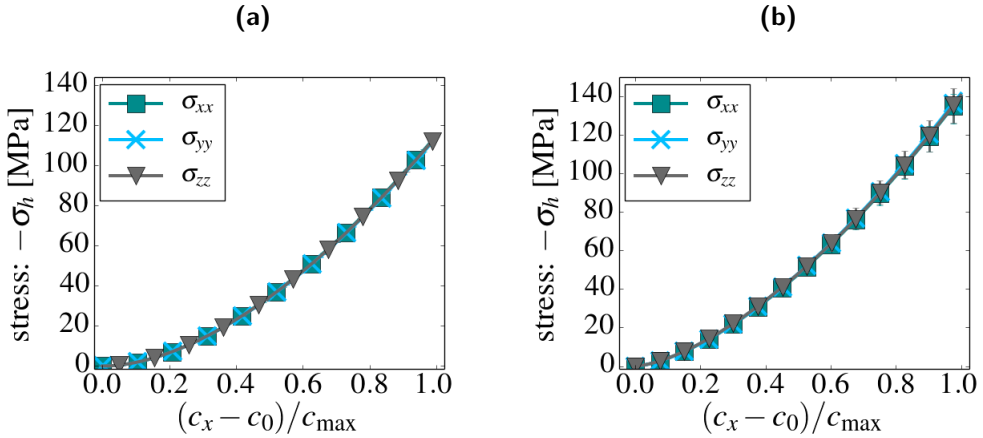

Figure 6.20.: Components of macroscopic stress during intercalation process within (a) monosized assemblies of pure active material with PF around 60.8% and (b) binary mixtures of active material and 12.5% solid volume fraction CB with PF around 69.4%; calculated for LFP

each binary composition during calendering, is reduced. We assume, this is related to reduced rearrangement in the particle structure.

In a next step, material properties depending on the lithium concentration, occurring e.g. in graphite anodes, are applied. To model those, we assume a linear change during the intercalation process. The influence of varying elastic properties (E_{var}) on the macroscopic stress is shown in Fig. 6.21 for monosized assemblies, containing active material only. For comparison, calculations with constant properties of graphite and LiC_6 are shown additionally. The stress found for the varying material properties is between the results found for the initial and final material properties. It was shown in section 6.2.1 that Eq. 6.9 correlates the hydrostatic stresses found for structures

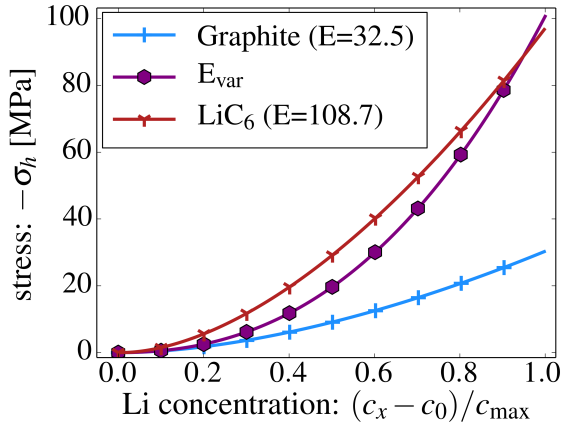

Figure 6.21.: Influence of changing material properties during the intercalation process modeled for assemblies of graphite as standard anode material

with different material properties. Assuming a linear change of E_{var} in Eq. 6.9 allows to calculate $\sigma_h(E_{var})$ based on the hydrostatic stress found for assemblies with either graphite and LiC_6 material properties. The results are in good agreement for the complete intercalation process. As the effect of different material properties—even changing material properties—can be calculated based on Eq. 6.9, we will use only one set of material properties in the following—those of LFP.

The macroscopic stress obtained numerically in [159] with substrate curvature tests for porous graphite composite electrodes, however, is with -10 MPa one order of magnitude smaller than the numerical results found for graphite anodes. Possible reasons for such a significant deviation between simulation and experiment can, on the one hand, be found in the simplifications made in the modeling approach—this will be discussed in detail in section 6.4. On the other hand, also the stress in the substrate curvature experiment is not measured directly, but it is calculated based on the deflection of the electrode-substrate composition. In their calculations, Sethuraman et al. assume a constant Young's Modulus of graphite of 10 GPa. Thus, not only the maximum stress deviates by one order of magnitude but also the elastic properties considered to determine the stress. Scaling the numerically obtained, hydrostatic stress with a Young's Modulus of 10 GPa in accordance with Eq. 6.9 leads to σ_h around -10 MPa for the maximum intercalation. This is in the same order of magnitude as the experimental determined values.

Influence of morphology and composition

To study the influence of the packing factor on the stress during intercalation, the different PF groups, introduced in section 6.2.1 (Table 6.2), are examined. An increase of stress with increasing PF can be seen in Fig. 6.22a, as it was already observed during calendering (Fig. 6.7a). As only the active material is undergoing volume change, this effect is most likely amplified by the larger total amount of AM found in the electrodes with high PF. In contrast to the calendering simulations, the deviation between the three assemblies per group is less significant as the variation between the groups.

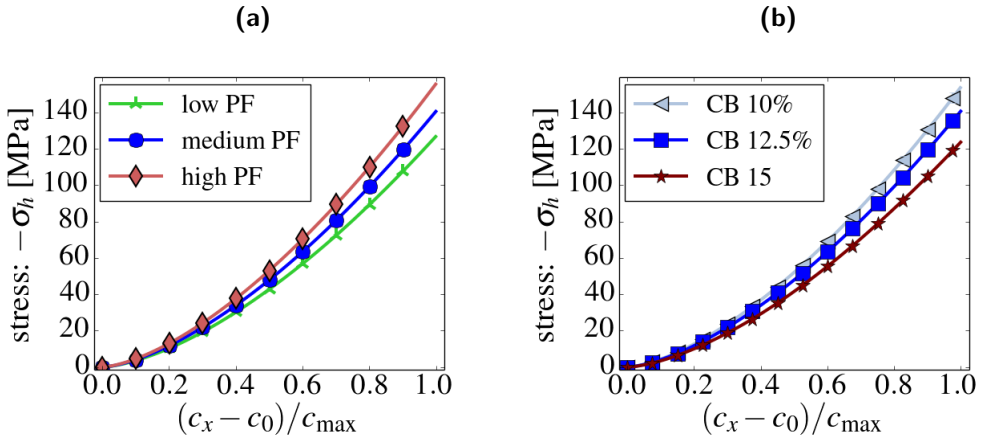

Figure 6.22.: Hydrostatic stress during the intercalation process of (a) different PF and solid volume fractions CB of 12.5% and (b) assemblies with PF around 69.4% and different volume fractions of CB

Further, examining the influence of the different solid volume fraction of CB—the same were already studied in section 6.2.1—on the macroscopic stress (Fig. 6.22b) shows that a decreasing amount of AM is correlated to lower stress development during intercalation. The effect a lower amount of the stiffer AM component in mixtures with higher volume fractions of CB—observed for calendering (Fig. 6.7b)—is intensified by the overall lower amount of volume change in structures with high volume fractions of CB, in accordance with the findings for the different PF groups.

6.3.3. Connectivity during intercalation

To study the influence of the intercalation process on the connectivity, the percolation probability of CB is calculated for different packing factors (Fig. 6.23a) and different volume fractions of CB (Fig. 6.24a).

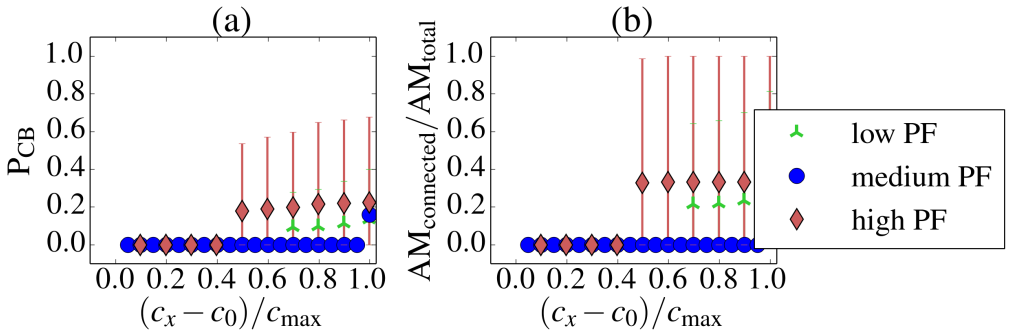

Figure 6.23.: (a) Percolation probability of the CB phase and (b) the fraction of AM particles connected to a percolating CB network for different packing factors during intercalation

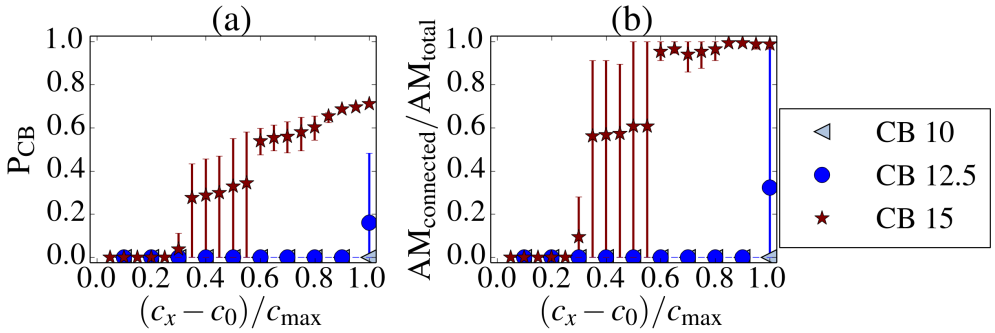

Figure 6.24.: (a) Percolation probability of the CB phase and (b) the fraction of AM particles connected to a percolating CB network for different solid volume fractions of CB during intercalation

In all here considered cases, the initial percolation probability is zero, and thus, no conducting connection exists. Even for the most favorable composition with 15% CB, the percolation threshold is only found for a Li-concentration higher than 50%. In accordance with the results found in section 6.2.2, the amount of connected active material is directly correlated to the percolation probability (Fig. 6.23a and 6.24b).

As explained previously (section 6.2.2), only those active material particles take part in the cell reaction, which are connected to the current collector through a percolated CB network. As also only those would—under real conditions—change their volume, at the beginning of the intercalation process no swelling would occur. Connectivity, however, is only obtained for a certain amount of volume change in the uncalendered assemblies. Thus, in the initial state, no swelling can take place, and therefore, no connectivity can build up. Based on this, we assume that uncalendered electrodes do not function properly. On this account, the intercalation process is studied further for pre-calendered electrodes.

6.3.4. Pre-calendered electrodes

To simulate pre-calendered electrodes, the microstructures were at first compressed uni-axially in x-direction; subsequently, the intercalation was modeled by a radius increase of the active material, as described in section 6.3.2. During the intercalation process, the compression strain in x-direction was maintained. The mechanical response to the combined loading process is shown in Fig. 6.25 exemplarily for the assemblies with a medium PF around 69.4% and a solid volume fraction of CB of 12.5%. The calendering strain is -0.015 and the radius increases 2% of r_0. The stress induced during calendering is in accordance with the findings of section 6.2;

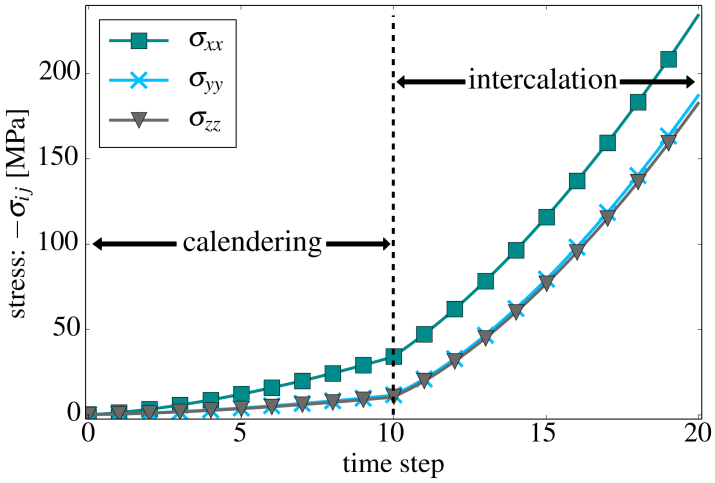

Figure 6.25.: Macroscopic stress for a complete loading process of calendering and intercalation for assemblies with PF around 69.4% and a solid volume fraction of CB of 12.5%, calendering strain of -0.015 and radius increase of 2% of r_0

however, the results for the intercalation differ from the findings in section 6.3.2: The anisotropy, induced by the calendering step, is preserved during the swelling of the intercalation process. Furthermore, the intercalation induced stress is larger for the pre-calendered structure. In the uncalendered electrodes, the swelling process leads to a maximum hydrostatic stress of 140 MPa; in the pre-calendered assemblies, the swelling process leads to a maximum σ_h of 182 MPa. The difference in the intercalation induced stress is due to the non-linearity of the granular system: for currently higher stress level, the slope of the stress-concentration relationship increases further.

Micromechanics in pre-calendered electrodes

To study this further, we calculated the macroscopic stress during intercalation for different pre-calendering loads on microstructures of a medium PF around 69.4% and a solid volume fraction of CB of 12.5%. The stress developing during the intercalation process is shown in Fig. 6.26 for different preloads. The total stress induced by the intercalation $(\sigma_h(c_{\max}) - \sigma_h(\varepsilon_{\text{cal}}))$ is summarized in Table 6.5. Clearly, larger preloads result in larger amounts of intercalation induced stress in the structures. The difference between the non-calendered structures and the structures pre-compressed with 2.0% is almost 40% of stress increase during intercalation only.

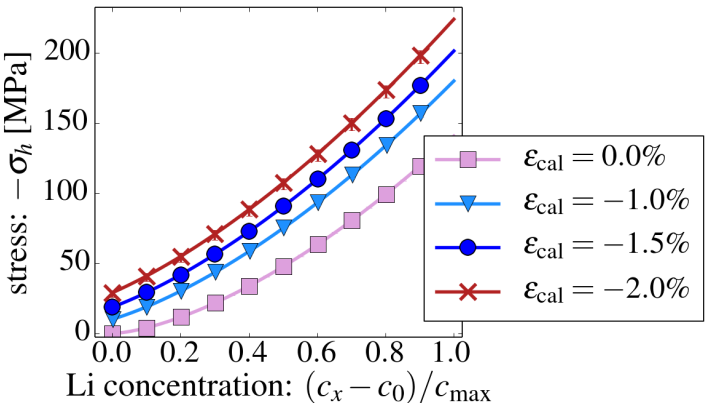

Figure 6.26.: Intercalation induced stress for different pre-compression loads in assemblies with medium PF around 69.4% and a solid volume fraction of CB of 12.5%

$-\varepsilon_{xx}$ [%]	$-\sigma_{\text{h,Li}}$ [MPa]
0.0	140.52
1.0	169.70
1.5	182.44
2.0	194.75

Table 6.5.: Total stress increase during the intercalation process $\sigma_{\text{h,Li}}$ for non-calendered and differently pre-calendered cases

Inevitably, the particle constraints and contact forces during intercalation aggravate the mechanical load acting on the particles, and thus, particle failure might be advanced. To reduce the macroscopic stress caused by intercalation to a minimum, it is preferable to choose the lowest possible calendering strain; sufficient percolation of the CB network and connectivity of the active material, however, still needs to be ensured.

Percolation in pre-calendered electrodes

To investigate which preload allows for sufficient connectivity in the structure during intercalation, the percolation probabilities and the connectivities of active material of the composition—pre-loaded with the different compression rates—were calculated (Fig. 6.27). It appears that percolation during intercalation is best preserved when calendering led to initial percolation probabilities of around 60%. Further, the deviation in percolation probability after calendering should be minimal; this indicates that the percolation threshold is reliably exceeded. This is found for the pre-loadings of -1.5 and -2.0%, for which the percolation probability as well as the connectivity is relatively constant throughout the intercalation process. For lower pre-compression, the percolation is not steady, especially for low Li concentrations, as can be seen in Fig. 6.27a. Again, the connectivity of active material to a CB cluster is closely related to the percolation probability (Fig. 6.26b).

Similar results were found for further configurations and varying preloads. In order to reduce the macroscopic stress during intercalation, the lowest sufficient calendering loads were chosen—based

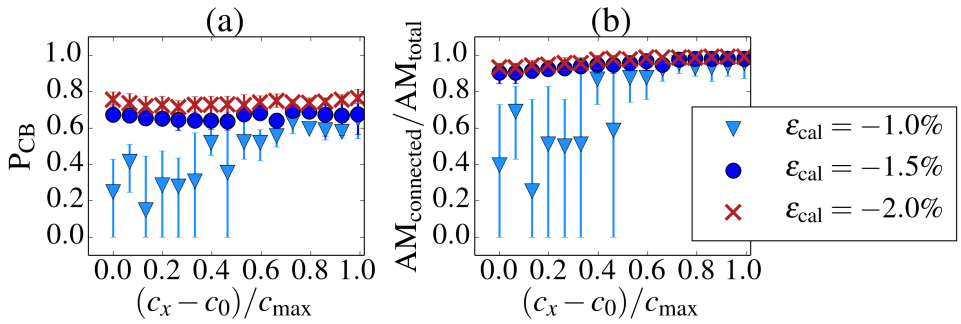

Figure 6.27.: (a) Percolation probability of CB phase and (b) the fraction of AM particle connected to a percolating CB network for a structure of medium PF and 12.5% CB with different preloads

on the results in section 6.2.2. The values applied in the following for the different compositions are summarized in Table 6.6.

PF [%]	ϕ_{CB} [%]	$-\varepsilon_{xx}$ [%]
69.4	10.0	2.5
69.4	12.5	1.5
69.4	15.0	1.0
67.3	12.5	2.0
70.9	12.5	1.5

Table 6.6.: Pre-calendering load for the different microstructures, necessary to achieve percolation in the CB phase

Influence of PF and composition on micromechanics of preloaded cells

The stress developing during intercalation in the preloaded assemblies is given in Fig. 6.28a for the different packing factors and in Fig. 6.28b for different volume fractions of CB. Comparison of the different packing factors shows that the higher initial stress due to the higher preload required for low packing factors is counterbalanced by the lower stress increase during intercalation. The small variation of stress during intercalation, found for the different PFs in uncalendered cells, is removed by the different preloads applied before the intercalation Examining different solid volume fractions, it is shown that a low concentration of CB is detrimental in terms of stress development: Besides the higher preload required, the stress increase during intercalation is higher for a larger amount of active material. Thus, the lowest stress is found for the highest amount of CB.

Regarding the stress only, it can be summarized that it is preferable to choose the lowest possible calendering strain, which still allows for sufficient connectivity. Further, a smaller amount of active materials leads to smaller intercalation induced stress. In terms of cell efficiency, however, a larger amount of CB correlates to a larger amount of ”dead material”, which is assumed to derogate the power density.

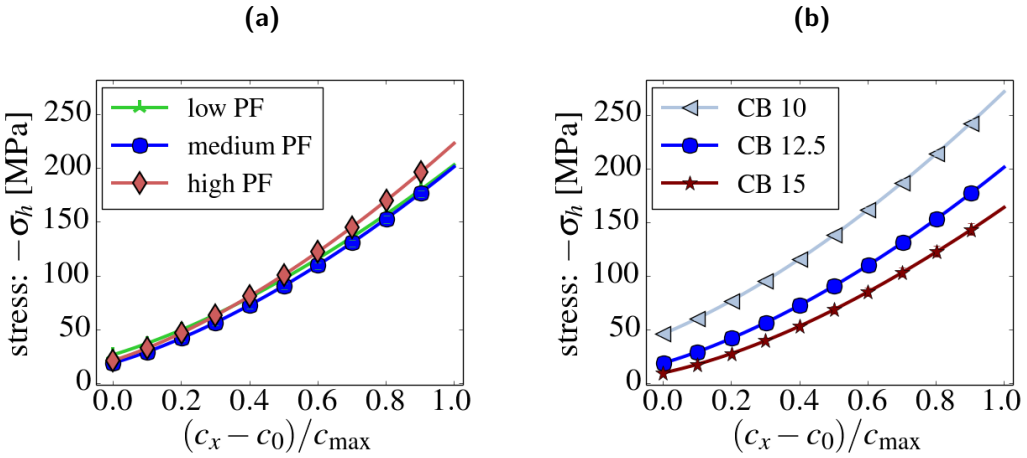

Figure 6.28.: Hydrostatic stress during the intercalation process of (a) different PF and solid volume fractions CB of 12.5% and (b) assemblies with PF around 69.4% and different volume fractions of CB

Connectivity in preloaded electrodes

In addition to the amount of additives, the amount of unconnected AM further impairs the power density. Hence, to estimate the influence of preload and composition on that, the percolation probability of CB and connectivity of AM have to be determined. As illustrated in Fig. 6.29 and Fig. 6.30, the applied preloads allow to preserve sufficient and nearly constant percolation probability throughout the intercalation process for medium and high PFs with 12.5% CB, as well as for a medium PF with 15% CB. Comparing those results with the ones found for uncalendered structures in Fig. 6.23 and Fig. 6.24, it clearly demonstrates the positive influence of calendering with regard to cell performance.

For assemblies with low PF as well as for microstructures with only 10% solid volume fraction CB, on the other hand, the percolating clusters disintegrate during the intercalation process. Recalculating the percolation probability for those structures—densified with higher preloads—did not improve the connectivity within the CB-phase. This indicates that a too low amount of

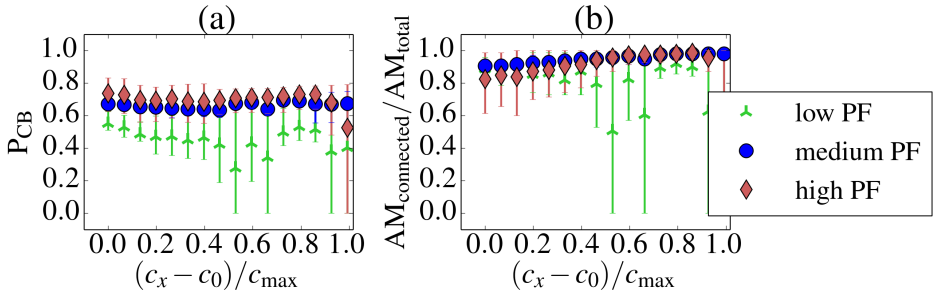

Figure 6.29.: (a) Percolation probability of CB phase and (b) the fraction of AM particle connected to a percolating CB network for different packing factors

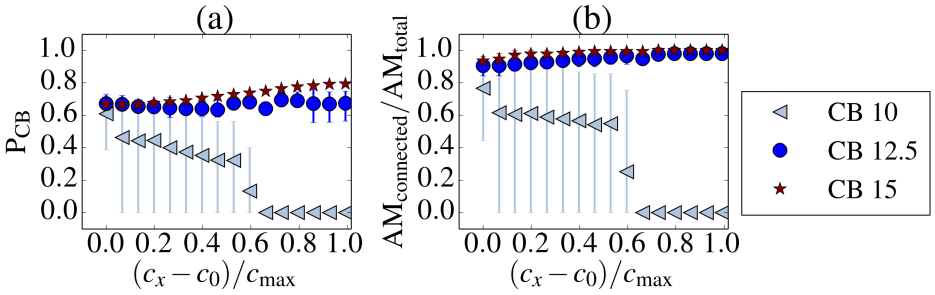

Figure 6.30.: (a) Percolation probability of CB phase and (b) the fraction of AM particle connected to a percolating CB network for solid volume fractions of CB

additives (i.e."dead material") is rather detrimental for cell performance, even though it might seem advantageous at first glance.

Free surface area in preloaded electrodes

We further analyzed the effect of pre-calendering on the active free surface area, which is an important factor for the reaction rate and activation losses, as explained section 6.2.2. The free surface area decreases in all preloaded cases during the intercalation process, as shown in Fig. 6.31. Since the connectivity of the AM particles to conducting CB networks is maintained during the

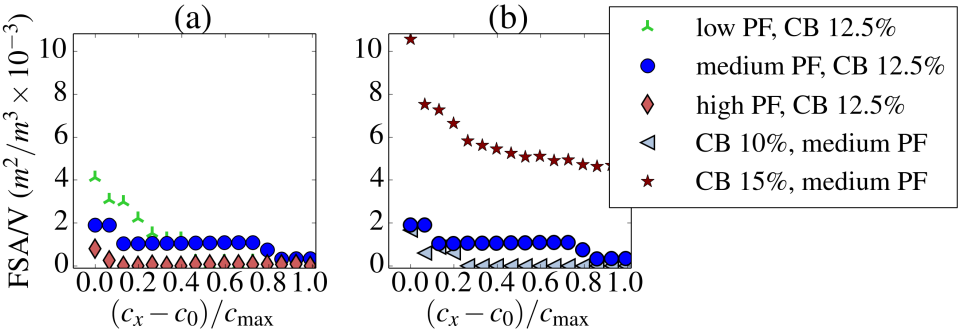

Figure 6.31.: Active free surface area per unit volume during intercalation for (a) assemblies with different packing factor and (b) different solid volume fractions of CB

intercalation process—for the volume fractions of 12.5% and 15% CB (Fig. 6.30b) with medium and high PF (Fig. 6.29b)—the decrease is most likely induced by enlarging solid-solid contacts. The contact area of AM-AM contacts is large in comparison to AM-CB contacts (Table 6.3, section 6.2.2), and thus, it is more relevant for the decrease in free surface area. Therefore, the coordination number $Z_{AM,AM}$—the number of contacts of one AM particle with other AM particles—is calculated for the intercalation process. The development during intercalation is

exemplarily displayed for the different compositions in Fig. 6.32. The increasing number of contacts is most likely the reason for the decrease in free surface area. In accordance with the findings for calendering (section 6.2.2), the lower amount of AM in the composition of 15% solid volume fraction CB seems beneficial for the amount of active free surface area, and thus, also for the reaction rates.

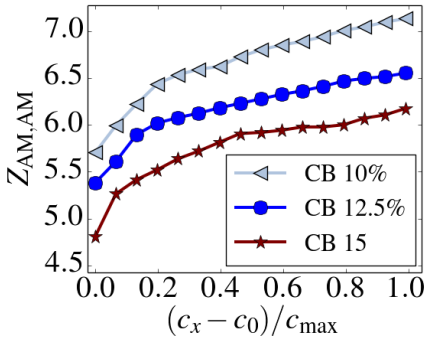

Figure 6.32.: Increase of coordination number $Z_{AM,AM}$ during intercalation exemplary for compositions with different solid volume fraction CB

Effective conductivity in preloaded electrodes

As a reliable connectivity of the CB network is required for satisfactory cell performance, we considered in the following only those compositions, which ensure constant percolation throughout the whole intercalation process: the effective conductivities for the low packing factors as well as for the low volume fractions of CB are not presented here. The directional effective conductivities of the remaining structures are given in Fig. 6.33. The higher preload required for the compositions with 12.5% CB and medium (Fig. 6.33a) or high (Fig. 6.33b) PF lead to larger effective conductivities and more pronounced anisotropy at the beginning of the intercalation process. The anisotropy is, however, mostly evened out during the intercalation process. The composition with 15% CB starts with lower conductivity—due to the lower preload required to obtain percolation—yet it shows the highest increase during the intercalation process. Similar to the directional variation found during calendering (section 6.2.3), no consistent preferential direction could be determined.

The reduction of the—only partially occurring—initial anisotropy might be either due to the isotropic mechanical loading during the swelling or, as discussed in section 6.2.3, due to relatively unconstrained movement of CB particles in the interstices. To investigate this, the displacement of the particles is calculated, relative to the volume length L. In Fig. 6.34 the displacement of large (Fig. 6.34a) and small (Fig. 6.34b) particles is shown exemplarily for the compositions of 12.5% CB and medium PF. The displacement found for the other structures is very similar. During

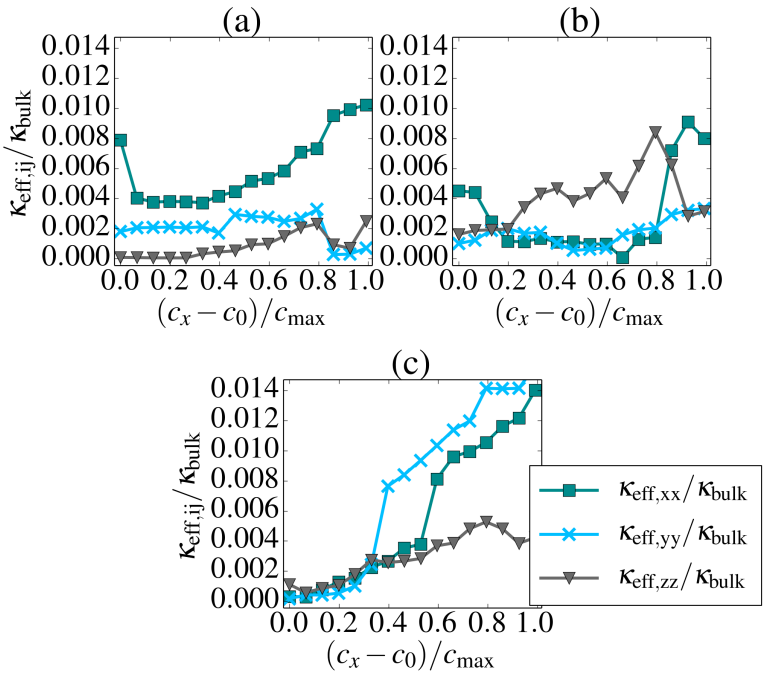

Figure 6.33.: Directional effective conductivity for (a) medium PF with 12.5% CB, (b) high PF with 12.5% CB and (c) medium PF with 15% CB

the first 15 time steps, the assembly is compressed uni-axially; this causes large displacement in loading direction. During intercalation, on the other hand, the displacement in the direction perpendicular to the loading direction is more pronounced, in particular for the small particles. The particles are packed more densely in the loading direction and hence, displacement in this direction is suppressed. The larger rearrangement of the small particles in the perpendicular directions can result in larger variation in the effective conductivity and is most likely the reason, why no clear preferential directions can be seen. Again, this effect is hardly predictable with averaging methods.

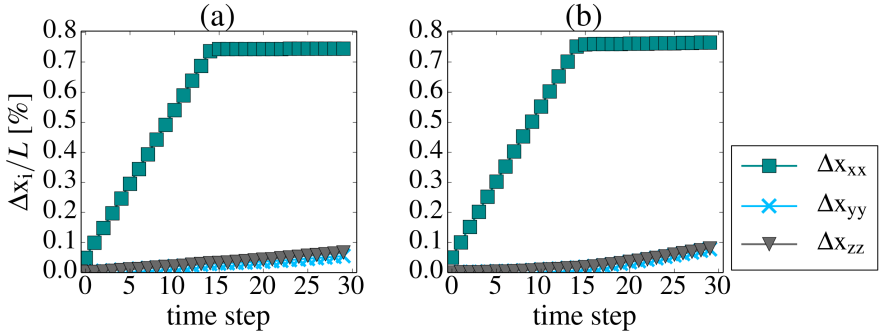

Figure 6.34.: Mean displacement of a (a) large and (b) small particle during calendering (time step < 15) and intercalation (time step > 15) in the assemblies of medium PF and 12.5% CB

6.3.5. Summary

In this section, the connection between intercalation, macroscopic stress, and its influence on the effective transport properties was examined. The importance of an adequate calendering load, applied previously to the intercalation process, was demonstrated in section 6.3.3. The adequate amount of this could be determined based on the investigations of the influence of calendering in connectivity in section 6.2.2. Additionally to an adequate preload, a sufficient amount of CB is required to enable reliable connectivity for the whole intercalation process. For the here examined examples, a preload correlated to 60% percolation probability shows good results. Considering effective conductivity and free surface area, which are both relevant for the cell performance, the microstructure with the highest amount of CB showed the best results, as already indicated for the calendering process (section 6.2). The low preload required in combination with the larger amount of CB softens the mechanical constraints, which the AM particles mutually apply on each other. This reduces not only to lower macroscopic stress but the solid-solid contact area, and thus, in turn, it results in an larger active surface. Here, an optimum between the positive effect on cell properties and its negative effect on power density needs to be found.

6.4. Assessment of simplifications in the model

The large amount of coupled influence parameters in LIB makes it difficult to study single parameters experimentally, as described in section 2.3. Simplified numerical models, on the other hand, allow to study influence parameters separately to gain a better understanding of their effect on cell performance. Due to the simplifications, comparison of experiments and modeling results is difficult; and thus, the accuracy of the simulations is hardly to estimate without tailored experiments. Hence, a critical reflection on the model's assumptions and simplifications is necessary. The most relevant simplifications are summarized here and are discussed in the sections 6.4.1 to 6.4.6:

- initial configuration:
  - The particle shape is idealized in form of a sphere.
  - The size distribution of the particles within one species is neglected.
- loading conditions:
  - The bounding box of the volume element is constrained in direction perpendicular to the calendering direction.
  - The intercalation is assumed to be uniform within the representative volume element.
- particle interaction:
  - Particle fracture is neglected.
  - The particle contact is assumed to be elastic.
  - The binder phase is neglected.

6.4.1. Particle shape

So far, the granular electrodes are approximated by mixtures of spheres, which are the simplest possible 3D representation of the granular materials. The initial configurations, generated with the RCP algorithm, contain randomly distributed, monosized or binary sized particles. In reality, however, the shape varies for the different materials and processing steps: LFP particles for example, are almost sphere-like [164], LMO particles are rather angular [156], and graphite particles are flake-like [159]. In short, all kinds of shapes can be found or formed in the wide variety of materials investigated as cathode materials for LIB. Thus, the assumption of spherical particles is not incorrect and was considered as sufficient. Finally, as discussed in section 6.1, the discrete element modeling is more accurate than continuum models—even with simplified shapes, such as spheres.

6.4.2. Particle size distribution

Furthermore, the particles have been assumed to be of the same size within each species of the mixtures, leading to binary sized assemblies. With the binary size distribution, the most significant size variation of the two components of the electrode is represented. Nevertheless, the particles of each species have varying particle sizes.

In order to consider those, the RCP algorithm, introduced in section 4.1.1, was modified to enable the generation of polydispers packings. Therefore, a method based on the Box-Muller algorithm [165, 166, 167] was implemented to obtain a Gaussian distribution for the particle radii based on uniformly distributed, random numbers Ψ_i in the range from 0 to 1. First, those numbers are converted to a rectangular distribution in the range from -1 to 1 by $\psi_i = 2.0\Psi_i - 1$. Subsequently, pairs of independent random numbers ψ_1 and ψ_2 are transformed in polar coordinates with radius $s = \sqrt{\psi_1^2 + \psi_2^2}$ limited to the interval $]0, 1]$ and two independent variables Q_1 and Q_2 are calculated from this pair

$$Q_1 = \psi_1 \sqrt{\frac{-2ln(s)}{s}}, \qquad Q_2 = \psi_2 \sqrt{\frac{-2ln(s)}{s}}. \tag{6.23}$$

To generate a particle size distribution with the target mean particle radius r_{mean} and a Gaussian distribution of a predefined standard deviation SD, the variables Q_i are multiplied with the distribution width SD and scaled with the mean particle radius:

$$r_i = r_{\text{mean}}(1 + SDQ_i). \tag{6.24}$$

In Fig. 6.35, two binary assemblies with a Gaussian distribution of $SD = 0.1$ for the particle size are depicted, with the particles colored accordingly to their size. In the left assembly (Fig. 6.35a), the large particles have a size distribution and the small particles are of equal size—and vice versa in Fig. 6.35b.

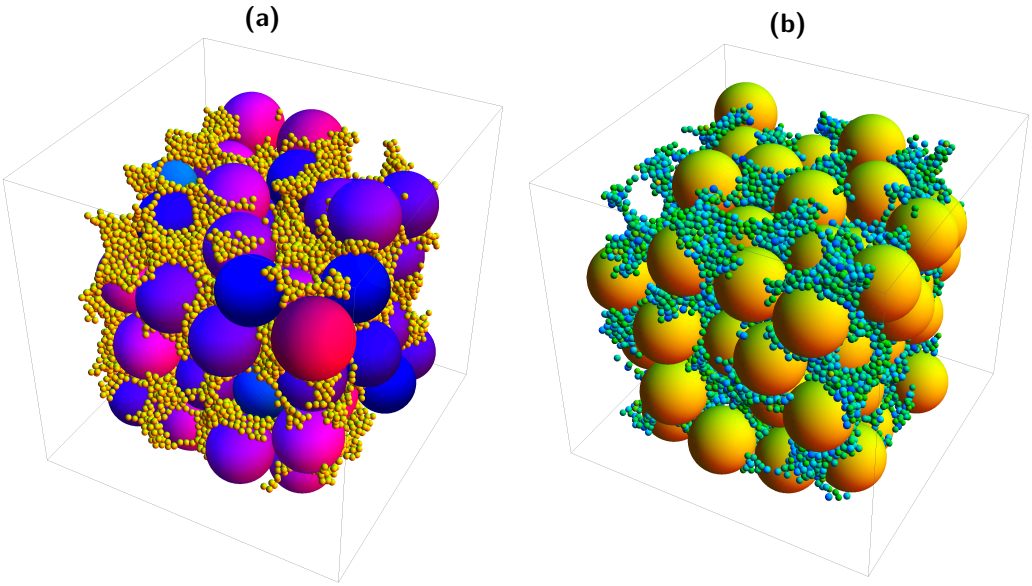

Figure 6.35.: Binary assemblies with Gaussian distribution of (a) the large particles and (b) the small particles with particles colored accordingly to their size

To examine the influence of size distribution on the mechanics of the system, different binary assemblies were generated, with size distribution of either the large AM particles (Fig. 6.35a), or the small CB particles (Fig. 6.35b), or packings with both AM and CB phase with size distribution. For each of those three possible systems, standard deviations SD of 0.05 (denoted as $d1$) and 0.1 ($d2$) were realized, and three assemblies per configuration were generated. For comparability to the previous calculations, the size ratio of the mean particle radii remained 10 and the packing factor was set around 69.4% for all structures. The probability density functions of the size distributions are shown in Fig. 6.36 exemplarily for both standard deviations in the CB phase.

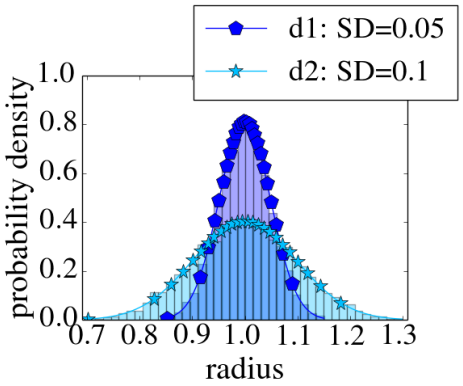

Figure 6.36.: Probability density of CB particle radii in structures with two different Gaussian size distributions

The hydrostatic stress due to uni-axial compression is shown in Fig. 6.37 for all configurations, considering LFP as active material (Table 6.1). Obviously, in none of the considered cases varies the stress response due to different size distributions. Further, comparing the results to the

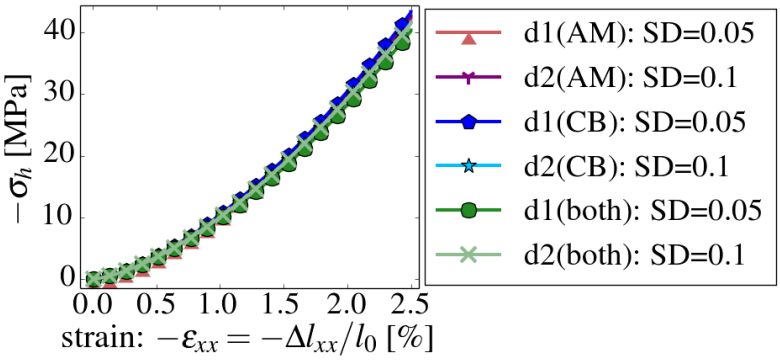

Figure 6.37.: Hydrostatic stress during calendering for assemblies with size distribution either within the AM phase, the CB phase or both phases, considering 2 different standard deviations;LFP as active material

stress response of binary sized mixtures without particle size distribution within the phases (Fig. 6.4b) indicates that the size distribution can be neglected, as it does not influence the results significantly.

6.4.3. Flexible boundary conditions

With regard to the loading conditions, two scenarios have been simulated so far: the calendering and the intercalation process. For both scenarios, the surfaces of the volume element, which are not in loading direction, have been constrained to zero displacement ($\varepsilon_{ii} = 0$). This may replicate an electrode in a fixed casing. Assuming soft casings, as for example given in mostly experimentally used pouch cells—this assumption is no longer valid. Therefore, the influence of elastic boundary conditions, deforming due to the stress within the assembly, are examined in this section. Especially the influence on the stress development during cycling is of interest, as that is related to mechanical degradation. Hence, we focused on the mechanical response of the representative volume element during intercalation.

In order to develop more realistic boundary conditions, the surrounding electrode of the simulated volume element (RVE) has to be considered, as shown in Fig. 6.38. First, the implementation of flexible boundary conditions in in-plane direction of the current collector (y- and z-direction) is introduced with constrained boundaries in x-direction ($\varepsilon_{xx} = 0$). Subsequently, flexible boundaries were additionally implemented for the direction perpendicular to the current collector (x-direction).

Constraints due to current collector

Assuming ideal contact between electrode material and current collector, the deformation of electrode in y- and z-direction is constrained by the elastic properties of the current collector[9], as the material is stiffer than the granular electrode composite. This means that the macroscopic forces $f_{\mathrm{el,yy}}$ and $f_{\mathrm{el,zz}}$, emerging during intercalation in the electrode structure, are equal to the

[9] a thin layer in y- and z-direction

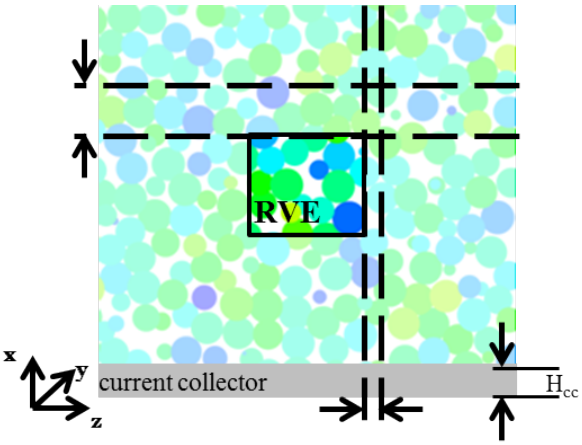

Figure 6.38.: Volume element (RVE) simulated with DEM constrained by the surrounding electrode structure

forces exerting on the current collector $f_{\mathrm{cc,yy}}$ and $f_{\mathrm{cc,zz}}$ in y- and z- direction respectively. Under consideration of the area A of the current collector and the volume element in the x-y plane, this leads to

$$\sigma_{\mathrm{cc,yy}} = \sigma_{\mathrm{el,yy}} \frac{A_{\mathrm{el}}}{A_{\mathrm{cc}}}, \qquad \sigma_{\mathrm{cc,zz}} = \sigma_{\mathrm{el,zz}} \frac{A_{\mathrm{el}}}{A_{\mathrm{cc}}}. \tag{6.25}$$

with $A_i = L_i \times H_i$. Assuming the same box length L for the current collector and electrode volume element, the fraction of areas $\frac{A_{\mathrm{el}}}{A_{\mathrm{cc}}}$ reduces to the fractions of heights: $\frac{H_{\mathrm{el}}}{H_{\mathrm{cc}}}$. Typically, the heights of the current collector is in a range of 15 to 25 μm, and the heights of the electrode is—depending on the cell application—in the range from 50 to 300 μm [11]. For the following calculation we chose 25 μm for H_{cc} and 250 μm for H_{el}. Based on that, the deformation of the current collector in in-plane direction of the thin layer can calculated for plane stress conditions [168], p. 500 ff:

$$\begin{aligned} \varepsilon_{yy,cc} &= \frac{1}{E_{cc}} \left(\sigma_{yy,cc} - \nu_{cc} \sigma_{zz,cc} \right) \\ \varepsilon_{zz,cc} &= \frac{1}{E_{cc}} \left(\sigma_{zz,cc} - \nu_{cc} \sigma_{yy,cc} \right). \end{aligned} \tag{6.26}$$

Here, $\sigma_{yy,cc}$ and $\sigma_{zz,cc}$ are the macroscopic stress components of the current collector calculated with Eq. 6.25 from the stress within the electrode caused by intercalation process. E_{cc} and ν_{cc} are the elastic properties of the current collector; in cell manufacturing, the materials are chosen to obtain electrochemical stability of the system. Thus, a thin aluminium layer is usually used in cathode and a copper current collector in the anode. The material properties are given in Table 6.7.

	Young's modulus E [GPa]	**Poisson's ratio ν**
aluminium	70	0.34
copper	130	0.343

Table 6.7.: Material properties of the current collector used in the DEM simulation of LIB electrodes according to [169]

Subsequently, the calculated deformation of the current collector is applied to calculated the new dimensions of the bounding box of the granular system—assuming linear displacement of the boundaries without tilting or bending:

$$\varepsilon_{xx,el} = 0, \qquad \varepsilon_{yy,el} = \varepsilon_{yy,cc}, \qquad \varepsilon_{zz,el} = \varepsilon_{zz,cc}. \tag{6.27}$$

Based on the new dimensions of the volume element, the particles in the box are moved accordingly, as described for the calendering in section 6.2.1 and the balanced state is determined. The complete process is sketched in Fig. 6.39: For each loading step, the macroscopic stress σ_{el} within the electrode structure is calculated with constrained boundaries. Ongoing from the stress, the deformation of the volume element is calculated with Eqs. 6.25, 6.26 and 6.27. Subsequently, the deformations in y- and z-direction are applied as boundary conditions, and the macroscopic stress in the relaxed volume element is calculated before the next intercalation step.

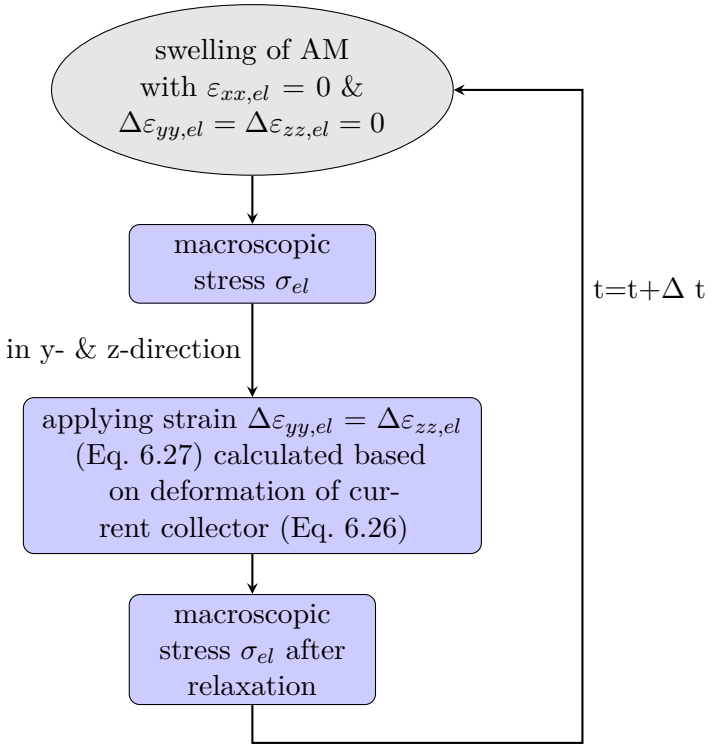

Figure 6.39.: Schematic diagram of the implementation of flexible boundary conditions in y- and z-direction

In order to reduce influence factors due to varying compositions, we chose monosized assemblies for the simulations. For comparability to simulations with constrained boundaries, the initial configurations have a PF of around 60.75, as previously used. The macroscopic stress shown in Fig. 6.40a is obtained for LFP as active material and aluminium as current collector. For comparison, the results for the same configurations simulated with fixed boundary conditions are given in Fig. 6.40b.

Due to the flexible boundary conditions, the maximum macroscopic stress is reduced by around 15 % for the maximum lithium concentration. Additionally, the isotropy—observed for intercalation with fixed boundaries (Fig. 6.40b)—is lost by enabling displacement of the boundaries in in-plane

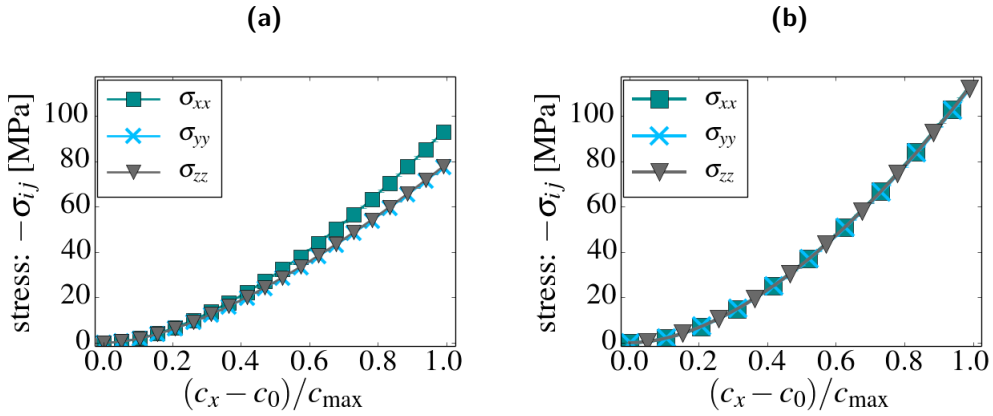

Figure 6.40.: Macroscopic stress in LFP cathodes during intercalation for (a) flexible boundary conditions with aluminium as current collector and (b) fixed boundary conditions for comparison.

direction of the current collector: the stress in y- and z-direction is smaller than in x-direction due to the relaxation in this directions. Further simulations with copper as current collector material showed only little influence of the different material properties on the stress response.

The displacement causing the relaxation in y- and z-direction is equivalent in both directions, as can be seen in Fig. 6.41a. The strain introduced by the current collector is small compared to the loading applied during calendering. Further, a linear stress-strain relationship between the relaxation of the electrode volume and the macroscopic stress of the assembly is found, as shown in Fig. 6.41b. As the granular systems considered in here usually show a non-linear behavior (see

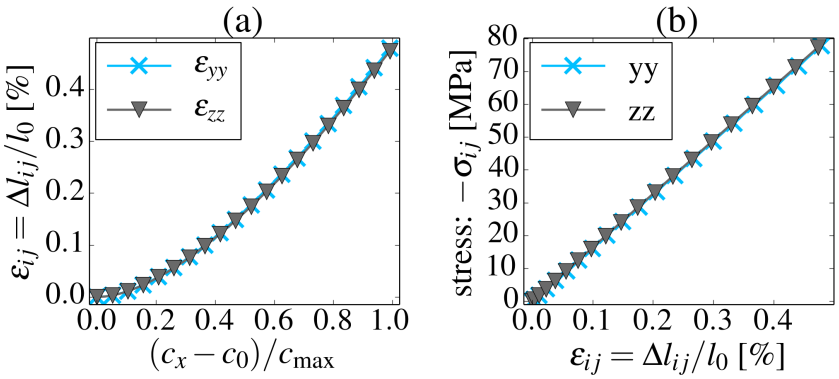

Figure 6.41.: (a) Relaxation of the electrode during Li intercalation and (b) macroscopic stress within the electrode vs relaxation strain

section 6.2.1), this might indicate the influence of the linearity of the current collector's elasticity. Interestingly, studying this stress-strain relationship for a soft LMO material (E=10 GPa) leads to the same linear relationship: The stiffness $\sigma_{yy}/\varepsilon_{yy} = \sigma_{zz}/\varepsilon_{zz}$ is equal for both systems throughout the whole intercalation process (Fig. 6.42) and around 1/4 of the Young's Modulus of the current collector. The scaling law (Eq. 6.9), which relates the stress to the systems bulk Young's Modulus, however, does no longer hold true.

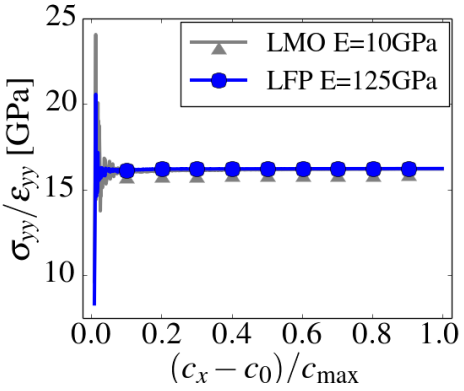

Figure 6.42.: Stiffness $\sigma_{yy}/\varepsilon_{yy}$ during the intercalation process for different active material properties

Unconstrained volume element

As described, the deformations in y- and z-direction are constrained by the elastic properties of the current collector. In x-direction, on the other hand, the possible deformation depends on the surrounding electrode structure as well as the opposing electrode. To estimate the maximum possible deformation—coinciding with the lower stress limit—we consider a free-standing electrode, unconstrained by the opposing electrode, casing, or further cell layers. The assumption of a free-standing assembly in x-direction leads to

$$\sigma_{xx,el} = 0, \tag{6.28}$$

and in y- and z-direction

$$\varepsilon_{yy,el} = \varepsilon_{yy,cc}, \qquad \varepsilon_{zz,el} = \varepsilon_{zz,cc} \tag{6.29}$$

as boundary conditions. Stress-controlled simulations in DEM, however, have to be realized through displacement controlled calculations [114]: the strain is adjusted in order to achieve a specified stress condition. As in this type of calculation the stress has to be readjusted for each swelling step, we require a numerically efficient approach. The servo-controlled approach—this means iteratively readjusting the strain step-wise until the target stress level is reached—is numerically rather expensive. To approximate the strain required to reach $\sigma xx, el = 0$ after a previous intercalation step, we assume that a linear stress-strain relationship for small strains. In analogy to thermal strains [168], the intercalation induced strain ε_{xx}^{Li} is given by

$$\varepsilon_{xx}^{Li} = \frac{c_x - c_0}{c_{\max}} \frac{\overline{\Omega}}{3}, \tag{6.30}$$

as described in section 6.3.2. The total strain ε_{xx} comprises additionally an elastic part ε_{xx}^{m}, which is related to the macroscopic stress σ_{xx}

$$\varepsilon_{xx} = \varepsilon_{xx}^{Li} + \varepsilon_{xx}^{m}. \tag{6.31}$$

With the constraining boundary condition $\varepsilon_{ij} = 0$, applied for the intercalation process, ε_{xx}^{m} can be considered as a counter strain for the intercalation process and is related to the intercalation induced stress by

$$\varepsilon_{xx}^{Li} = -\varepsilon_{xx}^{m} = \frac{\sigma_{xx}}{E_{xx}}. \tag{6.32}$$

Applying a relaxing strain $\varepsilon_{xx}^{m,re}$, equivalent to the absolute value of $\varepsilon_{xx}^{m} = \sigma_{xx}/E_{xx}$, in the opposite direction of ε_{xx}^{m}:

$$\varepsilon_{xx} = \underbrace{\varepsilon_{xx}^{Li} + \varepsilon_{xx}^{m}}_{=0} - \varepsilon_{xx}^{m,re} \tag{6.33}$$

leads to stress relaxation in the electrode. For a linear elastic material, the stress σ_{xx} can be reduced to 0 with this approach.

In order to calculate $\varepsilon_{xx}^{m,re}$, the Young's Modulus of the electrode structure must be determined in addition to the macroscopic stress. The elastic properties of granular materials are not only dependent on the state of intercalation, but they also depend on the stress level within the structures. Hence, they change during the simulation as a result of the intercalation as well as the applied strain. Therefore, for each loading step, two separate calculations are necessary: First, the elastic properties of the system have to be determined for the current state. Subsequently, the possible deformation can be estimated based on that material properties.

Elastic properties of the granular structure The mechanical response of granular material is usually non-linear. Nevertheless, when the deformation around an arbitrary state of the configuration is small, the material response in this narrow range can be assumed as linear. Thus, Hook's law is applicable. In Einstein notation this is written as

$$\sigma_{ij} = \mathbb{C}_{ijkl}\varepsilon_{kl} \tag{6.34}$$

with $\mathbb{C}_{ijkl}$ as the $ijkl$-component of the fourth-rank elasticity tensor. Considering the symmetry, with Voigt notation this can be reduced to

$$\begin{bmatrix}\sigma_{11}\\ \sigma_{22}\\ \sigma_{33}\\ \sigma_{23}\\ \sigma_{13}\\ \sigma_{12}\end{bmatrix} = \begin{bmatrix}C_{11} & C_{12} & C_{13} & C_{14} & C_{15} & C_{16}\\ C_{12} & C_{22} & C_{23} & C_{24} & C_{25} & C_{26}\\ C_{13} & C_{23} & C_{33} & C_{34} & C_{35} & C_{36}\\ C_{14} & C_{24} & C_{34} & C_{44} & C_{45} & C_{46}\\ C_{15} & C_{25} & C_{35} & C_{45} & C_{55} & C_{56}\\ C_{16} & C_{26} & C_{36} & C_{46} & C_{56} & C_{66}\end{bmatrix} \begin{bmatrix}\varepsilon_{11}\\ \varepsilon_{22}\\ \varepsilon_{33}\\ \varepsilon_{23}\\ \varepsilon_{13}\\ \varepsilon_{12}\end{bmatrix} \tag{6.35}$$

containing 21 independent components in the elasticity tensor [170]. To determine all components the strain $\Delta\varepsilon_{kl}$ has to be applied in all 6 directions, and the corresponding changes in σ_{ij} allow for calculation of $\mathbb{C}_{\mathrm{ijkl}}$ with

$$\frac{\Delta\sigma_{ij}}{\Delta\varepsilon_{kl}} = \mathbb{C}_{\mathrm{ijkl}}. \tag{6.36}$$

In the here considered case, only the direction perpendicular to the current collector is relevant, as only this direction (x-direction) is unconstrained. Hence, the stress-response for strain in x- direction, ε_{xx}, has to be calculated. To obtain these information from DEM simulations, I implemented an additional routine: the assembly in an arbitrary state, for which the elastic properties are required, is compressed by a small amount ($\Delta\varepsilon_{xx} = -0.00005$). The macroscopic stress $\boldsymbol{\sigma}_E$ of the balanced state is then calculated and subsequently, the system is relaxed to its previous state ($\Delta\varepsilon_{xx} = +0.00005$). Finally, the stress difference $\Delta\sigma_{ij}$ of $\boldsymbol{\sigma}_E$ and the current stress $\boldsymbol{\sigma}_t$ is determined and applied in Eq. 6.36 to calculate the relevant elements of the elasticity tensor $\mathbb{C}_{ijkl}$, i.e. C_{13}, C_{23} and C_{33}.

As previously shown in section 6.3.1, the granular composite material is isotropic for the intercalation process. For isotropic material, the elasticity tensor $\mathbb{C}_{ijkl}$ can be reduced to [170]

$$\begin{bmatrix} C_{11} & C_{12} & C_{12} & & & & \\ C_{12} & C_{11} & C_{12} & & & & \\ C_{12} & C_{12} & C_{11} & & & & \\ & & & C_{44} & & & \\ & & & & C_{44} & & \\ & & & & & C_{44} & \\ , & & & & & & \end{bmatrix} \tag{6.37}$$

with only 3 independent components. Based on that, the two independent material properties E_t and ν_t [170] at loading time step t can be calculated according to

$$\begin{aligned} C_{11} &= \frac{E_t(1-\nu_t)}{(1+\nu_t)(1-2\nu_t)} \\ C_{12} &= \frac{E_t\nu_t}{(1+\nu_t)(1-2\nu_t)} \end{aligned} \tag{6.38}$$

as

$$\begin{aligned} \nu_t &= \frac{C_{12}}{C_{11}+C_{12}} \\ E_t &= (C_{11}+2C_{12})(C_{11}-C_{12}) \\ &. \end{aligned} \tag{6.39}$$

Unconstrained deformation of the electrode With the calculated properties of the electrode material, the deformation of the volume element in x-direction can be calculated according to Hook's law

$$\Delta\varepsilon_{xx}^{m,re} = \frac{\sigma_{xx}^{t} - \sigma_{xx}^{t-1}}{E_t}. \tag{6.40}$$

with σ_{xx}^{t} as the current macroscopic stress and σ_{xx}^{t-1} the macroscopic stress at the end of the previous loading step. Due to the non-linearity of the stress-strain relationship in granular materials and the stress dependence of its material properties, the boundary condition σ_{xx}=0 is most likely not met exactly. Especially overestimation of $\Delta\varepsilon_{xx}^{m,re}$ can lead to tensile stress in the microstructure, and the simulations can become numerically unstable. To suppress this instability, the calculated strain is not applied completely. Rather, $\Delta\varepsilon_{xx}$ is multiplied by a factor b, slightly smaller than 1. That factor has to be adjusted based on the configuration to ensure numerical stability. In here b is 0.95.

Results for unconstrained volume elements As in the previous section, the intercalation process is simulated for monosized assemblies of LFP particles. Here, the volume element is constrained by the current collector in y- and z direction and unconstrained in x-direction.

As shown in Fig. 6.43a, the target stress of $\sigma_{xx} = 0$ is not met exactly, stress around 1 MPa are obtained in x-direction. The deviation from $\sigma_{xx} = 0$ has two causes: (i) as explained previously, the applied strain is reduced slightly from the calculated value to maintain numerical stability; and (ii) due to the non-linearity of the system, the system's response is only approximated with the applied linear stress-strain relationship. In y-and z-direction of the unconstrained assembly the

stress is reduced enormously: It drops from values around 90 MPa, obtained for the intercalation process with $\varepsilon_{xx} = 0$, to values around 4 MPa. Even though the stress σ_{xx} does not comply exactly with the boundary condition of $\sigma_{xx} = 0$, the results provide a good approximation of an unconstrained structure.

The almost stress-free boundary in x-direction leads to significant strain in this direction, as can be seen in Fig. 6.43b. The deformation of the current collector (y- and z-direction) is reduced

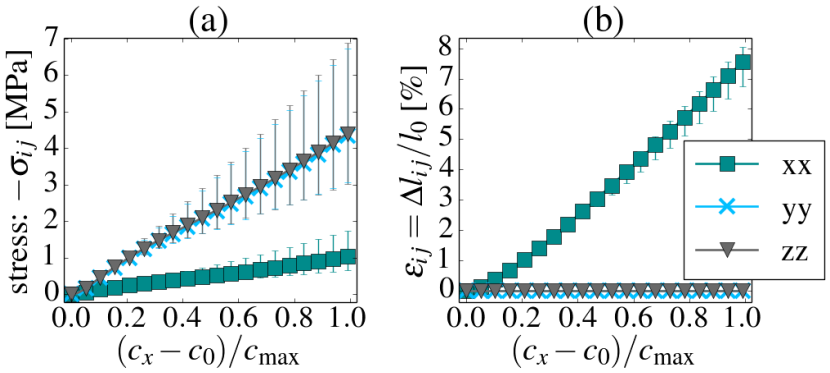

Figure 6.43.: (a) Macroscopic stress and (b) strain due to Li-intercalation within the electrode for a Young's Modulus of 125 GPa

in comparison to the previous results (Fig. 6.41a) due to the low macroscopic stress within the assemblies. Further, the previously small deviation between the results of three different assemblies increases significantly, especially for the stress. Probably, the large expansion of the volume element, corresponding to larger particle movement, affects this: the more displacement the particles experience, the more likely it is, that a deviation between two initially similar assemblies of randomly distributed particles occurs. This effect is most likely amplified by the influence of the present state on the stress dependent effective material properties. Determined for the present configuration, they are used to calculate the future expansion, which then will vary due to previous variations in stress.

Examining the stress-strain relationship for the unconstrained simulations, illustrated in Fig. 6.44, shows different behavior for the different directions: For the directions constrained by the current collector (Fig. 6.44b), a linear relationship is found in the whole range, as in the previously simulated situation. The deformation in x-direction shows, after an initially non-linear range, a linear relationship for $\varepsilon_{xx} > 1\%$. It should be noted, that the gradient of the stress-strain curves—equivalent to the Young's Modulus in the linear range—is much smaller in x-direction, reflecting on the the softer material behavior in this direction.

This is additionally illustrated in Fig. 6.45; for comparison results for a softer bulk material are

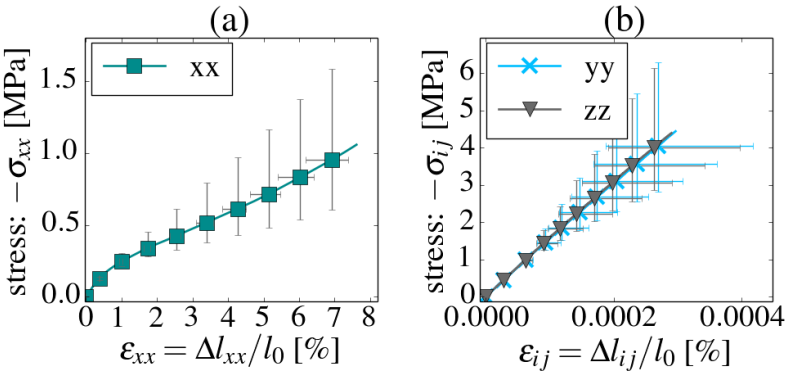

Figure 6.44.: Macroscopic stress vs strain during Li intercalation for (a) the unconstrained direction and (b) directions constrained by the current collector for a Young's Modulus of 125 GPa

given as well: In Fig. 6.45a, the stiffness of the system in y-direction is given for a bulk Young's Modulus of 125 GPa as well as of 10 GPa. Those results show little difference to the stiffness

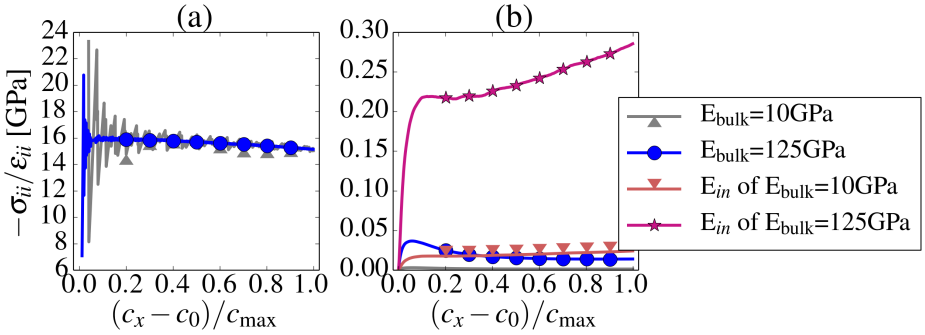

Figure 6.45.: Stiffness $\sigma_{ii}/\varepsilon_{ii}$ during the intercalation process for different material properties (a) in y-direction and (b) in x-direction, plus the intrinsically calculated Young's Modulus E_{in}

of systems constrained in x-direction ($\varepsilon_{xx} = 0$), as shown in Fig. 6.42. As expected from the stress-strain relationship, the free deformation in x-direction leads to a much softer material response in x-direction, which is shown in Fig. 6.45b. Here, we distinguish between the extrinsic stiffness (or secant modulus), calculated as $\sigma_{xx}/\varepsilon_{xx}$, and an intrinsic stiffness E_{in}. The intrinsic stiffness denotes in this work the stiffness E_t determined within the DEM simulation for the each intercalation step by the additional loading loop as the current stiffness of the assembly. Both, the intrinsic and the extrinsic stiffness, are comparatively low. For the extrinsic stiffness, the influence of the bulk material is negligible; the intrinsic stiffness, on the other hand, is affected by the material properties.

6.4.4. Uniform intercalation

A further assumption with regard to loading conditions is that the intercalation process is uniform within the volume element. Harris et al. [171], however, showed experimentally that during cycling an intercalation front passes through the electrode, starting with swelling particles near

the separator. This effect is especially pronounced in thick electrodes. Nevertheless, as long as the simulated volume element is small compared to the dimensions of the electrode[10], it can be considered as representative volume element (RVE), with equal spacial conditions within. As the volume elements studied in this work are, in particular with regard to thick electrodes, small in comparison to the electrode dimensions, it is valid to consider the intercalation process as uniform. Based on the performed simulations, the stress distribution within the continuous electrode, as an example, can be represented by the macroscopic stresses of the RVE at different states of Li concentration. If, in contrast, a bigger volume element—corresponding to the whole electrode—would be modeled, the intercalation gradient should be considered.

Furthermore, all active material particles are taking part in the intercalation process. This requires that they all are sufficiently connected to the current collector, assuming a percolating CB network. As was shown in section 6.3.3, this is not valid for insufficiently calendered electrode structures. The calculations are only valid, when the AM particles are fully connected. Based on the assessment made in section 6.3.3, I decided to focus on sufficiently pre-calendered electrodes; and for those, the simulations are considered as sufficiently accurate. Nevertheless, the influence of non-connected particles on the microstructure and the mechanical response of the system during the intercalation process would be interesting to study in future work.

6.4.5. Particle fracture

The microstructure of electrodes is additionally influenced by particle fracture, as monitored experimentally in e.g. [156]. It is widely assumed that the particle fracture is caused by internal particle stress due to concentration gradients and/or phase segregation during intercalation (e.g. [172, 152]). As to date, however, no general description for particle cracking in LIB exists, it is not considered in the scope of this work. Nevertheless, DEM allows for the consideration of particle fracture [139]; and thus, it will be a useful tool to study the influence of particle failure on the microstructure once a failure criterion is defined.

6.4.6. Binder

With regard to particle interactions, the contacts are so far only described in form of Hertz-Mindlin contacts (section 6.1), assuming elastic material behavior. As most cathode materials are brittle and do not deform plastically, this is a valid assumption for active material in direct contact. The binder phase is neglected so far; however, it is employed to maintain a stable microstructure and preserve the connectivity of the solid components. Furthermore, the stress absorbing effect of the soft binder material was discussed in [26, 159]. Therefore, it seems probable that the binder influences the mechanics of the system; this influence will be examined here.

The binding material used in LIB electrodes is a polymer, which has to possess flexibility, insolubility in the electrolyte, compactness, chemical and electrochemical stability, and easy application in the production process—besides the actual binding [11]. This leads to the use of polyvinylidenefluoride (PVDF) and styrene-butadiene copolymer (SBR) in the anode, and in the cathode mainly PVDF is used. In the operational temperature range of LIB, PVDF shows visco-elastic behavior—this means that the material response to stress contains a spontaneous elastic component as well as an irreversible, time- and rate-dependent viscous component. Hence,

[10] and, of course, still large enough to represent the electrode structure statistically

in order to study the effect of the binder phase on the microstructure, an additional visco-elastic force law has to be implemented in DEM to consider the stress absorbing effect of the binding phase in LIB.

Rheological models for visco-elasticity

In DEM, the force-displacement relation of two contacting particle are often displayed in form of rheological models. To simulate visco-elastic behavior, the models comprise massless Hookean springs for the elastic part and Newtonian dashpots for the viscous components. The stress-strain behavior of a spring is given as

$$\sigma = E\varepsilon \tag{6.41}$$

while the stress of the dashpot element depends the time derivative of the strain $\dot{\varepsilon}$:

$$\sigma = \eta\dot{\varepsilon} \tag{6.42}$$

with η as viscosity. The most basic models are known as Maxwell model, depicted in Fig. 6.46a, and Kelvin model (Fig. 6.46b) [114]. The Maxwell model reacts to a continuously applied strain

Figure 6.46.: Rheological model of (a) Maxwell's contact law and (b) Kelvin's contact law

with stress-relaxation (equilibrium module $E_{eq} = 0$); and the Kelvin model reproduces creep behavior (spontaneous module $E_{spon} \to \infty$): the application of constant stress leads to an increase of strain with time [173]. Both creep and stress-relaxation are, however, necessary to describe the time-dependent material behavior for most polymers, including PVDF. In order to consider both effects in a material model, the Maxwell model and the Kelvin model are combined in series as shown in Fig. 6.47. This formulation is known as Burgers law, and it allows for the consideration of the relevant visco-elastic material characteristics. For the derivation of the constitutive Burgers

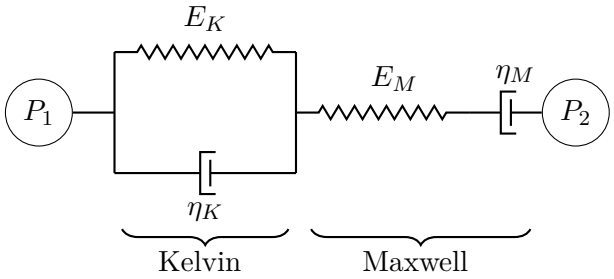

Figure 6.47.: Rheological model of Burgers contact law

model, the deformation is divided in its three parts: the displacement in the Kelvin section (ε_K), the deformation of the Maxwell spring, and the Maxwell dashpot ($\varepsilon_{\mathrm{MS}}$ and $\varepsilon_{\mathrm{MD}}$)

$$\varepsilon = \varepsilon_K + \varepsilon_{\mathrm{MS}} + \varepsilon_{\mathrm{MD}}. \tag{6.43}$$

Due to the series connection, the stress is equal in the Kelvin and the Maxwell section. The stress-strain relationship of the Kelvin section is

$$\sigma = E_K \varepsilon_K + \eta_K \dot{\varepsilon}_K, \tag{6.44}$$

and of the Maxwell section it is:

$$\sigma = E_M \varepsilon_{\mathrm{MS}} = \eta_M \dot{\varepsilon}_{\mathrm{MD}}. \tag{6.45}$$

Considering first and second derivatives of the equations leads to

$$\ddot{\sigma} \frac{\eta_K \eta_M}{E_K E_M} + \dot{\sigma}\left(\frac{\eta_M + \eta_K}{E_K} + \frac{\eta_M}{E_M}\right) + \sigma = \ddot{\varepsilon} \frac{\eta_M \eta_K}{E_K} + \eta_M \dot{\varepsilon}. \tag{6.46}$$

As shown in [174], the experimentally derived, time-dependent material behavior of PVDF can be fitted accurately with Burgers law when temperature dependent parameters are considered. The parameters relevant in the temperature range of LIB are given in Table 6.8, and were used in the calculations in here. Further, for the active material, the properties of LFP were used (Table 6.1).

E_M [MPa]	E_K [MPa]	η_M [10^{12}Pas]	η_K [10^{12}Pas]
1200	280	1	28

Table 6.8.: Fit parameter found for Burgers contact law [174]

Core-shell model

To implement the binder phase in the discrete element model, we chose a core-shell approach as model representation. As sketched in Fig. 6.48, the purely elastic active material is surrounded by a visco-elastic shell, representing the binder phase. The shell is only implemented as model to guarantee a buffering effect for each contact, it should not be considered as a closed shell. Furthermore, in this approach, the CB is assumed to be dissolved in the polymer phase, and thus, it was not included as a separate phase in the following section.

Based on the initial RCP configuration, with the particles just in contact with almost no overlap, two possible layouts were considered, depicted in Fig. 6.48: the shell of L_{shell} can be added at the outside of the particle, as sketched in Fig. 6.48a, or, as in Fig. 6.48b, it can be added half inside and half outside of the initial particle surface. The first configuration, denoted as configuration A, has the Hertz contact of the active material and the visco-elastic contact of the binding material in parallel.The second possibility, denoted as configuration B, reduces the initial active material radius in order to generate a gap between the active material particles. This gap, then, is filled with binder phase, as shown in Fig. 6.48b. For this approach, the initial particle radii is reduced by half of the shell thickness, while the other half of the shell thickness is added on top of it in order to create an initial overlap. In both cases, the contact radius $r_{\mathrm{c,shell}}$ depends on the overlap and affects the visco-elastic contact forces. Further, the shell thickness L_{shell} can be used as a measure of the volume fraction of the polymer.

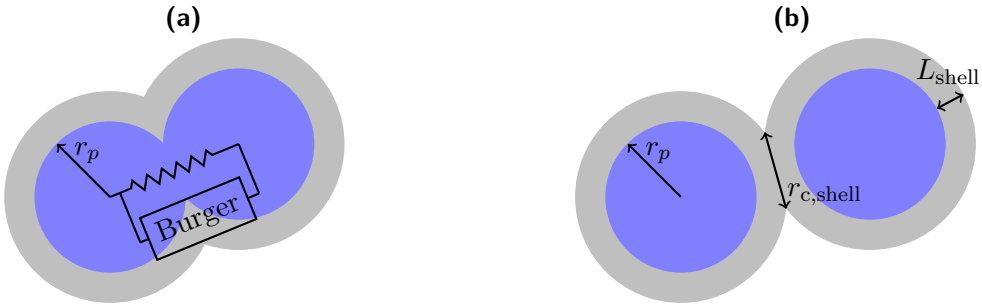

Figure 6.48.: Core-shell model of particles in contact with (a) Burgers model and Hertz contact in parallel and (b) visco-elastic material only. Dark spheres represent the active material, lighter shell the polymer phase, assuming CB to be distributed within the polymer matrix

Burgers model as force law

In discrete element modeling the contact behavior is given in terms of force and displacement; thus, the Burgers model (Eq. 6.46) must be reformulated in those terms for its implementation in the existing code. Speaking generally, the force is related to the stress by the relevant area A, which allows to rewrite the stress-strain relationship for Hookean springs (Eq. 6.41) as

$$f = \frac{EA\Delta l}{l_0} \tag{6.47}$$

with l_0 as the initial length and $\Delta l = l - l_0$. The force-displacement relationship of the dashpot element can be given as

$$f = \eta A \frac{\Delta l}{\Delta t l_0}. \tag{6.48}$$

Those terms are adapted for the core-shell approach of two overlapping binder particles by considering $A = a_c = \pi r_{\text{c,shell}}^2$ as contact area, $l_0 = L_{\text{shell,P1}} + L_{\text{shell,P2}}$ as the uncompressed shell thickness, and $\Delta l = \delta$ as the overlap. To rewrite Eq. 6.46 as force-displacement relationship, the stress terms are replaced by

$$\sigma = \frac{f}{A} = \frac{f_N}{a_c} \tag{6.49}$$

and the strain terms by

$$\varepsilon = \frac{\Delta l}{l_0} = \frac{\delta}{L_{\text{shell,P1}} + L_{\text{shell,P2}}}. \tag{6.50}$$

The time derivatives in Eq. 6.46 are approximated by

$$\dot{()} = \frac{()^{t+1} - ()^t}{\Delta t} \tag{6.51}$$

with () replaced by the contact force or the change in overlap. In accordance with [175], the normal force f_N^{t+1} can then be calculated as

$$f_N^{t+1} = f_N^t + \Delta t \frac{E_M a_c}{l_0} (\dot{\delta}_{\text{total}}^{t+1} + \frac{E_K}{\eta_K} \delta_K^{t+1} - f_N^t \frac{\eta_M + \eta_K}{\eta_M * \eta_K}). \tag{6.52}$$

The total overlap of the current configuration is given as $\delta_{\text{total}}^{t+1}$, while δ_K^{t+1} gives the part of the displacement, which is in the Kelvin section:

$$\delta_K^{t+1} = \delta_K^t + \Delta t * \frac{1}{\eta_K a_c / l_0} (f_N^t - \delta_K^t \frac{E_K a_c}{l_0}). \tag{6.53}$$

The rate-dependence of the visco-elastic force law manifests in the dependence of f_N and δ_K on the loading history. For newly build contacts ($t = 0$) it is assumed, that the initial overlap only effects the spontaneous deformation, taking place in the elastic part of the Maxwell section. For $t = 0$, this leads to the following initial conditions for the Kelvin section of the overlap:

$$\delta_K^{t=0} = 0 \tag{6.54}$$

and for the contact force f_N

$$f_N^{t=0} = \frac{E_M a_c}{l_0} \delta_{\text{total}}^{t=0}, \tag{6.55}$$

with $\delta_{\text{total}}^{t=0}$ as the total initial overlap. For the sake of simplicity, the visco-elastic tangential force f_T^{t+1} is calculated in analogy to the normal force in accordance with Liu et al. [176], as sketched in Fig. 6.49.

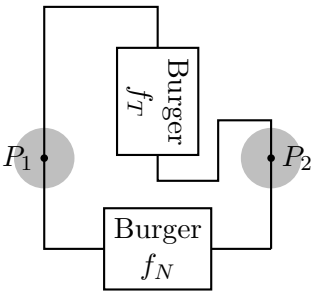

Figure 6.49.: Combination of normal and tangential force in core-shell model

To demonstrate the rate-dependence of the force law with a basic example, the force-response of two pure PVDF particles in contact is calculated for increasing overlap. Approaching particle centers with different loading rates $\dot{\varepsilon} = \frac{\Delta\delta}{\Delta t}$ allow to demonstrate the rate-dependence of the force, as can be seen in Fig. 6.50: For low loading rates, the force response can be described

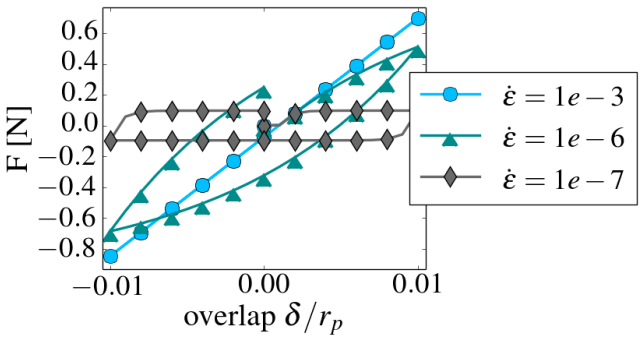

Figure 6.50.: Force calculated for two binder particles loaded with different rates

by a hysteresis with decreasing maximum force for decreasing loading rate. With increasing

loading rate, on the other hand, the material response approaches almost linear behavior, as it is dominated by the elastic part of the Burgers model.

In order to consider that rate-dependence of the visco-elastic material behavior, we can no longer use the quasi-static approach in the discrete element modeling. As explained in section 6.1, in a quasi-static approach, the particle positions are rearranged in an iterative loop after each loading step until the kinetic energy is minimized. For a time-dependent approach, such a loop is not practical, as the loading history is considered to determine the viscous part of the Burgers model. In order to represent the rate-dependence of the forces, a dynamic approach was used for the following calculations. In this, after each loading step only one step of rearrangement of the particles is performed. The omission of the iteration steps of the quasi-static approach leads most likely to configurations further away from equilibrium, unless very small time steps are chosen. Thus, a higher macroscopic stress within the assembly is likely.

Micromechanical simulations

In the following section, possible configurations, volume fractions, and loading rates are studied in order to get a basic understanding of the newly introduced influence parameters. For comparability to previous calculations, we chose monosized assemblies with a PF of around 60%. As the CB phase is assumed to be dissolved in the binder phase, its explicit consideration, as in the binary assemblies previously used, is no longer necessary. For the material properties of the active material, LFP was chosen (see Table 6.1). Uni-axial compression in x-direction ($\varepsilon_{xx} = -2.5\%$ in total) is applied in combination with constrained boundaries in the perpendicular directions ($\varepsilon_{yy} = \varepsilon_{zz} = 0$).

Influence of the configuration To study the viscous effect of the configurations in particular, a low strain rate of $\dot{\varepsilon}_{xx} = 0.0001$ was chosen. This correlates to a total loading time of 250 seconds for the calendering process. Obviously, this is very slow; as, however, for faster loading rates spontaneous response of the Burgers law dominates the material behavior ($f \sim E_M \delta$), we apply slow rates to study the impact of viscosity in proximity to the equilibrium response. A shell thickness L_{shell} of 10% of the initial particle radii (0.1 r_p) is applied; this corresponds to a total volume fraction of 0.15 for the assumption of a closed shell, when neglecting the overlaps.

To examine the influence of the different configurations A and B, the directional stress response for the uni-axial compression is shown in Fig. 6.51. Comparison of the results for configuration A (Fig. 6.51a) with dynamic calculations without binder phase showed that by considering the binder in parallel to Hertz contacts, the active material clearly dominates the stress responds—with only marginal impact of the binder phase. Further, the difference to the stress in previous results in section 6.2.1, (Fig. 6.3b) shows the deviation of quasi-static and dynamic calculations: the dynamic approach induces higher stresses in loading direction, while the response in directions perpendicular to the loading directions are similar. The quasi-static stress response can be considered as the lower limit of the stress for the considered model. In contrast to the macroscopic stress found for configuration A, configuration B reduces the stress enormously, as illustrated in Fig. 6.51b. This clearly demonstrates the stress absorbing effect of binder in all contacts.

The 3D reconstruction of a cathode by Hutzenlaub et al. [63], which resolved active material and binder phase separately, suggests, however, that both type A and type B contacts can be found in the electrode structure. Even though this information exists only for one example, it is

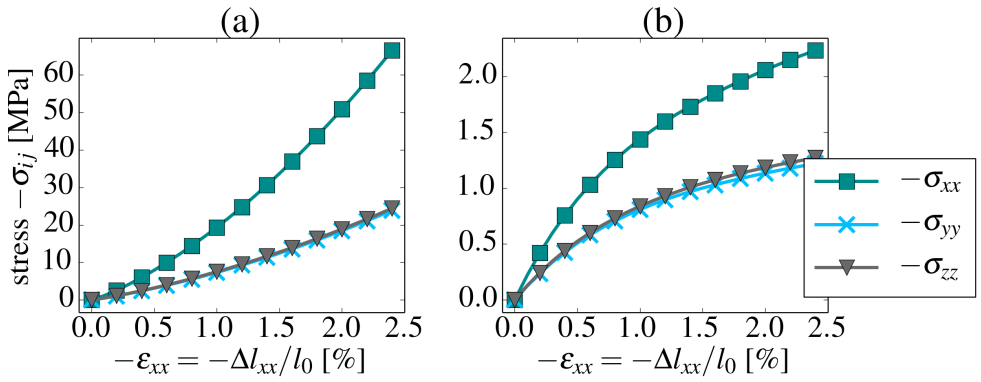

Figure 6.51.: Macroscopic stress response for structures with a polymer shell thickness of 10% of the particle radii for (a) configuration A and (b) configuration B; simulated with a strain-rate $-\dot{\varepsilon} = 0.0001$

unlikely that all particles of an electrode are exclusively of type A or of type B due to the random distribution of particles and binder phase during electrode manufacturing. Further, an electrode with solely type A would suppress the stress absorbing effect of the binder phase completely; and thus, it would lead large stress. Type B particles, on the other hand, would hinder the ion transport within in the cell; and thus, they would result in insufficient cell performance. Consequently, we assume that both, type A and type B contacts, exist in a realistic electrode structure. As only little information on the binder phase distribution exists, exemplary percentage portions of type A and B particles were considered in the next simulations.

The effect on the hydrostatic stress is illustrated in Fig. 6.52. As the difference between low and high percentage of type A contacts is significant, the simulations with low percentage of type A are replotted in Fig. 6.52b for better visibility. Already for 10% of type B contacts, the binder phase reduces the stress by 40% and shows its stress absorbing influence. Further, for 50% and higher, the stress is drastically reduced to values of below 4 MPa.

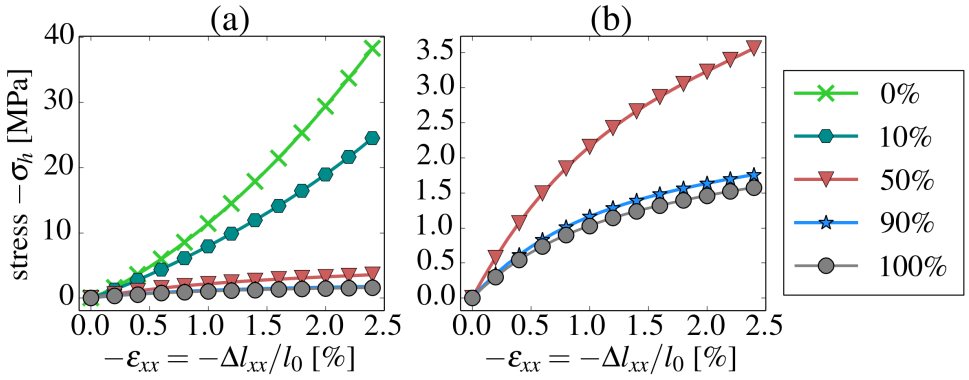

Figure 6.52.: Hydrostatic stress response for structures with a polymer shell thickness of 10% and $-\dot{\varepsilon} = 0.0001$ with different percentage portions of configuration A and B in (a) given as percentage of type B contacts. For better visibility the low stress values are additionally plotted in (b)

As the effect of parameter variation is especially pronounced for configurations of 100% type B particles, those were chosen to study the influence of further parameter. Of interest are the shell thickness L_{shell}, reflecting on the amount of binder phase, and the influence of loading rate.

Influence of the shell thickness Assuming a closed shell of constant thickness around the active material core, the shell thickness can be used to estimate the solid volume fraction ϕ_{PVDF} of the binder phase as

$$\phi_{\text{PVDF}} = \frac{r_{\text{out}}^3 - r_{in}^3}{r_{\text{out}}^3} \tag{6.56}$$

with r_{out} as the outer radius of the shell and r_{in} the inner radius. This neglects the overlap of the polymer shells, and thus, it overestimates the volume fraction to some extent. Taking the porosity into account, the total volume fraction can be determined as well. The values are given in Table 6.9. In Fig. 6.53, the impact of different shell thicknesses on the macroscopic stress is shown

L_{shell}	ϕ_{PVDF}	$\phi_{\text{PVDF}}(1-\epsilon)$
0.1	0.259	0.156
0.01	0.030	0.018
0.005	0.015	0.009

Table 6.9.: Volume fractions of the binder phase calculated from the shell thickness L_{shell} under the assumption of a closed shell around the core

for a strain rate of $\dot{\varepsilon} = 0.0001$. Decreasing volume fractions of PVDF reduce the macroscopic

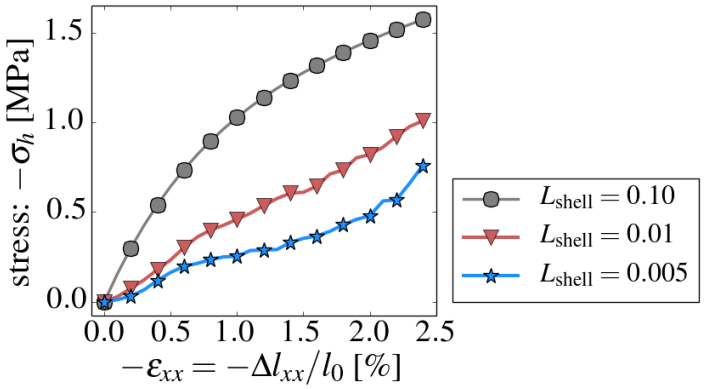

Figure 6.53.: Hydrostatic stress response for structures for different shell thicknesses and loading rate $\dot{\varepsilon}$=0.0001

stress, and the thickest shell induces the highest stress. As half of the shell thickness is applied outside the initial radii, which are just in contact at the beginning of the calculation, the overlap and the contact area generated by a thicker shell is obviously larger than by a thin shell. This, is turn, results in larger contact forces and allows to explain the larger macroscopic stress. It was expected that—at least for smaller volume fractions—the polymer is pressed out of the gap during the loading process at some point. Thereby, the active material particles come in direct contact, which would induce higher stress. This most likely causes the increase of stress at the end of the loading process for the smallest volume fraction of PVDF; with further loading this

effect probably becomes more pronounced. For the parameters considered here, however, the stress remains smaller than the values found for higher volume fractions of PVDF.

Influence of the loading rate Next, the influence on loading rate is studied. As already demonstrated in Fig. 6.50 for two approaching particles, the mechanical response depends significantly on the loading rate: For fast loading, the elastic part of the Burgers model dominates the behavior; for slow loading rates, the viscous parts affects the results. This behavior was also determined for the assemblies considered here, as illustrated in Fig. 6.54. The fastest loading rate in this corresponds to a calendering time of 5 seconds and the slowest to 500 seconds. In experimental cell production, the loading times are around 1 second for simple compression and for calendering, the loading velocity is around 1 m/min. The subsequent relaxation process is not considered in the simulations [177].

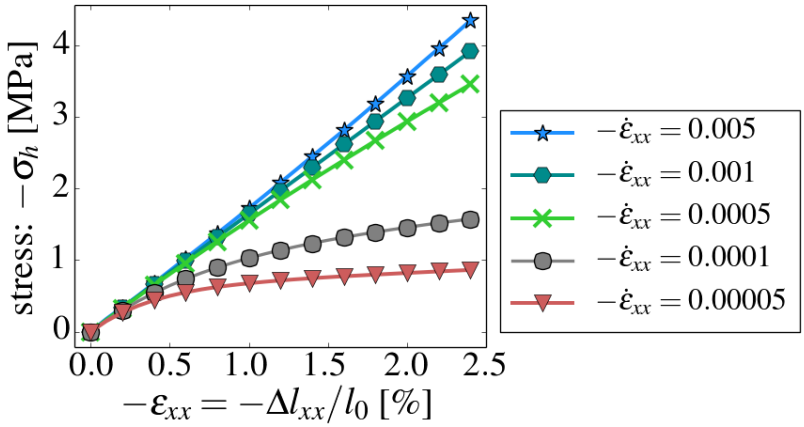

Figure 6.54.: Hydrostatic stress response obtained for different loading rates for structures with L_{shell}=0.1

For loading rates larger than $\dot{\varepsilon}$=0.0001, the stress-strain response is linear. This linearity is in contrast to non-linear behavior found for Hertz-Mindlin contacts—this is due to the linear spring within the Burgers model. The slope of the linear relationship increases with increasing loading rates. For $\dot{\varepsilon}$=0.0001 and smaller, the stress response is influenced by the viscous part of the Burgers law; this reduces the stress further for lower loading rates.

Calendering, however, is a rather fast performed loading process—so, the stress-response is in the elastic regime of the Burgers model; and the stress reduction in comparison to the simulations in section 6.2 is probably due to the softer material. Due to the subsequent relaxation process, the internal stress is in general further reduced. The mechanical stress building up during the intercalation process is of more relevance, as it is assumed to influence the mechanical degradation. Here, it is interesting to determine the range of loading rate, for which spontaneous material response of the Burgers law starts to dominate the material behavior ($f \sim E_M \delta$), as this leads to increasing stress in the electrode structure. For the intercalation process, the loading rate can be related to the charge rate or the total time required for charging in accordance with the C-rates. In Fig. 6.55, the total time required for a complete intercalation process is given, as those values are more meaningful than loading rates. Relatively high charging rates are applied in order to determine the threshold from viscous to the spontaneous elastic material response. The

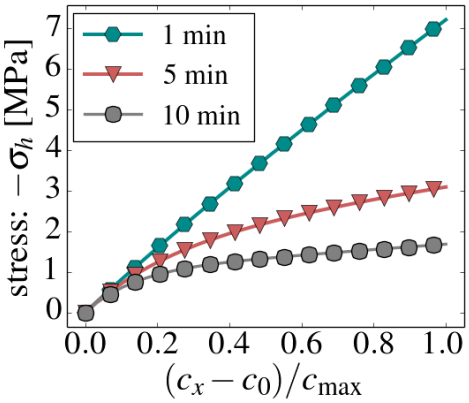

Figure 6.55.: Hydrostatic stress response during intercalation for structures with shell thickness L_{shell}=0.1 for different intercalation rates, given in form of the total loading time

highest rate—corresponding to complete intercalation in 1 min or C= 1/60—clearly shows a linear response; in contrast, the two slower rates (with 5 min corresponding to C= 1/12 and 10 min to C= 1/6) show the impact of the viscous phase on the response. Hence, it is valid to assume that for usually applied charging rates (C $\geq$ 1/20), the material response is in the visco-elastic range of the PVDF.

6.4.7. Summary

In this final section, the impact of the simplifications of the initial modeling approach were evaluated.

With regard to the initial microstructure, the particle size distribution was found to be negligible as the impact on the stress response was marginally.

Regarding boundary conditions, two scenarios were implemented: (i) deformation of the volume element was applied in accordance with the deformation of the current collector, and (ii) additionally in direction perpendicular to the current collector, the volume element was unconstrained. The first approach reduces the stress of the intercalation process by around 10%. The second approach, on the other hand, allows to determine the expansion, which would occur in an free-standing electrode: 8% deformation is correlated to a nearly stress-free state.

Further, the binder phase is considered to have a significant influence on the stress-response on the material. To investigate this, the Burgers model was implemented in a dynamic DEM approach to reflect on the visco-elastic behavior of the PVDF. Based on that, different contact configuration, volume fractions of binder, and loading rates were studied. The exact distribution of the binder phase in electrodes is to date not known; however, it is of large relevance for the stress response: For the binder phase in parallel to the Hertz contact of AM particles (Fig. 6.48a), it only shows marginal influence on the stress-response; and the stress obtained was similar to the results without its consideration. For the binder phase in a gap between the AM particles (Fig. 6.48b), a large stress reduction was observed. Even if only 10% of the contacts are filled with polymer layer in the gap between active material particles, the stress is reduced by around 35%. Besides the configuration, the loading rate is of significance: As for high loading rates, the

elastic part of the Burgers law dominates the stress response, the loading has to be slow enough to benefit most of the stress absorbing effect of the visco-elastic material. The dominance of the elastic part is relevant for calendering or very fast charging rate. For usually applied charging- or discharging-rates, on the other hand, the impact of the viscous material response was shown.

7. Conclusion

The objective of this work was to study the electrode microstructure and its influence on parameters relevant for the performance of solid oxide fuel cells (SOFCs) and lithium ion batteries (LIBs), as it is a determining factor to improve the actual cell efficiency. For performance optimization, porous electrode structures, formed by random mixtures of ion conducting particles and electron conducting particles, are already applied widely; in this way, the transport path lengths are reduced and the active surface areas are increased.

Reviewing the experimental findings, percolation of both phases in SOFC and of the electron conducting additives in LIB was determined as an important parameter for cell performance. Additionally, the active surface area and the effective conductivity—in SOFC in particular the ion conductivity—are significant for electrode efficiency. Variation in composition and morphology, however, has contradicting impact on those parameters: Improving effective conductivity usually reduces the active area and vice versa. Thus, a trade-off between high effective conductivity and increased active surface area is beneficial for high cell performance. Beyond this general recommendation, there remains little consensus on what constitutes a good microstructure.

To provide a more complete picture of the connection between microstructure and cell performance, reduced one-dimensional models are commonly used to study the electrochemical cell behavior . In those models, the heterogeneous electrode structure is replaced with a hypothetical material which yields the same response for the same conditions. The equivalent properties of this hypothetical material are referred to as effective properties [64]. As the influence of microstructure is condensed to the effective cell properties used as input data, a careful approximation of those parameters is essential. To find an adequate approach for the approximation, several models were reviewed and compared. As the effective media approach and the analytic calculation of the percolation probability based on the concept of coordination numbers, neglect important microstructural factors, Monte-Carlo simulations were chosen in this work. In those, the microstructure is represented by a three-dimensional assembly of randomly distributed, spherical particles, which are either ion or electron conducting. Based on this, different methods were developed and implemented to simulate the fabrication process and the relevant effective properties for those three-dimensional structures.

For the generation of the microstructures, a random close packing (RCP) algorithm was used, leading to a densely packed structure with very few contacting particles. In contrast to the widely used drop-and-roll algorithm, the overall coordination number is not predefined. To obtain a more realistic electrode structure, further densification steps were performed in accordance with the fabrication process: The sintering process during the manufacturing of SOFC electrodes is mimicked by increasing the particle radii without rearranging the particle centers. The calendering during LIB fabrication is simulated with a discrete element approach, which allows for the consideration of mechanical interaction of the particles and their rearrangement as consequence. Further, the intercalation process during cycling of LIB electrodes was modeled with discrete element modeling (DEM) as well.

To determine the percolation probabilities of the structures, the Hoshen-Kopelman algorithm (HK) was adapted for the conditions of the electrode microstructures and implemented in the scope of this work. Subsequently, a resistor-network approach was implemented in order to determine the effective conductivity of the electrode structures based on the information on connectivity obtained with the HK algorithm. For the resistor-network approach, different fit-laws were developed in here to calculate the resistance between two contacting particles under consideration of the different contact types resulting from the different fabrication processes.

To study the impact of electrode composition in SOFCs, a vast amount of numerically generated microstructures was generated, considering a wide range of volume fractions and particle size ratios varying from 1 to 10. Especially for the investigation of SOFC microstructures the analytic percolation approach—based on the concept of coordination number—is widely used. Therefore, the results obtained for the numerically generated microstructures were compared to the assumptions made in the analytic method. This comparison enabled us to demonstrate how the geometric characteristics of the numerically generated microstructure deviate significantly from the assumptions made in the analytic approaches for PF and coordination numbers. Additionally, the numerically determined percolation probabilities differ significantly from the analytic findings: the percolating range was larger in the numerical examination, especially for large size ratios. Further, the findings of that section led to reasonable doubt regarding the correlation between the critical coordination number Z_c and the percolation threshold. The results indicate that Z_c is not a constant value, it rather seems to be influenced by size ratio or the ratio of box length to particle radius.

As the effective conductivity $\kappa_{\mathrm{eff,YSZ}}$ and the active three-phase boundary (TPB) were experimentally identified to be mainly responsible for cell performance, those values were investigated next. The numeric and the analytic results deviate significantly for those parameters as well: the numerically determined effective conductivities were in general lower than the values predicted by the analytic approaches. Conversely, the active TPB length found numerically was larger than the one found for the analytic approach. Nevertheless, the tendencies of an increase of the effective conductivity with volume fraction and a decrease of the active area (TPB) with size ratio were predicted correctly with the analytic approach. Both effective parameters improve—independent of size ratio—with increasing densification, which is a measure for the degree of sintering. But, due to the necessity of a connected pore space, the densification is restricted. Assuming a minimum pore space of 15% as required, the monosized assemblies offer more potential for densification, as their initial PF is lower than the one of binary sized assemblies. A study on the impact of the size ratio with assemblies densified to the maximum allowable packing factor might offer further insight in the influence of densification. Further, compositions with a large size ratio and large YSZ particles, in combination with small volume fractions of the electron conducting phase, are favorable in order to achieve high ionic conductivity of the structure. Conversely, the largest extent of active TPB was found for monosized assemblies with a mixture of 50:50% volume fraction. Additionally, a large size ratio reduces the extent of active TPB significantly. In order to assess those contradicting recommendations, an adapted Tanner-Fung-Virkar (TFV) model was implemented, which enables us to estimate the combined effect of those two parameters on the effective cell resistance. The positive influence of densification on the cell efficiency—which is inversely proportional to the overall cell resistance—is pointed out by those results as well. Additionally, the negative influence of size ratio on the cell resistance seems less pronounced, as assumed based on the results for active TPB. It appears that the choice of volume fractions appropriate for an arbitrary size ratio is much more relevant. Considering an optimized mixture for each size ratio, monosized assemblies with a volume fraction of the electron conducting phase

slightly above 30% are the most promising. Clearly, the TFV model is a very simplified approach, and thus, the revaluation of these findings with more advanced cell level models is recommendable. Additionally, the implementation of numerically determined effective transport properties in advanced cell level models implies the possibility to obtain enhanced insight in the absolute effect of morphological variations. The studies performed so far based on the analytically determined effective properties might be influenced by the overestimation of the effective conductivity and the underestimation of the active TPB.

The LIB electrode structures were approximated as a mixture of active material (AM) and carbon black (CB) with a size ratio of 10. The densification of the microstructures was performed via DEM, which is an appropriate tool to predict microstructural rearrangement due to mechanical loading. A comparison of the macroscopic stress during intercalation process to values obtained from substrate-curvature experiments showed a good agreement. During calendering as well as during intercalation, the stress-load response is non-linear. For a combined calendering-intercalation process, this results in a higher stress increase during intercalation for larger applied preloads. Thus, a low preload is beneficial in terms of stress development during intercalation. Further, a dependence of the macroscopic stress on the material properties of active material can be seen. Varying PFs and volume fractions of CB show little influence on the stress-load relationship. Their effect on macroscopic stress increases slightly for the intercalation process, as a variation in composition is correlated to a varying amount of AM and thus, a varying amount of overall volume change.

Studying the percolation probability of the densified structures as function of the applied load demonstrated clearly the necessity of an adequate calendering load: only insufficient connectivity is found for uncalendered cells, this results most likely in unreliable cell performance. For the here considered cases, a preload correlated to 60% of percolation seems to ensure constant connectivity during the intercalation process. Regardless of the preload, a sufficient amount of CB (around 8.7% of total volume fraction) is required. Besides the electron conductivity, also the amount of connected active material and the free surface area are correlated to the percolation probability. A decrease of the free surface area with compression, as supposed in experimental studies [23], was only found in few cases. During intercalation, the decrease becomes more pronounced, most likely due to increasing solid-solid contacts between AM particles. Even though the percolation probability is neglected in today's research, its importance should be revaluted considering the findings of this work, in particular for active material of poor electron conductivity (e.g. LMO and LFP). A determination of the percolation probability based on the concept of coordination number is unfeasible, as no universal critical coordination number was found.

Above the percolation threshold, the effective conductivities found numerically for the different assemblies were in a similar range and one order of magnitude smaller than the values predicted by Bruggeman's equation. Further, no clear correlation could be found to the directional macroscopic stress: the anisotropy, induced during calendering, does not necessarily reflect on the effective conductivity. Thus, a realistic estimation of effective transport properties for further microstructures can best be obtained with the Monte-Carlo methods as implemented in this work in form of a coupled approach of DEM and RN-models.

Considering all performed simulations, the microstructure with the highest amount of CB showed the best results: the low percolation threshold allows for low preloads, and thus, the stress increase during intercalation is the smallest. Further, smaller amounts of active material in combination with lower stress leads to a reduced solid-solid contact area, which, in turn, maintains a larger

active surface area. Here, an optimum between the positive effect on cell properties and its negative effect on power density needs to be found.

Finally, the simplifications in the modeling of the LIB electrode microstructure and their micromechanics were examined, and the influence of the most relevant ones were investigated further. Besides the main particle size distribution of AM and CB, size distributions within each phase seem to have negligible influence on the stress-load relationship. Additionally, the impact of more flexible boundary conditions was investigated. The difference in the stress development during intercalation in a completely constrained and a quasi free-standing electrode structure was demonstrated to be significant. This indicates the importance to further consider the relevant casing conditions in order to estimate the stress-development as well es the electrode expansion accurately. Furthermore, the impact of the visco-elastic material behavior of the binder phase was studied: Therefore, Burgers law was implemented as additional force law. Here, the distribution of the binder phase in the electrode structure and the loading velocity showed significant influence. Thus, for a more realistic stress-strain relationship, further knowledge regarding the distribution of this additional phase would be helpful. Concerning the loading rates, the elastic part of the Burgers law dominates the stress response for high rates; thus, the loading has to be slow enough to benefit most of the stress absorbing effect of the visco-elastic material. The dominance of the elastic part is relevant for calendering or very fast charging rate. For usually applied charging- or discharging-rates, on the other hand, the impact of the viscous material response was shown.

In conclusion, it can be said that the approach developed in the scope of this work offers a powerful tool to study the microstructural impact on parameters relevant for cell performance in detail. Comparison to the often applied analytic solutions demonstrated the importance of the more detailed consideration of the microstructure for the estimation of those parameters. Especially the variations caused by the manufacturing processes were significant, and those are only poorly represented with the standard methods. In addition to the more frequently performed microstructure modeling of the SOFC structures, the coupling with DEM enables us to reflect on the micromechnical changes, occurring in LIB electrodes. The importance of the percolation of CB was pointed out and can only be recommended for consideration in future LIB research. Further adaption of the DEM allows to additionally consider flexible boundary conditions, similar to experimental cells, as well as the influence of binder on the microstructure—properties which have been mostly neglected so far in research.

A. Derivation of Effective-Medium Approximations

For the derivation of the different effective-medium approximations used in this work, we consider a mixture of matrix phase with volume fraction ϕ_1 and spherical inclusions of with volume fraction ϕ_2, as described in section 3.1.1. We assume, that for a certain composition 0 the effective conductivity of this composition $\kappa_{\text{eff},0}$ is known. Thus it can be treat as a homogeneous medium and will be considered as matrix material in the following reflection.

Now, this medium 0 is slightly changed by substituting matrix material with a small volume fraction ϕ_i, where i can be either denoting phase 1 or 2. The changed effective conductivity $\kappa_{\text{eff},\Delta\phi_\text{i}}$ can be determined via Eq. 3.7, considering $\kappa_{\text{eff},0}$ as the conductivity of the matrix respectively the initial medium 0:

$$\frac{\kappa_{\text{eff},\Delta\phi_\text{i}} - \kappa_{\text{eff},0}}{\kappa_{\text{eff},\Delta\phi_\text{i}} + 2\kappa_{\text{eff},0}} = \phi_i \frac{\kappa_i - \kappa_{\text{eff},0}}{\kappa_i + 2\kappa_{\text{eff},0}}, \tag{A.1}$$

with κ_i as the bulk conductivity of the added volume fraction. Rewritten explicitly for $\kappa_{\text{eff},\Delta\phi_\text{i}}$, this leads to

$$\kappa_{\text{eff},\Delta\phi_\text{i}} = \kappa_{\text{eff},0} \frac{1 + 2\phi_i \frac{\kappa_i - \kappa_{\text{eff},0}}{\kappa_i + 2\kappa_{\text{eff},0}}}{1 - \phi_i \frac{\kappa_i - \kappa_{\text{eff},0}}{\kappa_i + 2\kappa_{\text{eff},0}}}. \tag{A.2}$$

By expanding Eq. A.2 in a Taylor's series about $\phi_i = 0$ considering only the the first two terms we obtain

$$\kappa_{\text{eff},\Delta\phi_\text{i}} = \kappa_{\text{eff},0}(1 + 3\phi_i \frac{\kappa_i - \kappa_{\text{eff},0}}{\kappa_i + 2\kappa_{\text{eff},0}}). \tag{A.3}$$

Based on this expression, both the self-consistent approximation (Eq. 3.8) as well as the differential approximation (Eq. 3.11) can be derived—based on different assumptions on the construction of the composite, as will be shown in the following.

A.1. Self-consistent approximation

For the sake of clarity, the volume fractions of an arbitrary binary mixture are denoted as ϕ_1 and ϕ_2 thereby. Due to the symmetry of the system, however, ϕ_1 and ϕ_2 can be interchanged with each other.

First, following Bruggeman's approach [70] to derive the *self-consistent effective-medium approximation* (Eq. 3.8), the volume fractions, ϕ_1 and ϕ_2, of the binary mixture are divided in arbitrary small subunits with the requirements that

$$\begin{aligned} \phi_1^* + \phi_1^{**} + \phi_1^{***} + ... &= \phi_1 \\ \phi_2^* + \phi_2^{**} + \phi_2^{***} + ... &= \phi_2, \end{aligned} \tag{A.4}$$

and $\phi_1 + \phi_2 = 1$.

Replacing a small amount of a homogeneous medium with an effective conductivity $\kappa_{\text{eff},0}$ by ϕ_1^* leads according to Eq. A.3 to

$$\kappa_{\text{eff}} = \kappa_{\text{eff},\Delta\phi_1} = \kappa_{\text{eff},0}(1 + 3\phi_1^* \frac{\kappa_1 - \kappa_{\text{eff},0}}{\kappa_1 + 2\kappa_{\text{eff},0}}). \tag{A.5}$$

Subsequently, such an amount of ϕ_2^* is used to replace matrix material, that the previous conductivity $\kappa_{\text{eff},0}$ is restored

$$\kappa_{\text{eff},\Delta\phi_2} = \kappa_{\text{eff},0} = \kappa_{\text{eff},\Delta\phi_1}(1 + 3\phi_2^* \frac{\kappa_2 - \kappa_{\text{eff},\Delta\phi_1}}{\kappa_2 + 2\kappa_{\text{eff},\Delta\phi_1}}). \tag{A.6}$$

Inserting Eq. A.6 in Eq. A.5 leads to

$$1 = (1 + 3\phi_2^* \frac{\kappa_2 - \kappa_{\text{eff}}}{\kappa_2 + 2\kappa_{\text{eff}}})(1 + 3\phi_1^* \frac{\kappa_1 - \kappa_{\text{eff}}(1 + 3\phi_2^* \frac{\kappa_2 - \kappa_{\text{eff}}}{\kappa_2 + 2\kappa_{\text{eff}}})}{\kappa_1 + 2\kappa_{\text{eff}}(1 + 3\phi_2^* \frac{\kappa_2 - \kappa_{\text{eff}}}{\kappa_2 + 2\kappa_{\text{eff}}})}). \tag{A.7}$$

Under the assumption of $\phi_2^* \times \phi_1^* \ll \phi_i^*$, this can be simplified to

$$0 = \phi_1^* \frac{\kappa_1 - \kappa_{\text{eff}}}{\kappa_1 + 2\kappa_{\text{eff}}} + \phi_2^* \frac{\kappa_2 - \kappa_{\text{eff}}}{\kappa_2 + 2\kappa_{\text{eff}}}. \tag{A.8}$$

This step is repeated until the complete initial matrix is replaced by volume fractions ϕ_1 and ϕ_2 (assuming that this adds up to the final volume fractions). Summing up the equations of the type of Eq. A.8 leads for a binary, unbiased and symmetric composition on average to Eq. 3.8.

A.2. Differential approximation

To derive the differential approximation (Eq. 3.11), the influence of an infinitesimal increment of ϕ_i on the effective conductivity is considered and calculated with Eq. A.3 [67]. To do so, we suppose that the effective conductivity $\kappa_{\text{eff},0}(\phi_2)$ of a two-phase composite is known for a certain value of ϕ_2, and then, we can treat $\kappa_{\text{eff},0}(\phi_2)$ as the composite host conductivity.

To calculate the influence of an infinitesimal increase of ϕ_2 on the effective conductivity, we need to replace a certain amount of phase 1 with phase 2. In a random and homogeneous composition, however, removing randomly a certain amount of the composition—to replace it with phase 2 material—always removes a part of the present phase 1 and phase 2. Under consideration of proportions, by adding $\Delta\phi_2$ only the amount $\Delta\phi_2 * \phi_1$ is changed. To actually increase the volume fraction ϕ_2 to $\phi_2 + \Delta\phi_2$ (by randomly replacing composite material with phase 2 material), the required amount of phase 2 material has to be calculated relative to ϕ_1; and thus, $\Delta\phi_2/\phi_1$ ($=\Delta\phi_2/(1-\phi_2)$) of the composite has to be replaced by phase 2 material in order to obtain a composite with $\phi_2 + \Delta\phi_2$.

Inserting this in Eq. A.3

$$\kappa_{\text{eff},\Delta\phi} - \kappa_{\text{eff},0} = 3\kappa_{\text{eff},0} \frac{\kappa_2 - \kappa_{\text{eff},0}}{\kappa_2 + 2\kappa_{\text{eff},0}} \frac{\Delta\phi_2}{1 - \phi_2}. \tag{A.9}$$

This becomes a differential equation for an infinitesimal small amount of inclusion ($\Delta\phi_2 \to 0$).

$$(1-\phi_2)\frac{d\kappa_{\text{eff}}}{d\phi_2} = 3\kappa_{\text{eff}}\frac{\kappa_2-\kappa_{\text{eff}}}{\kappa_2+2\kappa_{\text{eff}}} \tag{A.10}$$

Separation of variables (Eq. A.11) and transforming (Eq. A.12) leads to an expression that can be integrated analytically:

$$\frac{\kappa_2+2\kappa_{\text{eff}}}{3\kappa_{\text{eff}}(\kappa_2-\kappa_{\text{eff}})}d\kappa_{\text{eff}} = \frac{1}{1-\phi_2}d\phi_2 \tag{A.11}$$

$$\frac{(\kappa_2-\kappa_{\text{eff}})+3\kappa_{\text{eff}}}{3\kappa_{\text{eff}}(\kappa_2-\kappa_{\text{eff}})}d\kappa_{\text{eff}} = (\frac{1}{3\kappa_{\text{eff}}}+\frac{1}{\kappa_2-\kappa_{\text{eff}}})d\kappa_{\text{eff}} = \frac{1}{1-\phi_2}d\phi_2. \tag{A.12}$$

Integration of the indefinite expressions leads to

$$\frac{ln(3)}{3} - ln(\kappa_2-\kappa_{\text{eff}}) = -ln(1-\phi_2)+C \tag{A.13}$$

with an constant of integration C. With the initial condition $\kappa_{\text{eff}}(\phi_2=0)=\kappa_1$ C is defined as

$$C = \frac{1}{3}(ln(\kappa_1) - 3ln(\kappa_2-\kappa_1)). \tag{A.14}$$

Insert C and using exponential function leads to

$$(\frac{\kappa_2-\kappa_{\text{eff}}}{\kappa_2-\kappa_1})(\frac{\kappa_1}{\kappa_{\text{eff}}})^{1/3} = 1-\phi_2. \tag{A.15}$$

Finally, for phase 2 being isolating this can be transformed to Archie's law:

$$\frac{\kappa_{\text{eff}}}{\kappa_1} = \phi_1^{3/2}. \tag{A.16}$$

B. Coordination Number $Z_{k,j}$

The coordination number $Z_{k,j}$ for $k \neq j$ can be derived from the sum over all contacts in a binary composition of particles of phase k and l:

$$n_{ges} Z_0 = n_k Z_{k,k} + n_k Z_{k,j} + n_j Z_{j,j} + n_j Z_{j,k}. \tag{B.1}$$

Writing n_i/n_{ges} as ξ_i and considering the contact number conservation (Eq. 3.13), this leads to

$$Z_0 = \xi_k Z_{k,k} + \xi_j Z_{j,j} + 2\xi_k Z_{k,j}. \tag{B.2}$$

With Eq. 3.17 this can be rewritten as

$$0.5 Z_0 (1 - \xi_k \zeta_k - \xi_j \zeta_j) = \xi_k Z_{k,j}. \tag{B.3}$$

With $\zeta_k = 1 - \zeta_j$ this is

$$\begin{aligned} 0.5 Z_0 (1 - \xi_k (1 - \zeta_j) - \xi_j \zeta_j) &= \\ 0.5 Z_0 (1 - \xi_k + \xi_k \zeta_j - \xi_j \zeta_j) &= \xi_k Z_{k,j}, \end{aligned} \tag{B.4}$$

and with $\xi_k = 1 - \xi_j$ follows

$$\begin{aligned} 0.5 Z_0 (\xi_j + \xi_k \zeta_j - \xi_j \zeta_j) &= \\ 0.5 Z_0 (\xi_j + \zeta_j (\xi_k - \xi_j) &= \\ 0.5 Z_0 (\xi_j + \zeta_j (1 - \xi_j - \xi_j) &= \\ 0.5 Z_0 (\xi_j + \zeta_j (1 - 2\xi_j) &= \\ 0.5 Z_0 \zeta_j (\frac{\xi_j}{\zeta_j} + 1 - 2\xi_j) &= \xi_k Z_{k,j}. \end{aligned} \tag{B.5}$$

Substituting the surface-area fraction ζ_j with $\frac{\xi_j r_j^2}{\sum_i^M \xi_i 2_i^2}$ leads to

$$\begin{aligned}
0.5Z_0\zeta_j(\frac{\xi_j}{\frac{\xi_j r_j^2}{\sum_i^M \xi_i r_i^2}} + 1 - 2\xi_j) &= \\
0.5Z_0\zeta_j(\frac{\sum_i^M \xi_i r_i^2}{r_j^2} + 1 - 2\xi_j) &= \\
0.5Z_0\zeta_j(\frac{\sum_i^M \xi_i r_i^2 + r_j^2 - 2\xi_j r_j^2}{r_j^2}) &= \\
0.5Z_0\zeta_j(\frac{\sum_i^M \xi_i r_i^2 + r_j^2 - 2\xi_j r_j^2}{r_j^2}) &= \\
0.5Z_0\zeta_j(\frac{\xi_j r_j^2 + \xi_k r_k^2 + r_j^2 - 2\xi_j r_j^2}{r_j^2}) &= \\
0.5Z_0\zeta_j(\frac{\xi_k r_k^2 + r_j^2 - \xi_j r_j^2}{r_j^2}) &= \\
0.5Z_0\zeta_j(\frac{\xi_k r_k^2}{r_j^2} + 1 - \xi_j) &= \xi_k Z_{k,j}. \qquad \text{(B.6)}
\end{aligned}$$

With $\xi_k = 1 - \xi_j$ this leads to

$$\begin{aligned}
0.5Z_0\zeta_j(\xi_k(\frac{r_k^2}{r_j^2} + 1)) &= \xi_k Z_{k,j} \\
0.5Z_0\zeta_j(\frac{r_k^2}{r_j^2} + 1) &= Z_{k,j} \qquad \text{(B.7)}
\end{aligned}$$

C. Tanner-Fung-Virkar Model

In this chapter, the derivation of the effective cell resistance for a simplified electrode structure is given, closely following the calculations of Tanner et al. [135, 136]: As described, steady-state conditions lead for the simplified electrode structure shown in Fig. 5.18 to

$$I_1 + I_2 + I_3 = I_4, \tag{C.1}$$

with the subscripts indicating the boundaries through which the currents enter or leave the electrode. To derive an analytic expression of the effective cell resistance based on Eq. C.1, the current through each surface first needs to derived separately based on Ohm's law.

The current through facet 1 of length $w = (1 - \epsilon)l$ and thickness t is

$$I_1 = \frac{\Delta\varphi}{R_1} = -\frac{wt}{R_{ct}}(\varphi(h + d/2) - \varphi^s), \tag{C.2}$$

with $\varphi(h + d/2)$ as the potential slightly below facet 1. The resistance R_1 is converted in the area specific resistance R_{ct} of the surface in accordance with $R_1 = R_{ct}/(wt)$.

The current through facet 3 can be determined in analogy to I_1:

$$I_3 = -\frac{\epsilon lt}{R_{ct}}(\varphi(d/2) - \varphi^s), \tag{C.3}$$

with ϵl as length of facet 3 and $\varphi(d/2)$ as the potential slightly below it.

For calculation of the current through facet 2, the variation of the potential along the left side of facet 2 has to be considered. To do so, the electrode is divided in small volume elements of heights Δy, as shown in Fig. C.1. The currents I_C of all elements have to be determined and added up to I_2. For the small volume element, steady-state conditions lead to

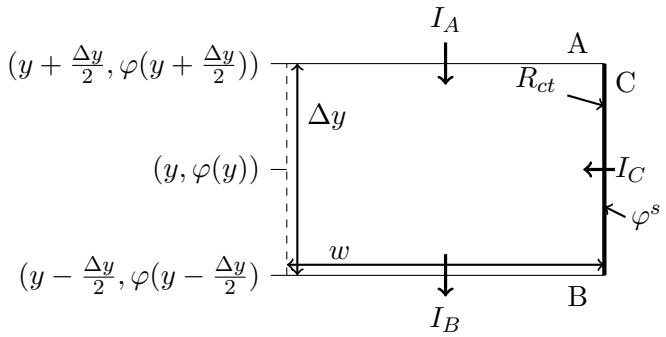

Figure C.1.: A section of the electrode shown in Fig. 5.18, considered to derive the current through facet 2

$$I_A + I_B + I_C = 0, \tag{C.4}$$

with the subscripts denoting the facets through which the current crosses. Again, the currents have to be determined separately for each facet. The ohmic behavior leads for facet A to

$$I_A = \frac{\varphi(y + \Delta y/2) - \varphi(y)}{R_A}. \tag{C.5}$$

Since the inner part of the columns is dense material, the resistance R_A can be calculated in accordance with Eq. 5.3 as

$$R_A = \frac{\rho h_A}{A_A} = \frac{\Delta y/2}{\kappa_{\text{bulk,YSZ}} wt}, \tag{C.6}$$

which leads to

$$I_A = \kappa_{\text{bulk,YSZ}} wt \frac{\varphi(y + \Delta y/2) - \varphi(y)}{\Delta y/2}. \tag{C.7}$$

For $\Delta y/2 \to 0$, this leads to the differential equation

$$I_A = \kappa_{\text{bulk,YSZ}} wt \frac{d\varphi}{dy} \mid_{y+\Delta y/2} . \tag{C.8}$$

The differential equation for I_B can be derived in analogy:

$$I_B = -\kappa_{\text{bulk,YSZ}} wt \frac{d\varphi}{dy} \mid_{y-\Delta y/2} . \tag{C.9}$$

Since we also assume ohmic behavior for the surface reactions, I_C is

$$I_C = \frac{\varphi^s - \varphi(y)}{R_C} = \frac{A_C}{R_{ct}}(\varphi^s - \varphi(y)) = \frac{t\Delta y}{R_{ct}}(\varphi^s - \varphi(y)), \tag{C.10}$$

with R_{ct} as the area specific charge-transfer resistance. Inserting Eqs. C.8, C.9 and C.10 in Eq. C.4 leads to

$$\kappa_{\text{bulk,YSZ}} wt \left(\frac{d\varphi}{dy} \mid_{y+\Delta y/2} - \frac{d\varphi}{dy} \mid_{y-\Delta y/2)}\right) + \frac{t\Delta y}{R_{ct}}(\varphi^s - \varphi(y)) = 0. \tag{C.11}$$

Dividing by $\frac{t\Delta y}{R_{ct}}$ gives

$$\kappa_{\text{bulk,YSZ}} w R_{ct} \frac{\left(\frac{d\varphi}{dy} \mid_{y+\Delta y/2} - \frac{d\varphi}{dy} \mid_{y-\Delta y/2}\right)}{\Delta y} + \varphi^s - \varphi(y) = 0. \tag{C.12}$$

With the definition

$$\frac{d^2\varphi}{dy^2} = \frac{\left(\frac{d\varphi}{dy} \mid_{y+\Delta y/2} - \frac{d\varphi}{dy} \mid_{y-\Delta y/2}\right)}{\Delta y}, \tag{C.13}$$

this can be written as

$$\kappa_{\text{bulk,YSZ}} w R_{ct} \frac{d^2\varphi}{dy^2} + \varphi^s = \varphi(y). \tag{C.14}$$

Integration of Eq. C.14 leads in general form to

$$\varphi(y) = \varphi^s + C_1 e^{\frac{-(y-d/2)}{a}} + C_2 e^{\frac{y-d/2}{a}} \tag{C.15}$$

with

$$a = \sqrt{\kappa_{\text{bulk,YSZ}} w R_{ct}} \tag{C.16}$$

As defined by the boundary conditions, immediately beneath facet 1 at $h + \frac{d}{2}$, the current across the surface I_1 (Eq. C.2) must be identical to the current inside the column $I_A \mid_{y=h+d/2}$ (Eq. C.8):

$$-\frac{wt}{R_{ct}}(\varphi(h+\frac{d}{2})) = \kappa_{\text{bulk,YSZ}} wt \frac{d\varphi(y)}{dy} \mid_{y=h+d/2} . \tag{C.17}$$

Under consideration of Eq. C.15, $\varphi(h + d/2)$ is $\varphi^0 + C_1 e^{-h/a} + C_2 e^{h/a}$. Further, $\frac{d\varphi(y)}{dy}|_{y=h+d/2}$ is $-\frac{1}{a}C_1 e^{-h/a} + \frac{1}{a}C_1 e^{h/a}$. Solving for C_2 gives

$$C_2 = C_1 \beta e^{-2h/a}, \tag{C.18}$$

with

$$\beta = \frac{\kappa_{\text{bulk,YSZ}} R_{ct} - a}{\kappa_{\text{bulk,YSZ}} R_{ct} + a}. \tag{C.19}$$

This leads to

$$\varphi(y) = \varphi^0 + C_1 e^{\frac{-(y-d/2)}{a}} + C_1 \beta e^{\frac{-2h+y-d/2}{a}}. \tag{C.20}$$

The current through a differential element of facet 2 is

$$dI_2 = -\frac{t}{R_{ct}}(\varphi(y) - \varphi^0)dy \tag{C.21}$$

With $\varphi(y)$ given in Eq. C.20 inserted in Eq. C.21, integration over the height h of the electrode leads to

$$I_2 = \frac{C_1 ta}{R_{ct}}(e^{-h/a} - 1)(1 + \beta e^{-h/a}) \tag{C.22}$$

Finally, the current through facet 4 is determined from the current density j_4, as the facet is not a surface, but in the middle of the dense electrolyte layer:

$$I_4 = ltj_4 = lt\kappa_{\text{bulk,YSZ}} \nabla\varphi_4. \tag{C.23}$$

Because of the assumption of horizontal equipotential lines, the electrolyte behaves like a dense block of material with a constant gradient in potential from $y = -d/2$ to $y = +d/2$. Therefore $\nabla\varphi$ at facet 4 is the same as $(\varphi(d/2) - \varphi(0))/d/2$ [136], which leads to

$$I_4 = lt\kappa_{\text{bulk,YSZ}} \frac{\varphi(d/2) - \varphi(0)}{d/2}. \tag{C.24}$$

For simplicity, $\varphi(0)$ was defined as 0. With $\varphi(y)$ defined by Eq. C.20 this leads to

$$I_4 = \frac{\kappa_{\text{bulk,YSZ}} lt}{d/2}(\varphi^s + C_1(1 + \beta e^{-2h/a})). \tag{C.25}$$

Further, Eq. C.2 and Eq. C.3 can be rewritten with $\varphi(y)$, defined by Eq. C.20, to

$$I_1 = -\frac{wt}{R_{ct}}(1 + \beta)C_1 e^{-2h/a} \tag{C.26}$$

for facet 1, and to

$$I_3 = -\frac{\epsilon lt}{R_{ct}} C_1(1 + \beta e^{-2h/a}) \tag{C.27}$$

for facet 3.

Substituting the terms C.22, C.26, C.27 and C.25 into Eq. C.1 allows to determine C_1. Due to the complexity of the equation, Mathematica was used to solve for C_1. Finally, substituting I_4 in Eq. 5.13 in section 5.5.1 allows to determine the area specific resistance of the electrode R_{eff}, as given in Eq. 5.14.

Bibliography

[1] M. Granovskii, I. Dincer, and M. A. Rosen. “Economic and environmental comparison of conventional, hybrid, electric and hydrogen fuel cell vehicles”. In: *Journal of Power Sources* 159.2 (206), pp. 1186–1193.

[2] J. Kunze and U. Stimming. “Electrochemical Versus Heat-Engine Energy Technology: A Tribute to Wilhelm Ostwald’s Visionary Statements”. In: *Energy & Environmental Science* 4 (2011), pp. 9230–9237.

[3] *http://de.statista.com: Wirkungsgrad von ausgewählten Stromspeichern*. Apr. 2014.

[4] E. D. Wachsman and K. T. Lee. “Lowering the Temperature of Solid Oxide Fuel Cells”. In: *Science* 334 (2011), pp. 935–939.

[5] A. Weber. “Entwicklung von Kathodenstrukturen für die Hochtemperatur-Brennstoffzelle SOFC”. PhD thesis. Universität Karlsruhe, 2002.

[6] W. Bujalski, C. M. Dikwal, and K. Kendall. “Cycling of three solid oxide fuel cell types”. In: *Journal of Power Sources* 171.1 (2007), pp. 96–100.

[7] M. F. Ashby and J. Polyblank. “Materials for Energy Storage Systems - a White Paper”. In: *GRANTA teaching resources* (2012).

[8] D. A. Noren and M. A. Hoffman. “Clarifying the Butler-Volmer equation and related approximations for calculating activation losses in solid oxide fuel cell models”. In: *Journal of Power Sources* 152 (2005), pp. 175–181.

[9] B. C. H. Steele and A. Heinzel. “Materials for fuel-cell technologies”. In: *Nature* 414.15 (2001), pp. 345–352.

[10] J.-M. Tarascon and M. Armandi. “Issues and challanges facing rechargeable lithium batteries”. In: *Nature* 414.15 (Nov. 2001), pp. 359–367.

[11] M. Yoshio, R. J. Brodd, and A. Kozawa, eds. *Lithium-Ion Batteries*. Springer New York, 2009.

[12] T. R. Ferguson and M. Z. Bazant. “Nonequilibrium thermodynamics of porous electrodes”. In: *Journal of Electrochemical Society* 159.12 (2012), A1967–A1985.

[13] K. Zaghib et al. “Safe and fast-charging Li-ion battery with long shelf life for power applications”. In: *Journal of Power Sources* 196.8 (2011), pp. 3949–3954.

[14] A. T. Duong and D. R. Mumm. “Microstructural Optimization by Tailoring Particle Sizes for LSM-YSZ Solid Oxide Fuel Cell Composite Cathodes”. In: *The Electrochemical Society* 159.1 (2011), B39–B52.

[15] C.-H. Lu and S.-W. Lin. “Influence of the particle size on the electrochemical properties of lithium manganese oxide”. In: *Journal of Power Sources* 97–98 (2001), pp. 458–460.

[16] W.-J. Zhang. “Structure and performance of $LiFePO_4$ cathode materials: A review”. In: *Journal of Power Sources* 196.6 (2011), pp. 2962–2970.

[17] J. S. Cronin et al. “Three-dimensional reconstruction and analysis of an entire solid oxide fuel cell by full-field transmission X-ray microscopy”. In: *Journal of Power Sources* 233.174 - 179 (2013).

[18] R. Dominko et al. “The role of carbon black distribution in cathodes for Li-ion batteries”. In: *Journal of Power Sources* 119-121 (2003), pp. 770–773.

[19] S. Kakaç, A. Pramuanjaroenkij, and X. Y. Zhou. “A review of numerical modeling of solid oxide fuel cells”. In: *International Journal of Hydrogen Energy* 32.7 (2007), pp. 761–786.

[20] J. S. Cronin et al. “Effect of Firing Temperature on LSM-YSZ Composite Cathodes: A Combined Three-Dimensional Microstructure and Impedance Spectroscopy Study”. In: *Journal of The Electrochemical Society* 159.4 (2012), B385–B393.

[21] C. Daniel. “Materials and processing for lithium-ion batteries”. In: *JOM* 60.9 (2008), pp. 43–48.

[22] H. Zheng et al. “Calendering effects on the physical and electrochemical properties of $Li[Ni_{1/3}Mn_{1/3}Co_{1/3}]O_2$ cathode”. In: *Journal of Power Sources* 208 (2012), pp. 52–57.

[23] J. Illig et al. “Separation of Charge Transfer and Contact Resistance in $LiFePO_4$-Cathodes by Impedance Modeling”. In: *Journal of The Electrochemical Society* 159.7 (2012), A952–A960.

[24] J. Vetter et al. “Ageing mechanisms in lithium-ion batteries”. In: *Journal of Power Sources* 147.1-2 (2005), pp. 269–281.

[25] D. Sarantaridis and A. Atkinson. “Redox Cycling of Ni-Based Solid Oxide Fuel Cell Anodes: A Review”. In: *Fuel Cells* 7.3 (2007), pp. 246–258.

[26] A. Mukhopadhyay and B. W. Sheldon. “Deformation and stress in electrode materials for Li-ion batteries”. In: *Progress in Materials Science* 63 (2014), pp. 58–116.

[27] M. Winter and R. J. Brodd. “What are batteries, fuel cells, and supercapacitors?” In: *Chemical reviews* 104.10 (2004), pp. 4245–4270.

[28] M. Park et al. “A review of conduction phenomena in Li-ion batteries”. In: *Journal of Power Sources* 195.24 (2010), pp. 7904–7929.

[29] L. Shen and Z. Chen. “Critical review of the impact of tortuosity on diffusion”. In: *Chemical Engineering Science* 62.14 (2007), pp. 3748–3755.

[30] M. Barrande, R. Bouchet, and R. Denoyel. “Tortuosity of Porous Particles”. In: *Analytical Chemistry* 79.23 (2007), pp. 9115–9121.

[31] M. B. Clennell. “Tortuosity: a guide through the maze”. In: *Geological Society, London, Special Publications* 122.1 (1997), pp. 299–344.

[32] I. V. Thorat et al. “Quantifying tortuosity in porous Li-ion battery materials”. In: *Journal of Power Sources* 188.2 (2009), pp. 592–600.

[33] P. Costamagna, P. Costa, and V. Antonucci. “Micro-modelling of solid oxide fuel cell electrodes”. In: *Electrochimica Acta* 43.3-4 (1998), pp. 375–394.

[34] B. Völker and R. M. McMeeking. “Impact of particle size ratio and volume fraction on effective material parameters and performance in solid oxide fuel cell electrodes”. In: *Journal of Power Sources* 215 (2012), pp. 199–215.

[35] J. Newman and W. Tiedemann. “Porous-electrode theory with battery applications”. In: *AIChE Journal* 21.1 (1975), pp. 25–41.

[36] P. R. Shearing, D. J. L. Brett, and N. P. Brandon. “Towards intelligent engineering of SOFC electrodes: a review of advanced microstructural characterisation techniques”. In: *International Materials Reviews* 55.6 (2010), pp. 347–363.

[37] S. Babinec et al. “Composite cathode structure/property relationships”. In: *Journal of Power Sources* 174.2 (2007), pp. 508–514.

[38] T. Saito. *Effect of Ni and ZrO_2 on anode performance in SOFC Micromodeling*. Tech. rep. Swiss Federal Office of Energy, Berne: Internal Energy Agency, 1992.

[39] F. Zhao and A. V. Virkar. “Dependence of polarization in anode-supported solid oxide fuel cells on various cell parameters”. In: *Journal of Power Sources* 141 (2005), pp. 79–95.

[40] Z. Chen et al. “Microstructure and electrical conductivity of NI/YSZ cermets for SOFC”. In: *16 th International conference on composite materials, Kyoto, Japan*. 2007.

[41] R. Clemmer and S. Corbin. “Influence of porous compositie microstructure on the processing and properties of solid oxide fuel cell anodes”. In: *Solid State Ionics* 166 (2004), pp. 251–259.

[42] K. Zaghib et al. “Effect of carbon source as additives in $LiFePO_4$ as positive electrode for lithium-ion batteries”. In: *Electrochemical and Solid-State Letters* 8.4 (2005), A207–A210.

[43] T. J. Patey et al. “Electrochemistry of $LiMn_2O_4$ nanoparticles made by flame spray pyrolysis”. In: *Phys. Chem. Chem. Phys.* 11.19 (2009), pp. 3756–3761.

[44] Z. Gao and S. A. Barnett. “Effects of Reduced Firing Temperature on Anode-Supported Solid Oxide Fuel Cells”. In: *Journal of The Electrochemical Society* 161.5 (2014), F600–F604.

[45] T. Suzuki et al. “Impact of Anode Microstructure on Solid Oxide Fuel Cells”. In: *Science* 325.5942 (2009), pp. 852–855.

[46] A. van Bommel and R. Divigalpitiya. “Effect of Calendering $LiFePO_4$ Electrodes”. In: *Journal of Electrochemical Society* 159.11 (2012), A1791–1795.

[47] M. Mogensen and S. Skaarup. “Kinetic and geometric aspects of solid oxide fuel cell electrodes”. In: *Solid State Ionics* 86-88 (1996), pp. 1151–1160.

[48] D. J. L. Brett et al. “What Happens Inside a Fuel Cell? Developing an Experimental Functional Map of Fuel Cell Performance”. In: *ChemPhysChem* 11.13 (2010), pp. 2714–2731.

[49] J. W. Fergus. “Recent developments in cathode materials for lithium ion batteries”. In: *Journal of Power Sources* 195.4 (2010), pp. 939–954.

[50] J. R. Wilson et al. “Three-dimensional reconstruction of a solid-oxide fuel-cell anode”. In: *Nature materials* 5.7 (2006), pp. 541–544.

[51] A. P. Cocco et al. “Three-dimensional microstructural imaging methods for energy materials”. In: *Physical Chemistry Chemical Physics* 15.39 (2013), pp. 16377–16407.

[52] L. A. Giannuzzi and F. A. Stevie. *Introduction to focused ion beams: instrumentation, theory, techniques and practice*. Springer, 2005.

[53] J. Izzo Jr. et al. “Nondestructive reconstruction and analysis of SOFC anodes using X-ray computed tomography at sub-50 nm resolution”. In: *Journal of the Electrochemical Society* 155.5 (2008), B504–B508.

[54] J. R. Wilson et al. “Effect of composition of $La_0.8Sr_0.2MnO_3$-Y_2O_3-stabilized $Zr0_2$ cathodes: Correlating three-dimensional microstructure and polarization resistance”. In: *Journal of Power Sources* 195.7 (2010), pp. 1829–1840.

[55] H. Zheng et al. “Cathode Performance as a Function of Inactive Materials and Void Fractions”. In: *Journal of Electrochemical Society* 157.10 (2010), A1060–A1066.

[56] M. M. Gaberšček et al. “The Importance of Interphase Contacts in Li-ion Electrodes: The Meaning of the High-Frequency Impedance Arc”. In: *Electrochemical and Solid-State Letters* 11.10 (2008), A170–A174.

[57] Y.-H. Chen et al. “Porous cathode optimization for lithium cells: Ionic and electronic conductivity, capacity, and selection of materials”. In: *Journal of Power Sources* 195 (2010), pp. 2851–2862.

[58] X. Qi et al. “Understanding the influence of conductive carbon additives surface area on the rate performance of $LiFePO_4$ cathodes for lithium ion batteries”. In: *Carbon* 64 (2013), pp. 334–340.

[59] R. Dominko et al. “Influence of carbon black distribution on performance of oxide cathodes for Li-ion batteries”. In: *Electrochimica Acta* 48 (2003), pp. 3709–3716.

[60] M. G. Lazarraga et al. “$LiMn_2O_4$-based composites processed by a chemical-route: Microstructural, electrical, electrochemical, and mechanical characterization”. In: *Journal of Power Sources* 115.2 (2003), pp. 315–322.

[61] H. Zheng et al. “Cooperation between Active Material, Polymeric Binder and Conductive Carbon Additive in Lithium Ion Battery Cathode”. In: *The Journal of Physical Chemistry C* 116.7 (2012), pp. 4875–4882.

[62] M. Ebner et al. “X-Ray Tomography of Porous, Transition Metal Oxide Based Lithium Ion Battery Electrodes”. In: *Advanced Energy Materials* 3.7 (2013), pp. 845–850.

[63] T. Hutzenlaub et al. “Three-Dimensional Reconstruction of a $LiCoO_2$ Li-Ion Battery Cathode”. In: *Electrochemical and Solid-State Letters* 15.3 (2012), A33–A36.

[64] M. Wang and N. Pan. “Predictions of effective physical properties of complex multiphase materials”. In: *Materials Science and Engineering: R: Reports* 63.1 (2008), pp. 1–30.

[65] R. E. Meredith and C. W. Tobias. “Conduction in heterogeneous Systems”. In: *Advances in electrochemistry and electrochemical engineering*. Ed. by C. W. Tobias. Vol. 2. Interscience Publishers, 1962. Chap. 2, pp. 15–48.

[66] T. C. Choy. *Effective medium theory: principles and applications*. 102. Oxford University Press, 1999.

[67] S. Torquato. *Random heterogeneous materials: microstructure and macroscopic properties*. Interdisciplinary applied mathematics. New York: Springer, 2002.

[68] Z. Hashin and S. Shtrikman. “A Variational Approach to the Theory of the Effective Magnetic Permeability of Multiphase Materials”. In: *Journal of Applied Physics* 33.10 (1962), pp. 3125–3131.

[69] J. K. Carson et al. “Thermal conductivity bounds for isotropic, porous materials”. In: *International Journal of Heat and Mass Transfer* 48 (2005), pp. 2150–2158.

[70] D. A. G. Bruggeman. “Berechnung verschiedener physikalischer Konstanten von heterogenen Substanzen. I. Dielektrizitätskonstanten und Leitfähigkeiten der Mischkörper aus isotropen Substanzen”. In: *Annalen der Physik* 416.7 (1935), pp. 636–664.

[71] R. B. MacMullin and G. A. Muccini. “Characteristics of porous beds and structures”. In: *AIChE Journal* 2.3 (1956), pp. 393–403.

[72] M. Doyle et al. “Comparison of Modeling Predictions with Experimental Data from Plastic Lithium Ion Cells”. In: *Journal of The Electrochemical Society* 143.6 (1996), pp. 1890–1903.

[73] J. Christensen. “Modeling Diffusion-Induced Stress in Li-Ion Cells with Porous Electrodes”. In: *Journal of The Electrochemical Society* 157.3 (2010), A366–A380.

[74] R. E. García et al. “Microstructural Modeling and Design of Rechargeable Lithium-Ion Batteries”. In: *Journal of The Electrochemical Society* 152.1 (2005), A255–A263.

[75] Y.-H. Chen et al. “Selection of Conductive Additives in Li-Ion Battery Cathodes”. In: *Journal of the Electrochemical Society* 154.10 (2007), A978–A986.

[76] D. Stauffer and A. Aharony. *Introduction to percolation theory; rev. version*. London: Taylor and Francis, 1991.

[77] S. R. Broadbent and J. M. Hammersley. “Percolation processes”. In: *Mathematical Proceedings of the Cambridge Philosophical Society* 53.3 (1957), pp. 629–641.

[78] J. Roussenq et al. “Size dependence of the percolation threshold of square and triangular network”. In: *Journal de Physique Lettres* 37.5 (1976), pp. 99–101.

[79] M. Sahini and M. Sahimi. *Applications of percolation theory*. CRC Press, 1994.

[80] M. J. Powell. “Site percolation in randomly packed spheres”. In: *Phys. Rev. B* 20.10 (1979), pp. 4194–4198.

[81] A. Hunt and R. Ewing. “Percolation Theory: Topology and Structure”. In: *Percolation Theory for Flow in Porous Media*. Vol. 771. Lecture Notes in Physics. Springer Berlin Heidelberg, 2009, pp. 1–36.

[82] J. Fitzpatrick, R. Malt, and F. Spaepen. “Percolation theory and the conductivity of random close packed mixtures of hard spheres”. In: *Physics Letters A* 47.3 (1974), pp. 207–208.

[83] L. Oger et al. “Properties of disordered sphere packings II. Electrical properties of mixtures of conducting and insulating spheres of different sizes”. In: *Powder Technology* 46.2-3 (1986), pp. 133–140.

[84] D. Bouvard and F. Lange. “Relation between percolation and particle coordination in binary powder mixtures”. In: *Acta metall. mater.* 39.12 (1991), pp. 3083–3090.

[85] L. Oger et al. “Properties of disordered sphere packings I. Geometric structure: Statistical model, numerical simulations and experimental results”. In: *Powder Technology* 46.2-3 (1986), pp. 121–131.

[86] C.-H. Kuo and P. K. Gupta. “Rigidity and conductivity percolation threshold in particulate composites”. In: *Acta metall. mater.* 43.1 (1995), pp. 397–403.

[87] M. J. Powell. “Site percolation in random networks”. In: *Phys. Rev. B* 21.8 (1980), pp. 3725–3728.

[88] A. Bertei and C. Nicolella. “A comparative study and an extended theory of percolation for random packings of rigid spheres”. In: *Powder Technology* 213 (2011), pp. 100–108.

[89] D. Chen et al. “Percolation theory to predict effective properties of solid oxide fuel-cell composite electrodes”. In: *Journal of Power Sources* 191 (2009), pp. 240–252.

[90] M. Suzuki and T. Oshima. “Co-ordination number of a multi-component randomly packed bed of spheres with size distribution”. In: *Powder Technology* 44.3 (1985), pp. 213–218.

[91] D. Pinson et al. “Coordination number of binary mixtures of spheres”. In: *Journal of Physics D: Applied Physics* 31.4 (1998), p. 457.

[92] C. Martin and D. Bouvard. “Isostatic compaction of bimodal powder mixtures and composites”. In: *International Journal of Mechanical Sciences* 46.6 (2004), pp. 907–927.

[93] A. Bertei et al. “Percolating behavior of sintered random packings of spheres”. In: *Powder Technology* 231 (2012), pp. 44–53.

[94] H. F. Fischmeister, E. Arzt, and L. R. Olsson. “Particle deformation and sliding during compaction of spherical powders: a study by quantitative metallography”. In: *Powder Metallurgy* 21.4 (1987), pp. 179–187.

[95] A. Bertei and C. Nicolella. “Percolation theory in SOFC composite electrodes: Effects of porosity and particle size distribution on effective properties”. In: *Journal of Power Sources* 196.22 (2011), pp. 9429–9436.

[96] A. K. Opitz et al. “Thin film cathodes in SOFC research: How to identify oxygen reduction pathways?” In: *Journal of Materials Research* 28.16 (2013), pp. 2085–2105.

[97] M. Shishkin and T. Ziegler. “Direct modeling of the electrochemistry in the three-phase boundary of solid oxide fuel cell anodes by density functional theory: a critical overview”. In: *Phys. Chem. Chem. Phys.* 16.5 (2014), pp. 1798–1808.

[98] J. Fleig. “Solid oxide fuel cell cathodes: polarization mechanisms and modeling of the electrochemical performance”. In: *Annual Review of Materials Research* 33.1 (2003), pp. 361–382.

[99] X. Ge, C. Fu, and S. Chan. “Three phase boundaries and electrochemically active zones of lanthanum strontium vanadate-yttria-stabilized zirconia anodes in solid oxide fuel cells”. In: *Electrochimica Acta* 56.17 (2011), pp. 5947–5953.

[100] K. N. Grew and W. K. Chiu. “A review of modeling and simulation techniques across the length scales for the solid oxide fuel cell”. In: *Journal of Power Sources* 199 (2012), pp. 1–13.

[101] S. Sunde. “Monte Carlo Simulations of Conductivity of Composite Electrodes for Solid Oxide Fuel Cells”. In: *Journal of The Electrochemical Society* 143.3 (1996), pp. 1123–1132.

[102] S. Sunde. “Simulations of Composite Electrodes in Fuel Cells”. In: *Journal of Electoceramics* 5.2 (2000), pp. 153–182.

[103] A. Gupta et al. “Effective Transport Properties of $LiMn_2O_4$ Electrode via Particle-Scale Modeling”. In: *Journal of The Electrochemical Society* 158.5 (2011), A487–A497.

[104] A. Bertei, B. Nucci, and C. Nicolella. “Microstructural modeling for prediction of transport properties and electrochemical performance in SOFC composite electrodes”. In: *Chemical Engineering Science* 101 (2013), pp. 175–190.

[105] J. Sanyal et al. “A particle-based model for predicting the effective conductivities of composite electrodes”. In: *Journal of Power Sources* 195.19 (2010), pp. 6671–6679.

[106] D.-W. Chung et al. “Particle Size Polydispersity in Li-Ion Batteries”. In: *Journal of The Electrochemical Society* 161.3 (2014), A422–A430.

[107] B. Kenney et al. “Computation of TPB length, surface area and pore size from numerical reconstruction of composite solid oxide fuel cell electrodes”. In: *Journal of Power Sources* 189.2 (2009), pp. 1051–1059.

[108] A. Z. Zinchenko. “Algorithm for Random close packing of spheres with periodic boundary conditions”. In: *Journal of Computational Physics* 114 (1994), pp. 298–307.

[109] W. Jodrey and E. Tory. “Computer simulation of close random packing of equal spheres”. In: *Pysical Review A* 32.4 (1985), pp. 2347–2351.

[110] S. Torquato, T. M. Truskett, and P. Debenedetti. “Is random close packing of spheres well defined?” In: *Physical Review Letters* 84.10 (2000), pp. 2064–2067.

[111] N. Xu, J. Blawzdziewicz, and C. S. O’Hern. “Random close packing revisited: Ways to pack frictionless disks”. In: *Physical Review E* 71 (2005),

[112] G. Y. Onoda and E. G. Liniger. “Random loose packings of uniform spheres and the dilatancy onset”. In: *Phys. Rev. Lett.* 64.22 (1990), pp. 2727–2730.

[113] Y.-B. Yi, C.-W. Wang, and A. M. Sastry. “Compression of packed particulate systems: simulations and experiments in graphitic Li-ion anodes”. In: *Journal of Engineering Materials and Technology* 128.1 (2006), pp. 73–80.

[114] C. O’Sullivan. *Particulate discrete element modelling: a geomechanics perspective*. Applied geotechnics ; 4. Spon Press, 2011.

[115] C. Song, P. Wang, and H. A. Makse. “A phase diagram for jammed matter”. In: *Nature* 453.7195 (2008), pp. 629–632.

[116] Y. Gan. “Thermo-Mechanics of Pebble Beds in Fusion Blankets”. PhD thesis. Insitut für Materialforschung, Forschungszentrum Karlsruhe, 2008.

[117] Y. Gan, M. Kamlah, and J. Reimann. “Computer simulation of packing structure in pebble beds”. In: *Fusion Engineering and Design* 85.10–12 (Dec. 2010), pp. 1782–1787. DOI: http://dx.doi.org/10.1016/j.fusengdes.2010.05.042.

[118] J. Ott et al. “A micromechanical model for effective conductivity in granular electrode structures”. In: *Acta Mechanica Sinica* 29.5 (2013), pp. 682–698.

[119] A. M. M. William Johnston. *A Transition to Advanced Mathematics : A Survey Course: A Survey Course*. Oxford University Press, USA, 2008.

[120] F. Babalievski. “Cluster counting: the ”Hoshen-Kopelman” algorithm versus spanning tree approaches”. In: *International Journal of Modern Physics C* 9.1 (1998), pp. 43–60.

[121] J. Hoshen and R. Kopelman. “Percolation and cluster distribution. I. Cluster multiple labeling technique and critical concentration algorithm”. In: *Phys. Rev. B* 14 (1976), pp. 3438–3445.

[122] A. Al-Futaisi and T. Patzek. “Extension of Hoshen-Kopelman algorithm to non-lattice environments”. In: *Physica A* 231 (2003), pp. 665–678.

[123] T. Metzger, A. Irawan, and E. Tsotsas. “Remarks on the paper ”Extension of Hoshen-Kopelman algorithm to non-lattice environments” by A. Al-Futaisi and T.W. Patzek, Physica A 321 (2003) 665-678”. In: *Physica A* 363 (2006), pp. 558–560.

[124] T. Hutzenlaub et al. “Three-dimensional electrochemical Li-ion battery modeling featuring a focused ion-beam/scanning electron microscopy based three-phase reconstruction of a $LiCoO_2$ cathode”. In: *Electrochimica Acta* 115 (2014), pp. 131–139.

[125] J. Golbert, C. Adjiman, and N. Brandon. “Microstructural modeling of solid oxide fuel cell anodes”. In: *Industrial and Engineering Chemistry Research* 47.20 (2008), pp. 7693–7699.

[126] J. Tobochnik, D. Lain, and G. Wilson. “Randon-walk calculations of conductivity in continuum percolation”. In: *Physical Review A* 41.6 (1990), pp. 3052–3058.

[127] A. Einstein. *Investigations on the Theory of the Brownian Movement*. Courier Dover Publications, 1956.

[128] G. Kirchhoff. “Über den Durchgang eines elektrischen Stromes durch eine Ebene, insbesondere durch eine kreisförmige”. In: *Annalen der Physik und Chemie* 64.4 (1845), pp. 497–519.

[129] H. Frohne and F. Moeller, eds. *Moeller Grundlagen der Elektrotechnik*. 22nd ed. Studium. Wiesbaden: Vieweg + Teubner, 2011.

[130] C. Argento and D. Bouvard. “Modeling the effective thermal conductivity of random packing of spheres through densification”. In: *International Journal of Heat and Mass Transfer* 39.7 (1996), pp. 1343–1350.

[131] B. Jacob and G. Guennebaud. *Eigen: http://eigen.tuxfamily.org/*.

[132] L. Schneider et al. “Discrete modelling of the electrochemical performance of SOFC electrodes”. In: *Electrochimica Acta* 52 (2006), pp. 314–324.

[133] A. V. Kyrylyuk, A. Wouterse, and A. P. Philipse. “Percolation and jamming in random heterogeneous materials with competing length scales”. In: *Trends in Colloid and Interface Science XXIII*. Springer, 2010, pp. 29–33.

[134] J. D. Nicholas et al. “Use of the Simple Infiltrated Microstructure Polarization Loss Estimation (SIMPLE) model to describe the performance of nano-composite solid oxide fuel cell cathodes”. In: *Phys. Chem. Chem. Phys.* 14.44 (2012), pp. 15379–15392.

[135] C. W. Tanner, K. Fung, and A. V. Virkar. “The Effect of Porous Composite Electrode Structure on Solid Oxide Fuel Cell Performance: I. Theoretical Analysis”. In: *Journal of The Electrochemical Society* 144.1 (1997), pp. 21–30.

[136] J. D. Nicholas. *Derivation of the Simple Infiltrated Polarization Estimation Loss Model*.

[137] P. A. Cundall and O. D. L. Strack. “A discrete numerical model for granular assemblies”. In: *Geotechnique* 29.1 (1979), pp. 47–65.

[138] Y. Gan and M. Kamlah. “Discrete element modelling of pebble beds: With application to uniaxial compression tests of ceramic breeder pebble beds”. In: *Journal of Mechanics and Physics of Solids* 58 (2010), pp. 129–144.

[139] S. Zhao. “Multiscale Modeling of Thermomechanical Properties of Ceramic Pebbles”. PhD thesis. Karlsruhe Institute of Technology (KIT), 2010.

[140] A. Awarke et al. “Percolation-tunneling modeling for the study of electric conductivity in $LiFePO_4$ based Li-ion battery cathodes”. In: *Journal of Power Sources* 196 (2011), pp. 405–411.

[141] A. Paolone et al. “The charge order transition and elastic/anelastic properties of $LiMn_2O_4$”. In: *Journal of Physics: Condensed Matter* 15.3 (2003), pp. 457–465.

[142] J. Zhu, K. Zeng, and L. Lu. “Cycling effects on surface morphology, nanomechanical and interfacial reliability of $LiMn_2O_4$ cathode in thin film lithium ion batteries”. In: *Electrochimica Acta* 68 (2012), pp. 52–59.

[143] M. Huttin and M. Kamlah. “Phase-field modeling of stress generation in electrode particles of lithium ion batteries”. In: *Applied Physics Letters* 101.13 (2012), pp. 133902–133902.

[144] X. Zhang, W. Shyy, and A. Sastry. “Numerical Simulation of Intercalation-Induced Stress in Li-Ion Battery Electrode Particles”. In: *Journal of the Electrochemical Society* 154.10 (2007), A910–A916.

[145] J. Sugiyamat, T. Tamura, and H. Yamauchi. “Elastic/anelastic behaviour during the phase transition in spinel $LiMn_2O_4$”. In: *Journal of Physics: Condensed Matter* 7.50 (1995), pp. 9755–9764.

[146] D. Leisen. “Nanoindentierung als Methode zur mikromechanischen Charakterisierung von Li-Batteriewerkstoffen”. MA thesis. Karlsruhe Institute of Technology (KIT), 2010.

[147] D. Leisen et al. “A novel and simple approach for characterizing the Young’s modulus of single particles in a soft matrix by nanoindentation”. In: *Journal of Materials Research* 27.24 (2012), pp. 3073–3082.

[148] H.-Y. Amanieu et al. “Mechanical property measurements of heterogeneous materials by selective nanoindentation: Application to $LiMn_2O_4$ cathode”. In: *Materials Science and Engineering: A* 593 (2014), pp. 92–102.

[149] T. Maxisch and G. Ceder. “Elastic properties of olivine Li_xFePO_4 from first principles”. In: *Phys. Rev. B* 73.17 (2006),

[150] Y. Qi et al. “Threefold Increase in the Young’s Modulus of Graphite Negative Electrode during Lithium Intercalation”. In: *Journal of The Electrochemical Society* 157.5 (2010), A558–A566.

[151] V. L. Popov, ed. *Kontaktmechanik und Reibung : Ein Lehr- und Anwendungsbuch von der Nanotribologie bis zur numerischen Simulation*. Springer Berlin Heidelberg, 2009.

[152] M. Huttin. “Phase-field modeling of the influence of mechanical stresses on charging and discharging processes in lithium ion batteries”. PhD thesis. Karlsruhe Institute of Technology (KIT), 2014.

[153] H. Gabrisch, J. Wilcox, and M. M. Doeff. “TEM Study of Fracturing in Spherical and Plate-like $LiFePO_4$ Particles”. In: *Electrochemical and Solid-State Letters* 11.3 (2008), A25–A29.

[154] D. Wang et al. “Cracking causing cyclic instability of $LiFePO_4$ cathode material”. In: *Journal of Power Sources* 140.1 (2005), pp. 125–128.

[155] A. H. Wiedemann et al. “Effects of three-dimensional cathode microstructure on the performance of lithium-ion battery cathodes”. In: *Electrochimica Acta* 88 (2013), pp. 580–588.

[156] D. Chen. “Microscopic Investigations of Degradation in Lithium-Ion Batteries”. PhD thesis. Karlsruhe Institute of Technology (KIT), 2012.

[157] A. Mukhopadhyay et al. “Stress development due to surface processes in graphite electrodes for Li-ion batteries: A first report”. In: *Electrochimica Acta* 66 (2012), pp. 28–37.

[158] Z. Choi, D. Kramer, and R. Mönig. “Correlation of stress and structural evolution in $Li_4Ti_5O_{12}$ -based electrodes for lithium ion batteries”. In: *Journal of Power Sources* 240 (2013), pp. 245–251.

[159] V. Sethuraman et al. “Real-time stress measurements in lithium-ion battery negative-electrodes”. In: *Journal of Power Sources* 206 (2012), pp. 334–342.

[160] E. K. Rahani and V. B. Shenoy. “Role of Plastic Deformation of Binder on Stress Evolution during Charging and Discharging in Lithium-Ion Battery Negative Electrodes”. In: *Journal of The Electrochemical Society* 160.8 (2013), A1153–A1162.

[161] W. Wu et al. “A Microstructural Resolved Model for the Stress Analysis of Lithium-Ion Batteries”. In: *Journal of The Electrochemical Society* 161.5 (2014), A803–A813.

[162] A. Awarke et al. “Quantifying the effects of strains on the conductivity and porosity of ”$LiFePO_4$” based ”Li”-ion composite cathodes using a multi-scale approach”. In: *Computational Materials Science* 50.3 (2011), pp. 871–879.

[163] A. K. Padhi, K. S. Nanjundaswamy, and J. B. Goodenough. “Phospho-olivines as Positive-Electrode Materials for Rechargeable Lithium Batteries”. In: *Journal of The Electrochemical Society* 144.4 (1997), pp. 1188–1194.

[164] Y. Gu et al. “Synthesis of 3D-hiearchical $LiMPO_4$ (M = Fe, Mn) microstructures as cathode materials for lithium-ion batteries”. In: *CrystEngComm* 15.24 (2013), pp. 4865–4870.

[165] G. E. P. Box and M. E. Muller. “A Note on the Generation of Random Normal Deviates”. In: *The Annals of Mathematical Statistics* 29.2 (1958), pp. 610–611.

[166] J. R. Bell. “Algorithm 334: Normal Random Deviates”. In: *Commun. ACM* 11.7 (1968), p. 498.

[167] R. Knop. “Remark on Algorithm 334 [G5]: Normal Random Deviates”. In: *Commun. ACM* 12.5 (1969), p. 281.

[168] J. Gere. *Mechanics of materials*. 6th ed. Brooks/Cole, 2004.

[169] M. F. Ashby and D. R. H. Jones. *Metalle, Keramiken und Gläser, Kunststoffe und Verbundwerkstoffe*. Ed. by M. Heinzelmann. 3. Elsevier GmbH, 2006.

[170] J. Rösler, H. Harders, and M. Bäker. *Mechanisches Verhalten der Werkstoffe*. Teubner Verlag, 2006.

[171] S. J. Harris et al. “Direct in situ measurements of Li transport in Li-ion battery negative electrodes”. In: *Chemical Physics Letters* 485.4-6 (2010), pp. 265–274.

[172] K. Zhao et al. “Fracture of electrodes in lithium-ion batteries caused by fast charging”. In: *Journal of Applied Physics* 108.7 (2010), p. 073517.

[173] I. M. Ward and J. Sweeney. *An Introduction to the Mechanical Properties of Solid Polymers*. Vol. 2nd Edition. John Wiley and Sons, Ltd, 2004.

[174] V. Goodarzi et al. “Prediction of long-term mechanical properties of PVDF/$BaTiO_3$ nanocomposite”. In: *Journal of Applied Polymer Science* 131.16 (2014).

[175] J. Chen. “Discrete Element Method (DEM) Analyses for Hot-Mixed Asphalt (HMA) Mixture Compaction”. PhD thesis. University of Tennessee - Knoxville, 2011.

[176] Y. Liu, Q. Dai, and Z. You. “Viscoelastic model for discrete element simulation of asphalt mixtures”. In: *Journal of engineering mechanics* 135.4 (2009), pp. 324–333.

[177] W. Bauer. *calendering velocity*. private communication. July 2015.

Acknowledgment

The present thesis was realized at the Institute for Applied Materials (IAM-WBM) of the Karlsruhe Institute of Technology (KIT). Parts of this work were performed at the Department of Engineering of the University of California, Santa Barbara (UCSB) and at the School of Civil Engineering of the University of Sydney.

During my Ph.D., I met so many people who have directly and indirectly contributed to this work; and at this place I want to express them all my gratitude. First, I want to thank my supervisor Prof. Dr. Marc Kamlah most sincerely for giving me the opportunity to work on such an interesting project. I am especially grateful to him for the many helpful discussions, for giving me the freedom to explore so many aspects of my project, and for his openness to new ideas. Further, I would like to thank the members of my thesis comittee: Prof. Dr. H. J. Seifert and Prof. Dr.-Ing. T. Schulenberg. I am especially thankful to Prof. Dr. H. J. Seifert for accepting to be the second referee.

Additionally, I would like to thank all my collaborators. I am very grateful to Prof. Dr. Robert M. McMeeking and Benjamin Völker for inviting me to Santa Barbara. They introduced me to the topic of fuel cells and percolation—I am very grateful that I could learn so much from them. Additionally, I want to thank them for their warm hospitality and the great time I had there. Further, I want to thank Yixiang Gan for his enormous help with the Discrete Element Modeling, the fruitful discussions on granular materials, and his warm hospitality during my stay in Sydney. At this point, I would also like to thank the members of his group for their hospitality and entertainment. Furthermore, I want to thank Lothar Kunz for giving me the opportunity to work with him for a Bosch project—it was a great experience to get insight in present questions outside the scientific world.

Finally, I would like to thank all my colleagues for the good atmosphere at the institute, for friendships and all the fun moments, and also for supporting me whenever I needed help.